

Electronic Thesis and Dissertation Repository

---

5-26-2023 2:00 PM

## Advancing non-invasive imaging techniques for tracking cellular therapeutics in vivo

Olivia C. Sehl, *University of Western Ontario*

Supervisor: Foster, Paula J., *The University of Western Ontario*

A thesis submitted in partial fulfillment of the requirements for the Doctor of Philosophy degree in Medical Biophysics

© Olivia C. Sehl 2023

Follow this and additional works at: <https://ir.lib.uwo.ca/etd>



Part of the [Medical Biophysics Commons](#)

---

### Recommended Citation

Sehl, Olivia C., "Advancing non-invasive imaging techniques for tracking cellular therapeutics in vivo" (2023). *Electronic Thesis and Dissertation Repository*. 9305.

<https://ir.lib.uwo.ca/etd/9305>

This Dissertation/Thesis is brought to you for free and open access by Scholarship@Western. It has been accepted for inclusion in Electronic Thesis and Dissertation Repository by an authorized administrator of Scholarship@Western. For more information, please contact [wlsadmin@uwo.ca](mailto:wlsadmin@uwo.ca).

## Abstract

Cell therapies, including mesenchymal stem cells (MSC) and regulatory T cells (Tregs) have shown potent and long-lasting therapeutic benefit in several disease applications. Unfortunately, the effectiveness of these therapies is variable and following administration, it is largely unknown where therapeutic cells traffic and how many persist over time. This thesis aims to advance and compare iron- and fluorine-19 ( $^{19}\text{F}$ )-based magnetic resonance imaging (MRI) and magnetic particle imaging (MPI) for therapeutic cell tracking.

First, we developed a trimodal imaging approach to study MSC fate *in vivo*. In a mouse model, iron-labeled MSC were detected by MRI and MPI, and each modality provided unique information on MSC quantity (MPI) and anatomical localization (MPI) *in vivo*. In these same mice,  $^{19}\text{F}$  MRI was used to assess inflammatory influx to the injection site after intravenous administration of  $^{19}\text{F}$ -perfluorocarbon agent. Next, the sensitivity and cellular detection limits of  $^{19}\text{F}$  MRI were compared to MPI. MPI showed superior sensitivity, as fewer iron-labeled cells could be detected with MPI (4000 MSCs) compared to  $^{19}\text{F}$ -labeled cells with  $^{19}\text{F}$  MRI (256,000 MSCs) using the same imaging time. For cell tracking, estimation of cell number is critical, so we sought to develop and test four methods to select and quantify MPI signal from an image. In this project, it is demonstrated that while MPI signal scales directly linear with the amount of iron present, 3 users showed more accurate and precise quantification when they considered a larger area for each signal in the image. In the final chapter, we demonstrate a clinically-applicable  $^{19}\text{F}$  MRI imaging approach for tracking *in vivo* biodistribution of Tregs. This approach involved a dual tuned MRI surface coil with sensitive bSSFP imaging sequence on a 3 Tesla human MRI. The ability to non-invasively quantify and image injected cells *in vivo* with high sensitivity will improve the efficacy and safety of cell therapy.

## Keywords

Magnetic resonance imaging (MRI), fluorine-19 ( $^{19}\text{F}$ ), magnetic particle imaging (MPI), superparamagnetic iron oxide nanoparticle (SPION), perfluorocarbon (PFC), cell tracking, cell therapy, mesenchymal stem cells (MSC), regulatory T cells (Tregs), detection limits, image quantification

## Summary for Lay Audience

Cell therapy is a new treatment for many diseases and works by using stem cells or immune cells. These cells can be grown and modified in a lab so that there are enough cells with the right function that can be given to a patient. Although very promising, there are many questions remaining that can only be answered using imaging, such as where do cells go after implanted? how long do they last? how many are there? There are four projects in this thesis where we use imaging methods to answer these questions: magnetic resonance imaging (MRI), fluorine-19 ( $^{19}\text{F}$ ) MRI, and magnetic particle imaging (MPI). For these imaging modalities to work, cells must be labeled with an imaging agent, either iron or  $^{19}\text{F}$ . First, we used all these methods in combination to study stem cells after injection to mice and the immune response that happens after the injection. Each imaging method gives us new information about stem cells; MRI shows the injection site, MPI measures how many stem cells are present over time, and  $^{19}\text{F}$  MRI measures the immune response. Combining 3 modalities gives us a full picture to understand what is happening to stem cells after they are administered. It is also important to understand the limitations of these imaging methods. We found that MPI could detect fewer cells compared to  $^{19}\text{F}$  MRI and this is considered an advantage. MPI is a newer imaging modality and in many publications, it was unclear how to measure imaging signals. We created and compared four methods to see which gave the most accurate measurement with minor differences between the person who measures it. Finally, it is important that the imaging technique could be used for humans, not just mice. In the last project we label immune cells called regulatory T cells with  $^{19}\text{F}$  and image these cells using a human MRI. With  $^{19}\text{F}$  MRI we can see where these T cells migrate in mice and measure the number of cells at each location. We are confident that these imaging methods will help to better understand and monitor cell therapies in patients.

## Co-Authorship Statement

Chapter 1 and 6 contains material from a previously published review paper. Sehl, Olivia C., Julia J. Gevaert, Kierstin P. Melo, Natasha N. Knier, and Paula J. Foster. A perspective on cell tracking with magnetic particle imaging. *Tomography*. 2020; 6(4):315-324. OCS, JJG, and PJF wrote the majority of the manuscript. KPM and NNK also contributed preparation of the manuscript.

Chapter 1 and 6 contains material from a published book chapter. Sehl, Olivia C., Ashley V. Makela, and Paula J. Foster.  $^{19}\text{F}$  for quantitative tracking of immune cells involved in cancer progression and therapy (in press). OCS, AVM, and PJF all contributed to writing and editing of the manuscript.

Chapter 2 and 7.1 (supplemental information) is reprinted from: Sehl, Olivia C., Ashley V. Makela, Amanda M. Hamilton, Paula J. Foster. Trimodal cell tracking *in vivo*: combining iron- and fluorine-based magnetic resonance imaging with magnetic particle imaging to monitor the delivery of mesenchymal stem cells and the ensuing inflammation. *Tomography*. 2019; 5(4):367-376. OCS wrote the majority of the manuscript. AVM, AMH, and PJF all contributed to editing of the manuscript.

Chapter 3 and 7.1 (supplemental information) is reprinted from: Sehl, Olivia C., and Paula J. Foster. The sensitivity of magnetic particle imaging and fluorine-19 magnetic resonance imaging for cell tracking. *Scientific Reports*. 2021; 11:22198. OCS wrote the majority of the manuscript and PJF edited this manuscript.

Chapter 4 is reprinted from: Sehl, Olivia C., Brice Tiret, Maryam A. Berih, Ashley V. Makela, Patrick W. Goodwill, and Paula J. Foster. MPI region of interest (ROI) analysis and quantification of iron in different volumes. *International Journal of Magnetic Particle Imaging*. 2022. OCS and BT wrote the majority of this manuscript. MAB, AVM, PG, and PJF all contributed to editing of the manuscript.

Chapter 5 contains material that is currently unpublished. This is a collaborative study conducted by Olivia C. Sehl, Corby Fink, Katherine N. MacDonald, John Kelly, John A. Ronald, Megan K. Levings, Gregory A. Dekaban, and Paula J. Foster. OCS wrote the majority of this chapter. CF and PJF contributed to editing of this chapter.

Chapter 7.2.1 and 7.2.2 contains material from two abstracts that were submitted to the World Molecular Imaging Congress (WMIC) and the Imaging Network of Ontario (IMNO) in 2022. This work was completed by Olivia C. Sehl, Maryam A. Berih, and Paula J. Foster. Chapter 7.2.3 contains unpublished material that was written by Olivia C. Sehl and conducted by Olivia C. Sehl, Corby Fink, Gregory A. Dekaban, and Paula J. Foster.

## Acknowledgments

I really enjoyed being in graduate school and I attribute this to having Dr. Paula Foster as my advisor. Paula, I am extremely fortunate to receive your supervision, mentorship, and friendship. You have profoundly impacted my life and inspire me every day. I did not have to think much about the decision to stay a few more years for a PhD because being in your lab is so rewarding. Thank you for all the fun times – I have such fond memories of our many celebrations and travel together. Thank you for your never-ending support with everything. You helped me progress in my career, prepare for exams, and even encouraged me to take vacation and time off. You have always valued my opinions and intuitions, and treated me as a valued colleague, which was so empowering. I am so proud of what we achieved together.

I would like to express immense gratitude to the members of my advisory committee, Drs. Gregory Dekaban, Timothy Scholl, and Lisa Hoffman. You were truly my cheerleaders. Thank you Greg for being a close collaborator and encouraging me to learn immunology. This inspired me to take four courses in immunology, join the Immuno-Oncology Journal Club, and the Translational Immuno-oncology Research Group. Tim, I appreciate that you challenged me to think critically about the techniques and methods in my work. Lisa, thank you for encouraging me to think about how my work fits into the bigger picture. You all provided me with excellent advice and challenged me in rigorous exams (PhD reclassification and comprehensive midlevel). Thank you also to my PhD examining committee, Drs. Mangala Srinivas, Eugene Wong, Jonathan Thiessen, and Ting-Yim Lee, for taking the time to read my thesis and prepare detailed questions for the exam.

I am forever grateful for my mentors. Dr. Ashley Makela, I cannot thank you enough for teaching me and passing on practical knowledge as I started graduate school. You are my go-to person and I have looked up to you from the start. It has been a pleasure to continue to work on projects with you. Dr. Jeff Gaudet, you truly paved the way for me! I remember attending ISMRM in 2019 and receiving such encouragement from you to include MPI in my thesis. This changed everything. It has always been a thrill to network with you at conferences. Dr. Brice Tiret, thank you for inspiring some of the work in my thesis and I appreciate all your advice. It was so fun to meet in San Francisco and I hope to visit more in

the future. Dr. Corby Fink, thank you for answering my endless number of questions with extreme detail. You taught me many foundational techniques such as  $^{19}\text{F}$  NMR and flow cytometry. Working with you is nothing short of amazing -- your organization, experience, and jokes were always appreciated! Dr. Laura Lechermann, you became my best friend in an isolated time. I love chatting with you and meeting in Greece was unbelievable. I thank you for getting me interested to learn about PET, as this led me to many opportunities. You are a strong mentor to me and I look forward to continued friendship.

To my lab mates, Dr. Julia Gevaert, Dr. Natasha Knier, Veronica Dubois, Ryan Williams, Kierstin Melo, Nitara Fernando, Sam Flood, and Sophia Trozzo. We shared many fond memories together – traveling, working on projects in the lab, and attending fun events that I will always remember. I am confident in the success of our newest lab members! A special acknowledgement to (soon-to-be Dr.) Maryam Berih, who was my graduate school sidekick. You are so smart and excited about research. Congratulations on your acceptances to medical school – your future is bright!

Thank you to many close collaborators; it has been a great pleasure and honor to work with you. Dr. John Ronald, I learned so much from you through several research projects together. You always asked phenomenal questions that got me to think about things in a new way. Thank you for writing me many letters of support over the years. Dr. Amanda Hamilton, thank you for teaching me fundamental techniques in the lab, and not only *how* to do them but *why* each step was being performed. I admire your strong passion for research. To Dr. Carlos Rinaldi-Ramos, Hayden Good, Dr. Adam Shuhendler, and Nick Calvert, I am so grateful for the opportunity to collaborate with you. Working with and learning from you was one of the best experiences in graduate school and I always looked forward to our meetings. Thank you to Drs. Megan Levings and Katherine MacDonald for closely working with our group on Treg imaging. Thank you to all past and current members of the Cellular and Molecular Imaging Group (CMIG) at Robarts for your ongoing friendship and support.

Thank you to Natural Sciences and Engineering Research Council of Canada (NSERC), Ontario Graduate Scholarship (OGS), Cancer Research and Technology Transfer (CARTT), Translational Breast Cancer Research Unit (TBCRU), the Western University Molecular Imaging Collaborative Graduate Program, and the generous donors for supporting this work.



Thank you to my family for the never-ending support in my passion for learning. You were so excited to hear about every little success and knew when I needed breaks. I always felt you were on the journey with me. I cannot put into words all that you have done to help me. You taught me from a very young age the importance of determination, curiosity, creativity, and helping others, which are all qualities that are involved with research and progress.

## Dedication

This thesis is dedicated to my dear Aunt Anne Marie Hammer (Sehl) “Auntie Me”. Thank you for your continual encouragement and inspiration.

# Table of Contents

Abstract.....	ii
Summary for Lay Audience.....	iv
Co-Authorship Statement.....	v
Acknowledgments.....	vii
Table of Contents.....	xi
List of Tables.....	xviii
List of Figures.....	xix
List of Abbreviations.....	xxxi
Chapter 1.....	1
1 Introduction*.....	1
1.1 Cell therapies.....	1
1.2 Mesenchymal Stem Cell (MSC) Therapy.....	4
1.2.1 Differentiation potential of MSC.....	5
1.2.2 Paracrine properties of MSCs.....	6
1.2.3 Immunomodulatory properties of MSCs.....	7
1.2.4 Transplant-associated inflammation.....	7
1.3 Regulatory T Cell Therapy.....	9
1.3.1 Treg development.....	10
1.3.2 Immunosuppressive functions of Tregs.....	13
1.3.3 Engineering Treg specificity.....	15
1.4 Magnetic Resonance Imaging.....	16
1.4.1 Nuclear Magnetic Resonance (NMR).....	16
1.4.2 Creating an image.....	18
1.4.3 MRI parameters.....	20

1.4.4	Balanced steady state free precession sequence .....	21
1.4.5	Direct and <i>in situ</i> cell labeling for cellular MRI .....	23
1.4.6	Iron-based MRI cell tracking .....	26
1.4.7	Fluorine-19 based MRI cell tracking .....	28
1.5	Magnetic particle imaging .....	33
1.5.1	A definition of superparamagnetism.....	33
1.5.2	Creating an image .....	34
1.5.3	Sensitivity and resolution for MPI.....	35
1.5.4	SPION-based MPI cell tracking.....	36
1.6	Purpose of thesis .....	40
1.6.1	Thesis synopsis and hypotheses.....	40
1.6.2	Other contributions .....	41
1.7	Chapter 1 references .....	43
Chapter 2.....		60
2	Trimodal Cell Tracking In vivo: Combining Iron- and Fluorine-Based Magnetic Resonance Imaging with Magnetic Particle Imaging to Monitor the Delivery of Mesenchymal Stem cells and the Ensuing Inflammation <sup>†</sup> .....	60
2.1	Introduction.....	61
2.2	Methodology .....	63
2.2.1	MSC preparation.....	63
2.2.2	Animal model.....	64
2.2.3	<sup>1</sup> H/ <sup>19</sup> F MRI acquisition .....	64
2.2.4	Quantification of signal loss due to iron-labeled MSC.....	65
2.2.5	<sup>19</sup> F signal quantification.....	65
2.2.6	Evaluation of ferumoxytol as an MPI tracer.....	65
2.2.7	MPI acquisition.....	65
2.2.8	MPI calibration and signal quantification.....	66

2.2.9	Histological analysis .....	66
2.2.10	Statistical analysis .....	67
2.3	Results .....	67
2.3.1	Evaluation of ferumoxytol as an MPI tracer .....	67
2.3.2	Relationship between iron content and MPI signal .....	69
2.3.3	Assessment of MSC labeling with ferumoxytol .....	69
2.3.4	Detection of ferumoxytol-labeled MSC with <sup>1</sup> H MRI and PFC-labeled immune cells with <sup>19</sup> F MRI .....	71
2.3.5	Quantification of temporal changes in iron voids, <sup>19</sup> F signal, and MPI signal .....	73
2.3.6	Microscopy and immunohistochemistry .....	75
2.4	Discussion .....	77
2.4.1	Ferumoxytol as a dual <sup>1</sup> H MRI and MPI cell tracking agent .....	77
2.4.2	Imaging inflammation with <sup>19</sup> F MRI .....	78
2.4.3	Potential limitations .....	79
2.5	Conclusion .....	81
2.6	Chapter 2 references .....	81
Chapter 3 .....		85
3	The Sensitivity of Magnetic Particle Imaging and Fluorine-19 Magnetic Resonance Imaging for Cell Tracking <sup>‡</sup> .....	85
3.1	Introduction .....	86
3.1.1	Sensitivity for MPI .....	86
3.1.2	Sensitivity for <sup>19</sup> F MRI .....	87
3.2	Methodology .....	88
3.2.1	Cell culture .....	88
3.2.2	Cell labeling .....	89
3.2.3	Evaluation of cell labeling .....	89

3.2.4	Preparation of cell pellets for imaging.....	89
3.2.5	MPI of ferucarbotran-labeled cells .....	90
3.2.6	<sup>19</sup> F MRI of perfluorocarbon-labeled cells.....	91
3.2.7	<i>In vivo</i> detection of MSC using MPI and <sup>19</sup> F MRI.....	92
3.2.8	Image analysis.....	93
3.2.9	Statistical analysis.....	94
3.3	Results.....	95
3.3.1	MPI cellular sensitivity.....	95
3.3.2	<sup>19</sup> F MRI cellular sensitivity.....	98
3.3.3	<i>In vivo</i> sensitivity of MPI and <sup>19</sup> F MRI.....	101
3.4	Discussion.....	105
3.5	Conclusion .....	109
3.6	Chapter 3 references .....	109
Chapter 4	.....	114
4	MPI region of interest (ROI) analysis and quantification of iron in different volumes <sup>∇</sup> .....	114
4.1	Introduction.....	115
4.1.1	Study objectives .....	116
4.2	Methodology.....	117
4.2.1	<i>In vitro</i> sample preparation and imaging .....	117
4.2.2	ROI selection methods.....	118
4.2.3	MPI signal calibration.....	120
4.2.4	Inter-user reproducibility .....	121
4.2.5	ROI selection for <i>in vivo</i> quantification.....	121
4.3	Results.....	122
4.3.1	MPI signal calibration.....	122

4.3.2	Quantification of <i>in vitro</i> phantoms .....	124
4.3.3	Inter-user reproducibility .....	126
4.3.4	<i>In vivo</i> quantification .....	129
4.4	Discussion .....	132
4.5	Conclusion .....	136
4.6	Chapter 4 references .....	138
Chapter 5	.....	143
5	Fluorine-19 MRI as a quantitative <i>in vivo</i> migration assay for regulatory T cell immunotherapy .....	143
5.1	Introduction.....	144
5.2	Methodology.....	146
5.2.1	Treg isolation .....	146
5.2.2	Polyclonal Treg expansion.....	146
5.2.3	HER2-CAR Treg generation.....	147
5.2.4	<sup>19</sup> F-PFC labeling of Tregs.....	148
5.2.5	Treg viability and phenotype assessment .....	148
5.2.6	Fluorescence microscopy.....	149
5.2.7	<sup>19</sup> F NMR spectroscopy.....	149
5.2.8	Animal work .....	149
5.2.9	Adoptive cell transfer.....	150
5.2.10	<sup>19</sup> F MRI acquisition and analysis.....	150
5.2.11	Post MRI verification of <i>in vivo</i> <sup>19</sup> F signal .....	152
5.3	Results.....	152
5.3.1	<sup>19</sup> F-PFC labeling of Tregs.....	152
5.3.2	<sup>19</sup> F MRI monitors PFC+ Tregs biodistribution <i>in vivo</i> .....	154
5.3.3	HER2-CAR Tregs preferentially home to HER2+ MBT2.1 tumors and populate sentinel lymph nodes.....	157

5.4	Discussion .....	160
5.4.1	Labeling Tregs with PFCs .....	160
5.4.2	<i>In vivo</i> tracking of PFC+ Tregs.....	161
5.4.3	<sup>19</sup> F MRI sensitivity and novel findings.....	163
5.4.4	Limitations .....	164
5.5	Conclusion .....	165
5.6	Chapter 5 references .....	166
6	Summary and Future Work.....	172
6.1	Discussion and conclusions .....	173
6.1.1	Chapter 2.....	173
6.1.2	Chapter 3.....	174
6.1.3	Chapter 4.....	176
6.1.4	Chapter 5.....	177
6.2	Challenges and limitations.....	178
6.2.1	Surface coil for MRI.....	178
6.2.2	Commercial availability of PFCs and SPIONs.....	179
6.2.3	Quantification and Interpretation of MRI and MPI.....	181
6.3	Future work.....	182
6.3.1	Improving the MSC microenvironment with image assistance.....	182
6.3.2	Anatomical co-registration.....	183
6.3.3	Multispectral “color” imaging for cell tracking.....	183
6.4	Concluding statement.....	184
6.5	Chapter 6 references .....	185
7	Appendices.....	191
7.1	Appendix A: Supplementary figures .....	191
7.2	Appendix B: Additional experiments .....	200



7.2.1	Understanding the dynamics of cellular iron uptake and retention using live cell microscopy and magnetic particle imaging.....	200
7.2.2	The environment surrounding iron oxide nanoparticles influences sensitivity and resolution for magnetic particle imaging.....	204
7.2.3	<sup>19</sup> F MRI detection of PFC+ PBMC after intraperitoneal administration to mice.....	208
7.3	Appendix C: Permissions.....	212
7.4	Appendix D: Curriculum Vitae.....	214

## List of Tables

Table 1: Physical properties of MR-detectable nuclei, including nuclear spin quantum number, natural abundance, gyromagnetic ratio, and resonance frequency at 3T.....	17
Table 2: Comparison of the strengths and limitations of SPION-based MRI, MPI, and PFC-based MRI for cell tracking. ....	37
Table 3: Summary of temporal changes measured in <sup>1</sup> H MRI, MPI, and <sup>19</sup> F MRI, resultant of the presence of ferumoxytol-labeled MSCs and PFC-labeled macrophages.....	75
Table 4: Ten samples created by dilution of ferucarbotran in different volumes of saline. .	118
Table 5: Inter-user reproducibility measures for ROI methods 1-4. The average difference for each user pair, standard error of measurement (SEM) and coefficient of variance are reported. ....	128
Table 6: Comparison of ROI methods 1-4 in terms of size of the ROI, time spent on analysis, user variability, the ability to create custom shaped ROIs, and the quantification accuracy of iron in different volumes.....	132

## List of Figures

- Figure 1: General process for adoptive cell therapy. Cells are extracted from a donor, then they are cultured *in vitro* and expanded to generate higher cell numbers. Cells may also be treated *in vitro* with additives before they are collected and introduced to the patient recipient. Figure created with BioRender.com. .... 2
- Figure 2: Properties of a stem cell. Stem cells are capable of self-renewal and differentiation to become other types of cells, such as myocytes, osteoblasts, chondrocytes, adipocytes. Figure created with BioRender.com. .... 6
- Figure 3: A. The primary lymphoid organs are the thymus and bone marrow, and secondary lymphoid organs include the lymph nodes and spleen. Lymph nodes are located throughout the body. B. Locations of lymph nodes in a mouse are outlined in a cartoon, including the axillary, inguinal, lumbar, and popliteal lymph nodes. Figure created with BioRender.com. 11
- Figure 4: Activation of CD4<sup>+</sup> T cells occurs in the presence of two signals from APC. Signal 1 is from the engagement of peptide-MHC class II bound to a specific TCR. Signal 2 comes from co-stimulatory molecule CD28 on the T cell binding to its ligand B7 on the APC. Figure created with BioRender.com. .... 12
- Figure 5: Tregs are known to block the two signals required for T cell activation, to favor immunosuppression. i. Tregs express CTLA-4 which has a stronger affinity to B7 than CD28, blocking co-stimulation. Tregs also express LFA-1 which binds strongly to ICAM-1 on APC and produces a strong immune synapse between Treg and APC. ii. Treg binding to APC can result in removal of cell surface molecules, including MHC class II (troglucytosis) and B7 capture (transendocytosis), preventing APC ability to activate other T effector cells. Furthermore, Tregs may directly kill APC expressing a target antigen through the release of perforin and granzyme. Figure created with BioRender.com. .... 14
- Figure 6: Tregs can be genetically engineered to express chimeric antigen receptors (CAR) which consist of an extracellular antigen binding domain and a transmembrane domain, linking the intracellular T cell co-stimulatory signaling domains. CARs allow the engineered cell to specifically bind to an antigen of interest. Figure created with BioRender.com. .... 15

Figure 7: A. Orientation of the x, y, and z planes. The magnetic field  $B_0$  is aligned with the z-direction. B. In the presence of  $B_0$ , nuclei with non-zero spin align with the magnetic field in both parallel and anti-parallel directions. The sum of these vectors produces a net magnetization  $M_0$  which aligns with  $B_0$  (+z). C.  $M_0$  precesses about  $B_0$  at the Larmor frequency. Figures adapted from *From-Picture-to-Proton, 2<sup>nd</sup> ed., Cambridge University Press*.<sup>51</sup> ..... 17

Figure 8:  $T_1$  and  $T_2$  relaxation diagrams. (A) Longitudinal magnetization  $M_Z$  increases exponentially over time after an RF pulse is applied. (B) Directly after the RF pulse ( $t_1$ ), the magnetization vector is at the designated flip angle away from z-axis into the xy plane ( $\alpha=90^\circ$  is shown) and the spins begin to relax ( $t_2$ ) until realigned with  $B_0$  ( $t_3$ ). (C) Transverse magnetization  $M_{XY}$  decreases over time after an RF pulse is applied. (D) Directly after the RF pulse ( $t_1$ ), the magnetization vector is forced into the xy plane and over time the spins dephase ( $t_2$ ) until there is the net magnetization vector reaches zero ( $t_3$ ). (E) Summary diagram showing that the magnetization vector is excited towards the xy plane and over time, the longitudinal magnetization is regained, and transverse magnetization is lost. (F,G) If RF pulses are quickly repeated ( $TR \ll T_1, T_2$ ), full  $T_1$  and  $T_2$  relaxation do not occur therefore RF pulses are applied to the remaining magnetization vector at the end of each TR. A steady state magnetization is reached in (F) the  $M_Z$  direction ( $M_{SS}$ ) and (G) the  $M_{XY}$  direction ( $M'_{SS}$ ). Figure adapted from the PhD thesis of Ashley V. Makela<sup>52</sup>. ..... 19

Figure 9: Pulse sequence diagram for bSSFP. A radiofrequency (RF) pulse with a set flip angle ( $\alpha$ ) is applied at each repetition time (TR). The magnetic gradients in the slice selection ( $G_{SS}$ ), phase-encoding ( $G_{PE}$ ), and frequency encoding ( $G_{FE}$ ) directions are balanced. The MRI signal is acquired at echo time ( $TE$ ) =  $TR/2$ .<sup>54</sup> Image adapted from *From-Picture-to-Proton*<sup>51</sup>. ..... 22

Figure 10: *In vitro* cell labeling with SPIO nanoparticles or PFC nanoemulsions. SPIO or PFC are co-incubated with cells by adding these agents to the cell media. After 12-24 hours, cells are collected from culture, washed with saline, then a SPIO- or PFC-labeled cell product is obtained. Successful labeling can be confirmed with Perl's Prussian blue (PPB) stain (iron oxides) or by visualizing nanodroplets (PFC nanoemulsions) in the cytoplasm of cells. Cartoon figures created with BioRender.com are not to scale. .... 23

Figure 11: A. Intravenously administered SPIO or PFC agents accumulate in phagocytic macrophages located in the reticuloendothelial system and sites of inflammation. Figure created with BioRender.com. B. Following SPIO intravenous administration, the SPIO acts as a negative contrast agent and the resulting MRI shows darkening of the liver and spleen. C. Comparatively, SPIOs act as tracers for MPI and the resulting image shows bright signals in the liver and spleen with the absence of signals from other tissues. D. Following PFC intravenous administration, hotspot  $^{19}\text{F}$  signal is detected in the liver, spleen, and lymph nodes.  $^{19}\text{F}$  signal is overlaid to  $^1\text{H}$  MRI for anatomical localization. .... 25

Figure 12: A. Superparamagnetic materials have no net alignment in the absence of a magnetic field and B. saturate strongly to align with an applied magnetic field. C. The magnetic particle imaging magnetic gradient system saturates SPIONs which are outside the field free region (FFR). Within the imaging FFR, SPIONs can freely respond to the excitation magnetic field and produce signals. Figure created with BioRender.com..... 33

Figure 13: A. The Langevin function describes the non-linear change in SPION magnetization that occurs in response to an applied magnetic field. Magnetization saturation is denoted as M. B. The derivative of this Langevin function is the MPI signal in the form of a point spread function (maximum value, max.). .... 34

Figure 14: Ferumoxytol evaluation and magnetic particle imaging (MPI) signal calibration. (A) Relaxometer data showing the point spread functions for 30  $\mu\text{g}$  and 5.5  $\mu\text{g}$  ferumoxytol. The full-width half maximum (FWHM) is labeled for the positive 30  $\mu\text{g}$  iron relaxometer data. (B) A projection of 3-dimensional MPI images (in 3D isotropic mode) of ferumoxytol samples used to create a calibration line (C). (D) The relationship between iron content and MPI signal remains linear at low concentrations of iron. .... 68

Figure 15: Figure 2: (A) Assessment of mesenchymal stem cells (MSC) labeling with ferumoxytol. Perl's Prussian Blue (PPB) identifies the presence of iron in ferumoxytol-labeled MSCs. (B) MPI of MSC pellets ( $0.24 \times 10^6$ ,  $0.6 \times 10^6$ , and  $1 \times 10^6$  cells) confirms the linear relationship between cell number and MPI signal (C). It was determined that  $1 \times 10^6$  cells contained  $2.430 \pm 0.211$  pg/cell on the day of MSC implantation. (D) PPB of unlabeled cells reveals the absence of iron and (E)MPI images of cell pellets contain no signal above

background levels. (F) References containing 3  $\mu\text{g}$  and 1.5  $\mu\text{g}$  were included for visualization of the signal. The color look up table (CLUT) for the MPI images in (B) and (E) is shown in (F). 40x magnification with scale bar = 100  $\mu\text{m}$  (A, D). ..... 70

Figure 16: (A) *In vivo*  $^1\text{H}/^{19}\text{F}$  MRI and MPI. In  $^1\text{H}$  images, ferumoxytol-positive MSCs were detected as regions of signal loss, 1 and 12 days following MSC implantation (labeled Fe). (B) In  $^{19}\text{F}$  MRI, PFC-positive immune cells are detected in the bone marrow (BM), lymph nodes (LN), and in the muscle surrounding the MSC implant. (C) Ferumoxytol-positive MSCs are also detected in MPI images as bright spots (labeled Fe). In these images, iron in the gut of the mice (*i.e.*, food) is also detected by MPI. The range of the MPI images is 0-0.14 arbitrary units, which is equivalent to 0-9.8 ng iron/ $\text{mm}^3$ . Mice that received unlabeled MSCs (controls) had no signal voids present in  $^1\text{H}$  MRI (D) and  $^{19}\text{F}$  signal persisting (E), in response to the implant. The CLUT is displayed above each image. All images of the same type are windowed identically for comparison. .... 72

Figure 17: (A) The volume of signal void in  $^1\text{H}$  MR images created by ferumoxytol-labeled MSCs declined over 12 days (by 64%) in all 10 mice. (B)  $^{19}\text{F}$  signal detected from perfluorocarbon (PFC)-positive immune cells remained constant over these 12 days in all 15 mice. There was no significant difference in  $^{19}\text{F}$  signal between mice with ferumoxytol-labeled (n = 10 mice) or unlabeled (n = 5 mice) MSCs. (C) MPI signal and iron content (determined by MPI) declined over 12 days (67% reduction between days 1 and 12) in all 5 mice. (D) The number of MSCs (estimated using MPI data) also declined over time in these same mice. .... 74

Figure 18: (A) Histological validation showing the presence of MSCs surrounded in connective tissue (CT) and muscle (M) in hematoxylin and eosin (H&E) at 10x magnification (scale bar = 500  $\mu\text{m}$ ) and (B) 40x magnification. (C) PPB staining with nuclear fast red counterstain confirms the presence of iron within MSCs. Black arrows indicate PPB-positive cells. (D) F4/80 staining with hematoxylin counterstain reveals macrophage infiltration within the same region as the MSCs. Expected F4/80 staining is shown in the reference indicator (R). Black arrows indicate F4/80-positive cells. 40x magnification, scale bars = 100  $\mu\text{m}$  (B,C,D). .... 76

Figure 19: (A) Image of a preclinical Momentum MPI and sample holder (white arrow), where individual ferucarbotran-labeled cell samples were placed for imaging. (B) Photos of a clinical 3 Tesla MRI with the dual-tuned ( $^1\text{H}/^{19}\text{F}$ ) surface coil, used for  $^{19}\text{F}$  imaging of 6 cell samples. (C) A strong linear relationship exists between MPI signal and iron mass ( $R^2 = 0.9997$ ). This was determined by imaging multiple samples of ferucarbotran (0.34–33  $\mu\text{g}$ ) and measuring the MPI signal from each sample. The linear equation is subsequently used to convert a measure of MPI signal from ferucarbotran-labeled cells to a measure iron content ( $\mu\text{g}$ ). (D)  $^1\text{H}$  and  $^{19}\text{F}$  images of two reference phantoms, containing known amount of  $^{19}\text{F}$  content ( $3.33 \times 10^{16} \text{ }^{19}\text{F}$  spins/ $\mu\text{L}$ ), are used for quantification of  $^{19}\text{F}$  in cell samples.. 91

Figure 20: MPI detection of ferucarbotran-labeled 4T1 cells. (A) 2D MPI of individual 4T1 cell pellets containing the indicated cell numbers ( $M = 10^6$ ,  $k = 10^3$ ). As few as 8000 cells (0.074  $\mu\text{g}$  ferucarbotran) could be detected with  $\text{SNR} > 5$  in 1.5 min. 2D MPI signal (and the associated iron content) significantly increases with the number of 4T1 cells ( $*p < .05$ ,  $**p < .01$ ,  $***p < .001$ ,  $****p < .0001$ ). (B) With 8 signal averages, the same result was found. (C) In 3D, the detection of 4000 cells (0.037  $\mu\text{g}$  ferucarbotran) with  $\text{SNR} > 5$  was possible in 23 min. Images with  $\text{SNR} < 5$  have white boxes to indicate the placement of the cell sample. .... 96

Figure 21: MPI detection of ferucarbotran-labeled MSC. (A) 2D MPI of individual MSC pellets containing the indicated cell numbers ( $M = 10^6$ ,  $k = 10^3$ ). As few as 4000 MSC (0.076  $\mu\text{g}$  ferucarbotran) could be detected with  $\text{SNR} > 5$  in 1.5 min. 2D MPI signal (and the associated iron content) significantly increases with the number of MSC ( $*p < .05$ ,  $**p < .01$ ,  $***p < .001$ ,  $****p < .0001$ ). (B) With 8 signal averages, the same result was found. (C) In 3D, the detection of 2000 cells (0.038  $\mu\text{g}$  ferucarbotran, with  $\text{SNR} > 5$ ) and 1000 cells (0.019  $\mu\text{g}$  ferucarbotran, with  $\text{SNR} > 3$ ) was possible in 23 min. Images with  $\text{SNR} < 5$  have white boxes to indicate the placement of the cell sample. .... 97

Figure 22: (A) The number of ferucarbotran-labeled MSC and 4T1 cells is strongly correlated with iron content measured by MPI ( $R^2 > 0.998$ ). The slope of the line for MSC is higher than 4T1 ( $p < .0001$ ), indicating higher sensitivity and enhanced uptake of iron in MSC compared to 4T1 cells as shown with PPB stain (B). (C) A strong linear correlation

exists between the number of PFPE-labeled MSC and detected  $^{19}\text{F}$  signal ( $R^2 = 0.9983$ ). (D) PFPE labeling identified as nanodroplets in microscopy (black arrows). ..... 98

Figure 23:  $^{19}\text{F}$  MRI detection of PFPE-labeled MSC. (A)  $^{19}\text{F}$  images of six samples with various cell numbers ( $M = 10^6$ ,  $k = 10^3$ ) imaged 1.5 min/pellet. As few as  $256 \times 10^3$  cells ( $9.01 \times 10^{16}$   $^{19}\text{F}$  atoms) could be detected with  $\text{SNR} > 5$ . (B) With longer imaging time (4.5 min/pellet), the detection of  $128 \times 10^3$  cells ( $4.51 \times 10^{16}$   $^{19}\text{F}$  atoms) was possible with  $\text{SNR} > 5$ . (C) Quantification revealed significant differences in  $^{19}\text{F}$  signal between different numbers of MSC ( $*p < .05$ ,  $**p < .01$ ). Significantly more  $^{19}\text{F}$  signal was detected from  $1.024 \times 10^6$  cell samples with longer imaging times ( $p < .01$ ). ..... 100

Figure 24: (A) Cartoon showing subcutaneous (SQ), intraperitoneal (IP), and intravenous (IV) injection in mice. (B) Comparison of MPI signal from 2D scans of  $2 \times 10^6$  ferucarbotran-labeled MSC in a cell pellet to subcutaneous injection. (C) Measured MPI signal from  $2 \times 10^6$  MSC was similar *in vivo* and *ex vivo*. (D) Detection in 2D of  $1 \times 10^5$  ferucarbotran-labeled MSC as a cell pellet and after subcutaneous, intraperitoneal, and intravenous injection. (E) Measured MPI signal from  $1 \times 10^5$  cells is reduced *in vivo* compared to signal in the pellet. (F) Some background MPI signal exists owing to iron in mouse digestion. This signal was minimized with 12-h fasting and accounted for by subtracting pre-injection signal from post-injection signal for each mouse. .... 103

Figure 25: Detection of  $2 \times 10^6$  PFPE-labeled MSC *in vivo*.  $^{19}\text{F}$  signal is detected at the injection site following (A) subcutaneous injection (white arrows) and (B) intraperitoneal injection (white ovals). A cell pellet of the same cell number was imaged alongside the mouse for comparison (shown in A). (C) After subcutaneous administration,  $1 \times 10^5$  cells were undetected, as this cell number is below the detection threshold for MSC. Images are sagittal (left) and axial (right). M = million, k = thousand. (D)  $^{19}\text{F}$  signal measured from  $2 \times 10^6$  cells injected subcutaneous (SQ) was reduced compared to signal measured from the cell pellet, however, elevated  $^{19}\text{F}$  signal was measured from cells following intraperitoneal (IP) injection. (E) The dual-tuned surface coil is approximately the same size as a mouse and is placed directly over the injection site for imaging. .... 104



Figure 26: (A) A demonstration of ROI methods 1 – 4 on two samples of ferucarbotran (Samples 1 and 10). The minimum value (a.u.), area (mm<sup>2</sup>), and mean value (a.u.) is recorded for each ROI. (B) A depiction of ROI selection method 2. .... 120

Figure 27: (A) MPI calibration performed by imaging 10 samples of known ferucarbotran mass (0.34 – 55 µg). (B) Using each ROI method, a linear relationship between iron content and MPI signal was established as MPI signal (A.U.) = m \* iron content (µg), where m is the slope of each line. .... 123

Figure 28: (A) Projection images showing the same amount of ferucarbotran (34.4 µg) increasing volumes of saline. Image values displayed are 0-1000 A.U. (B) Line profiles showing differences in signal intensity and resolution from Samples 1-10. Undiluted ferucarbotran (Sample 1) produces higher signal intensity as the sample is concentrated, while the point source spreads out more as the sample is diluted. Iron content (µg) measured from Samples 1-10 using methods 1 and 2 (C), and methods 3 and 4 (D). .... 125

Figure 29: (A) Various threshold factors are applied to the maximum value (a = 0.1, 0.5, and 0.7) to quantify Samples 1-10. For ROI method 1, quantification of iron is overestimated for dilute samples regardless of the scaling factor. (B) Various threshold factors are applied to the background SD (c = 5, 10, 25). Using method 4, iron mass is consistent across scaling factors and accurate with dilution of ferucarbotran. .... 126

Figure 30: Analysis of inter-user reproducibility for ROI methods 1-4. (A) For each method, the range of iron content measured by each user for samples 1-10 is shown. The dotted line indicates the true iron mass (34.4 µg). (B) Bland-Altman plots comparing absolute difference between users with average measured iron content (µg). The dotted lines indicate the maximum difference and the average difference (bolded line) between users. Method 4 had the lowest user differences (mean = 0.08 µg). .... 127

Figure 31: Demonstration of *in vivo* quantification using methods 1-4 following the (A) intravenous administration of 100 µg ferucarbotran or an (B) intramuscular injection of 25 µg ferucarbotran, followed by a (C) subcutaneous injection of 25 µg ferucarbotran. (D) Signal calibration to determine the relationship between iron mass (ferucarbotran) and MPI signal using 3.0 T/m gradients (the same parameters as *in vivo* images). MPI signal of calibration

samples was measured using all 4 methods. (E-G) Iron mass measured from respective *in vivo* images A-C, comparing ROI methods 1-4..... 130

Figure 32: Application of alternative threshold values using methods 1 and 4 for *in vivo* analysis. (A) ROI method 1 with  $a = 0.7$  was applied to the signal associated with ferucarbotran in the mouse liver and spleen. This creates a larger ROI than  $c = 0.5$  but did not return an accurate estimate of SPION mass (153.3  $\mu\text{g}$ ). (B) ROI method 4 with high value of  $c$  ( $= 100$ ) applied to the same mouse results in accurate quantification (99.47  $\mu\text{g}$ ). (C) With ROI method 4, increasing  $c$  ( $=35$ ) allows for separate quantification of two iron sources *in vivo* but quantitative accuracy is reduced. .... 131

Figure 33: PFC labeling of Tregs. A. Compared to unlabeled Tregs, 98% of Tregs had associated red-fluorescent signal from incorporated PFC. Microscopy images of (B) unlabeled Tregs and (C) red-PFC<sup>+</sup> Tregs reveal that red-PFC is localized intracellularly surrounding DAPI-stained nuclei. Additional confocal microscopy reveals that compared to (D) unlabeled cells, (E) red-PFC is localized in the cytoplasm of labeled Tregs. (F) Treg viability was measured with fixable vital dye and Tregs were phenotype for CD4, CD8, CD25, Foxp3, and Helios expression with flow cytometry. (G) Treg viability is reduced by  $< 10\%$  when comparing donor cells with or without (UL = unlabeled) PFC labeling ( $n = 5$ , paired t-test,  $p < .01$ ). (H) No differences in Treg phenotype were detected with PFC labeling ( $n = 5$ , paired t-tests,  $p > .05$ ). (I) <sup>19</sup>F NMR measurements of non-fluorescent PFC<sup>+</sup> Tregs indicate that Tregs incorporate an average of  $8.673 \times 10^{11}$  <sup>19</sup>F atoms per cell. The dark red data point corresponds to a trial with HER2<sup>+</sup> CAR Tregs. .... 153

Figure 34: PFC<sup>+</sup> Treg biodistribution after subcutaneous administration. A. <sup>19</sup>F/<sup>1</sup>H MRI shows <sup>19</sup>F signal from PFC<sup>+</sup> Tregs in inguinal lymph nodes (shown in axial sections), popliteal lymph nodes, and the spleen (shown in coronal sections), 24h and 48h p.i. The estimated number of cells based on <sup>19</sup>F content at each location is recorded for this representative mouse. See Figure 42 in Appendix A for similar images and quantification of Tregs in the other 3 mice. B. Quantification of number of Tregs (% of total administered cells) for all 4 mice at 24h and 48h p.i. show no statistical differences (paired t-tests). Lymph node signals are a sum of the signals on left/right sides of the mouse. C. Excised popliteal

lymph node and spleen analysed with flow cytometry reveals positive human CD45 staining.  
..... 155

Figure 35: PFC+ Treg biodistribution after intravenous administration. A.  $^{19}\text{F}/^1\text{H}$  MRI shows  $^{19}\text{F}$  signal from PFC+ Tregs in lumbar lymph nodes (shown in axial sections), and the inguinal, renal, and axillary lymph nodes (shown in coronal sections), 24h, 48h, and 96h p.i..  $^{19}\text{F}$  signals were also found in the spleen of one mouse (see Figure 43 in Appendix A). The estimated number of cells based on  $^{19}\text{F}$  content at each location is recorded for this representative mouse. See Figure 43 in Appendix A for similar images and quantification of Tregs in the other 3 mice. B. Quantification of number of Tregs (% of total administered cells) for all 4 mice at 24h and 48h p.i. show no statistical differences (paired t-tests). Lymph node signals are a sum of the signals on left/right sides of the mouse. C. Excised inguinal lymph node and spleen analysed with flow cytometry reveals positive human CD45 staining.  
..... 157

Figure 36: PFC+ HER2-CAR Treg biodistribution after intravenous administration to HER2+ and parental MBT2.1 tumor-bearing mice. A.  $^{19}\text{F}/^1\text{H}$  MRI shows  $^{19}\text{F}$  signal from PFC+ HER2-CAR Tregs in HER2+ and parental MBT2.1 tumors (shown in axial sections), and the axillary and lumbar lymph nodes (coronal sections) at 24h, 48h, and 72h p.i. The estimated number of cells based on  $^{19}\text{F}$  content at each ROI is recorded. B. Quantification of number of Tregs (and % of total administered cells) reaching HER2+ (orange) and parental (grey) MBT2.1 tumor across the 3 timepoints. C. Quantification of the number of Tregs (and % total of administered cells) reaching lymph nodes on the side ipsilateral or contralateral to the HER2+ MBT2.1 tumor. There were no significant differences between the  $^{19}\text{F}$  signal on either side of the mouse. D. Excised sentinel/axillary lymph nodes analysed with flow cytometry reveals positive human CD45 staining on both the side ipsilateral (orange) and contralateral (grey) to the HER2+ MBT2.1 tumor. .... 160

Figure 37: Full MPI image set for 3 mice, showing changes in detected ferumoxytol-labeled MSCs, 1, 5, and 12 days following MSC implantation. The full dynamic range (FDR) of the region where MSCs were implanted is displayed for each mouse. .... 191

Figure 38: Overlay of 2D MPI acquisition to optical image of mouse. MPI signal is localized to the gut and the region where ferumoxytol-labeled MSCs were implanted. (B) Overlay of 2D MPI acquisition to optical image shows MPI signal from mouse feed. .... 192

Figure 39: Optimization of  $^{19}\text{F}$  flip angle at 3 T. (A) Two reference phantoms ( $3.33 \times 10^{16}$   $^{19}\text{F}$  spins/ $\mu\text{L}$ ) were imaged using 3D bSSFP with 80 excitations and various flip angles: 20, 30, 40, 50, 60, 70, and 80 degrees. (B) The average signal of the reference tubes, the standard deviation of background noise, and the SNR were measured for each flip angle. .... 193

Figure 40: (A) Various threshold ( $5 \times \text{SD}_{\text{noise}}$  -  $12 \times \text{SD}_{\text{noise}}$ ) were used to segment  $^{19}\text{F}$  signal from  $2 \times 10^6$  PFPE-labeled MSC, in a pellet or *in vivo* (subcutaneous; SQ, intraperitoneal; IP). These images are shown in Figure 25. Regardless of the threshold value used,  $^{19}\text{F}$  signal measured from cells administered IP exceeded that of SQ and from pellets. In this quantification there is no correction applied to signal values. (B) Voxel distribution of background  $^{19}\text{F}$  noise was non-Gaussian and left-skewed, indicating there is a Rician distribution of noise. (C) A demonstration of the segmentation method described in Bouchlaka *et al.* (2016) from a single coronal slice of the mouse administered PFPE-cells IP (also shown in Figure 7B).  $^{19}\text{F}$  signal between  $5 \times \text{SD}_{\text{noise}}$  -  $8 \times \text{SD}_{\text{noise}}$  (green) was corrected with a factor of 0.655 and  $^{19}\text{F}$  signal exceeding  $8 \times \text{SD}_{\text{noise}}$  (blue) was not corrected. Signal above  $5 \times \text{SD}_{\text{noise}}$  was included for  $^{19}\text{F}$  quantification. .... 194

Figure 41: The standard deviation of background noise ( $\text{SD}_{\text{noise}}$ ) for MPI was measured from an empty sample holder at the beginning ( $t = 0\text{h}$ ), middle ( $t = 3\text{h}$ ), and end ( $t = 6\text{h}$ ) of six imaging sessions. There were no significant differences in measured  $\text{SD}_{\text{noise}}$  between (A) imaging days or (B) the 3 timepoints..... 195

Figure 42:  $^1\text{H}/^{19}\text{F}$  MRI for all 4 mice receiving  $10 \times 10^6$  PFC+ Tregs by subcutaneous administration (except for the final mouse that received  $5 \times 10^6$  PFC+ Tregs). The experiment was repeated with cells from the same donor ( $n = 2$  mice per replicate). The first replicate of Tregs were labeled with  $3.15 \times 10^{11}$   $^{19}\text{F}$  atoms/cell (left) and the second replicate of Tregs were labeled with  $3.62 \times 10^{11}$   $^{19}\text{F}$  atoms/cell (right). The red arrows indicate the injection site (if within the selected plane). Each mouse was imaged at 24h and 48h p.i.  $^{19}\text{F}$  signals were seen in the spleen (white dotted ovals), and the popliteal (orange boxes) and inguinal (white brackets) lymph nodes of all mice at both time points. The estimated Treg

cell numbers associated with each  $^{19}\text{F}$  signal are indicated and the total sum signal per mouse is recorded..... 196

Figure 43:  $^1\text{H}/^{19}\text{F}$  MRI for all 4 mice receiving  $10 \times 10^6$  PFC+ Tregs by intravenous administration. The experiment was repeated with cells from the same donor ( $n = 2$  mice per replicate). The first replicate of Tregs were labeled with  $5.6 \times 10^{12}$   $^{19}\text{F}$  atoms/cell (left) and the second replicate of Tregs were labeled with  $6.28 \times 10^{11}$   $^{19}\text{F}$  atoms/cell (right). Each mouse was imaged at 24h and 48h p.i, and for one mouse a later timepoint was explored (96h p.i.). Mice with no signals present at 48h p.i. are not shown.  $^{19}\text{F}$  signals were seen in the spleen (one mouse, white ovals), and the lumbar (teal boxes), axillary (green circle), renal (yellow diamonds), and inguinal (white brackets) lymph nodes of mice. The estimated Treg cell numbers associated with each  $^{19}\text{F}$  signal are indicated and the total sum signal per mouse is recorded..... 197

Figure 44: Establishment of parental (mouse left) and HER2+ (mouse right) MBT2.1 tumors for HER2-CAR Treg in vivo migration study. Flow cytometry confirms HER2 expression in HER2 engineered MBT2.1 cells (purple) and confirmed lack of HER2 expression in parental MBT2.1 cells (black) and against control unstained HER2-expressing MBT2.1 cells (grey).  
..... 198

Figure 45:  $^1\text{H}/^{19}\text{F}$  MRI for the other 2 mice receiving  $4 \times 10^6$  PFC+ HER2-CAR Tregs by intravenous administration. These HER2-CAR Tregs were loaded with  $4.79 \times 10^{11}$   $^{19}\text{F}$  atoms/cell. Axial  $^{19}\text{F}/^1\text{H}$  MRI shows  $^{19}\text{F}$  signal from PFC+ HER2-CAR Tregs in HER2+ MBT2.1 tumors (orange) but not parental MBT2.1 tumors (white) in these 2 mice. Coronal images show that PFC+ HER2-CAR Tregs were also detected in the axillary (green circles) and lumbar (teal boxes) lymph nodes at 24h, 48h, and 72h p.i. The estimated number of cells based on  $^{19}\text{F}$  content at each ROI is recorded. .... 199

Figure 46: (i) Microscopy of mesenchymal stem cells incubated with ferucarbotran without (left) and with (right) TAs. (ii) Time course imaging shows cells approach ferucarbotran nanocomplexes and engulf a portion of the cluster. The movement of a cell away from the cluster is shown with the white arrow over 8 frames. In the process, a portion of the ferucarbotran nanocomplex detaches from the cell and is not incorporated (white circle). (iii-vi) Proliferation of stem cells reduces the amount of iron per cell. (iii) MPI of  $1 \times 10^6$

ferucarbotran-labeled stem cells collected from culture over 5 days shows decreasing MPI signal over time. Scale bars indicate the image full dynamic range. (iv) Quantification of iron mass (pg) per cell with MPI shows significant decreases over time (\*\*  $p < 0.01$ , \*\*\*\*  $p < 0.0001$ ). (v) PPB stain validates a decrease in intracellular iron over time. (vi) Live cell imaging showing partitioning of iron in daughter progeny of a dividing cell. .... 202

Figure 47: MPI relaxometry curves for ferucarbotran (A) and ferucarbotran labeled cells (B) in saline, 0.5%, 2.5%, or 5% agarose. The adjacent plots show measurements of sensitivity and resolution from these curves (C, D). MPI images of ferucarbotran (E) in saline or 5% agarose also show differences in MPI signal intensity and resolution, but ferucarbotran-labeled cells (F) do not. .... 206

Figure 48:  $^{19}\text{F}/^1\text{H}$  MRI overlay of mice showing detection of  $5 \times 10^6$  PFC+ PBMC after intraperitoneal administration. PFC+ cells accumulate in popliteal lymph nodes (LNs), inguinal lymph nodes, and the spleen. The measurement of cells from each lymph node is indicated. Images were acquired both at 24 and 48 hours after administration. The color scale bar represents  $^{19}\text{F}$  spins. .... 210

## List of Abbreviations

$^{19}\text{F}$	Fluorine-19
$^1\text{H}$	Hydrogen-1
3D	3-dimensional
ACT	adoptive cell transfer
ANCOVA	analysis of co-variance
ANOVA	analysis of variance
APC	antigen presenting cell
AU	arbitrary units
$B_0$	static magnetic field (MRI)
BCAM	body conforming animal mold
BLI	bioluminescence imaging
BM	bone marrow
BSA	bovine serum albumin
bSSFP	balanced steady-state free precession
BW	bandwidth
CAR	chimeric antigen receptor
CB-17	CB17/Icr-Prkdcscid/IcrIcoCrl mice
CCR7	C-C chemokine receptor 7
CD	cluster of differentiation

CLUT	color look up table
CoV	coefficient of variation
CTLA-4	cytotoxic T-lymphocyte associated antigen 4
DAB	3,3'-diaminobenzidine tetrahydrochloride
DMEM	Dulbecco's modified eagle medium
FA	flip angle
FBS	fetal bovine serum
FDR	full dynamic range
FFL	field free line (MPI)
FFP	field free point (MPI)
FFR	Field free region (MPI)
FID	free induction decay (MRI)
FOV	field of view
Foxp3	Forkhead box protein
FWHM	full-width at half maximum
$G_{FE}$	frequency-encoding gradient (MRI)
GM-CSF	granulocyte macrophage colony-stimulating factor
$G_{PE}$	phase-encoding gradient (MRI)
$G_{SS}$	slice-select gradient (MRI)
GvHD	grafts-versus-host disease



H&E	Hematoxylin and eosin
HBSS	Hank's balanced salt solution
HER2	human epidermal growth factor receptor 2
ICAM-1	intracellular adhesion molecule 1
ID	injected dose
IL	interleukin
IP	intraperitoneal
IV	intravenous
LFA-1	lymphocyte function-associated antigen 1
LN	lymph node
LPS	lipopolysaccharide
mAb	monoclonal antibody
MHC	major histocompatibility complex
MOI	multiplicity of infection
MPI	magnetic particle imaging
MRI	magnetic resonance imaging
MSCs	mesenchymal stem cells
M <sub>SS</sub>	magnetization at steady state (MRI)
NEX	number of excitations
NIS	sodium iodide symporter

NMR	nuclear magnetic resonance
NSG	NOD/SCID/IL2rg <sup>-/-</sup> mice
PAMPs	pattern associated molecular patterns
PBMC	peripheral blood mononuclear cells
PBS	phosphate buffered saline
PC	phase cycles (MRI)
PET	positron emission tomography
PFC	perfluorocarbon
PFPE	perfluoropolyether
pi	post-injection
PPB	Perl's Prussian blue
PSF	point spread function
RF	radiofrequency
ROI	region of interest
scFv	single-chain variable fragment
SD	standard deviation
SNR	signal-to-noise ratio
SEM	standard error of measurement
SPECT	single photon emission computed tomography
SPIONs	superparamagnetic iron oxide nanoparticles
SQ	subcutaneous

SUV	standard uptake value
T <sub>1</sub>	spin-lattice relaxation (MRI)
T <sub>2</sub>	spin-spin relaxation (MRI)
TCR	T cell receptor
TE	echo time (MRI)
TGF- $\beta$	transforming growth factor $\beta$
TR	repetition time (MRI)
Tregs	regulatory T cells
USPIOs	ultrasmall superparamagnetic iron oxides
W/L	window/level

## Chapter 1

### 1 Introduction\*

This thesis develops and applies magnetic resonance imaging (MRI) and magnetic particle imaging (MPI) techniques to study the fate of cellular therapeutics *in vivo*. These cellular therapies include mesenchymal stem cells (MSC) and regulatory T cells (Tregs). This chapter provides background on these cell therapies and the motivation for using these cellular imaging techniques.

#### 1.1 Cell therapies

Cellular therapeutics are becoming prominent worldwide and involve the administration of living cells for the treatment of disease. These therapeutic cells are isolated from a donor, the cell population is expanded and/or modified in a laboratory, then reintroduced to a recipient<sup>1</sup> (Figure 1). This process is known as adoptive cell transfer (ACT). Autologous ACT refers to when cells are isolated then returned to the same patient, whereas allogenic ACT involves a separate donor. There are a variety of cell types used for ACT, including stem cells and immune cells. This thesis focuses on MSC and Treg cell therapies.

---

\* This chapter contains sections which have been previously published. Chapter 1 contains material from a previously published review paper: [Sehl OC](#), Gevaert JJ, Melo KP, Knier NN, Foster PJ. A perspective on cell tracking with magnetic particle imaging. *Tomography*. 2020; 6(4):315-324. Chapter 1 also contains material from a previously published book chapter. [Sehl OC](#), Makela AV, Foster PJ. <sup>19</sup>F for quantitative tracking of immune cells involved in cancer progression and therapy.

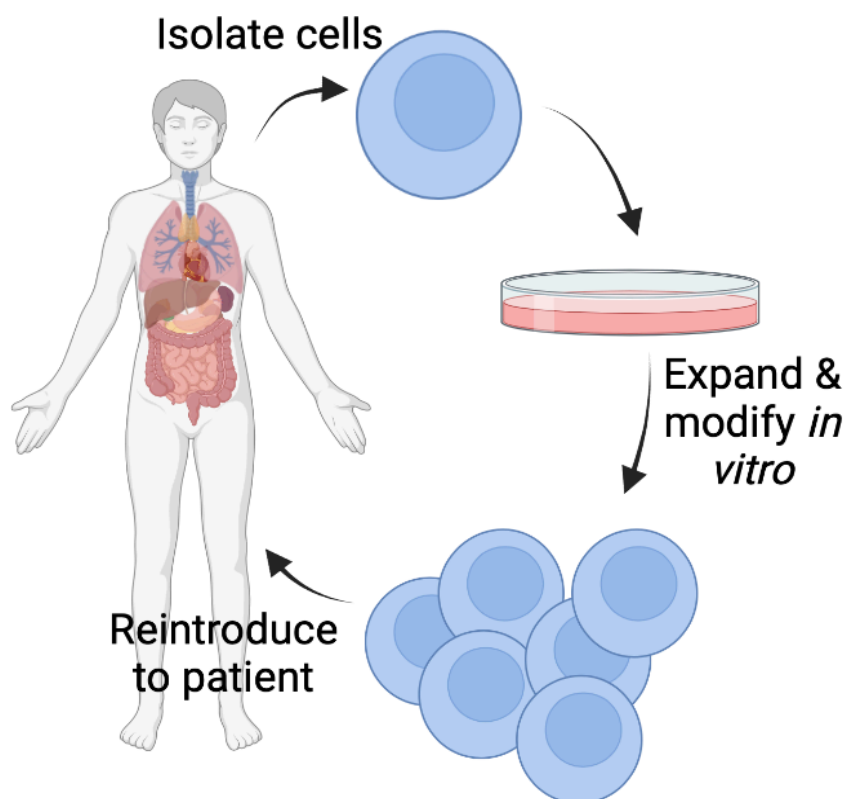


**Figure 1: General process for adoptive cell therapy. Cells are extracted from a donor, then they are cultured *in vitro* and expanded to generate higher cell numbers. Cells may also be treated *in vitro* with additives before they are collected and introduced to the patient recipient. Figure created with BioRender.com.**

Despite the immense potential of MSC and Treg cell therapies, clinical results have been variable and discordant because of dissimilarities and disparities in cell source, preparation, and route of administration/implantation methodology. Once cells are administered to patients, it is unknown whether these cells are providing immediate therapeutic benefit and it can take up to months before clinical feedback becomes available<sup>2</sup>. It remains difficult, if not impossible to spatially, and quantitatively, track the migration and accumulation of cells at the target site(s). Many critical questions about the presence, numbers, persistence, and delivery of cells remain unanswered<sup>3</sup>.

For MSC therapy, it would be valuable to confirm that MSC were administered to the correct location<sup>4</sup> within or adjacent to the site of cartilage or bone defect. Secondly, it is important to know how many MSC persist in the days after administration *in vivo* and to correlate this metric with patient outcomes. Imaging on the day of transplantation can provide information about cell delivery and subsequent sessions can help to determine whether the labeled cells reached the target, how many are present, and how long the cells persist<sup>2,5,6</sup>. The immune infiltrate at the site of MSC administration is also a marker of successful outcomes for MSC therapy (Part 1.2.4)<sup>4,7</sup>. For Treg therapy, the magnitude of the immunosuppressive response is proportional to the quantity of Tregs that reach the targets, including the lymph nodes and the site of an allogenic graft. A major unmet need is to know whether the injected Treg reach these target sites and how many<sup>8</sup>.

Biopsies and histology can provide detailed molecular and morphological information regarding cell fate but are limited to the interrogation of a single time point and portion of tissue. *In vivo* cellular imaging has the potential to answer these fundamental questions about the cell therapies after administration. The ideal approach for monitoring cellular therapies is non-invasive, non-ionizing, sensitive, specific, and quantitative to provide an accurate measure of cell number. Chapter 1 will provide an overview of MSC and Treg cellular therapies, then describe 3 cellular imaging techniques and their application to *in vivo* imaging of MSCs, inflammation associated with transplantation, and Tregs.

## 1.2 Mesenchymal Stem Cell (MSC) Therapy

MSCs have therapeutic potential for a growing list of autoimmune, degenerative, and infectious diseases as well as trauma/wound healing. MSCs possess therapeutic properties including potential for *in vitro* differentiation (Part 1.2.1), pleotropic support (Part 1.2.2) and immunomodulatory properties (Part 1.2.3)<sup>9</sup>. These later functions contribute significantly to the therapeutic potential of MSCs, where *in vivo* administered MSCs instruct tissue-specific progenitor cells to regenerate the injured tissue<sup>10</sup>. MSCs are also recognized by the names of mesenchymal stromal cells, multipotent stromal cells, marrow stromal cells, and medicinal signaling cells. There are currently over 1,000 clinical trials registered at ClinicalTrials.gov and 18 trials have published results, primarily in China and the United States<sup>10</sup>. These studies are largely focused on applications in traumatology, pneumology, neurology, cardiology, and immunology, and no serious adverse events have been reported.

MSCs are naturally located in many tissues, including adult bone marrow and adipose tissues, as well as neonatal tissues including the umbilical cord<sup>9,11,12</sup>. Their role *in vivo* is to regulate homeostasis of hematopoietic niches and to differentiate to replace tissue-specific cells of the mesodermal lineage<sup>12</sup>. For cell therapies, MSCs are most commonly obtained from the bone marrow<sup>10</sup> through an invasive surgical procedure from the iliac crest of the pelvic bone or from femoral heads. After isolation, these cells can be expanded *in vitro* then administered to the patient or cryo-preserved. MSCs are naturally present in low abundance *in vivo*, however in clinical trials, a minimum of 1-200 million cells are delivered which displays the importance of this *in vitro* cell expansion step<sup>9,10</sup>.

### 1.2.1 Differentiation potential of MSC

A stem cell is a specialized cell type with two unique properties (Figure 2). Firstly, they are capable of self-renewal meaning that they can replicate themselves for long periods of time. Second, they can differentiate to become other specialized cell types. There are several categories of stem cell differentiation potentials; totipotent cells can create any cell at any stage of development (*e.g.*, cells of a zygote), pluripotent cells can generate any cell type in the adult body (*e.g.*, embryonic stem cells), and multipotent cells can give rise to several different cell types in a specific category of cells.

MSCs are considered multipotent and can give rise to cells that build connective tissues, including bones, cartilage, tendons, ligaments, muscle, and bone marrow<sup>9</sup>. MSCs can differentiate to become osteoblasts, adipocytes, and chondroblasts<sup>9</sup>. The differentiation potential of MSC can be exploited for orthopedics and degenerative diseases, for example for bone regeneration and repair of cartilage, tendons, and ligaments<sup>11</sup>. Bone defects arise from trauma, revision arthroplasty, and tumor resection, and cartilage damage can arise from conditions such as osteoarthritis<sup>10</sup>. For cell therapy, MSC are differentiated *in vitro* under specific inductive conditions to become the desired cell type, prior to *in vivo* administration<sup>9</sup>.



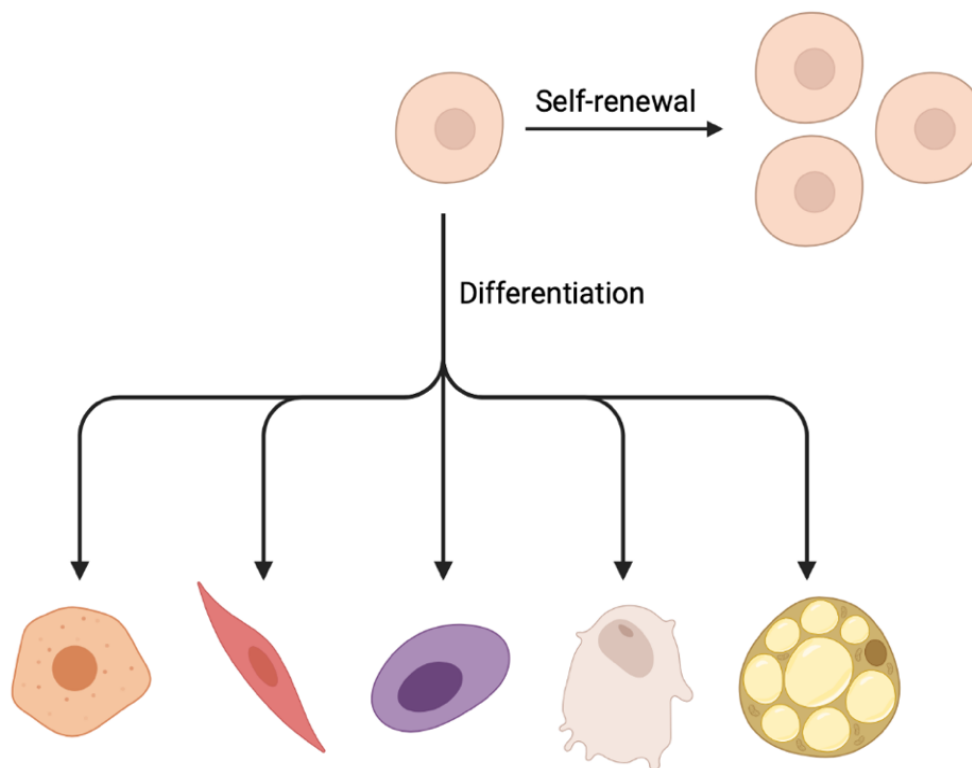


**Figure 2: Properties of a stem cell. Stem cells are capable of self-renewal and differentiation to become other types of cells, such as myocytes, osteoblasts, chondrocytes, adipocytes. Figure created with BioRender.com.**

### 1.2.2 Paracrine properties of MSCs

MSCs are known to secrete factors as extracellular vesicles or exosomes. These vesicles are  $< 200$  nm in diameter and contain cell surface receptors, proteins, and genetic materials that are passed to nearby cells. The composition of these vesicles coincides with the components contained within the cell of origin, including growth factors with anti-apoptotic effects<sup>9,13,14,15</sup>, factors that promote angiogenesis<sup>11–13,16</sup>, cytokines, chemokines that block or stimulate cell chemotaxis<sup>9,12</sup>, components of the extracellular matrix, proteins involved with adhesion, enzymes<sup>9,12</sup>. The result of these factors is to protect adjacent cells from apoptosis, induce proliferation, stimulate angiogenesis, induce differentiation of endogenous stem cells, and immunomodulatory effects.

### 1.2.3 Immunomodulatory properties of MSCs

MSCs can modulate the immune system either by direct cell-cell contact or paracrine mechanisms and are generally immuno-suppressive. These immuno-suppressive properties have been widely exploited to alleviate graft-versus-host disease (GvHD) for patients receiving hematopoietic stem cell transplant (also known as bone marrow transplant)<sup>11</sup>. For this application there are several approved MSC products, the first was Prochymal® (Osiris Therapeutics)<sup>12,17</sup> and more recently Remestemcel-L® (Mesoblast)<sup>12,18-21</sup>.

MSCs in general have an anti-inflammatory effect due to secretion of cytokines and regulating immune cells that participate in tissue repair. Anti-inflammatory cytokines secreted by MSC include interleukin (IL)-10, TGF- $\beta$ , and IL-1 receptor antagonist (IL1Ra)<sup>9,12,14,15</sup>. MSC signalling results in the transformation of pro-inflammatory (M1) macrophages to the anti-inflammatory (M2) phenotype<sup>15,22,23</sup> and increase the mobilization of macrophages to the region. MSC also prevent mobilization of neutrophils into local tissue<sup>24,25</sup>. Importantly, MSC promote the expansion and differentiation of Tregs, which are inherently immunosuppressive (Part 1.3)<sup>9,14,15,26</sup>.

### 1.2.4 Transplant-associated inflammation

The immune response of the MSC-transplant recipient is an important barrier to clinical translation<sup>4,27</sup>. In current clinical trials, autologous MSC represent the primary source for transplant<sup>11</sup>. However autologous therapies are not always feasible or practical since it may be difficult to obtain sufficient MSC from some patients and it is a time consuming and expensive process<sup>17</sup>. Additionally, it has been shown that MSC from elderly donors have decreased differentiation and regenerative potential<sup>10,17</sup>. For these reasons, allogenic MSC from young, healthy donors are beneficial and can become a readily available product. However allogenic MSC are likely to lead to immune-mediated rejection.

The first phase of immune recognition of allogenic MSC transplants is hyperacute rejection which involves an innate immune response upon implantation (within 0-96 hours). This innate response results from tissue stress and expression of pattern associated molecular patterns (PAMPs) on the MSC which are recognized by sentinel immune cells,

including macrophages and dendritic cells. These cells synthesize and release pro-inflammatory cytokines leading to further recruitment of immune cells to the tissue (*i.e.*, neutrophils and macrophages), cell damage, inflammation, and loss of the transplant. Tissue inflammation is also initiated by complement activation, in which pre-existing antibodies or complement proteins bind and mark alloantigens on MSC for destruction. This process is known as opsonization and attracts macrophages and neutrophils that recognize and phagocytose these alloantigens.

Upon transplantation, MSC are exposed to a hostile pro-inflammatory environment, which is challenging to survive in. Many of the cells undergo apoptosis and this further leads to influx of macrophages and monocytes from the blood, which phagocytose and remove cellular debris<sup>4,15</sup>. There is an overall increase in both pro-inflammatory (M1-type) and anti-inflammatory (M2-type) macrophages at the site of transplantation, where pro-inflammatory cells contribute to stem cell rejection and anti-inflammatory macrophages promote stem cell engraftment and wound healing<sup>4,28</sup>.

At the same time, a slower immune response (10-13 days), known as acute rejection, occurs in response to MSC transplantation; this involves the adaptive immune system. This response is mediated by CD8<sup>+</sup> cytotoxic T cells which recognize foreign major histocompatibility complexes (MHC) class I alleles which differ on allogenic MSC compared to the host<sup>27</sup>. T cells respond by releasing perforin and granzymes to initiate apoptosis of these transplanted cells ultimately leading to immune rejection. Commonly, donor/recipient immunophenotyping can help to find a match with minimized genetic differences in MHC alleles. Fortunately, allogenic MSC express low/modest levels of MHC class I molecules, so are considered to have relatively low immunogenicity<sup>17,29</sup>. While the acute rejection response still contributes to MSC rejection<sup>17</sup>, in this thesis we focus on the hyperacute rejection phase which largely determines the fate of MSC outcomes. This topic of acute rejection is relevant to Treg therapy in the context of organ transplantation.

### 1.3 Regulatory T Cell Therapy

Regulatory T cells (Tregs) are immunosuppressive cells that are involved in maintaining self-tolerance and immune homeostasis<sup>8,30</sup>. The immunosuppressive capacity of Tregs can be exploited to re-establish tolerance in conditions involving overactive immune responses, including allograft rejection<sup>31,32</sup>. Humans receiving solid organ transplants are at lifelong risk for graft rejection and take conventional immunosuppressive drugs, including steroids, ciclosporin, and biologics, which prolong the lifetime of the graft but are short-lived and often lead to widescale immunosuppression and toxicities<sup>33</sup>. Comparatively, Tregs as a living cell therapy have great potential to offer specific and long-lived immunosuppression.

There are now several completed clinical trials with Treg cell therapies to reduce GvHD in patients with organ or hematopoietic bone marrow cell transplants. The timing of Treg administration is variable; in some cases, Tregs were infused 4 days prior to transplant<sup>34,35</sup>, within the same day or day after transplant<sup>36-38</sup>, and in other cases Tregs were administered after the development of acute GvHD<sup>39,40</sup>. There are also completed trials with Treg cell therapies administered within 10 days of receiving kidney or heart transplantation<sup>32,41</sup>. These studies show that Tregs can be safely infused in a range of doses up to  $3 \times 10^8$  Treg/kg and that Treg cell therapy is promising to alleviate the number of patients that develop GvHD and/or the severity of symptoms<sup>36-38,40</sup>. Additionally, patients with Treg infusions could receive a reduced dose of other immunosuppressive drugs or avoid them altogether, without compromising outcomes<sup>34,40,41</sup>. Some studies have reported that patients receiving Treg therapy over of standard-of-care drugs have reduced risk of developing infection from opportunistic pathogens<sup>34,41</sup>.

### 1.3.1 Treg development

Primary lymphoid organs are the sites in which T lymphocytes arise and mature (*e.g.*, bone marrow and thymus, respectively). Tregs develop in the thymus and are a subset of CD4<sup>+</sup> helper T cells<sup>31,42,43</sup>. Tregs go on to escape the thymus and circulate to secondary lymphoid organs, including the lymph nodes and spleen (Figure 3). Tregs (and all T cells exiting the thymus) express CD62-ligand and chemokine receptor 7 (CCR7) to enhance their migration to these sites<sup>30</sup>. A network of lymphatic vessels drain lymphocytes throughout the body and into lymph nodes, which are present in clusters in the neck, axilla (underarm), chest, abdomen, and groin. The lymph fluid eventually empties into the thoracic duct (vein) which returns lymphocytes to the blood circulation. Naïve T cells constantly recirculate in and out of secondary lymphoid organs in search of antigens they recognize.

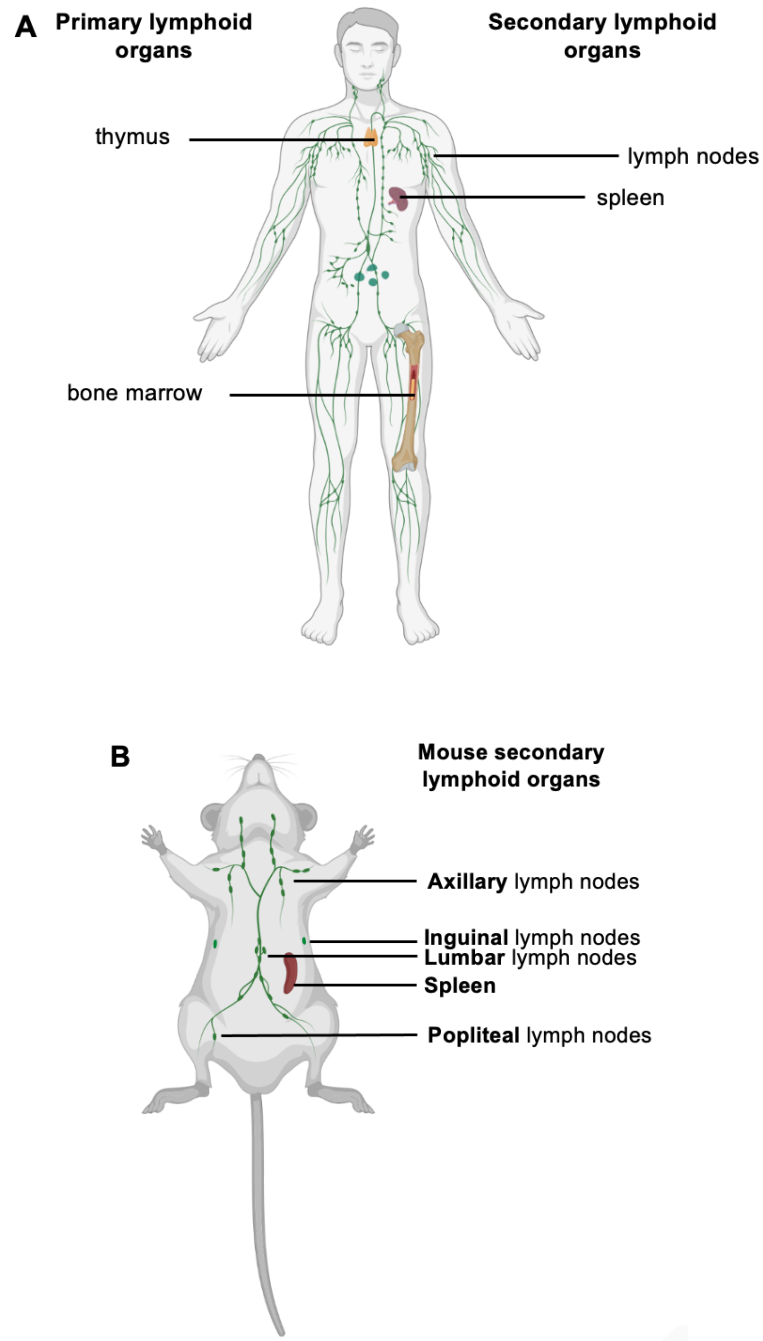


**Figure 3: A. The primary lymphoid organs are the thymus and bone marrow, and secondary lymphoid organs include the lymph nodes and spleen. Lymph nodes are located throughout the body. B. Locations of lymph nodes in a mouse are outlined in a cartoon, including the axillary, inguinal, lumbar, and popliteal lymph nodes.**

**Figure created with BioRender.com.**

T cells receive signals for activation and proliferation from antigen presenting cells (APC) in secondary lymphoid tissues. APC including dendritic cells and macrophages, are constantly surveilling their environment by phagocytosing proteins from the extracellular space or other cells. These proteins are degraded into peptides then presented on MHC class II molecules to CD4<sup>+</sup> naïve T cells. Two signals are required for T cell activation and involve binding interactions between the APC and T cell (Figure 4). Signal 1 involves a specific binding interaction between peptide-MHC II on APC and the TCR of a CD4<sup>+</sup> T cell. Signal 2 comes from the binding of a co-stimulatory molecule (e.g., B7, also known as CD80/86) expressed on an APC to a CD28 receptor on T cells.

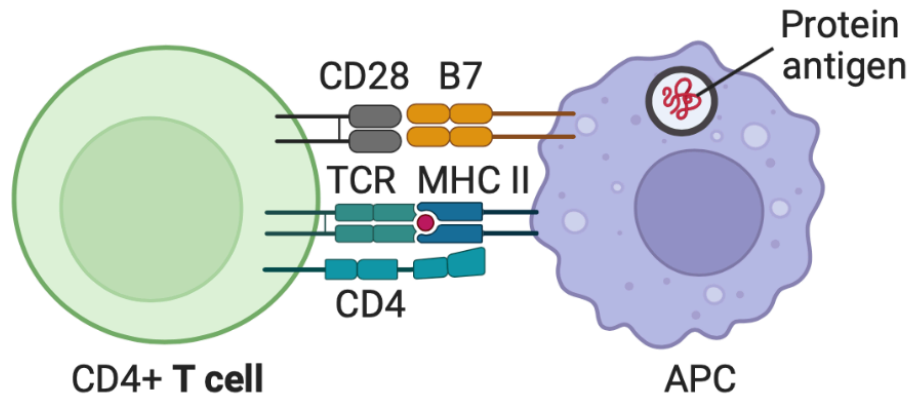


**Figure 4: Activation of CD4<sup>+</sup> T cells occurs in the presence of two signals from APC. Signal 1 is from the engagement of peptide-MHC class II bound to a specific TCR. Signal 2 comes from co-stimulatory molecule CD28 on the T cell binding to its ligand B7 on the APC. Figure created with BioRender.com.**

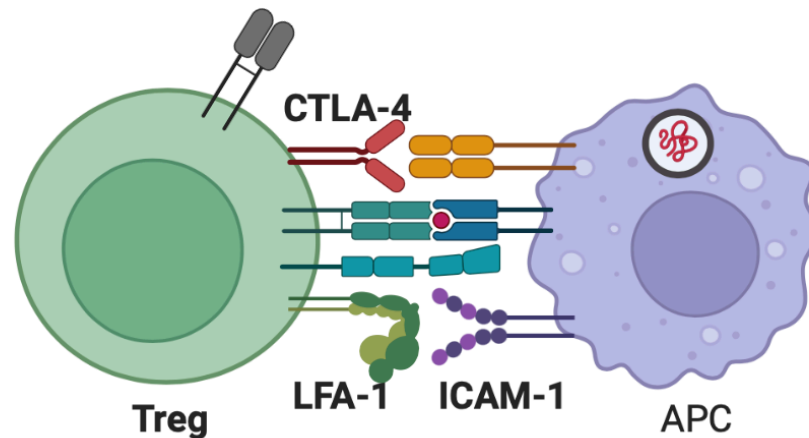
### 1.3.2 Immunosuppressive functions of Tregs

Activated Tregs exert immunosuppression by secreting anti-inflammatory cytokines, such as IL-10 and TGF- $\beta$ <sup>8,31</sup>. These cytokines promote a tolerogenic local microenvironment by suppressing the activity of other nearby T cells and APC. Additionally Tregs express CD25, which is part of the trimeric high-affinity IL-2 receptor, therefore Treg also sequester the local environment of pro-inflammatory cytokine IL-2<sup>31,33</sup>. This limits IL-2 availability for conventional T lymphocytes and instead favors Treg activity and development.

Tregs also modulate the function of the adaptive immune system by blocking effector T cell activation in lymph nodes. Firstly, Tregs form stronger immune synapses with APC compared to conventional T lymphocytes, due to the presence of the integrin lymphocyte function-associated antigen 1 (LFA-1) on Tregs which interacts with intracellular adhesion molecule 1 (ICAM-1) on APC<sup>44,45</sup>. Not only does this limit the availability of conventional T lymphocyte interaction with APC, but Tregs can also release perforins and granzymes to kill APC through this contact dependent manner<sup>8,46</sup>. Tregs are known to express high levels of cytotoxic T lymphocyte-associated antigen 4 (CTLA-4). CTLA-4 is an inhibitory molecule that has higher affinity for B7 than CD28, furthering Tregs to out-compete conventional T cells for binding ligands of APC. CTLA-4 binding to B7 can lead to a process known as transendocytosis, which involves the capture of B7 from APC and degradation of this co-stimulatory molecule by Treg<sup>47</sup>. Similarly, Tregs can participate in trogocytosis which refers to the depletion of peptide-MHC class II complexes from APC<sup>31,45</sup>. Overall, these processes directly inhibit APC ability to activate conventional T cells and thus adaptive immune responses become more tolerogenic (Figure 5).



i. Stronger immune synapses



ii. Initiation of APC apoptosis, B7 capture, and trogocytosis

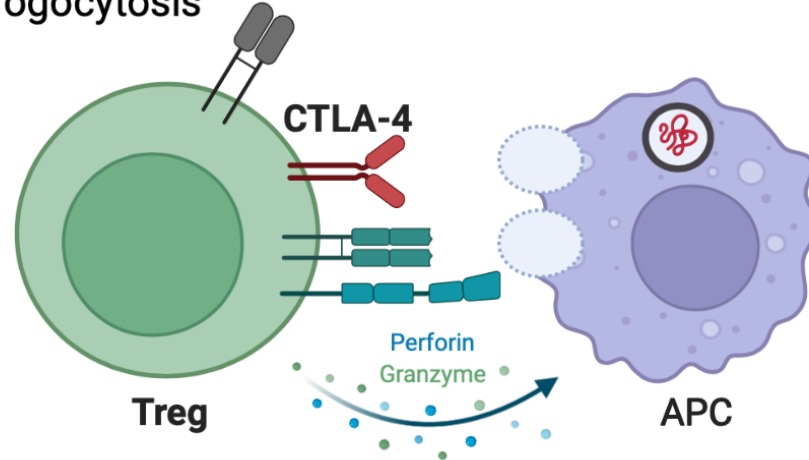


**Figure 5: Tregs are known to block the two signals required for T cell activation, to favor immunosuppression. i. Tregs express CTLA-4 which has a stronger affinity to B7 than CD28, blocking co-stimulation. Tregs also express LFA-1 which binds strongly to ICAM-1 on APC and produces a strong immune synapse between Treg and APC. ii. Treg binding to APC can result in removal of cell surface molecules, including MHC class II (trogocytosis) and B7 capture (transendocytosis), preventing APC ability to activate other T effector cells. Furthermore, Tregs may directly kill APC expressing a target antigen through the release of perforin and granzyme.**

Figure created with BioRender.com.

### 1.3.3 Engineering Treg specificity

Isolated Tregs are polyclonal, meaning very few of these cells would have specificity towards a target antigen. This implicates that a large number of Tregs would be needed to achieve therapeutic effects and there is risk for off-target immunosuppression<sup>8,48</sup>. While it is possible to isolate and expand antigen-specific Tregs in low yields, a more prominent and sophisticated technique is to engineer Tregs to obtain the desired specificity through ex vivo genetic modification<sup>31</sup>. A chimeric antigen receptor (CAR) combines the antigen recognition portion of an antibody with the signal transduction domain of a TCR (Figure 6)<sup>48,49</sup>. The antigen binding domain is extracellular and is the portion of the CAR that confers specificity towards the target antigen. Commonly, this domain is derived from a single-chain variable fragment (scFv) derived from an antibody. The intracellular signalling domain(s) provides co-stimulatory signals required for Treg activation, such as CD28. The transmembrane connects the antigen-binding domain with the signaling domain(s) and anchors the CAR into the cell membrane. Overall, engineering Tregs with CARs is a promising technique to achieve specific potency and re-direct immunosuppression towards a desired target<sup>30,31,49,50</sup>.

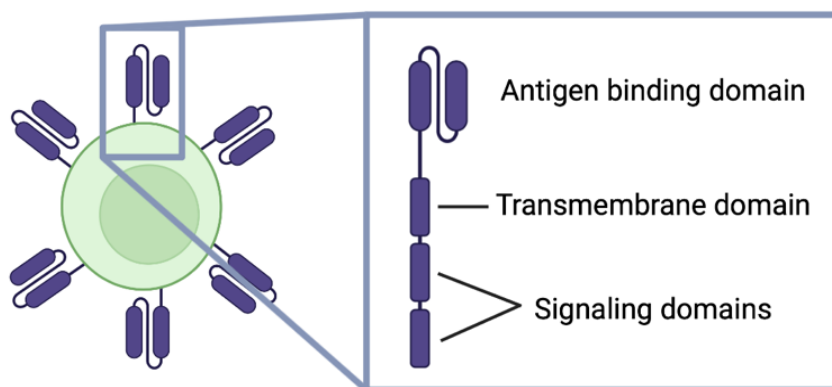


**Figure 6: Tregs can be genetically engineered to express chimeric antigen receptors (CAR) which consist of an extracellular antigen binding domain and a transmembrane domain, linking the intracellular T cell co-stimulatory signaling domains. CARs allow the engineered cell to specifically bind to an antigen of interest. Figure created with BioRender.com.**

In this thesis, magnetic resonance imaging (MRI) and magnetic particle imaging (MPI) are used to track MSC and Tregs. Parts 1.4 and 1.5 provide a description of these imaging modalities and how cells are prepared for imaging. Additionally, these subchapters contain a summary of previous work related to cell tracking of MSC, cell transplant-associated inflammation, and Tregs.

## 1.4 Magnetic Resonance Imaging

### 1.4.1 Nuclear Magnetic Resonance (NMR)

All nuclei possess a characteristic spin number ( $I$ ) and nuclei with non-zero spins ( $I = 1/2, 3/2, \dots$ ) produce magnetic resonance signal. An element will have non-zero nuclear spin if the number of neutrons plus protons are odd, such is the case for hydrogen ( $^1\text{H}$ , 1 proton and no neutrons) and fluorine ( $^{19}\text{F}$ , 9 protons and 10 neutrons). MRI relies on a strong static magnetic field  $B_0$  (e.g., 3 Tesla) that is in an orientation defined as the z-direction (Figure 7A)<sup>51</sup>. When placed within  $B_0$ , nuclei with non-zero spin align with (parallel) or against (anti-parallel) the magnetic field and the vector sum of these spins is the net magnetization ( $M_0$ ) (Figure 7B). Thermal motion prevents full magnetization alignment and nuclei experience torque and precess (oscillate) about  $B_0$  (Figure 7C) at a rate described by the Larmor equation<sup>51</sup>:

$$\omega_0 = \frac{\gamma}{2\pi} B_0$$

where  $\omega_0$  is the frequency in Hz. The frequency of nuclear precession is dependent on the strength of the magnetic field ( $B_0$ ) as well as an intrinsic property known as the gyromagnetic ratio ( $\gamma$ ). Each nucleus has a different resonance frequency since they differ in  $\gamma$ . Table 1 summarizes physical properties of MR-detectable nuclei.

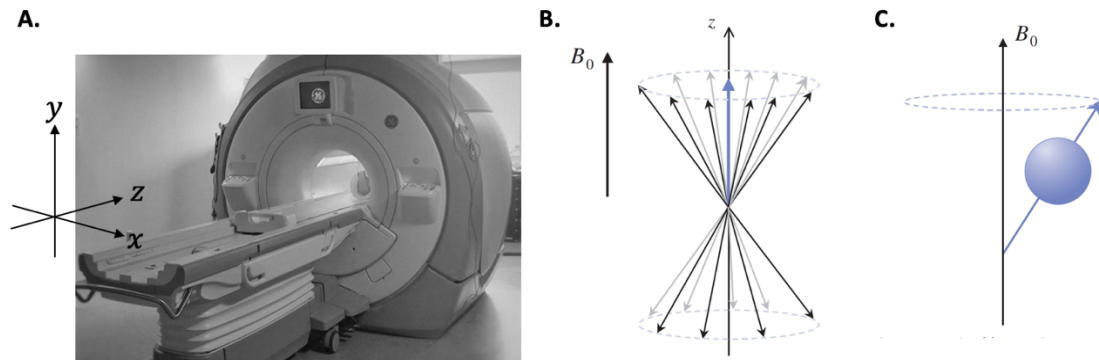


**Figure 7: A. Orientation of the x, y, and z planes. The magnetic field  $B_0$  is aligned with the z-direction. B. In the presence of  $B_0$ , nuclei with non-zero spin align with the magnetic field in both parallel and anti-parallel directions. The sum of these vectors produces a net magnetization  $M_0$  which aligns with  $B_0$  (+z). C.  $M_0$  precesses about  $B_0$  at the Larmor frequency. Figures adapted from *From-Picture-to-Proton*, 2<sup>nd</sup> ed., Cambridge University Press.<sup>51</sup>**

**Table 1: Physical properties of MR-detectable nuclei, including nuclear spin quantum number, natural abundance, gyromagnetic ratio, and resonance frequency at 3T.**

Element	Nuclear Spin ( $I$ )	Natural Abundance (%)	Gyromagnetic Ratio (MHz/T)	Resonance frequency at 3T (MHz)
$^1\text{H}$	1/2	99.98	42.58	127.74
$^{19}\text{F}$	1/2	100	40.08	120.24

### 1.4.2 Creating an image

To form an image, a radiofrequency (RF) excitation pulse is applied and creates a secondary magnetic field ( $B_1$ )<sup>51</sup>.  $B_1$  is perpendicular to  $B_0$  and oscillates at the Larmor frequency in the transverse ( $xy$ ) plane. This RF pulse tips the net magnetization  $M$  away from  $B_0$  (towards the  $xy$  plane) and is applied until a desired flip angle ( $\alpha$ ) is achieved, referring to the angle between the magnetization vector of excited nuclei from  $B_0$ . This process is known as excitation and involves the absorption of RF energy by nuclei.

After the RF pulse, the magnetic moment  $M$  realigns with  $B_0$  which releases energy that is detected as a voltage induced in a receive coil. The relaxation of  $M$  occurs in distinct paths along both the longitudinal ( $z$ ) and transverse ( $xy$ ) planes (Figure 8A-E). Spin-lattice ( $T_1$ ) relaxation refers to the intrinsic rate of  $M$  to align with  $B_0$  in the longitudinal direction where  $M_z$  exponentially returns to the value of  $M_0$ . Spin-spin ( $T_2$ ) relaxation refers to the exponential loss of spin coherence in the transverse plane, where nuclei rapidly dephase in a Free-induction decay (FID). Each of the individual magnetizations  $M_{xy}$  begin to relax and become out of phase until their vector sum reaches 0.  $T_2^*$  relaxation is the combined effect of  $T_2$  and additional dephasing caused by local inhomogeneities in the magnetic field, which causes the transverse magnetization to decay faster.

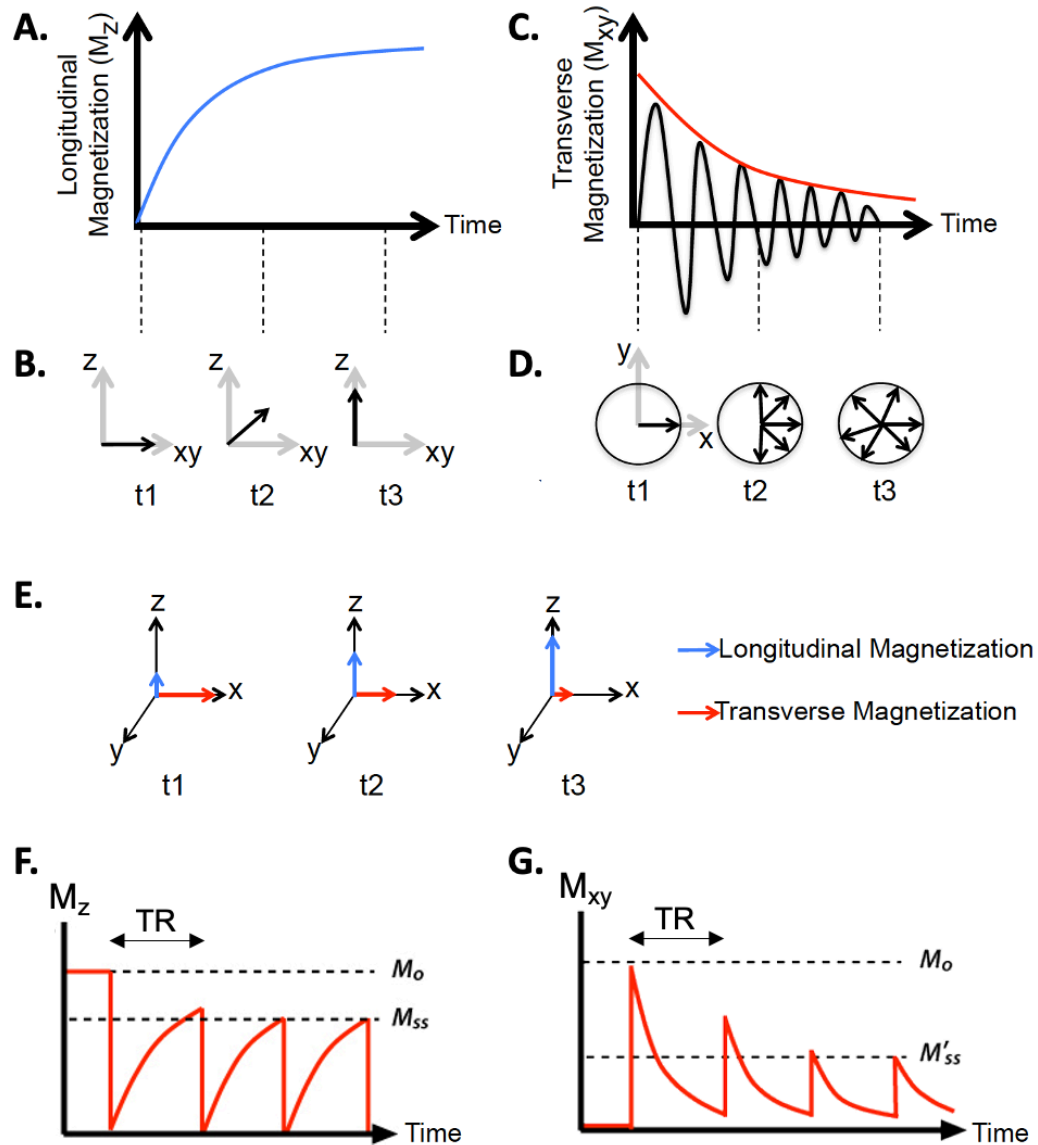


**Figure 8: T<sub>1</sub> and T<sub>2</sub> relaxation diagrams. (A) Longitudinal magnetization  $M_z$  increases exponentially over time after an RF pulse is applied. (B) Directly after the RF pulse (t<sub>1</sub>), the magnetization vector is at the designated flip angle away from z-axis into the xy plane ( $\alpha=90^\circ$  is shown) and the spins begin to relax (t<sub>2</sub>) until realigned with  $B_0$  (t<sub>3</sub>). (C) Transverse magnetization  $M_{xy}$  decreases over time after an RF pulse is applied. (D) Directly after the RF pulse (t<sub>1</sub>), the magnetization vector is forced into the xy plane and over time the spins dephase (t<sub>2</sub>) until there is the net magnetization vector reaches zero (t<sub>3</sub>). (E) Summary diagram showing that the**

**magnetization vector is excited towards the xy plane and over time, the longitudinal magnetization is regained, and transverse magnetization is lost. (F,G) If RF pulses are quickly repeated ( $TR \ll T_1, T_2$ ), full  $T_1$  and  $T_2$  relaxation do not occur therefore RF pulses are applied to the remaining magnetization vector at the end of each TR. A steady state magnetization is reached in (F) the  $M_z$  direction ( $M_{ss}$ ) and (G) the  $M_{xy}$  direction ( $M'_{ss}$ ). Figure adapted from the PhD thesis of Ashley V. Makela<sup>52</sup>.**

### 1.4.3 MRI parameters

The relaxation time (TR) designates the time between successive excitation pulses. The time at which signal is acquired after the RF pulse is the echo time (TE)<sup>51</sup>. TR can influence image weighting since it determines whether there will be full or partial relaxation of the magnetization in the longitudinal ( $T_1$ ) and transverse ( $T_2$ ) planes prior to the next RF pulse. If TR is shorter than  $T_2$  and  $T_1$  relaxation, a steady state free precession (SSFP) is reached, where RF pulses act on previous magnetization remaining at the end of a TR (Fig. 7 F,G). In this case  $T_1$  and  $T_2$  relaxations have not fully occurred, the weighting of SSFP sequences is mixed  $T_1$  and  $T_2$ .<sup>53</sup>

The imaging region is known as the field of view (FOV), which is divided by a matrix to form voxels. 3D isotropic voxels have equal dimensions in all x, y, and z directions and allow for multi-planar reformatting. To achieve spatial localization of voxels, magnetic field gradients, which are orders of magnitude smaller than  $B_0$ , are applied which influence precession frequency in each direction. The gradient forms a linear difference in magnetic field strength such that nuclei resonate faster or slower depending on their position, allowing for MR signal location to be mapped based on differences in frequency. At the center ( $x = 0$ ) the nuclei experience  $B_0$  and resonate at the Larmor frequency. Gradients in 3D are applied at separate times; a slice select gradient ( $G_{ss}$ ) is applied during RF excitation and defines the slice being imaged, a phase encoding gradient ( $G_{pe}$ ) is applied briefly after the RF pulse, and the frequency encoding gradient ( $G_{fe}$ ) is applied during signal output (echo). PE is repeated for each row of voxels and therefore the number of rows has a direct effect on scan time, so is commonly assigned to

the shortest anatomical axis to minimize scan time. During signal readout, a k-space matrix is filled which maps the phase and frequency of signals in a coordinate grid for each slice. A Fourier transform is applied to convert signals in the frequency domain to a spatial domain to produce an image.

An MRI pulse sequence consists of an arrangement of timed RF pulses and manipulation in magnetic field gradients. There are two broad categories of pulse sequences: spin echo and gradient echo. For spin echo sequences, a  $90^\circ$  pulse is applied followed by a second refocusing  $180^\circ$  pulse which reverses the direction of spins to form an echo.  $M_{xy}$  signal regains spin coherence and is rephased at TE. The advantage of this technique is that the signal is maximized in the transverse plane, giving high MRI sensitivity. Gradient echo sequences involve the application of a single RF pulse per TR, typically with flip angles  $<90^\circ$ . In the frequency encoding direction, first a dephasing magnetic gradient is applied followed by an inverted gradient to create an echo at TE. Compared to spin echo sequences, gradient echo sequences collect less signal per excitation but are advantageous because TR are much shorter. Gradient echo sequences are also susceptible to magnetic inhomogeneities and the presence of paramagnetic agents (*i.e.*, iron oxide), leading to  $T_2^*$  reductions.

#### 1.4.4 Balanced steady state free precession sequence

Balanced steady state free precession (bSSFP) is a fast gradient echo pulse sequence that is also commonly known as true fast imaging with steady precession (True FISP), balanced fast field echo (balanced FFE), or fast imaging employing steady-state acquisition (FIESTA), depending on the MRI vendor. bSSFP uses very short TR (often  $<10$  ms) which is designed to be shorter than  $T_1$  and  $T_2$  relaxation<sup>53</sup>. Therefore, a steady state of magnetization occurs over several TRs (at  $5 \cdot T_1 / TR$ ) where  $M_z$  and  $M_{xy}$  are in dynamic equilibrium (Figure 8F,G). Balanced SSFP has a specific sequence design (Figure 9), where there is no gradient-induced dephasing within each TR. Dephasing refers to rotation of the magnetization around the z-axis. Each applied gradient pulse in all 3 orientations ( $G_{ss}$ ,  $G_{PE}$ ,  $G_{FE}$ ) is compensated by a gradient pulse of opposite polarity after TE. TE occurs at  $TR/2$  such that the gradients are balanced on either side<sup>54</sup>. The



magnetization is refocused (rewound) such that a single magnetization vector remains at the end of TR and the next RF excitation pulse acts on this single vector. In contrast to a spoiled GE sequence where the net transverse magnetization after one TR is zero, the magnetization  $M_{xy}$  at the beginning and end of each TR is nearly identical for bSSFP. Alternating excitation pulses  $\pm\alpha$  are applied in steady state. The amplitude of the steady state magnetization is<sup>53</sup>:

$$M_{SS} = 0.5 * M_0 \sqrt{\frac{T_2}{T_1}}$$

As mentioned in part 1.5.3, bSSFP has mixed image contrast, which is dependent on the ratio of  $T_2/T_1$ . Interestingly, if  $T_1$  and  $T_2$  values are similar, the maximum signal that can be acquired is  $0.5 * M_0$ , meaning that with bSSFP it is possible to continuously acquire 50% of all total spins<sup>53</sup>. This leads to impressive sensitivity and bSSFP has the highest possible SNR per unit time of all known pulse sequences.

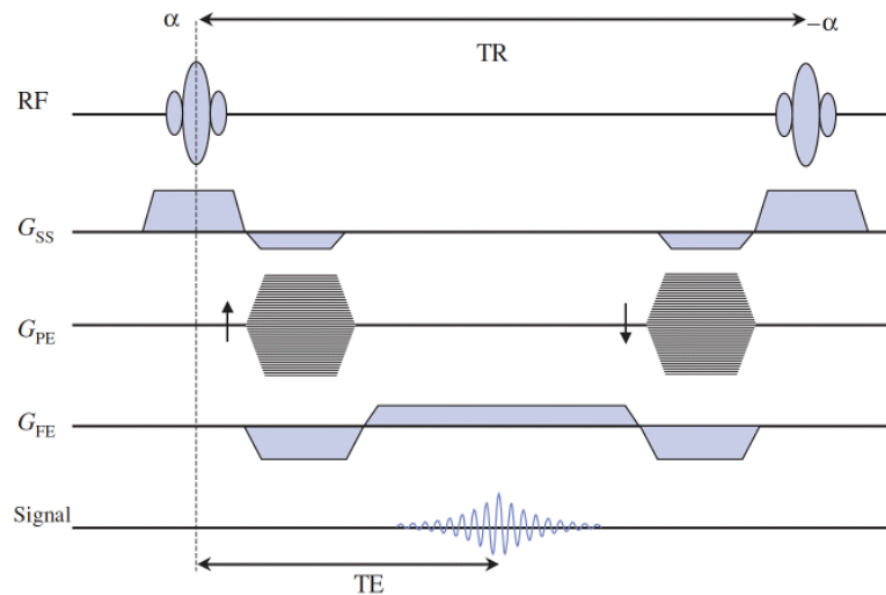


**Figure 9: Pulse sequence diagram for bSSFP. A radiofrequency (RF) pulse with a set flip angle ( $\alpha$ ) is applied at each repetition time (TR). The magnetic gradients in the slice selection ( $G_{SS}$ ), phase-encoding ( $G_{PE}$ ), and frequency encoding ( $G_{FE}$ ) directions are balanced. The MRI signal is acquired at echo time (TE) = TR/2.<sup>54</sup>**

**Image adapted from From-Picture-to-Proton<sup>51</sup>.**

### 1.4.5 Direct and *in situ* cell labeling for cellular MRI

MRI has been widely used for *in vivo* cell tracking<sup>2,55-57</sup>. Cellular MRI uses contrast agents for labeling specific cells, thereby enhancing their detectability. MRI cell tracking can be performed with magnetite ( $\text{Fe}_2\text{O}_3$ )-based superparamagnetic iron oxide nanoparticles (SPIOs) or  $^{19}\text{F}$ -perfluorocarbon (PFC) nanoemulsions by labeling cells *in vitro* prior to their injection or implantation (Figure 10). Direct cell labeling is achieved through co-incubation *in vitro*. Assessment of cell labeling can be performed with histology (Figure 10) and some agents are available with fluorescent probes which can be used to further validate labeling by fluorescent microscopy or flow cytometry<sup>58</sup>.

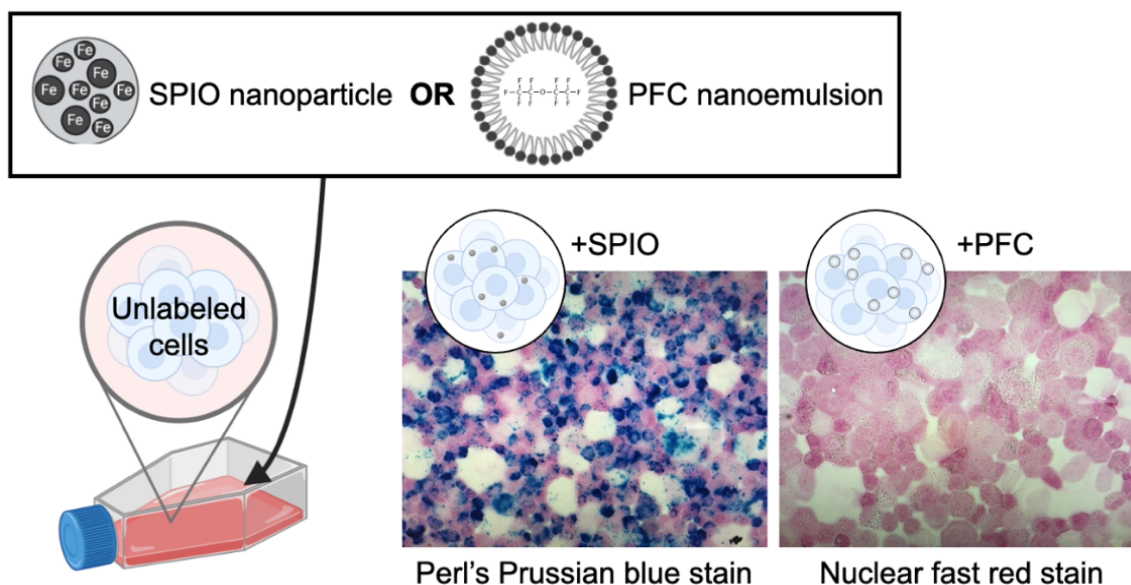


**Figure 10: In vitro cell labeling with SPIO nanoparticles or PFC nanoemulsions. SPIO or PFC are co-incubated with cells by adding these agents to the cell media. After 12-24 hours, cells are collected from culture, washed with saline, then a SPIO- or PFC-labeled cell product is obtained. Successful labeling can be confirmed with Perl's Prussian blue (PPB) stain (iron oxides) or by visualizing nanodroplets (PFC nanoemulsions) in the cytoplasm of cells. Cartoon figures created with BioRender.com are not to scale.**

SPIONs and PFC nanoemulsions can also be administered intravenously. These agents circulate and are taken up *in situ* by phagocytic macrophages<sup>7,59-61</sup>. Imaging is typically performed 1 day after the administration of the cell labeling agent to permit for the clearance of intravascular agent and the accumulation of the label into cells. In healthy subjects, SPIONs and PFC nanoemulsions can be detected in macrophage-dense tissues including the liver, spleen, and lymph nodes, and bone marrow, which make up the reticuloendothelial system<sup>60,62</sup>. A comparison of MRI (post-SPION administration), MPI (post-SPION administration, and <sup>19</sup>F MRI (post-PFC administration) is shown in Figure 11.

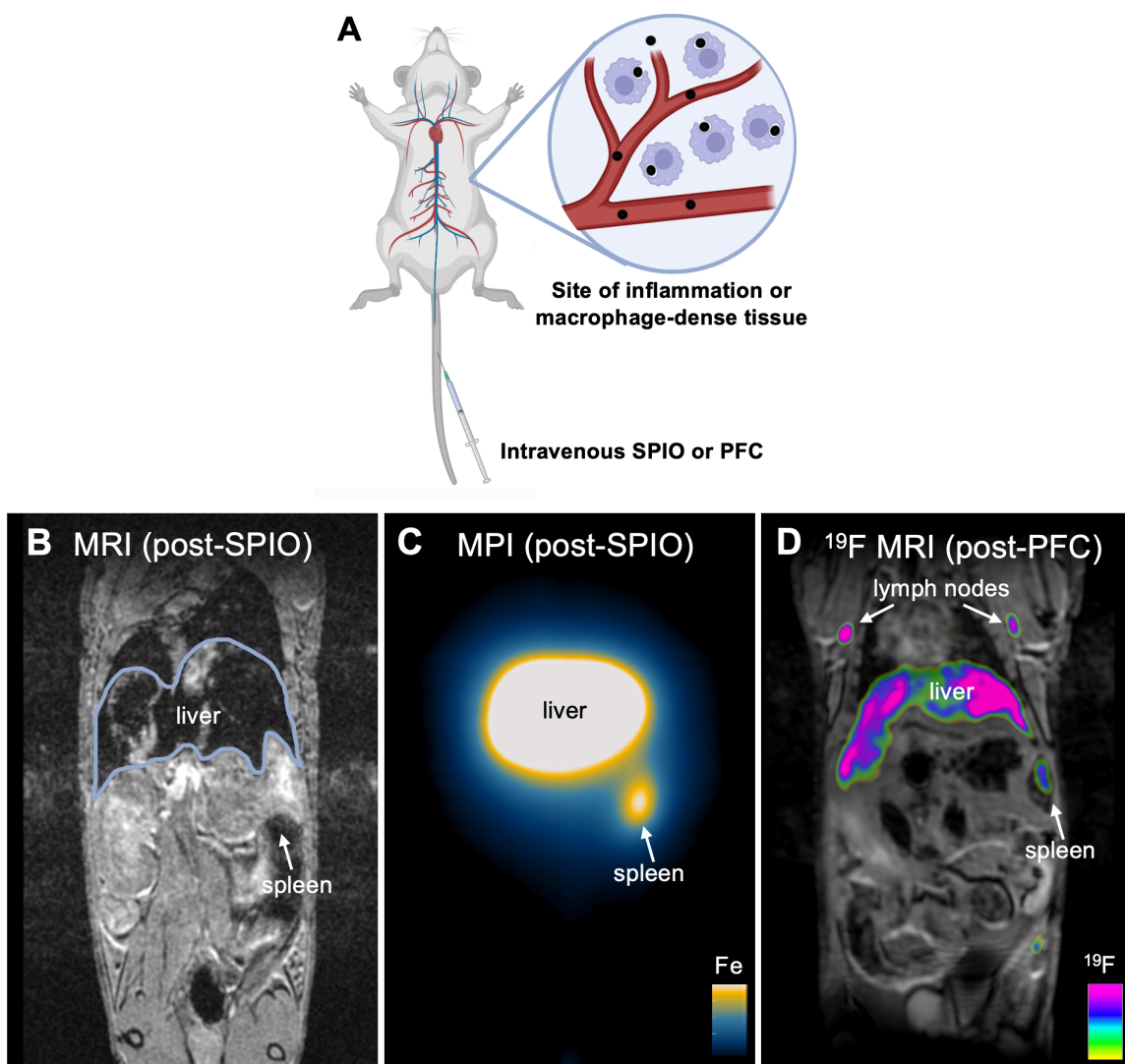


**Figure 11: A. Intravenously administered SPIO or PFC agents accumulate in phagocytic macrophages located in the reticuloendothelial system and sites of inflammation. Figure created with BioRender.com. B. Following SPIO intravenous administration, the SPIO acts as a negative contrast agent and the resulting MRI shows darkening of the liver and spleen. C. Comparatively, SPIOs act as tracers for MPI and the resulting image shows bright signals in the liver and spleen with the absence of signals from other tissues. D. Following PFC intravenous administration, hotspot  $^{19}\text{F}$  signal is detected in the liver, spleen, and lymph nodes.  $^{19}\text{F}$  signal is overlaid to  $^1\text{H}$  MRI for anatomical localization.**

### 1.4.6 Iron-based MRI cell tracking

To date, most cellular MRI involves tracking cells which are labeled with SPIONs. A major advantage of this technique is to visualize labeled cells relative to anatomical structures. SPIONs create a local magnetic field inhomogeneity that leads to signal hypointensities in  $^1\text{H}$  MRI. This is because SPIONs alter net local magnetization that nearby  $^1\text{H}$  atoms experience and lead to dephasing of these  $^1\text{H}$  atoms, creating shorter  $T_2$  and effective transverse relaxation times ( $T_2^*$ ) in GE sequences. Since SPIONs have this effect on surrounding nuclei the hypointense region occupies a space larger than the SPION itself, giving rise to what is known as the blooming artifact<sup>2,61,63-65</sup>. This effect can lead to enhanced sensitivity, permitting the imaging of single cells *in vivo*, under ideal conditions<sup>64,66</sup>. bSSFP is a unique GE sequence because field inhomogeneity induced dephasing will be nearly completely refocused (meaning, the magnetization vector is exactly aligned along the x-axis) at  $TE = TR/2$ , if spin phase is  $< \pm\pi$ .<sup>53</sup> However, this refocusing mechanism fails if dephasing between RF pulses exceeds  $\pm\pi$  in an imaging voxel and leads to a nearly complete collapse of the steady state signal. Therefore, SPIONs which lead to spin dephasing are a powerful contrast agent in combination with bSSFP<sup>63</sup>.

While the blooming artifact leads to high detection sensitivity, it complicates the quantification of iron-induced signal loss, since the signal void volume is not linear with the number of cells. Another limitation of SPION-based MRI the lack of specificity, owing to other low-signal regions in MR images arising to anatomical features, such as the air-filled lungs or a region of hemorrhage<sup>67</sup>. In some cases, this can be overcome with a pre-image to look for differences in contrast before and after cell transplantation.

#### 1.4.6.1 MSC tracking with iron-based MRI

There have been numerous studies confirming that the *in vivo* anatomical localization of SPION-labeled MSCs can be determined with MRI<sup>66,68-71</sup>. This imaging information is valuable to predict outcome of therapy since the restorative effects of MSC relies on arrival to target site. SPION-based MRI can identify cases of cell mis-injections, which can be common in the case of technical and challenging injection methodologies<sup>72</sup>. For

example, a preclinical study led by Gonzalez-Lara et al.<sup>73</sup> looked at SPION-labeled MSC that were administered directly into the center of a spinal cord injury. There were several missed injections which were only recognized as unsuccessful after identifying MR-signal loss outside the spinal cord. Similar findings have been demonstrated clinically<sup>74</sup>. The success of the cell therapies relies on correct injections, therefore, MRI tracking of the delivery of SPION-labeled cells provides immediate feedback on therapeutic status.

Many preclinical MRI studies have demonstrated detection of migrated SPION-labeled MSC to target site(s) after systemic administration using MRI and confirmed with histology<sup>68,75-78</sup>. This has also been demonstrated clinically<sup>79</sup>, with SPION-labeled stem cells for a patient with traumatic brain injury. Two weeks after cellular administration, hypointense MR signal appeared at the lesion site and the signal intensified at the 3<sup>rd</sup> week, suggesting migration of SPION-labeled stem cells from the site of injection to the lesion.

#### 1.4.6.2 Imaging inflammation with iron-based MRI

MRI has been used to monitor macrophage influx to stem cell transplant sites through intravenous delivery of SPION. The result is a large region of MRI signal-loss due to phagocytosis by infiltrating macrophages at the transplant site<sup>4,7,59,60</sup>. Gaudet *et al.*<sup>7</sup> showed this signal loss is absent in saline controls, indicating that SPION-mediated signal loss is a marker of macrophage infiltrate responding to the transplantation of cells, rather than the injection itself. In another study<sup>59</sup>, rats received intravenous SPIONs to preload macrophages of the RES, followed 48 hours later by either apoptotic or viable (unlabeled) stem cell transplants in an osteochondral defect of the femur. T2-MRI signal observed at the site of cell transplantation reflected macrophage infiltration. After 4 weeks the signal associated with apoptotic stem cells was significantly lower than that from viable stem cells. Similar imaging strategy with intravenous SPION and MRI has been applied to monitor atherosclerosis<sup>80</sup>, neuroinflammation<sup>81,82</sup>, and cancer<sup>83-85</sup>. Notably, this type of imaging with intravenous SPION has been used clinically<sup>86-89</sup>. However, the major limitation of SPION-based MRI is the lack of quantitation of immune cell infiltrate.

### 1.4.6.3 T cell tracking with iron-based MRI

Despite the growing use of T cell immunotherapy, there has not yet been a study involving T cell tracking in humans using MRI. Labeling T cells with SPIONs has been a major challenge due to small cytoplasmic volumes and limited phagocytic activity of T cells<sup>5</sup>. Techniques including co-incubation with transfection agents<sup>90-92</sup>, electroporation<sup>93</sup> mechanoporation<sup>94</sup>, and alteration of SPION surface chemistries<sup>95,96</sup> have been used to increase uptake of SPIONs by T cells. There are several studies of intravenously administered SPION-labeled T cells in mice that were detected with MRI; after migration to pancreatic islets<sup>97</sup>, autoimmune encephalomyelitis lesions in a spinal cord<sup>98</sup>, or melanoma tumors<sup>99</sup>. SPION-labeled T cells were detected as signal voids at these regions and confirmed by histology. The most striking result is the sensitivity of the technique, with as few as  $\sim 3$  cells per voxel in a tumor (determined by dual <sup>111</sup>In-oxine autoradiography)<sup>99</sup> or 200 cells in a lesion (number of cells estimate based on histology)<sup>98</sup>.

There is one preclinical study by Tremblay et al.<sup>100</sup> that labeled murine Tregs with ultrasmall SPIONs (Molday) and tracked the biodistribution after intravenous administration with MRI. Molday particles are small (35 nm) and unique since they have a positively charged surface which increases the interaction with the negatively charged cell membrane of the T cells<sup>101</sup>. SPION-labeled Tregs were detected as regions of signal loss in lymph nodes and cervical tumors, however these signals are not quantitative and this technique cannot provide a measure of Treg cell number.

### 1.4.7 Fluorine-19 based MRI cell tracking

<sup>19</sup>F MRI cell tracking addresses some of the limitations associated with iron-based MRI cell tracking. Firstly, PFC-labeled cells can be imaged by <sup>19</sup>F MRI with high specificity since there is very little endogenous fluorine in biological tissues. Second, the spins of <sup>19</sup>F nuclei are directly detected and the signal intensity is linearly proportional to the number of <sup>19</sup>F nuclei per voxel<sup>58</sup>. <sup>19</sup>F images are typically presented with a color scale to represent numerical values and overlaid onto the corresponding proton MRI for anatomical reference. A sample of PFC-labeled cells can be separately analyzed by <sup>19</sup>F NMR to

determine the average  $^{19}\text{F}$  per cell and this can be used to estimate the number of cells which contribute to the signal in the  $^{19}\text{F}$  image<sup>102</sup>. The ability to determine cell number *in vivo* from  $^{19}\text{F}$  images is the most compelling reason for using  $^{19}\text{F}$  MRI over other cellular imaging techniques.

The main limitation of  $^{19}\text{F}$  cell tracking is low sensitivity, requiring a minimum of  $10^3$ - $10^5$  labeled cells per imaging voxel<sup>56</sup>. Unlike  $^1\text{H}$  which is highly abundant in tissue and the primary nuclei imaged with MRI,  $^{19}\text{F}$  has low *in vivo* abundance. Therefore,  $^{19}\text{F}$  agents must be concentrated and optimization of MRI parameters is required to enable  $^{19}\text{F}$  MRI detection. bSSFP is considered a good sequence for  $^{19}\text{F}$  MRI because it offers fast imaging with highest SNR<sup>103,104</sup>. The sequence is fast owing to short TR, allowing for high numbers of signal averages. In this thesis a minimum of 40-200 averages are used for  $^{19}\text{F}$  imaging.

There is one clinical study with  $^{19}\text{F}$  MRI for the tracking of dendritic cells, where 3 patients received 10 million PFC-labeled cells intradermally in the quadriceps near the inguinal region<sup>105</sup>. The clinical imaging protocol used a 3 Tesla MRI scanner and a 7 cm diameter  $^1\text{H}/^{19}\text{F}$  surface coil.  $^{19}\text{F}$  signal was visualized at the injection site in images obtained 4 and 24 hours after administration. These cells were expected to migrate to the draining lymph node in this time, however no  $^{19}\text{F}$  signal was detected. In two patients that received lower doses (1 million DC)  $^{19}\text{F}$  signal was not detected. This study emphasizes the limitation of sensitivity for  $^{19}\text{F}$  MRI cell tracking.

#### 1.4.7.1 MSC cell tracking with $^{19}\text{F}$ MRI

Several studies which aim to image PFC-labeled MSC show hotspot signals at the location of administration for up to 2 weeks, with a decline in  $^{19}\text{F}$  signal over time<sup>7,106-111</sup>. Ribot *et al.*<sup>103</sup> compared detection and signal characteristics of SPION- or PFC-loaded MSC with MRI, where  $^{19}\text{F}$ -based MRI was determined to be superior due to highly specific hotspot signals and straightforward interpretation. Furthermore,  $^{19}\text{F}$  signal was directly quantitative, showing significant declines in signal at multiple timepoints, whereas measurements of the volume of the hypointensities in SPION-based MRI were not. Ultimately, SPION-based MRI overestimates the presence of MSC.



Due to quantitative nature of  $^{19}\text{F}$  MRI, MSC transplant outcomes can be distinguished. For example,  $^{19}\text{F}$  MRI was used to show that PFC-labeled mouse-derived MSC transplanted to immune-competent mice (C57Bl/6) underwent clearance from the site of implantation at a faster rate than human-derived MSC in immune compromised mice (nu/nu)<sup>110</sup>. This occurs at later timepoints (9 days) and would be expected due to immune rejection (outlined in Part 1.2.4) in immune-competent mice. This metric would be highly valuable for evaluating MSC persistence in clinical trials. However, all  $^{19}\text{F}$ -based MSC tracking mentioned has taken place at magnetic field strengths  $\geq 7$  T. This is due to limited detection sensitivity of  $^{19}\text{F}$  MRI at lower field strengths used clinically (e.g.,  $< 3$  T). Additionally, all studies focused on imaging MSC which were administered by point injection which concentrate  $^{19}\text{F}$  density per voxel (e.g., subcutaneous or directly to brain). It is unclear whether PFC-labeled MSC would be detected with  $^{19}\text{F}$  MRI after systemic administration and homing to a target site due to sensitivity limitations.

#### 1.4.7.2 Imaging inflammation with $^{19}\text{F}$ MRI

As previously described in Part 1.4.5, the intravenous delivery of PFCs allows for *in situ* labeling of inflammation and phagocytic cells of the reticuloendothelial system. With  $^{19}\text{F}$  MRI, this technique has been used to image cardiovascular and pulmonary inflammation<sup>112,113</sup>, tumor-associated macrophages<sup>85,114</sup>, and inflammation resulting from solid organ transplantation<sup>115,116</sup>. Ebner B. *et al.* (2010)<sup>113</sup> demonstrate  $^{19}\text{F}$  MRI detection of pulmonary inflammation, induced by lipopolysaccharide (LPS).  $^{19}\text{F}$  signals were seen in both lungs, which were not present in control mice, and  $^{19}\text{F}$  signals scaled with the amount of LPS administered (therefore, the degree of inflammation). Importantly, this type of quantitative inflammatory imaging in the lungs with SPION-based MRI is not possible, since SPION negative contrast could not be easily distinguished and quantified against the air-filled lungs. Interestingly, this group analyzed blood to show that 24-48 hours after PFC administration, circulating monocytes/macrophages are the predominant cells type becoming labeled by PFCs, with neutrophils being labeled to a lesser extent. Additionally,  $^{19}\text{F}$  signals in the lung were correlated with macrophage staining in *ex vivo* histology.

While  $^{19}\text{F}$  MRI has not previously been used to image inflammation resulting from cell transplantation (Part 1.2.4), the feasibility for this methodology is indicated by studies of organ transplantation. Fogel U. *et al.* (2011)<sup>115</sup> studied  $^{19}\text{F}$  imaging of transplant rejection in allograft or isograft (from the same mouse strain) heart transplants in mice.  $^{19}\text{F}$  signals were strong in mice receiving allograft transplants and increased over time with the extent of tissue rejection.  $^{19}\text{F}$  signals in isograft hearts were significantly lower and associated with surgical sites.  $^{19}\text{F}$  MRI signals are specific to PFCs, unlike SPION-based MRI where hypointense regions associated with hemorrhage resulting from rejection could be confused with the accumulation of SPION<sup>116</sup>.

#### 1.4.7.3 T cell tracking with $^{19}\text{F}$ MRI

There are several T cell tracking studies with PFC nanoemulsions and  $^{19}\text{F}$  MRI, but none with Tregs. PFC-labeling of T cells has been demonstrated for small cultures of T cells for over a decade<sup>58,117–119</sup>, and more recently, large clinical scale manufacturing<sup>120</sup>. T cells typically incorporate  $\sim 10^{11}$   $^{19}\text{F}$  atoms per cell with high labeling efficiencies<sup>121–123</sup>. The uptake of nanoemulsions is reliant on passive, endocytic processes<sup>124</sup>. For reference, phagocytic cell types such as dendritic cells, can uptake more PFCs on the order of  $10^{12}$ - $10^{13}$   $^{19}\text{F}$  atoms per cell<sup>105,125,126</sup>.

$^{19}\text{F}$  MRI may be promising for studying Treg trafficking and persistence *in vivo* in a quantitative manner. Previous work has demonstrated longitudinal tracking and homing of TCR-engineered (ovalbumin-specific) T cells with  $^{19}\text{F}$  MRI<sup>58</sup>. The antigen, ovalbumin, was administered subcutaneously to mice.  $^{19}\text{F}$  images over 21 days showed  $^{19}\text{F}$  signal in the lymph node draining the antigen. By day 7, approximately 40% of the T cells had accumulated in the draining lymph node, and over time, gradual clearance of PFC+ T cells was detected. Importantly, in control mice which received antigen-negative injections, T cells were detected only in the mesenteric region, and in control mice that received heat-killed ovalbumin-specific T cells,  $^{19}\text{F}$  signal was only observed near the bladder. Therefore, only the viable, antigen-specific T cells showed purposeful migration to the lymph node draining the antigen.

PFC+ T cells and CAR T cells have been tracked with  $^{19}\text{F}$  MRI in cancer mouse models, for multiple days following direct injections into subcutaneous U87 glioma tumors<sup>127</sup> or subcutaneous NALM6 leukemia tumors<sup>122</sup>. These studies demonstrate that  $^{19}\text{F}$  MRI can provide information on cell delivery to tumors. However, there are mixed results on whether  $^{19}\text{F}$  MRI can indicate T cell effectiveness. In glioma bearing mice,  $^{19}\text{F}$  signals from mice receiving PFC+ CAR T cells significantly decreased over time (by 60%) and inversely correlated with glioma burden, which may be useful as a therapeutic cell marker<sup>127</sup>. In mice bearing leukemia tumors,  $^{19}\text{F}$  signals from untransduced T cells and CAR T cells remained constant over time, despite CAR T cells invoking a significant reduction in leukemia growth<sup>122</sup>. In this instance,  $^{19}\text{F}$  signal cannot be used to distinguish effective (CAR T cells) versus ineffective (untransduced T cells) therapeutic responses.

## 1.5 Magnetic particle imaging

### 1.5.1 A definition of superparamagnetism

Iron oxide nanoparticles are a unique material that is known to be superparamagnetic. Each atom of iron has unpaired electrons, leading to an internal magnetic dipole. In the absence of a magnetic field, the magnetic dipoles of SPIONs are randomly oriented (Figure 12A). When a magnetic field is applied, the dipoles align with the magnetic gradient field lines (Figure 12B) and adjacent iron atoms act in unison to create a large magnetic moment. With higher applied fields, the dipoles are more strongly magnetized until they reach a magnetization saturation<sup>128,129</sup>. When the external magnetic field is shut off, the dipoles of the superparamagnetic material resume to random orientations and there is no residual magnetic interaction remaining<sup>130,131</sup>.

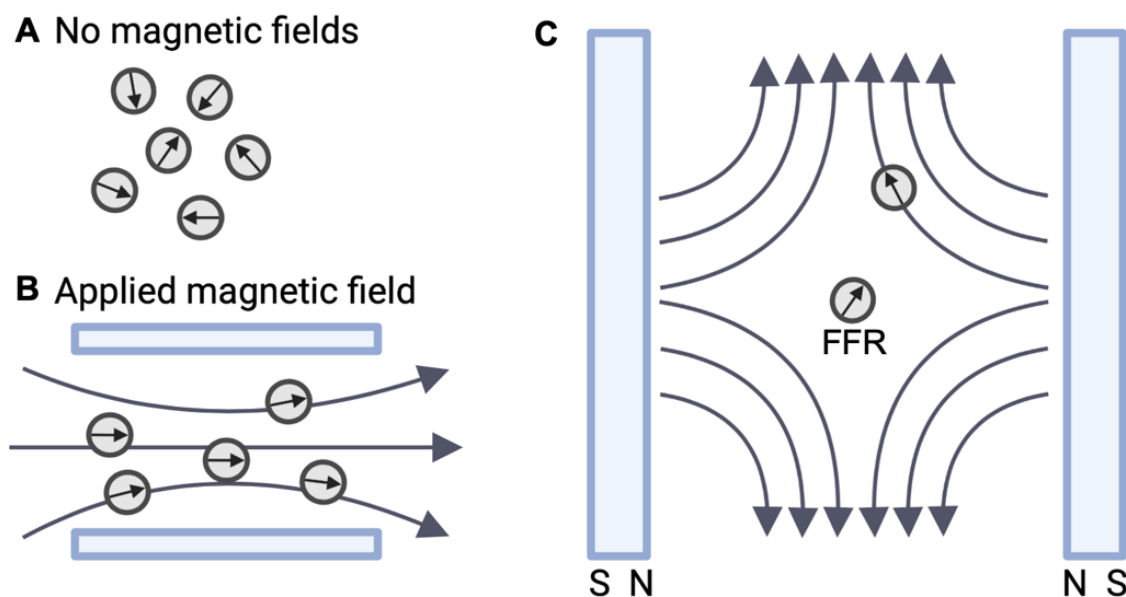


**Figure 12: A. Superparamagnetic materials have no net alignment in the absence of a magnetic field and B. saturate strongly to align with an applied magnetic field. C. The magnetic particle imaging magnetic gradient system saturates SPIONs which are outside the field free region (FFR). Within the imaging FFR, SPIONs can freely respond to the excitation magnetic field and produce signals. Figure created with BioRender.com.**

## 1.5.2 Creating an image

MPI is built around a gradient magnet system. Two opposing electromagnets form strong gradient magnetic fields (in the order of T), and a field free region (FFR) is created in the position where these gradient fields cancel out (Figure 12C)<sup>128,132</sup>. The gradient field (also known as the selection field)<sup>128</sup> saturates the magnetization of all SPIONs except for SPIONs at the FFR, which experience no magnetic field<sup>131,133</sup>. The FFR is shifted over an imaging volume, by changing the current through the electromagnets, to produce an image. When the FFR traverses a location containing SPIONs, the SPIONs' magnetization changes in response to a secondary sinusoidal excitation magnetic field (in the order of mT)<sup>131</sup>. This change in SPION magnetization, from saturation (i.e.,  $-M$ ) in one direction to the opposite (i.e.,  $+M$ ), is non-linear and follows the Langevin function (Figure 13A)<sup>128,129</sup>. A receive coil detects the voltage induced by the change in SPION magnetization and this signal strength is linearly proportional to the amount of SPION at the FFR. Signals are assigned to the instantaneous FFR location to reconstruct the final projection image. MPI output is a convolution of the SPION distribution with the point spread function (PSF), (Figure 13B) which is calculated as the derivative of the Langevin function<sup>132</sup>. To form a 3D tomographic image, multiple projections are reconstructed using a filtered back projection algorithm<sup>129</sup>.

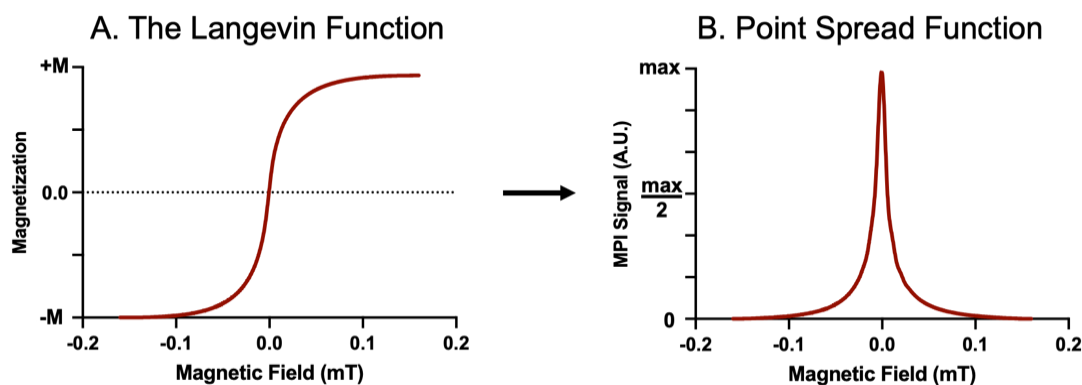


**Figure 13: A. The Langevin function describes the non-linear change in SPION magnetization that occurs in response to an applied magnetic field. Magnetization saturation is denoted as  $M$ . B. The derivative of this Langevin function is the MPI signal in the form of a point spread function (maximum value,  $\max$ ).**

### 1.5.3 Sensitivity and resolution for MPI

MPI sensitivity relies heavily on the type of SPION used, including the strength of the nanoparticle magnetization (stronger magnetization improves MPI signal)<sup>134,135</sup> and the rate of SPION relaxation at the FFR (i.e., the slope of the Langevin function at  $x = 0$ , where a faster rate of change in magnetization leads to higher maximum MPI signal)<sup>134</sup>. For cell tracking, the efficiency of the nanoparticle cell labeling influences MPI sensitivity (more iron per cell leads to higher sensitivity). MPI sensitivity can also be influenced by the MPI parameters, including the amplitude of the excitation field (higher excitation field leads to increased sensitivity)<sup>136,137</sup>, the gradient field strength (stronger gradients decrease the size of the FFR and linearly reduces sensitivity)<sup>138</sup> and number of projections (3D imaging combines 2D projections and leads to higher sensitivity).

MPI resolution is driven primarily by SPION relaxation. In response to the MPI excitation magnetic field, Neel relaxation refers to the reversal of the SPION magnetic moment, whereas Brownian relaxation refers to the physical rotation of the SPION<sup>136</sup>. The dominant relaxation mechanism primarily depends on the SPION iron core size and hydrodynamic diameter<sup>135,138</sup>, and the MPI resolution worsens with increasing Brownian relaxation. Theoretical modeling based upon the Langevin theory of SPIONs predicts that resolution improves with increasing core size. However, Tay *et al.*<sup>138</sup> found that improved resolution with increasing magnetic core size follows the steady-state prediction up to approximately 25 nm when the effects of SPION rotational times become significant owing to increasing Brownian relaxation. SPIONs above this size range experience increased drag, slowing their magnetization response and limiting resolution<sup>133,137</sup>. Resolution is also influenced by the interaction of the nanoparticle and the magnetic field gradient, where stronger gradients increase resolution but at the cost of sensitivity<sup>133</sup>.

In early MPI cell tracking, commercially available SPIONs used for MRI were evaluated for MPI including ferucarbotran, ferumoxytol<sup>139</sup> (see also Chapter 2), Synomag<sup>140–142</sup>, and micron-sized SPIONs<sup>143–145</sup>. Ferucarbotran has been the most widely used in MPI studies of mice to detect stem<sup>139,146–148</sup>, pancreatic islets<sup>149</sup>, and T cells<sup>150</sup>. However, ferucarbotran is no longer considered optimal for MPI because 70% of the particles are

small cores (~5 nm in diameter) which do not magnetize significantly to produce MPI signals<sup>151</sup>. Synomag produces superior MPI signal but has not been shown to effectively label cells by co-incubation alone. Previous reports have shown detection of as few as 1000 cells (27 pg ferucarbotran/stem cell)<sup>147</sup> but with custom nanoparticles as few as 250 cells (30 pg Fe/HeLa cell)<sup>152</sup> could be detected with MPI. The sensitivity of MPI is further investigated in Chapter 3. Resolutions of 1-5 mm can be achieved with commercially available SPIONs<sup>153</sup> and recently superferromagnetic chains have been shown to have > 10x better resolution (0.15 mm)<sup>154</sup>. However, these high resolution MPI-tailored particles have not been used to label cells. Continued optimization of SPIONs expressly for MPI is emerging as a powerful area of research and will be critical for improving sensitivity and spatial resolution<sup>155</sup>.

#### 1.5.4 SPION-based MPI cell tracking

MPI has the potential to overcome limitations of both SPION- and <sup>19</sup>F-based MRI cell tracking. As the MPI signal is generated only when the magnetic moments of the SPIONs rotate in response to the applied fields, there is no signal from tissue. This imbues MPI with a positive “hot-spot” contrast that provides spatial localization without ambiguity<sup>67</sup> (unlike SPION-MRI, similar to <sup>19</sup>F MRI). Another advantage is that MPI has high sensitivity (unlike <sup>19</sup>F MRI), as the signal derives from the direct detection of the electronic magnetization of SPION, which is 10<sup>8</sup> times larger than the nuclear magnetization of protons seen in MRI<sup>133</sup>. MPI signal is linearly quantitative with SPION concentration, and therefore, the number of SPION-labeled cells can be calculated<sup>156</sup> (similar to <sup>19</sup>F MRI). The shortcomings of MPI include a relatively low spatial resolution, compared to MRI, and the requirement that anatomical images must be acquired separately with a different imaging modality. Therefore, MPI has certain advantages over SPION-based MRI (specificity and quantification) and <sup>19</sup>F-based MRI (sensitivity) for cell tracking (Table 2.). Overall, there are fewer MPI cell tracking studies than MRI cell tracking, since it is a relatively newer modality. There have been no clinical (in-human) MPI studies to date.

**Table 2: Comparison of the strengths and limitations of SPION-based MRI, MPI, and PFC-based MRI for cell tracking.**

Criteria	SPION-based MRI	SPION-based MPI	<sup>19</sup> F-based MRI
Cell sensitivity	1-10 cells <sup>64</sup>	1000 cells <sup>147</sup>	10 <sup>3</sup> -10 <sup>5</sup> cells <sup>56</sup>
Resolution	μm <sup>3</sup>	mm <sup>3</sup>	mm <sup>3</sup>
Signal source	Indirect	Direct	Direct
Quantification of cell number	No	Yes	Yes
Anatomical reference	May require pre-scan	Additional image required	Additional image required

#### 1.5.4.1 MSC tracking with MPI

MPI has been used to track SPION-labeled MSC in several preclinical studies<sup>139,146-148,152,157</sup>. These studies demonstrate that SPION-labeled MSC can be detected as hotspot signals that are directly quantitative for up to 87 days<sup>147</sup>. Commonly, stem cells that were administered by point injections display a reduction in MPI signal over time<sup>139,147,157</sup>. The use of various SPION types for stem cell labeling can influence MPI signal characteristics. Stem cell tracking with ferucarbotran provided comparatively higher signals than ferumoxytol<sup>139</sup>, and custom cubic particles were shown to be superior to ferucarbotran<sup>152</sup>. There are also two studies that follow intravenously administered stem cells that initially trap in the lungs and later cleared by the liver<sup>148,152</sup>. These hotspot images provide clear visualization of the stem cell biodistribution, which is not possible with MRI due to contrast limitations *e.g.*, the hypointense air-filled lungs. These findings would also be challenging to obtain by <sup>19</sup>F MRI due to limited sensitivity when cells are widely distributed throughout large organs.



#### 1.5.4.2 Imaging inflammation with MPI

MPI has been applied to image inflammation in tumor models<sup>129,158-161</sup> and a model of traumatic brain injury<sup>162</sup> following intravenous delivery of SPIONs. This can be challenging to achieve because of high accumulation of SPIONs by liver Kupffer cells which result in strong MPI signals in the liver. The PSF can spread beyond the boundaries of the liver tissue, making it difficult to distinguish signals from surrounding tissues<sup>159</sup>. Interestingly, SPION characteristics (*e.g.*, surface coatings and particle size) can influence the biodistribution and hepatic clearance rates<sup>163</sup>. SPIONs with longer blood circulation times have longer opportunity to accumulate in phagocytic cells at inflammatory sites, enhancing signals at sites of inflammation<sup>159</sup>. One option to further increase targeting specificity includes conjugation of an immune-targeting antibody to the surface of SPIONs and this is termed Immuno-MPI. Chandrasekharan *et al.*<sup>129,161</sup> compared MPI signals after administration of anti-Ly6G-antibody functionalized SPIONs targeting neutrophils, compared to the standard ferucarbotran. At a region of LPS-induced myositis, anti-Ly6G targeting resulted in enhanced MPI contrast-to-noise ratio of 8-13 compared to ferucarbotran (ratio = 1-2). This type of imaging is similar to immuno-positron emission tomography (PET), without the use of radioactive molecules.

#### 1.5.4.3 T cell tracking with MPI

To the best of my knowledge, there are three studies to date involving MPI cell tracking of T cells<sup>94,150,164</sup>. Rivera-Rodriguez *et al.* (2021)<sup>150</sup> demonstrate that ferucarbotran-labeled T cells (1 pg/cell) can be detected by MPI with signal strength directly linear to cell number. They investigated the biodistribution of T cells in mice after different administration routes. MPI signal was observed in the mouse liver after T cells were administered intravenously and in the brain after intracerebroventricular and intravenous administration in a mouse glioma model. Interestingly, for T cells tracked to glioma tumors after intravenous administration two dynamic ranges were required to show MPI signal in the brain (low signal, range 1.68-2.32 ng Fe/mm<sup>2</sup>) relative to the liver (high signal, range 2-97 ng Fe/mm<sup>2</sup>). As few as 70-200 x 10<sup>3</sup> T cells were quantified in glioma tumors. Kiru *et al.* (2022)<sup>94</sup> demonstrate that fewer CAR T cells can be detected with MPI (2 x 10<sup>3</sup> cells) compared to MRI (2 x 10<sup>4</sup> cells) with a loading of 1.2 pg/cell using

ferumoxytol. These CAR T cells were subsequently administered intravenously to mice bearing osteosarcoma tumors. Intravenously delivered iron-labeled CAR T cells could be detected at the tumor by MPI for 2 weeks and MRI for 1 week, and the presence of CD3+ PPB+ cells was verified with histology. Subsequently, the same group labeled CAR T cells with MegaPro, achieving 2 pg/cell and tracked these cells to glioblastoma tumors after intracardiac administration<sup>164</sup>. In both studies<sup>94,164</sup>, they demonstrate that significantly more CAR T cells reach the tumors compared to untransduced T cells and this can be directly quantified by MPI. However, these publications do not show the full body biodistribution of the cells (only the tumor region).

## 1.6 Purpose of thesis

The overall goal of this thesis is to characterize and develop MRI and MPI cellular imaging strategies and apply these modalities to track and quantify MSC, inflammatory cells, and Tregs *in vivo*.

### 1.6.1 Thesis synopsis and hypotheses

**Chapter 2 of this thesis** applies iron-based MRI and MPI cell tracking to monitor and quantify transplanted MSCs *in vivo*. Secondly,  $^{19}\text{F}$  MRI is applied to imaging infiltrating macrophages at the MSC transplant site. Our hypothesis is that  $^1\text{H}$  MRI and MPI will provide unique and complementary information on the fate of SPION-labeled MSC *in vivo*.  $^{19}\text{F}$  MRI will allow for the imaging and measurement of infiltrating immune cells at the MSC transplant site using PFC nanoemulsions. This work was published as:

Sehl, Olivia C., Ashley V. Makela, Amanda M. Hamilton, and Paula J. Foster. Trimodal cell tracking *in vivo*: combining iron- and fluorine-based magnetic resonance imaging with magnetic particle imaging to monitor the delivery of mesenchymal stem cells and the ensuing inflammation. *Tomography* 2019; 5(4), 367-376.

**Chapter 3 of this thesis** directly compares the detection sensitivity of  $^{19}\text{F}$  MRI and MPI for cell tracking. This work was performed both *in vitro* (as cell pellets) and *in vivo*. Our hypothesis is that MPI with SPIONs as the cell labeling agent will be more sensitive (detect a lower cell number) than  $^{19}\text{F}$  MRI with PFC nanoemulsions as the cell labeling agent. This work was published as:

Sehl, Olivia C. and Paula J. Foster. The sensitivity of magnetic particle imaging and fluorine-19 magnetic resonance imaging for cell tracking. *Scientific Reports*, 2021; 11(1), 1-12.

**Chapter 4 of this thesis** is about developing and testing quantification strategies for MPI. Our hypothesis is that different strategies for drawing regions of interest (ROIs) in MPI images will lead to different quantitative accuracy and levels of interuser variability. This work was published as:

Sehl, Olivia C., Brice Tiret, Maryam A. Berih, Patrick Goodwill, and Paula J. Foster. MPI region of interest (ROI) analysis and quantification of iron in different volumes. *International Journal of Magnetic Particle Imaging*, 2022; 8(1).

**Chapter 5 of this thesis** applies  $^{19}\text{F}$  MRI as a quantitative *in vivo* migration assay for Treg and CAR Treg cell therapies. Our hypothesis is that  $^{19}\text{F}$  MRI will permit the *in vivo* tracking and quantitation of subcutaneously or intravenously administered PFC-labeled Tregs *in vivo*. This work has not been published in a scientific journal.

## 1.6.2 Other contributions

The imaging tools developed and implemented in this thesis have been applied to several other published studies from our group, on which I am an author, including:

Makela, Ashley V., Jeffrey M. Gaudet, Melissa A. Schott, Olivia C. Sehl, Christopher H. Contag, and Paula J. Foster. Magnetic particle imaging of macrophages associated with cancer: Filling the voids left by iron-based magnetic resonance imaging. *Molecular Imaging and Biology* 22 (2020): 958-968.

Fink, Corby, Michael Smith, Olivia C. Sehl, Jeff M. Gaudet, T. Craig Meagher, Nadeem A. Sheikh, Jimmy D. Dikeakos, Michael J. Rieder, Paula J. Foster, and Gregory A. Dekaban. Quantification and characterization of granulocyte macrophage colony-stimulating factor activated human peripheral blood mononuclear cells by fluorine-19 cellular MRI in an immunocompromised mouse model. *Diagnostic and Interventional Imaging* 101, no. 9 (2020): 577-588.

Sehl, Olivia C., Julia J. Gevaert, Kierstin P. Melo, Natasha N. Knier, and Paula J. Foster. A perspective on cell tracking with magnetic particle imaging. *Tomography* (2020): 6(4):315-324.

Dubois, Veronica P., Olivia C. Sehl, Paula J. Foster, and John A. Ronald. Visualizing CAR-T cell immunotherapy using 3 Tesla fluorine-19 MRI. *Molecular Imaging and Biology, Special Issue: Imaging in Immuno-oncology* (2021): 1-11.

Makela, Ashley V., Melissa A. Schott, Olivia C. Sehl, Julia J. Gevaert, Paula J. Foster, and Christopher H. Contag. Tracking the fates of iron-labeled tumor cells *in vivo* using magnetic particle imaging. *Nanoscale Advances* 4, no. 17 (2022): 3617-3623.

Gevaert, Julia, Kyle Van Beek, Olivia C. Sehl, and Paula J. Foster. VivoTrax+ improves the detection of cancer cells with magnetic particle imaging. *International Journal on Magnetic Particle Imaging* 8, no. 2 (2022).

Shalaby, Nourhan, John J. Kelly, Olivia C. Sehl, Julia J. Gevaert, Matthew S. Fox, Qi Qi, Paula J. Foster, Jonathan D. Thiessen, Justin W. Hicks, Timothy J. Scholl, and John A. Ronald. Complementary early-phase magnetic particle imaging and late-phase positron emission tomography reporter imaging of mesenchymal stem cells *in vivo*. *Nanoscale* (2023).

Williams, Ryan J., Olivia C. Sehl, Julia J. Gevaert, Shirley Liu, John J. Kelly, Paula J. Foster, and John A. Ronald. Dual Magnetic Particle Imaging and Akaluc Bioluminescence Imaging for Tracking Cancer Cell Metastasis. *Tomography* 9, no. 1 (2023): 178-194.

Good, Hayden J.\* and Olivia C. Sehl\*, Julia J. Gevaert, Bo Yu, Maryam A. Berih, Sebastian A. Montero, Carlos M. Rinaldi-Ramos, and Paula J. Foster. Inter-user comparison for quantification of superparamagnetic iron oxides with magnetic particle imaging across two institutions highlights a need for standardized approaches. *Under review* (2023). **\*Co-first authors.**

## 1.7 Chapter 1 references

1. Met, Ö., Jensen, K. M., Chamberlain, C. A., Donia, M. & Svane, I. M. Principles of adoptive T cell therapy in cancer. *Semin. Immunopathol.* **41**, 49–58 (2019).
2. Makela, A. V. *et al.* Cellular imaging with MRI. *Top. Magn. Reson. Imaging* **25**, 177–186 (2016).
3. Iafrate, M. & Fruhwirth, G. O. How Non-invasive in vivo Cell Tracking Supports the Development and Translation of Cancer Immunotherapies. *Front. Physiol.* **11**, 1–30 (2020).
4. Nejadnik, H., Tseng, J. & Daldrup-Link, H. Magnetic resonance imaging of stem cell–macrophage interactions with ferumoxytol and ferumoxytol-derived nanoparticles. *Wiley Interdiscip. Rev. Nanomedicine Nanobiotechnology* **11**, 1–13 (2019).
5. Ahrens, E. T. & Bulte, J. W. M. Tracking immune cells in vivo using magnetic resonance imaging. *Nature Reviews Immunology* (2013). doi:10.1038/nri3531
6. Chapelin, F., Capitini, C. M. & Ahrens, E. T. Fluorine-19 MRI for detection and quantification of immune cell therapy for cancer. *J. Immunother. Cancer* **6**, 1–11 (2018).
7. Gaudet, J. M., Hamilton, A. M., Chen, Y., Fox, M. S. & Foster, P. J. Application of dual <sup>19</sup>F and iron cellular MRI agents to track the infiltration of immune cells to the site of a rejected stem cell transplant. *Magn. Reson. Med.* **78**, 713–720 (2017).
8. Wardell, C. M., MacDonald, K. N., Levings, M. K. & Cook, L. Cross talk between human regulatory T cells and antigen-presenting cells: Lessons for clinical applications. *Eur. J. Immunol.* **51**, 27–38 (2021).

9. Andrzejewska A, Lukomska B, J. M. Concise Review: Mesenchymal Stem Cells: From Roots to Boost. *Stem Cells* **37**, 855–864 (2019).
10. Rodríguez-Fuentes, D. E. *et al.* Mesenchymal Stem Cells Current Clinical Applications: A Systematic Review. *Arch. Med. Res.* **52**, 93–101 (2021).
11. Han, Y. *et al.* Mesenchymal stem cells for regenerative medicine. *Cells* **8**, (2019).
12. Naji, A. *et al.* Biological functions of mesenchymal stem cells and clinical implications. *Cell. Mol. Life Sci.* **76**, 3323–3348 (2019).
13. Caplan, A. I. & Dennis, J. E. Mesenchymal stem cells as trophic mediators. *J. Cell. Biochem.* **98**, 1076–1084 (2006).
14. Jiang, W. & Xu, J. Immune modulation by mesenchymal stem cells. *Cell Prolif.* **53**, 1–16 (2020).
15. Harrell, C. R., Djonov, V. & Volarevic, V. The cross-talk between mesenchymal stem cells and immune cells in tissue repair and regeneration. *Int. J. Mol. Sci.* **22**, 1–13 (2021).
16. Hofer, H. R. & Tuan, R. S. Secreted trophic factors of mesenchymal stem cells support neurovascular and musculoskeletal therapies. *Stem Cell Res. Ther.* **7**, 1–14 (2016).
17. Zhang, J. *et al.* The challenges and promises of allogeneic mesenchymal stem cells for use as a cell-based therapy. *Stem Cell Res. Ther.* **6**, 1–7 (2015).
18. Galipeau, J. & Sensébé, L. Mesenchymal Stromal Cells: Clinical Challenges and Therapeutic Opportunities. *Cell Stem Cell* **22**, 824–833 (2018).
19. Kurtzberg, J. *et al.* A Phase 3, Single-Arm, Prospective Study of Remestemcel-L, Ex Vivo Culture-Expanded Adult Human Mesenchymal Stromal Cells for the Treatment of Pediatric Patients Who Failed to Respond to Steroid Treatment for Acute Graft-versus-Host Disease. *Biol. Blood Marrow Transplant.* **26** (2020).

20. Prasad, V. K. *et al.* Efficacy and Safety of Ex Vivo Cultured Adult Human Mesenchymal Stem Cells (Prochymal™) in Pediatric Patients with Severe Refractory Acute Graft-Versus-Host Disease in a Compassionate Use Study. *Biol. Blood Marrow Transplant.* **17**, 534–541 (2011).
21. Kurtzberg, J. *et al.* Allogeneic human mesenchymal stem cell therapy (Remestemcel-L, Prochymal) as a rescue agent for severe refractory acute graft-versus-host disease in pediatric patients. *Biol. Blood Marrow Transplant.* **20**, 229–235 (2014).
22. Melief, S. M. *et al.* Multipotent stromal cells induce human regulatory T cells through a novel pathway involving skewing of monocytes toward anti-inflammatory macrophages. *Stem Cells* **31**, 1980–1991 (2013).
23. Gao, S. *et al.* Mouse bone marrow-derived mesenchymal stem cells induce macrophage M2 polarization through the nuclear factor- $\kappa$ B and signal transducer and activator of transcription 3 pathways. *Exp. Biol. Med.* **239**, 366–375 (2014).
24. Munir, H., Luu, N. T., Clarke, L. S. C., Nash, G. B. & McGettrick, H. M. Comparative ability of mesenchymal stromal cells from different tissues to limit neutrophil recruitment to inflamed endothelium. *PLoS One* **11**, 1–18 (2016).
25. Munir, H., Ed Rainger, G., Nash, G. B. & McGettrick, H. Analyzing the effects of stromal cells on the recruitment of leukocytes from flow. *J. Vis. Exp.* 1–11 (2015). doi:10.3791/52480
26. Ghannam, S., Pène, J., Torcy-Moquet, G., Jorgensen, C. & Yssel, H. Mesenchymal Stem Cells Inhibit Human Th17 Cell Differentiation and Function and Induce a T Regulatory Cell Phenotype. *J. Immunol.* **185**, 302–312 (2010).
27. Petrus-Reurer, S. *et al.* Immunological considerations and challenges for regenerative cellular therapies. *Commun. Biol.* **4**, 798 (2021).
28. Margiana, R. *et al.* Clinical application of mesenchymal stem cell in regenerative medicine: a narrative review. *Stem Cell Res. Ther.* **13**, 1–22 (2022).



29. Lohan, P. *et al.* Changes in immunological profile of allogeneic mesenchymal stem cells after differentiation: Should we be concerned? *Stem Cell Res. Ther.* **5**, (2014).
30. MacDonald, K. N., Piret, J. M. & Levings, M. K. Methods to manufacture regulatory T cells for cell therapy. *Clin. Exp. Immunol.* **197**, 52–63 (2019).
31. Raffin, C., Vo, L. T. & Bluestone, J. A. Treg cell-based therapies: challenges and perspectives. *Nat. Rev. Immunol.* **20**, 158–172 (2020).
32. Bernaldo-de-quiros, E. *et al.* “First-in-human” clinical trial employing adoptive transfer of autologous thymus-derived Treg cells (thyTreg) to prevent graft rejection in heart-transplanted children. **104**, (2020).
33. Ferreira, L. M. R., Muller, Y. D., Bluestone, J. A. & Tang, Q. Next-generation regulatory T cell therapy. *Nat. Rev. Drug Discov.* **18**, 749–769 (2019).
34. Di Ianni, M. *et al.* Tregs prevent GVHD and promote immune reconstitution in HLA-haploidentical transplantation. *Blood* **117**, 3921–3928 (2011).
35. Martelli, M. F. *et al.* HLA-haploidentical transplantation with regulatory and conventional T-cell adoptive immunotherapy prevents acute leukemia relapse. *Blood* **124**, 638–644 (2014).
36. MacMillan, M. L. *et al.* First-in-human phase 1 trial of induced regulatory T cells for graft-versus-host disease prophylaxis in HLA-matched siblings. *Blood Adv.* **5**, 1425–1436 (2021).
37. Brunstein, C. G. *et al.* Umbilical cord blood-derived T regulatory cells to prevent GVHD: Kinetics, toxicity profile, and clinical effect. *Blood* **127**, 1044–1051 (2016).
38. Brunstein, C. G. *et al.* Infusion of ex vivo expanded T regulatory cells in adults transplanted with umbilical cord blood: Safety profile and detection kinetics. *Blood* **117**, 1061–1070 (2011).

39. Theil, A. *et al.* Adoptive transfer of allogeneic regulatory T cells into patients with chronic graft-versus-host disease. *Cytotherapy* **17**, 473–486 (2015).
40. Trzonkowski, P. *et al.* First-in-man clinical results of the treatment of patients with graft versus host disease with human ex vivo expanded CD4+CD25+CD127- T regulatory cells. *Clin. Immunol.* **133**, 22–26 (2009).
41. Sawitzki, B. *et al.* Regulatory cell therapy in kidney transplantation (The ONE Study): a harmonised design and analysis of seven non-randomised, single-arm, phase 1/2A trials. *Lancet* **395**, 1627–1639 (2020).
42. Poliani, P. L. *et al.* Early defects in human T-cell development severely affect distribution and maturation of thymic stromal cells: Possible implications for the pathophysiology of Omenn syndrome. *Blood* **114**, 105–108 (2009).
43. Caramalho, Í., Nunes-Cabaço, H., Foxall, R. B. & Sousa, A. E. Regulatory T-cell development in the human thymus. *Front. Immunol.* **6**, 1–7 (2015).
44. Chen, J. *et al.* Strong adhesion by regulatory T cells induces dendritic cell cytoskeletal polarization and contact-dependent lethargy. *J. Exp. Med.* **214**, 327–338 (2017).
45. Akkaya, B. *et al.* Regulatory T cells mediate specific suppression by depleting peptide–MHC class II from dendritic cells. *Nat. Immunol.* **20**, 218–231 (2019).
46. Grossman, W. J. *et al.* Human T regulatory cells can use the perforin pathway to cause autologous target cell death. *Immunity* **21**, 589–601 (2004).
47. Qureshi, O. S. *et al.* Trans-endocytosis of CD80 and CD86: A molecular basis for the cell-extrinsic function of CTLA-4. *Science (80-. ).* **332**, 600–603 (2011).
48. Giganti, G. *et al.* Treg cell therapy: How cell heterogeneity can make the difference. *Eur. J. Immunol.* **51**, 39–55 (2021).

49. Rosado-Sánchez, I. & Levings, M. K. Building a CAR-Treg: Going from the basic to the luxury model. *Cell. Immunol.* **358**, (2020).
50. Dawson, N. A. J. *et al.* Systematic testing and specificity mapping of alloantigen-specific chimeric antigen receptors in regulatory T cells. *JCI Insight* **4**, (2019).
51. McRobbie, D. W., Moore, E. A. & Graves, M. J. *MRI from picture to proton. MRI from Picture to Proton* (2017). doi:10.2214/ajr.182.3.1820592
52. Makela, A. V. PhD Thesis: In Vivo Tracking of Tumour Associated Macrophages in Breast Cancer with Magnetic Resonance Imaging. (2018).
53. Scheffler, K. & Lehnhardt, S. Principles and applications of balanced SSFP techniques. *Eur. Radiol.* **13**, 2409–2418 (2003).
54. Scheffler, K. & Hennig, J. Is TrueFISP a gradient-echo or a spin-echo sequence? *Magn. Reson. Med.* **49**, 395–397 (2003).
55. Modo, M., Hoehn, M. & Bulte, J. W. M. Cellular MR imaging. *Molecular Imaging* (2005). doi:10.1162/15353500200505145
56. Srinivas, M., Heerschap, A., Ahrens, E. T., Figdor, C. G. & de Vries, I. J. M. 19F MRI for quantitative in vivo cell tracking. *Trends Biotechnol.* **28**, 363–370 (2010).
57. Bulte, J. W. M. & Daldrup-Link, H. E. Clinical Tracking of Cell Transfer and Cell Transplantation: Trials and Tribulations. *Radiology* (2018). doi:10.1148/radiol.2018180449
58. Srinivas, M. *et al.* In vivo cytometry of antigen-specific T cells using 19F MRI. *Magn. Reson. Med.* **62**, 747–753 (2009).
59. Khurana, A. *et al.* Intravenous ferumoxytol allows noninvasive MR imaging monitoring of macrophage migration into stem cell transplants. *Radiology* **264**, 803–811 (2012).

60. Dousset, V. *et al.* In vivo macrophage activity imaging in the central nervous system detected by magnetic resonance. *Magn. Reson. Med.* **41**, 329–333 (1999).
61. Makela, A. V., Gaudet, J. M. & Foster, P. J. Quantifying tumor associated macrophages in breast cancer: a comparison of iron and fluorine-based MRI cell tracking. *Sci. Rep.* **7**, (2017).
62. Simon, G. H. *et al.* Ultrasmall Superparamagnetic Iron-Oxide – enhanced MR Imaging of Normal Bone Marrow in Rodents : Original Research. *Acad Radiol* **12**, 1190–1197 (2005).
63. Heyn, C., Bowen, C. V., Rutt, B. K. & Foster, P. J. Detection threshold of single SPIO-labeled cells with FIESTA. *Magn. Reson. Med.* (2005).  
doi:10.1002/mrm.20356
64. Heyn, C. *et al.* In vivo MRI of cancer cell fate at the single-cell level in a mouse model of breast cancer metastasis to the brain. *Magn. Reson. Med.* **56** (2006).
65. Hitchens, T. K. *et al.* Combining perfluorocarbon and superparamagnetic iron-oxide cell labeling for improved and expanded applications of cellular MRI. *Magn. Reson. Med.* **73**, 367–375 (2015).
66. Hinds, K. A. *et al.* Highly efficient endosomal labeling of progenitor and stem cells with large magnetic particles allows magnetic resonance imaging of single cells. *Blood* **102**, 867–872 (2003).
67. Bulte, J. W. M. Superparamagnetic iron oxides as MPI tracers: A primer and review of early applications. *Adv. Drug Deliv. Rev.* **138**, 293–301 (2019).
68. Arbab, A. S. *et al.* Efficient magnetic cell labeling with protamine sulfate complexed to ferumoxides for cellular MRI. *Blood* **104**, 1217–1223 (2004).
69. Daldrup-Link, H. E. *et al.* Detection of stem cell transplant rejection with ferumoxytol MR imaging: Correlation of MR imaging findings with those at intravital microscopy. *Radiology* **284**, 495–507 (2017).

70. Bakshi, A. *et al.* Lumbar puncture delivery of bone marrow stromal cells in spinal cord contusion: A novel method for minimally invasive cell transplantation. *J. Neurotrauma* **23**, 55–65 (2006).
71. Daadi, M. M. *et al.* Imaging neural stem cell graft-induced structural repair in stroke. *Cell Transplant.* **22**, 881–892 (2013).
72. De Vries, I. J. M. *et al.* Magnetic resonance tracking of dendritic cells in melanoma patients for monitoring of cellular therapy. *Nat. Biotechnol.* **23**, 1407–1413 (2005).
73. González-lara, L. E. PhD Thesis: In Vivo Cellular MRI In Experimental Traumatic Spinal Cord Injury. (2011).
74. Vries, I. J. M. De *et al.* Magnetic resonance tracking of dendritic cells in melanoma patients for monitoring of cellular therapy. **23**, 1407–1413 (2005).
75. Jendelová, P. *et al.* Magnetic Resonance Tracking of Transplanted Bone Marrow and Embryonic Stem Cells Labeled by Iron Oxide Nanoparticles in Rat Brain and Spinal Cord. *J. Neurosci. Res.* **76**, 232–243 (2004).
76. Callera, F. & De Melo, C. M. T. P. Magnetic resonance tracking of magnetically labeled autologous bone marrow CD34+ cells transplanted into the spinal cord via lumbar puncture technique in patients with chronic spinal cord injury: CD34+ cells' migration into the injured site. *Stem Cells Dev.* **16**, 461–466 (2007).
77. Daldrup-Link, H. E. *et al.* Migration of iron oxide-labeled human hematopoietic progenitor cells in a mouse model: In vivo monitoring with 1.5-T ME imaging equipment. *Radiology* **234**, 197–205 (2005).
78. Syková, E. & Jendelová, P. Magnetic resonance tracking of transplanted stem cells in rat brain and spinal cord. *Neurodegener. Dis.* **3**, 62–67 (2006).
79. Zhu, J., Zhou, L. & XingWu, F. Tracking Neural Stem Cells in Patients with Brain Trauma. *N. Engl. J. Med.* **355**, 2376–2378 (2006).

80. Kaneko, C. *et al.* MRI study of atherosclerotic plaque progression using ultrasmall superparamagnetic iron oxide in Watanabe heritable hyperlipidemic rabbits. *Br. J. Radiol.* **88**, (2015).
81. Walter, H. L. *et al.* In vivo analysis of neuroinflammation in the late chronic phase after experimental stroke. *Neuroscience* **292**, 71–80 (2015).
82. Oweida, A. J., Dunn, E. A., Karlik, S. J., Dekaban, G. A. & Foster, P. J. Iron-oxide labeling of hematogenous macrophages in a model of experimental autoimmune encephalomyelitis and the contribution to signal loss in fast imaging employing steady state acquisition (FIESTA) images. *J. Magn. Reson. Imaging* **26**, 144–151 (2007).
83. Daldrup-Link, H. E. *et al.* MRI of tumor-associated macrophages with clinically applicable iron oxide nanoparticles. *Clin. Cancer Res.* **17**, 5695–5704 (2011).
84. Shih, Y. Y. I. *et al.* Longitudinal study of tumor-associated macrophages during tumor expansion using MRI. *NMR Biomed.* **24**, 1353–1360 (2011).
85. Makela, A. V., Gaudet, J. M. & Foster, P. J. Quantifying tumor associated macrophages in breast cancer: A comparison of iron and fluorine-based MRI cell tracking. *Sci. Rep.* **7**, 1–9 (2017).
86. Iv, M. *et al.* Quantification of macrophages in high-grade gliomas by using ferumoxytol-enhanced MRI: A pilot study. *Radiology* **290**, 198–206 (2019).
87. Metz, S. & Rummeny, E. J. Ferumoxtran-10-enhanced MR imaging of the bone marrow before and after conditioning therapy in patients with non-Hodgkin lymphomas. 598–607 (2006). doi:10.1007/s00330-005-0045-9
88. Daldrup-link, H. E., Rummeny, E. J. & Link, T. M. Iron-oxide-enhanced MR imaging of bone marrow in patients with non-Hodgkin ' s lymphoma : differentiation between tumor infiltration and hypercellular bone marrow. 1557–1566 (2002). doi:10.1007/s00330-001-1270-5

89. Daldrup-Link, H. E. Ten things you might not know about iron oxide nanoparticles. *Radiology* **284**, 616–629 (2017).
90. Thu, M. S. *et al.* Self-Assembling Nanocomplexes by combining Ferumoxytol, Heparin And Protamine For Cell Tracking by MRI HHS Public Access Author manuscript. *Nat Med* **18**, 463–467 (2012).
91. Arbab, A. S. *et al.* Intracytoplasmic tagging of cells with ferumoxides and transfection agent for cellular magnetic resonance imaging after cell transplantation: Methods and techniques. *Transplantation* **76**, 1123–1130 (2003).
92. Wuerfel, E. *et al.* Electrostatically stabilized magnetic nanoparticles - An optimized protocol to label murine cells for in vivo MRI. *Front. Neurol.* **DEC**, 1–9 (2011).
93. Walczak, P. *et al.* Magnetoelectroporation: improved labeling of neural stem cells and leukocytes for cellular magnetic resonance imaging using a single FDA-approved agent. *Nanomedicine Nanotechnology, Biol. Med.* **2**, 89–94 (2006).
94. Kiru, L. *et al.* In vivo Imaging of Nanoparticle Labeled CAR T-cells. *Proc. Natl. Acad. Sci.* 1–17
95. Garden, O. A. *et al.* A rapid method for labelling CD4<sup>+</sup> T cells with ultrasmall paramagnetic iron oxide nanoparticles for magnetic resonance imaging that preserves proliferative, regulatory and migratory behaviour in vitro. *J. Immunol. Methods* **314**, 123–133 (2006).
96. Shapiro, E. M., Medford-Davis, L. N., Fahmy, T. M., Dunbar, C. E. & Koretsky, A. P. Antibody-mediated cell labeling of peripheral T cells with micron-sized iron oxide particles (MPIOs) allows single cell detection by MRI. *Contrast Media Mol. Imaging* **2**, 147–153 (2007).
97. Moore, A. *et al.* MRI of insulinitis in autoimmune diabetes. *Magn. Reson. Med.* **47**, 751–758 (2002).

98. Anderson, S. A. *et al.* Magnetic Resonance Imaging of Labeled T-Cells in a Mouse Model of Multiple Sclerosis. *Ann. Neurol.* **55**, 654–659 (2004).
99. Kircher, M. F. *et al.* In Vivo High Resolution Three-Dimensional Imaging of Antigen-Specific Cytotoxic T-Lymphocyte Trafficking to Tumors. *Cancer Res.* **63**, 6838–6846 (2003).
100. Tremblay, M. L. *et al.* Using MRI cell tracking to monitor immune cell recruitment in response to a peptide-based cancer vaccine. *Magn. Reson. Med.* **80**, 304–316 (2018).
101. Mcfadden, C., Mallett, C. L. & Foster, P. J. Labeling of multiple cell lines using a new iron oxide agent for cell tracking by MRI. *Contrast Media Mol. Imaging* (2011). doi:10.1002/cmml.456
102. Fox, M., Gaudet, J. & Foster, P. Fluorine-19 MRI Contrast Agents for Cell Tracking and Lung Imaging. *Magn. Reson. Insights* **8**, 53 (2016).
103. Ribot, E. J., Gaudet, J. M., Chen, Y., Gilbert, K. M. & Foster, P. J. In vivo MR detection of fluorine-labeled human MSC using the bSSFP sequence. *Int. J. Nanomedicine* **9**, 1731–1739 (2014).
104. Makela, A. V. & Foster, P. J. Preclinical 19F MRI cell tracking at 3 Tesla. *Magn. Reson. Mater. Physics, Biol. Med.* (2018). doi:10.1007/s10334-018-0715-7
105. Ahrens, E. T., Helfer, B. M., O’Hanlon, C. F. & Schirda, C. Clinical cell therapy imaging using a perfluorocarbon tracer and fluorine-19 MRI. *Magn. Reson. Med.* **72**, 1696–1701 (2014).
106. Ruiz-Cabello, J. *et al.* In Vivo “Hot Spot” MR Imaging of Neural Stem Cells using Fluorinated Nanoparticles. *Magn. Reson. Med.* **60**, 1506–1511 (2008).
107. Boehm-Sturm, P., Mengler, L., Wecker, S., Hoehn, M. & Kallur, T. In Vivo tracking of human neural stem cells with 19F magnetic resonance imaging. *PLoS One* **6**, (2011).



108. Bible, E. *et al.* Non-invasive imaging of transplanted human neural stem cells and ECM scaffold remodeling in the stroke-damaged rat brain by <sup>19</sup>F- and diffusion-MRI. *Biomaterials* **33**, 2858–2871 (2012).
109. Fox, M. *et al.* In vivo MR detection of fluorine-labeled human MSC using the bSSFP sequence. *Magn. Reson. Insights* **8**, 53 (2014).
110. Gaudet, J. M., Ribot, E. J., Chen, Y., Gilbert, K. M. & Foster, P. J. Tracking the fate of stem cell implants with fluorine-19 MRI. *PLoS One* **10**, 1–12 (2015).
111. Moonshi, S. S. *et al.* A unique <sup>19</sup>F MRI agent for the tracking of non phagocytic cells: In vivo. *Nanoscale* **10**, 8226–8239 (2018).
112. Flogel, U. *et al.* In vivo monitoring of inflammation after cardiac and cerebral ischemia by fluorine magnetic resonance imaging. *Circulation* **118**, 140–148 (2008).
113. Ebner, B. *et al.* Early assessment of pulmonary inflammation by <sup>19</sup>F MRI in vivo. *Circ. Cardiovasc. Imaging* **3**, 202–210 (2010).
114. Makela, A. V & Foster, P. J. Imaging macrophage distribution and density in mammary tumors and lung metastases using fluorine-19 MRI cell tracking. *Magn. Reson. Med.* **80**, 1138–1147 (2018).
115. Flögel, U. *et al.* Noninvasive detection of graft rejection by in vivo <sup>19</sup>F MRI in the early stage. *Am. J. Transplant.* **11**, 235–244 (2011).
116. Hitchens, T. K. *et al.* <sup>19</sup>F MRI detection of acute allograft rejection with in vivo perfluorocarbon labeling of immune cells. *Magn. Reson. Med.* **65**, 1145–1154 (2011).
117. Janjic, J. M., Srinivas, M., Kadayakkara, D. K. K. & Ahrens, E. T. Self-delivering nanoemulsions for dual fluorine-19 MRI and fluorescence detection. *J. Am. Chem. Soc.* **130**, 2832–2841 (2008).

118. Srinivas, M., Morel, P. A., Ernst, L. A., Laidlaw, D. H. & Ahrens, E. T. Fluorine-19 MRI for visualization and quantification of cell migration in a diabetes model. *Magn. Reson. Med.* **58**, 725–734 (2007).
119. Gonzales, C. *et al.* In-vivo detection and tracking of T cells in various organs in a melanoma tumor model by 19F-fluorine MRS/MRI. *PLoS One* **11**, 1–18 (2016).
120. O’Hanlon, C. F., Fedczyna, T., Eaker, S., Shingleton, W. D. & Helfer, B. M. Integrating a 19F MRI tracer agent into the clinical scale manufacturing of a T-cell immunotherapy. *Contrast Media Mol. Imaging* **2017**, (2017).
121. Chapelin, F. *et al.* Fluorine-19 nuclear magnetic resonance of chimeric antigen receptor T cell biodistribution in murine cancer model. *Sci. Rep.* **7**, 1–12 (2017).
122. Dubois, V. P., Sehl, O. C., Foster, P. J. & Ronald, J. A. Visualizing CAR-T cell Immunotherapy Using 3 Tesla Fluorine-19 MRI. *Mol. Imaging Biol.* (2021). doi:10.1007/s11307-021-01672-3
123. Hingorani, D. V. *et al.* Cell penetrating peptide functionalized perfluorocarbon nanoemulsions for targeted cell labeling and enhanced fluorine-19 MRI detection. *Magn. Reson. Med.* 1–14 (2019). doi:10.1002/mrm.27988
124. Staal, A. H. J. *et al.* In vivo clearance of 19F MRI imaging nanocarriers is strongly influenced by nanoparticle ultrastructure. *Biomaterials* **261**, 120307 (2020).
125. Bonetto, F. *et al.* A novel 19 F agent for detection and quantification of human dendritic cells using magnetic resonance imaging. **373**, 365–373 (2011).
126. Srinivas, M. *et al.* Customizable, multi-functional fluorocarbon nanoparticles for quantitative in vivo imaging using 19F MRI and optical imaging. *Biomaterials* **31**, 7070–7077 (2010).
127. Chapelin, F. & Okada, H. Assessing Oximetry Response to Chimeric Antigen Receptor T-cell Therapy against Glioma with 19 F MRI in a Murine Model. **19**, 1–9 (2021).

128. Gleich, B. & Weizenecker, J. Tomographic imaging using the nonlinear response of magnetic particles. *Nature* **435**, 1214–1217 (2005).
129. Chandrasekharan, P. *et al.* *Magnetic Particle Imaging for Vascular, Cellular and Molecular Imaging. Molecular Imaging* (Brian D. Ross and Sanjiv Sam Gambhir, 2021). doi:10.1016/b978-0-12-816386-3.00015-6
130. Dulińska-Litewka, J. *et al.* Superparamagnetic iron oxide nanoparticles-current and prospective medical applications. *Materials (Basel)*. **12**, (2019).
131. Rivera-Rodriguez, A. & Rinaldi-Ramos, C. M. Emerging Biomedical Applications Based on the Response of Magnetic Nanoparticles to Time-Varying Magnetic Fields. *Annu. Rev. Chem. Biomol. Eng.* **12**, 163–185 (2021).
132. Goodwill, P. W. *et al.* X-Space MPI: Magnetic nanoparticles for safe medical imaging. *Adv. Mater.* **24**, 3870–3877 (2012).
133. Saritas, E. U. *et al.* Magnetic particle imaging (MPI) for NMR and MRI researchers. *J. Magn. Reson.* **229**, 116–126 (2013).
134. Lu, C. *et al.* Engineering of magnetic nanoparticles as magnetic particle imaging tracers. *Chem. Soc. Rev.* **50**, 8102–8146 (2021).
135. Ferguson, R. M., Minard, K. R., Khandhar, A. P. & Krishnan, K. M. Optimizing magnetite nanoparticles for mass sensitivity in magnetic particle imaging. *Med. Phys.* **38**, 1619–1626 (2011).
136. Croft, L. R. *et al.* Low drive field amplitude for improved image resolution in magnetic particle imaging. *Med. Phys.* **43**, 424–435 (2016).
137. Riahi, K. *et al.* Effect of Changing Iron Content and Excitation Frequency on Magnetic Particle Imaging Signal : A Comparative Study of Synomag<sup>®</sup> Nanoparticles. **15**, 109–112 (2021).

138. Tay, Z. W., Hensley, D. W., Vreeland, E. C., Zheng, B. & Conolly, S. M. The Relaxation Wall: Experimental Limits to Improving MPI Spatial Resolution by Increasing Nanoparticle Core size. *Biomed Phys End Express* **3**, 1–21 (2017).
139. Nejadnik, H. *et al.* Ferumoxytol Can Be Used for Quantitative Magnetic Particle Imaging of Transplanted Stem Cells. *Molecular Imaging and Biology* (2018). doi:10.1007/s11307-018-1276-x
140. Paysen, H. *et al.* Cellular uptake of magnetic nanoparticles imaged and quantified by magnetic particle imaging. *Sci. Rep.* **10**, 1–8 (2020).
141. Williams, R. J. *et al.* Dual Magnetic Particle Imaging and Akaluc Bioluminescence. *Tomography* **9**, 178–194 (2023).
142. Gevaert, J. J., Fink, C., Dikeakos, J., Dekaban, G. A. & Paula, J. Magnetic Particle Imaging is a sensitive in vivo imaging modality for the quantification of dendritic cell migration. *Mol. Imaging Biol.* 1–29 (2021). doi:10.1007/s11307-022-01738-w
143. Parkins, K. M., Melo, K. P., Chen, Y., Ronald, J. A. & Foster, P. J. Visualizing tumour self-homing with magnetic particle imaging. *Nanoscale* **13**, 6016–6023 (2021).
144. Melo, K. P., Makela, A. V., Knier, N. N., Hamilton, A. M. & Foster, P. J. Magnetic microspheres can be used for magnetic particle imaging of cancer cells arrested in the mouse brain. *Magn. Reson. Med.* 1–11 (2021). doi:10.1002/mrm.28987
145. Mallett, C. L., Hix, J. M. L., Kiupel, M. & Shapiro, E. M. Effect of mouse strain and diet on feasibility of MRI-based cell tracking in the liver. *Magn. Reson. Med.* **83**, 2276–2283 (2020).
146. Bulte, J. W. M. *et al.* Quantitative “Hot-Spot” Imaging of Transplanted Stem Cells Using Superparamagnetic Tracers and Magnetic Particle Imaging. *Tomography* **1**, 91–97 (2015).

147. Zheng, B. *et al.* Magnetic particle imaging tracks the long-term fate of in vivo neural cell implants with high image contrast. *Sci. Rep.* **5**, 1–9 (2015).
148. Zheng, B. *et al.* Quantitative magnetic particle imaging monitors the transplantation, biodistribution, and clearance of stem cells in vivo. *Theranostics* (2016). doi:10.7150/thno.13728
149. Wang, P. *et al.* Magnetic particle imaging of islet transplantation in the liver and under the kidney capsule in mouse models. *Quant. Imaging Med. Surg.* **8**, 114–122 (2018).
150. Rivera-rodriguez, A. *et al.* Tracking Adoptive T Cell Therapy Using Magnetic Particle Imaging. *Nanotheranostics* **5**, 431–444 (2021).
151. Eberbeck, D., Wiekhorst, F., Wagner, S. & Trahms, L. How the size distribution of magnetic nanoparticles determines their magnetic particle imaging performance. *Appl. Phys. Lett.* **98**, 1–4 (2011).
152. Wang, Q. *et al.* Artificially Engineered Cubic Iron Oxide Nanoparticle as a High-Performance Magnetic Particle Imaging Tracer for Stem Cell Tracking. *ACS Nano* **14**, 2053–2062 (2020).
153. Sehl, O. C., Gevaert, J. J., Melo, K. P., Knier, N. N. & Foster, P. J. A perspective on cell tracking with magnetic particle imaging. *Tomography* **6**, (2020).
154. Tay, Z. W. *et al.* Superferromagnetic Nanoparticles Enable Order-of-Magnitude Resolution & Sensitivity Gain in Magnetic Particle Imaging. *Small Methods* **5**, 1–10 (2021).
155. Chandrasekharan, P. *et al.* Magnetic Particle Imaging in Vascular Imaging, Immunotherapy, Cell Tracking, and Noninvasive Diagnosis. *Mol. Imaging* **2023**, 1–22 (2023).
156. Wu, X. L. C. *et al.* A review of magnetic particle imaging and perspectives on neuroimaging. *Am. J. Neuroradiol.* **40**, 206–212 (2019).

157. Hariri, A., Kim, T., Lemaster, J. E., Jokerst, J. V & Chen, F. The Development of a Trimodal Contrast Agent for Acoustic and Magnetic Particle Imaging of Stem Cells. *ACS Appl. Nano Mater.* (2018). doi:10.1021/acsanm.8b00063
158. Yu, E. Y. *et al.* Magnetic Particle Imaging: A Novel in Vivo Imaging Platform for Cancer Detection. *Nano Lett.* **17**, 1648–1654 (2017).
159. Makela, A. V. *et al.* Magnetic Particle Imaging of Macrophages Associated with Cancer: Filling the Voids Left by Iron-Based Magnetic Resonance Imaging. *Mol. Imaging Biol.* (2020). doi:10.1007/s11307-020-01473-0
160. Dieckhoff, J. *et al.* Magnetic Particle Imaging of liver tumors in small animal models. *Int. J. Magn. Part. Imaging* **3**, (2017).
161. Chandrasekharan, P. *et al.* Non-radioactive and sensitive tracking of neutrophils towards inflammation using antibody functionalized magnetic particle imaging tracers. *Nanotheranostics* **5**, 240–255 (2021).
162. Orendorff, R. *et al.* First in vivo traumatic brain injury imaging via magnetic particle imaging. *Phys. Med. Biol.* **62**, 3501–3509 (2017).
163. Liu, S. *et al.* Long circulating tracer tailored for magnetic particle imaging. *Nanotheranostics* **5**, 348–361 (2021).
164. Wu, W. E. *et al.* Multimodal In Vivo Tracking of Chimeric Antigen Receptor T Cells in Preclinical Glioblastoma Models. *Under Rev. Investig. Radiol.* (2023).

## Chapter 2

### 2 Trimodal Cell Tracking In vivo: Combining Iron- and Fluorine-Based Magnetic Resonance Imaging with Magnetic Particle Imaging to Monitor the Delivery of Mesenchymal Stem cells and the Ensuing Inflammation<sup>†</sup>

The therapeutic potential of mesenchymal stem cells (MSCs) is limited, as many cells undergo apoptosis following administration. In addition, the attraction of immune cells (predominately macrophages) to the site of implantation can lead to MSC rejection. We implemented a trimodal imaging technique to monitor the fate of transplanted MSCs and infiltration macrophages *in vivo*. MSCs were labeled with an iron oxide nanoparticle (ferumoxytol) and then implanted within the hind limb muscle of 10 C57B1/6 mice. Controls received unlabeled MSCs (n = 5). A perfluorocarbon agent was administered intravenously for uptake by phagocytic macrophages *in situ*; 1 and 12 days later, the ferumoxytol-labeled MSCs were detected by proton (<sup>1</sup>H) magnetic resonance imaging (MRI) and magnetic particle imaging (MPI). Perfluorocarbon-labeled macrophages were detected by fluorine-19 (<sup>19</sup>F) MRI. <sup>1</sup>H/<sup>19</sup>F MRI was acquired on a clinical scanner (3 T) using a dual-tuned surface coil and balanced steady-state free precession (bSSFP) sequence. The measured volume of signal loss and MPI signal declined over 12 days, which is consistent with the death and clearance of iron-labeled MSCs. <sup>19</sup>F signal persisted over 12 days, suggesting the continuous infiltration of perfluorocarbon-labeled macrophages. Because MPI and <sup>19</sup>F MRI signals are directly quantitative, we calculated estimates of the number of MSCs and macrophages present over time. The presence of MSCs and macrophages was validated with histology following the last imaging session. This is the first study to combine the use of iron- and fluorine-based MRI with MPI cell tracking.

---

<sup>†</sup> This chapter was previously published and is included here with permission: [Sehl, Olivia C., Ashley V. Makela, Amanda M. Hamilton, and Paula J. Foster. Trimodal cell tracking \*in vivo\*: combining iron- and fluorine-based magnetic resonance imaging with magnetic particle imaging to monitor the delivery of mesenchymal stem cells and the ensuing inflammation. \*Tomography\* 2019; 5\(4\), 367-376.](#)

## 2.1 Introduction

Mesenchymal stem cells (MSCs) have shown promising results as a cellular therapeutic. Many studies involving MSCs aim to restore damaged tissues, including bone, cartilage, tendon, adipose, and muscle tissue, through tissue regeneration<sup>1,2</sup>. Moreover, several proposed therapies rely on the pleiotropic effects that MSCs impose on their local microenvironment through the release of extracellular vesicles, cytokines, and tropic factors<sup>3-5</sup>. MSCs have been shown to exert antimicrobial effects, promote local vascularization and cell growth, and modulate inflammation<sup>1,2,6</sup>. MSC survival and engraftment *in vivo* is critical in determining therapeutic outcomes. Unfortunately, many MSCs undergo apoptosis in the days following administration owing to the stresses of administration and subsequent lack of nutrients<sup>7,8</sup>. Apoptotic stem cells release cytokines that attract immune cells (predominately macrophages) to the implant site. A high influx of these cells can ultimately trigger stem-cell rejection<sup>8</sup>. The potential of MSC therapy is limited by MSC death and immune rejection; therefore, the development of a technique to quantitatively monitor MSC engraftment and ensuing inflammation over time would be invaluable for evaluating the course of therapy.

Many experimental studies of MSC engraftment have been conducted using histology, which provides detailed molecular and morphological information but is limited to the interrogation of a single time point and portion of tissue. Alternatively, cellular magnetic resonance imaging (MRI) has proven to be an effective technique for noninvasive and longitudinal cell tracking<sup>8-10</sup>. To date, most cellular MRI involves tracking cells, which are labeled with superparamagnetic iron oxide nanoparticles (SPIONs). In proton (<sup>1</sup>H) MRI images, SPION-labeled cells appear as regions of signal void. In a uniform magnetic field, SPIONs alter the net local magnetization that nearby <sup>1</sup>H atoms experience and this leads to increased R2\* relaxation rates of these <sup>1</sup>H atoms. These voids occupy a volume that is greater than the labeled cells, an effect referred to as the blooming artifact. This effect can lead to enhanced sensitivity of cell detection<sup>11</sup>, but it poses challenges for accurate quantification of cell number. Measuring the volume of signal voids is one metric to estimate the number of cells present; however, this is not a direct relationship. One other limitation of SPION-based cell tracking is lack of specificity in some



tissues<sup>9,12</sup>. There is some ambiguity when identifying these cells *in vivo*, as other regions in anatomic MRI appear dark (*i.e.*, the air-filled lungs).

Ultrasmall superparamagnetic iron oxides (USPIOs) are a subset of iron oxides used for MRI cell tracking. These nanoparticles are ~30 nm in diameter and are coated in dextran, and thus, they are biocompatible and biodegradable. Ferumoxytol is one such USPIO that is FDA-approved for iron replacement therapy for the treatment of anemia in patients and may be used off-label for iron-based MRI cell tracking<sup>13,14</sup>. In this study we will use ferumoxytol for iron oxide cell labeling of MSC, as it is the most clinically applicable agent.

Fluorine-19 (<sup>19</sup>F) MRI cell tracking is an alternative to iron oxide-based MRI. In this technique, cells are labeled with perfluorocarbon (PFC) nanoemulsions and detected with <sup>19</sup>F MRI in a hotspot image. Since there is little endogenous <sup>19</sup>F within biological tissues, these cells can be visualized with high specificity. The signal intensity of these images is directly linear to the number of <sup>19</sup>F atoms, which allows for the quantification of <sup>19</sup>F labeled cells *in vivo*<sup>8,9,15</sup>. One limitation of <sup>19</sup>F-based cell tracking is that the sensitivity of detection is much less than iron oxide agents, requiring a minimum of 10<sup>3</sup> - 10<sup>5</sup>-labeled cells per imaging voxel. PFC agents are clinically approved for cell tracking<sup>16</sup>.

Magnetic particle imaging (MPI) is an emerging modality that directly detects SPION nanoparticles. Similar to <sup>19</sup>F MRI, MPI produces positive contrast images of the distribution of labeled cells. MPI signal is linearly related to the quantity of iron oxide tracer that allows for accurate quantification of SPION-labeled cells<sup>13,17</sup>. It is not feasible to achieve this reliable specificity and quantification in SPION-based MRI cell tracking, although SPION-based MRI cell tracking may have superior detection sensitivity depending on tissue contrast. MPI has the potential to overcome the limitations of <sup>19</sup>F MRI (sensitivity) and iron-based MRI (specificity and quantification).

In this study, we use ferumoxytol for labeling and detecting MSCs with MPI, which has recently been shown to permit quantification of MSCs transplanted in a mouse model of osteoarthritis<sup>13</sup>. This group also showed that MPI of ferumoxytol-labeled cells was

sensitive to changes in cell number *in vivo* over time, whereas the voids detected in  $^1\text{H}$  MRI did not detect this change.

One strategy for detecting immune cells *in vivo* involves the intravenous administration of the labeling agent. This leads to uptake of the agent by phagocytic cells of the reticuloendothelial system (predominately macrophages) *in vivo*<sup>8,10,18</sup>. MRI is typically performed 1 day after the administration of the cell labeling agent to permit for the clearance of intravascular agent and the accumulation of the label into cells.

Our aim is to combine the use of iron-based MRI,  $^{19}\text{F}$  MRI, and MPI cellular imaging technologies to monitor and quantify the persistence of transplanted MSCs and infiltrating macrophages *in vivo*. These 3 modalities are complementary and provide additional information (specificity, sensitivity, and quantification of cell number) when integrated together. We explored the ability to label, detect, and quantify MSCs with ferumoxytol for detection in  $^1\text{H}$  MRI and MPI images, and infiltrating macrophages with PFC for  $^{19}\text{F}$  MRI detection.

## 2.2 Methodology

### 2.2.1 MSC preparation

MSCs derived from the bone marrow of C57BL/6 mice (MUBMX-01101 [BE], Cedarlane, Burlington, Ontario, Canada) were cultured at 37°C and 5%  $\text{CO}_2$  in low-glucose Dulbecco's modified Eagle's medium (Thermo Fisher Scientific, Waltham, Massachusetts). MSCs were passaged every 2 - 3 days for 10 days. When 80%–90% confluence was met, these cells were labeled with 50.4  $\mu\text{g}$  Fe/mL ferumoxytol (Feraheme, AMAG Pharmaceuticals), along with 60  $\mu\text{g}/\text{mL}$  protamine sulfate and 3 U/mL heparin (Sandoz Canada), as per protocol by Thu *et al.*<sup>19</sup>. After overnight incubation, the cells were washed 3 times with phosphate-buffered saline (PBS) before and after trypsin dissociation. Cell counting and viability was determined using the trypan blue exclusion assay (using Countess Automated Cell Counter; Invitrogen). Further,  $2 \times 10^5$  ferumoxytol and unlabeled cells were collected for PPB staining to assess

iron labeling<sup>20</sup>. Cell pellets ( $1 \times 10^6$  MSCs) were collected to determine iron content using MPI (see below).

### 2.2.2 Animal model

Ten C57B1/6 mice (Charles River, Canada, Pittsburgh) were obtained and cared for in accordance with the standards of the Canadian Council on Animal Care, under an approved protocol by the Animal Use Subcommittee of Western University's Council on Animal Care.  $1 \times 10^6$  UPSIO-labeled MSCs in 25- $\mu$ L PBS were implanted to the hind limb muscle of 10 immune-competent C57B1/6 mice (day 0). A second cohort of control mice ( $n = 5$ ) received  $1 \times 10^6$  unlabeled MSCs in 25- $\mu$ L PBS. Immediately after MSC implantation, mice were administered 200- $\mu$ L PFC agent (V-Sense, CelSense Inc.) intravenously via the tail vein to label phagocytic immune cells *in situ*. Injections were performed under 2% isoflurane in 100% oxygen anesthesia.

### 2.2.3 $^1\text{H}/^{19}\text{F}$ MRI acquisition

One and 12 days following MSC implantation, *in vivo* MRI images of all mice ( $n = 15$ ) were acquired on a 3 T clinical scanner (Discovery MR750, General Electric) using a 4.31-  $\times$  4.31-cm-diameter  $^1\text{H}/^{19}\text{F}$  dual-tuned RF surface coil (Clinical MR Solutions, Wisconsin) as previously described<sup>21</sup>. Both  $^1\text{H}$  and  $^{19}\text{F}$  images were acquired with 3-dimensional (3D) balanced steady-state free precession (bSSFP) sequences. Mice were anesthetized with 2% isoflurane in 100% oxygen during these scans.

$^1\text{H}$  imaging parameters were as follows: field of view (FOV) =  $60 \times 30$  mm; matrix size =  $150 \times 75$ , slice thickness = 0.4 mm ( $0.4 \times 0.4 \times 0.4$  mm<sup>3</sup> resolution), repetition time (TR)/echo time (TE) = 12.8 / 6.4 milliseconds, flip angle (FA) =  $20^\circ$ , bandwidth (BW) =  $\pm 31.25$  kHz, phase cycles (PC) = 12, number of excitations (NEX) = 1, total scan time = 9 minutes.  $^{19}\text{F}$  imaging parameters were: FOV =  $60 \times 30$  mm, matrix =  $60 \times 30$ , slice thickness = 1 mm ( $1 \times 1 \times 1$  mm<sup>3</sup> resolution), TR/TE = 5.6 / 2.8 milliseconds, FA =  $72^\circ$ , BW =  $\pm 10$  kHz, PC = 1, NEX = 100, total scan time = 18 minutes.

## 2.2.4 Quantification of signal loss due to iron-labeled MSC

$^1\text{H}$  images were assessed for abnormal regions of signal loss (dark regions), in the area where MSCs were implanted. These regions were manually contoured over multiple  $^1\text{H}$  slices to measure the signal void volume (Osirix, Pixemo SARL, Bernex, Switzerland).

## 2.2.5 $^{19}\text{F}$ signal quantification

$^{19}\text{F}$  images were overlaid onto  $^1\text{H}$  images (Osirix, Pixemo SARL) for anatomical reference.  $^{19}\text{F}$  signal in the limb ipsilateral to the MSC implant was manually delineated and quantified relative to reference tubes of known  $^{19}\text{F}$  content ( $3.33 \times 10^{16}$   $^{19}\text{F}/\mu\text{L}$ ). Owing to the presence of phagocytic immune cells in the bone marrow (BM) and lymph nodes (LN), any  $^{19}\text{F}$  signal in the contralateral limb was subtracted from the ipsilateral limb, to isolate the  $^{19}\text{F}$  signal detected in the region of MSC implantation.

## 2.2.6 Evaluation of ferumoxytol as an MPI tracer

The particle relaxometer module (RELAX<sup>TM</sup>) on the MOMENTUM<sup>TM</sup> system (Magnetic Insight Inc., Alameda, California) was used to characterize ferumoxytol as an MPI tracer. In this mode, the localizer gradient field is switched off and a negative magnetic field is turned on and then switched to a positive field (and vice versa). As a result, iron nanoparticles are driven from a negative magnetic saturation to positive (positive scan) and vice versa (negative scan). This measures the point spread function (PSF) of the nanoparticles and allows for measurements of properties such as full-width half-maximum (FWHM) (spatial resolution) and signal per gram of iron (sensitivity)<sup>22,23</sup>. We used FWHM to define tracer resolution, according to the Houston criterion<sup>24</sup>. The shift between the positive and negative PSF is a result of magnetic relaxation as described in some studies<sup>23,25</sup>. We acquired PSFs for 30  $\mu\text{g}$  and 5.5  $\mu\text{g}$  (in 1  $\mu\text{L}$ ) ferumoxytol.

## 2.2.7 MPI acquisition

For 5 of the 10 mice that had ferumoxytol-labeled MSC implanted and that were imaged with MRI, full-body *in vivo* MPI images of mice were acquired. Image acquisition occurred on days 1, 5, and 12 following MSC implantation, on a MOMENTUM<sup>TM</sup> system (Magnetic Insight Inc.) using the 3D isotropic mode. In this

mode, tomographic images were acquired using a 5.7 T/m gradient, 35 projections, 1 average, in an FOV of  $12 \times 6 \times 6$  cm, for a total scan time of  $\sim 1$  h per mouse. We have included day 5 images as an explorative, intermediate time point, to assess MPI detection of MSCs over time. Mice were anesthetized with 2% isoflurane in 100% oxygen during these scans. 3D isotropic images of MSC pellets were acquired using the same parameters on day 0.

### 2.2.8 MPI calibration and signal quantification

Calibration lines were produced to determine the relationship between iron content in ferumoxytol (30 mg/mL) and MPI signal. To construct this line, 1  $\mu$ L samples of ferumoxytol were scanned in the same mode as *in vivo* images (3D isotropic). Samples of iron content over 2 orders of magnitude were tested: 0.75  $\mu$ g, 1.125  $\mu$ g, 1.5  $\mu$ g, 2.25  $\mu$ g, 3  $\mu$ g, 7.5  $\mu$ g, 11.25  $\mu$ g, 15  $\mu$ g, 22.5  $\mu$ g, and 30  $\mu$ g iron.

All MPI images were displayed in full dynamic range and assessed for MPI signal corresponding to the samples (calibration samples, MSC pellets, or MSCs *in vivo*) with spatial reference to fiducial markers (Osirix, Pixemo SARL). To quantify the MPI signal in a specific region of interest (ROI), a 3D semi-automatic segmentation tool was used. Before delineating these ROIs, the window/level (W/L) was adjusted to each specific region, such that the full dynamic range of this region was displayed. Total MPI signal for the delineated volume was calculated by multiplying mean signal by volume. With samples of increasing iron content, both MPI signal and volume of the ROI increase. Total MPI signal was plotted against iron content to derive calibration lines, and this relationship was used to quantify iron content in MSC pellets and MSCs *in vivo*. All MPI images, including the calibration, MSC pellets, and *in vivo* images, were delineated and analyzed in the same way to ensure consistency.

### 2.2.9 Histological analysis

Following the last imaging sessions on day 12, mice were euthanized by isoflurane overdose and then perfusion-fixed with 4% paraformaldehyde. The right limb muscle of mice was excised and paraffin-embedded. Embedded tissues were sectioned (5  $\mu$ m in thickness) every 400  $\mu$ m to ensure entire sampling of the tissue. These sections were

stained with hematoxylin and eosin for general tissue morphology, PPB and nuclear fast red counterstain to identify the presence of ferumoxytol, or F4/80 immunohistochemical staining to identify macrophages. For F4/80 staining, sections underwent antigen retrieval in sodium citrate buffer, permeabilized using 0.4% Triton X-100 (Sigma-Aldrich, Oakville, Ontario, Canada), followed by overnight incubation in rat antimouse F4/80 primary antibody [1:100 dilution] (ab16911, Abcam). The next day, sections were incubated with biotinylated goat antirat IgG antibody [1:300 dilution] (BA-9401, Vector Laboratories) and then processed with ABC solution (PK4000, Vector Laboratories, Burlington, Ontario, Canada). Lastly, the slides were incubated in 3,3'-diaminobenzidine tetrahydrochloride (DAB) substrate solution (SK-4100, Vector Laboratories) and counterstained with hematoxylin. Histological images were acquired on the EVOS Imaging System (M7000, Thermo Fischer Scientific).

## 2.2.10 Statistical analysis

Linear correlations were conducted between total MPI signal and iron content to determine Pearson's correlation coefficient. Student *t*-tests were used to evaluate temporal changes in signal void volumes and  $^{19}\text{F}$  signal (day 1 vs 12). One-way ANOVA was used to determine statistical changes in MPI signal over time (days 1, 5, and 12). These analyses were conducted using Prism software (8.0.2, GraphPad Inc.), where  $p < .05$  was considered statistically significant. Values are presented as mean  $\pm$  standard deviation.

## 2.3 Results

### 2.3.1 Evaluation of ferumoxytol as an MPI tracer

We used the relaxometer mode on the Momentum<sup>TM</sup> scanner to measure the FWHM of 30  $\mu\text{g}$  and 5.5  $\mu\text{g}$  (in 1  $\mu\text{L}$  PBS) ferumoxytol. As seen in Figure 14A, we measured a FWHM of 66.335 mT. For a 6.1 T/m gradient, the resolution of this ferumoxytol is 1.088 cm. The amplitude of the 30  $\mu\text{g}$  PSF was  $\sim 4.5$  times the height of the 5.5- $\mu\text{g}$  PSF.

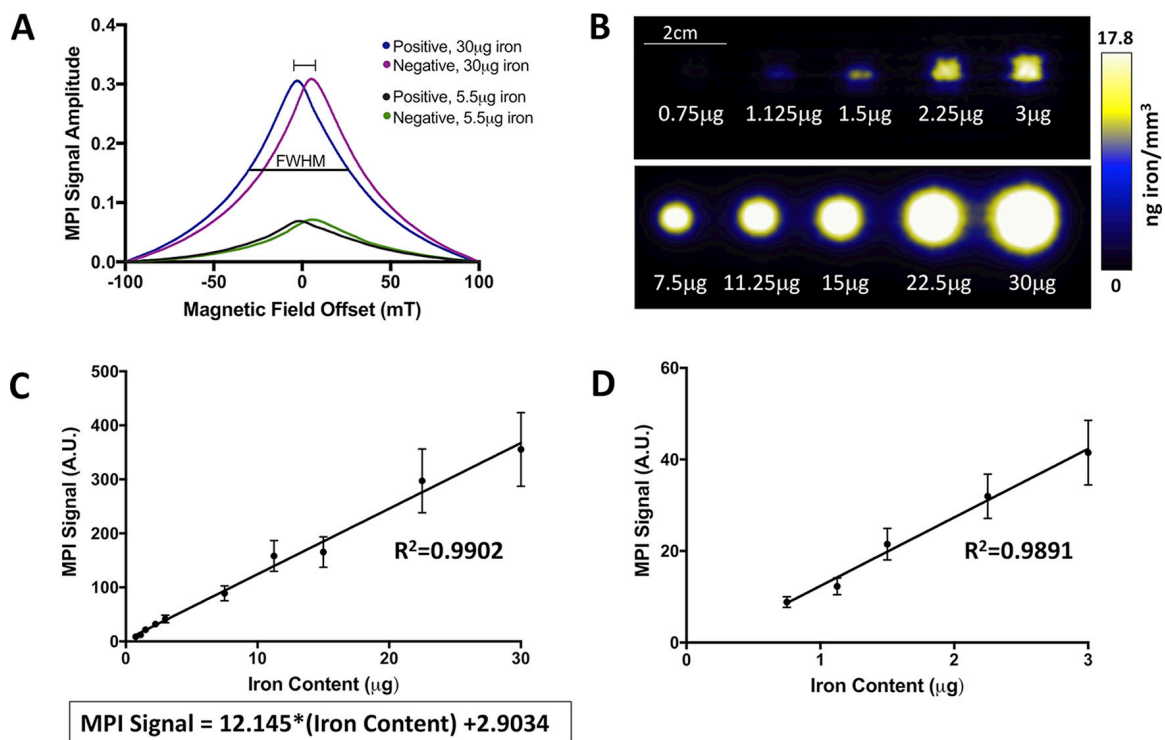


**Figure 14: Ferumoxytol evaluation and magnetic particle imaging (MPI) signal calibration. (A) Relaxometer data showing the point spread functions for 30 µg and 5.5 µg ferumoxytol. The full-width half maximum (FWHM) is labeled for the positive 30 µg iron relaxometer data. (B) A projection of 3-dimensional MPI images (in 3D isotropic mode) of ferumoxytol samples used to create a calibration line (C). (D) The relationship between iron content and MPI signal remains linear at low concentrations of iron.**

### 2.3.2 Relationship between iron content and MPI signal

We acquired images of ferumoxytol samples with known iron content (Figure 14B). These samples were separated by 2 cm on the MPI bed (5 samples/scan). There was a strong linear relationship ( $R^2 = 0.992$ ,  $p < .001$ ) between iron content and MPI signal (arbitrary units, A.U.) (Figure 14C). This relationship holds for small quantities of iron that are relevant for our investigation (Figure 14D). The equation of the line is: MPI Signal =  $12.145 \times (\text{Iron content}) + 2.9034$ . Using this relationship, iron content may be determined for a given MPI signal. We used these calibration lines to quantify iron content in ferumoxytol-labeled MSC pellets and ferumoxytol-labeled MSCs *in vivo*.

### 2.3.3 Assessment of MSC labeling with ferumoxytol

Uptake of ferumoxytol by MSCs was assessed using PPB staining (Figure 15A,D), and iron content in  $1 \times 10^6$ ,  $0.5 \times 10^6$ , and  $0.25 \times 10^6$  cells was quantified using MPI (Figure 15B,C). These 2 techniques indicated that MSCs were adequately labeled, with  $2.430 \pm 0.211$  pg iron/cell.

We also showed that there is a relationship between MPI signal and the number of ferumoxytol-labeled MSCS in the pellet on day 0. For pellets containing  $0.25 \times 10^6$ ,  $0.5 \times 10^6$ , and  $1 \times 10^6$  cells, iron content was determined to be  $0.876 \mu\text{g}$ ,  $1.227 \mu\text{g}$ , and  $2.208 \mu\text{g}$ , respectively (Figure 15C). The viability of these cells did not change with MSC labeling (97% viability before and after labeling).



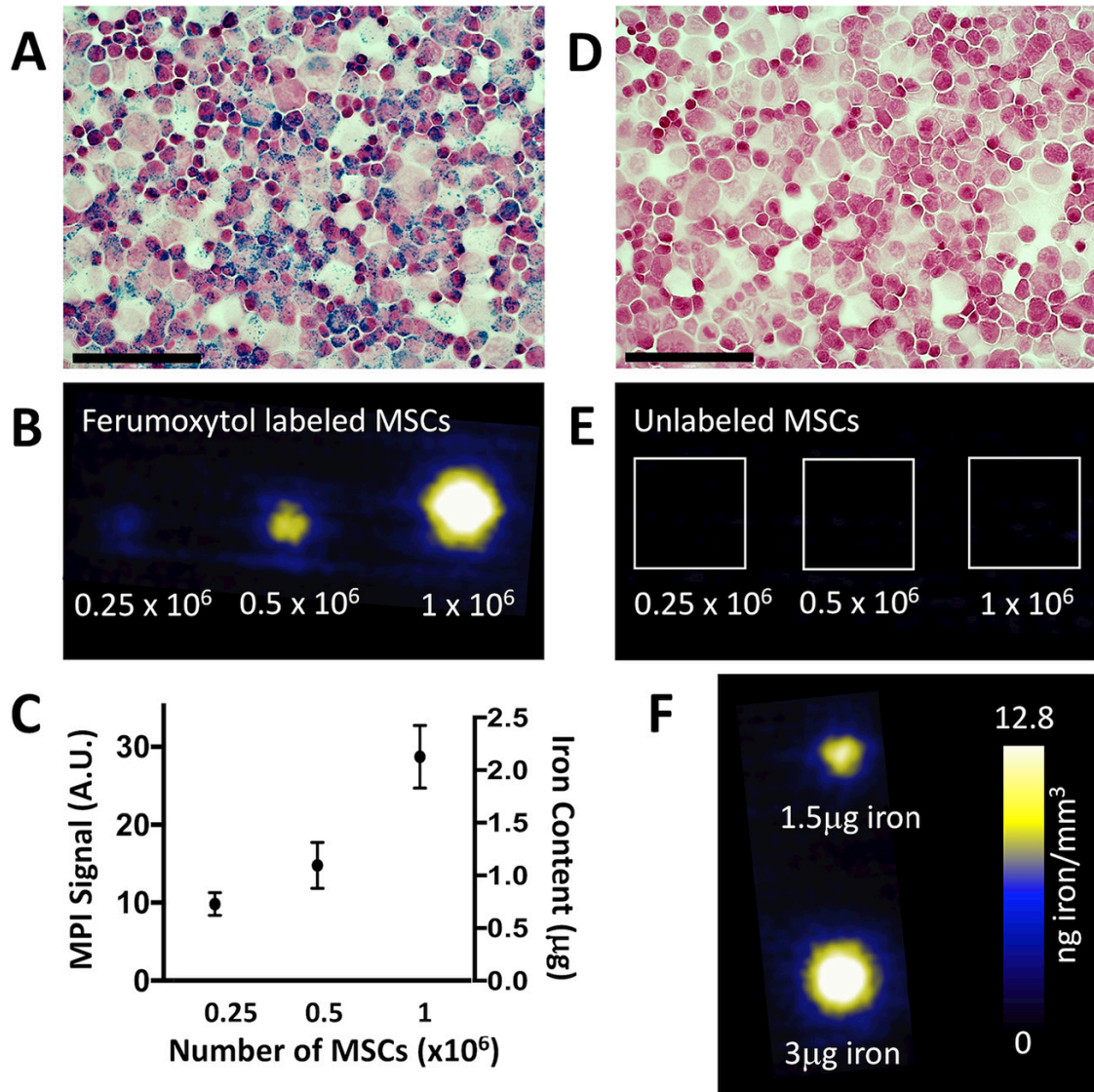


**Figure 15:** (A) Assessment of mesenchymal stem cells (MSC) labeling with ferumoxytol. Perl's Prussian Blue (PPB) identifies the presence of iron in ferumoxytol-labeled MSCs. (B) MPI of MSC pellets ( $0.24 \times 10^6$ ,  $0.6 \times 10^6$ , and  $1 \times 10^6$  cells) confirms the linear relationship between cell number and MPI signal (C). It was determined that  $1 \times 10^6$  cells contained  $2.430 \pm 0.211$  pg/cell on the day of MSC implantation. (D) PPB of unlabeled cells reveals the absence of iron and (E) MPI images of cell pellets contain no signal above background levels. (F) References containing  $3 \mu\text{g}$  and  $1.5 \mu\text{g}$  were included for visualization of the signal. The color look up table (CLUT) for the MPI images in (B) and (E) is shown in (F). 40x magnification with scale bar =  $100 \mu\text{m}$  (A, D).

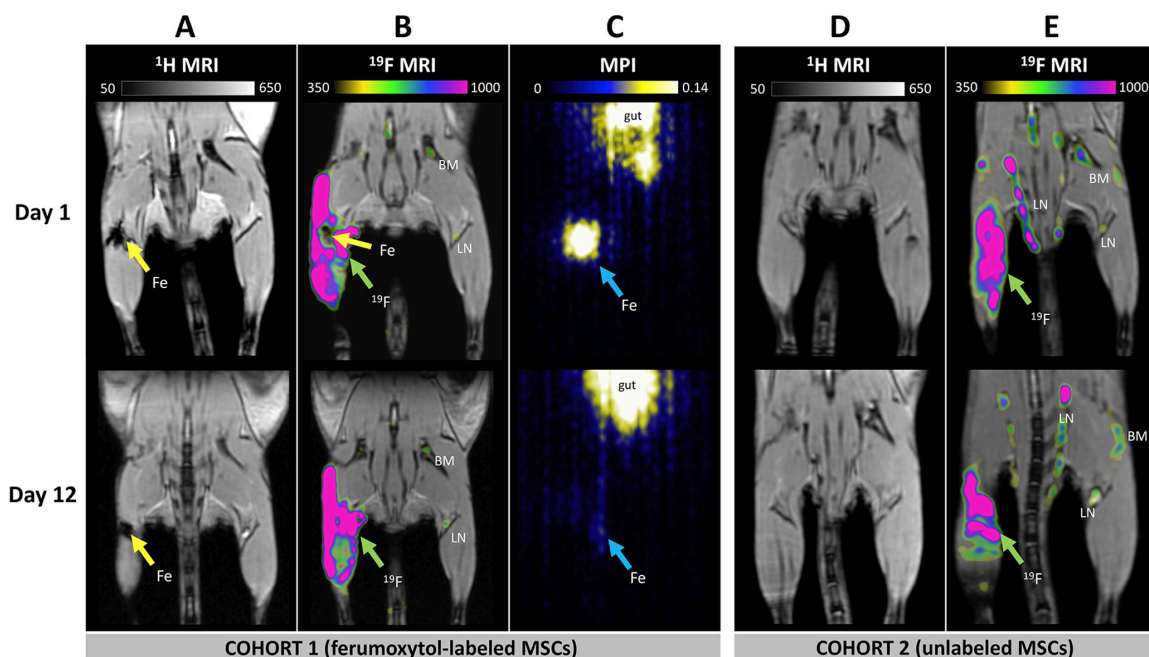
### 2.3.4 Detection of ferumoxytol-labeled MSC with $^1\text{H}$ MRI and PFC-labeled immune cells with $^{19}\text{F}$ MRI

Figure 16 shows  $^1\text{H}$ ,  $^{19}\text{F}$ , and MPI images of mice which received  $1 \times 10^6$  ferumoxytol-labeled MSCs (A-C) or unlabeled-MSCs (D,E). In  $^1\text{H}$  MRI, ferumoxytol-positive MSCs were detected as regions of signal void at the site of implantation in all mice ( $n = 10$ ), 1 and 12 days following MSC implantation (Figure 16A, labeled Fe). These voids were easily distinguishable on day 1 but were more challenging to locate by day 12 owing to the size reduction of the voids. In some cases, these voids were difficult to distinguish based on other anatomical features that appear dark on  $^1\text{H}$  MRI.

$^{19}\text{F}$  MRI was overlaid to  $^1\text{H}$  images and it revealed PFC uptake in BM and LNs, as well as in the muscle surrounding the MSC implant (Figure 16B). This is due to the presence of phagocytic immune cells in these regions.  $^{19}\text{F}$  images were first displayed according to their full dynamic range, then W/L to eliminate the background noise in the final images. This signal is unambiguous and directly related to the number of  $^{19}\text{F}$  atoms present in the tissue, which allows for assessment of relative cell number.

Ferumoxytol-labeled MSCs were also detected with MPI 1, 5, and 12 days after MSC implantation (Figure 16C and 37 in Appendix A). These MPI images were windowed to display the full dynamic range from a 1.5- $\mu\text{g}$  ferumoxytol reference (not shown). In day 12 images, MPI signal generated from ferumoxytol-positive MSCs was diminished but more clearly visible with windowing. In MPI images, signal was also detected in the gut regions, presumably owing to the presence of iron in mouse feed. Mouse feed was imaged separately by MPI and had substantial iron content (Figure 38 in Appendix A).

In control mice that received unlabeled MSCs ( $n = 5$ ), no regions of signal voids were detected in  $^1\text{H}$  images (Figure 16D). In these same mice,  $^{19}\text{F}$  signal was detected in the LNs, BM, and in the muscle where the MSC implant occurred, similar to the mice which received ferumoxytol-labeled MSCs (Figure 16E).



**Figure 16: (A) *In vivo*  $^1\text{H}/^{19}\text{F}$  MRI and MPI. In  $^1\text{H}$  images, ferumoxytol-positive MSCs were detected as regions of signal loss, 1 and 12 days following MSC implantation (labeled Fe). (B) In  $^{19}\text{F}$  MRI, PFC-positive immune cells are detected in the bone marrow (BM), lymph nodes (LN), and in the muscle surrounding the MSC implant. (C) Ferumoxytol-positive MSCs are also detected in MPI images as bright spots (labeled Fe). In these images, iron in the gut of the mice (*i.e.*, food) is also detected by MPI. The range of the MPI images is 0-0.14 arbitrary units, which is equivalent to 0-9.8 ng iron/mm<sup>3</sup>. Mice that received unlabeled MSCs (controls) had no signal voids present in  $^1\text{H}$  MRI (D) and  $^{19}\text{F}$  signal persisting (E), in response to the implant. The CLUT is displayed above each image. All images of the same type are windowed identically for comparison.**

### 2.3.5 Quantification of temporal changes in iron voids, $^{19}\text{F}$ signal, and MPI signal

Over 12 days, the measured iron void volumes in  $^1\text{H}$  images declined in all 10 mice, by 62% on average ( $p = .0003$ ) (Figure 17A). On day 1, the average void was  $9.216 \pm 4.136 \text{ mm}^3$  and by day 12,  $3.523 \pm 2.217 \text{ mm}^3$ .

$^{19}\text{F}$  signal, detected from PFC-labeled immune cells, was detected in both limbs in all 15 mice on day 1 and 12 (Figure 17B). On day 1,  $^{19}\text{F}$  signal in the limb ipsilateral to the MSC implant was  $(1.866 \pm 0.5825) \times 10^{19}$  spins and  $(2.522 \pm 2.101) \times 10^{18}$  spins in the contralateral limb. Signal in the contralateral limb was only present in the bone marrow and LNs. The difference in  $^{19}\text{F}$  signal between these limbs, representing signal solely from immune infiltration as a result of the MSC implantation, was  $(1.614 \pm 0.6604) \times 10^{19}$  spins. On day 12,  $(1.560 \pm 0.6535) \times 10^{19}$  spins were present in the ipsilateral limb and  $(8.518 \pm 7.227) \times 10^{18}$  spins in the contralateral limb, resulting in a difference of  $(1.470 \pm 0.6565) \times 10^{19}$  spins. There was no significant difference ( $p = .148$ ) in the  $^{19}\text{F}$  signal resulting from MSC implantation (*i.e.*, the differences between limbs) when comparing signal on day 1 and day 12. This indicates the persistent infiltration of immune cells. There was no significant difference ( $p = .841$ ) in  $^{19}\text{F}$  signal between mice administered ferumoxytol-labeled MSCs ( $1.530 \pm 0.746 \times 10^{19}$ ,  $n = 10$ ) and unlabeled MSCs ( $1.577 \pm 0.487 \times 10^{19}$ ,  $n = 5$ ).

*In vivo* iron content in MSCs measured by MPI on day 1 ( $1.510 \pm 0.206 \mu\text{g}$ ,  $n = 5$  mice) was significantly different from day 12 ( $0.492 \pm 0.131 \mu\text{g}$ ,  $n = 5$  mice;  $p = .002$ ) (Figure 17C). We imaged 3 of these mice on day 5 and the measured iron content ( $1.072 \pm 0.154 \mu\text{g}$ ) was also significantly higher than iron content measured on day 12 ( $p = .014$ ). Under the assumption that these cells retain iron *in vivo* ( $2.430 \pm 0.211 \text{ pg/cell}$ ), we detected  $6.21 \pm 0.847 \times 10^5$  MSCs 1 d after implantation ( $n = 5$  mice),  $4.410 \pm$

$0.634 \times 10^5$  MSCs on day 5 ( $n = 3$  mice), and  $2.027 \pm 0.539 \times 10^5$  MSCs on Day 12 ( $n = 5$  mice) (Figure 17D). These quantitative findings are summarized in Table 3.

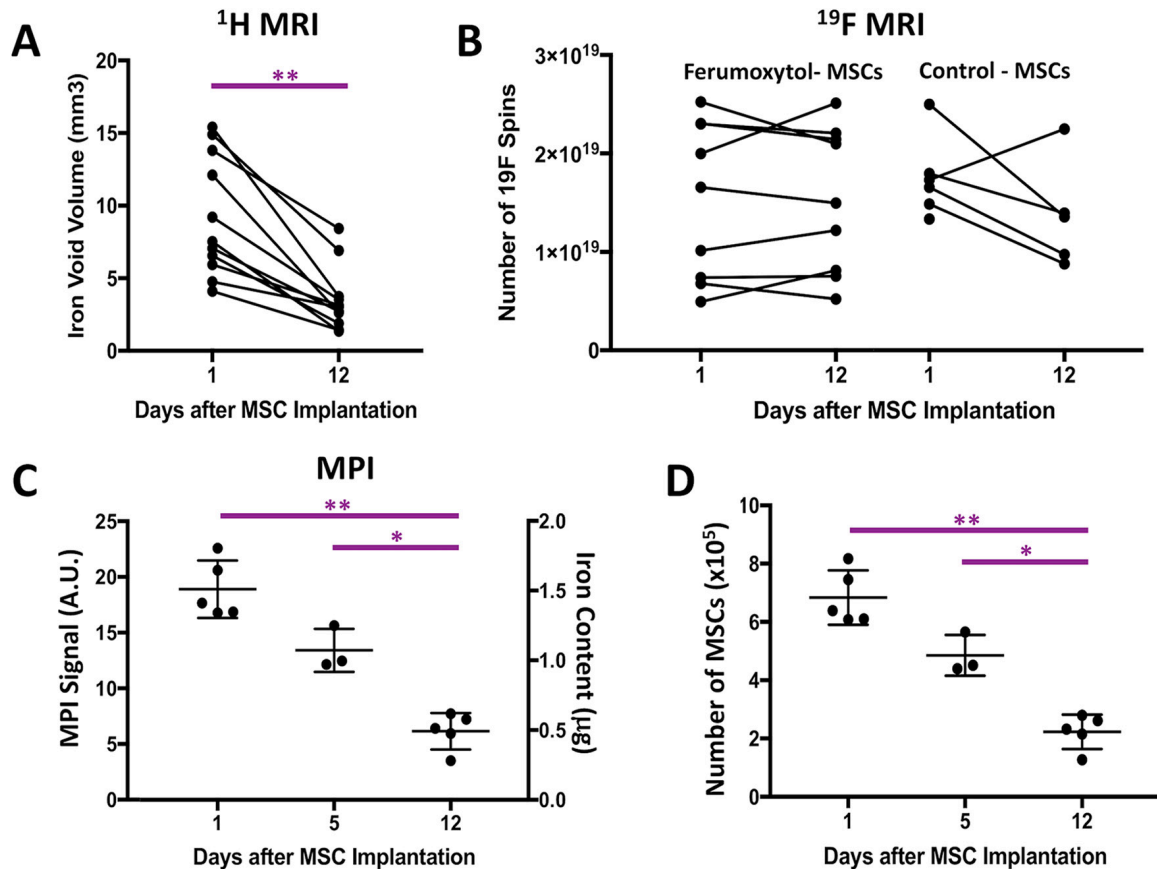


**Figure 17:** (A) The volume of signal void in <sup>1</sup>H MR images created by ferumoxytol-labeled MSCs declined over 12 days (by 64%) in all 10 mice. (B) <sup>19</sup>F signal detected from perfluorocarbon (PFC)-positive immune cells remained constant over these 12 days in all 15 mice. There was no significant difference in <sup>19</sup>F signal between mice with ferumoxytol-labeled ( $n = 10$  mice) or unlabeled ( $n = 5$  mice) MSCs. (C) MPI signal and iron content (determined by MPI) declined over 12 days (67% reduction between days 1 and 12) in all 5 mice. (D) The number of MSCs (estimated using MPI data) also declined over time in these same mice.

**Table 3: Summary of temporal changes measured in  $^1\text{H}$  MRI, MPI, and  $^{19}\text{F}$  MRI, resultant of the presence of ferumoxytol-labeled MSCs and PFC-labeled macrophages.**

<b>Measurement</b>	<b>Day 1</b>	<b>Day 12</b>	<b><i>p</i></b>
Iron Void Volume by $^1\text{H}$ MRI (n = 10)	$9.2 \pm 4.1 \text{ mm}^3$	$3.5 \pm 2.2 \text{ mm}^3$	<.001
MPI Signal (n = 5)	$18.8 \pm 2.9 \text{ A.U.}$	$4.4 \pm 1.9 \text{ A.U.}$	.002
$^{19}\text{F}$ Signal surrounding MSCs with iron (n = 10)	$1.5 \pm 0.8 \times 10^{19}$	$1.5 \pm 0.7 \times 10^{19}$	.953
$^{19}\text{F}$ Signal in control mice (n = 5)	$1.7 \pm 0.5 \times 10^{19}$	$1.4 \pm 0.5 \times 10^{19}$	.166

### 2.3.6 Microscopy and immunohistochemistry

MSCs were identified in hematoxylin and eosin sections among connective and muscular tissue (Figure 18A). PPB staining verified the presence of ferumoxytol in these MSCs (Figure 18B). F4/80 staining with DAB identified macrophages infiltrating the MSCs (Figure 18C). These are directly adjacent sections.

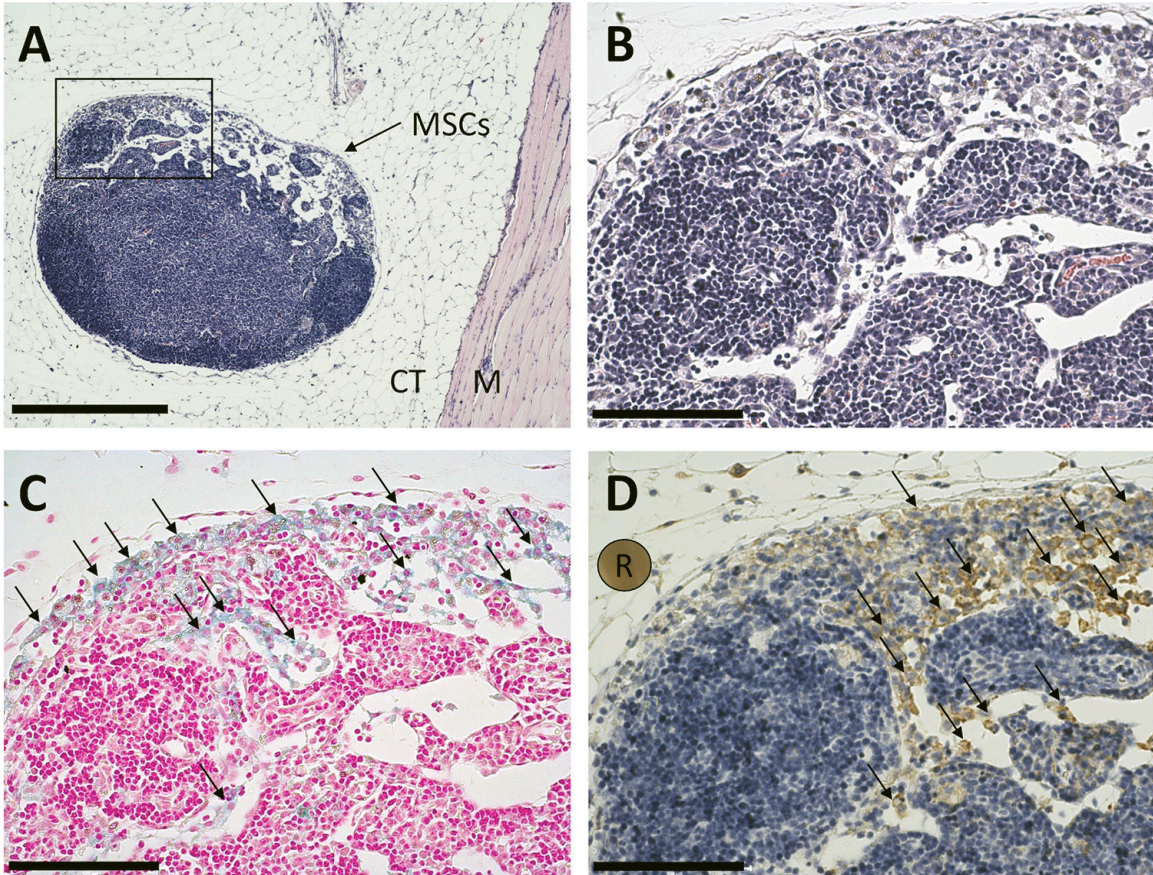


**Figure 18: (A) Histological validation showing the presence of MSCs surrounded in connective tissue (CT) and muscle (M) in hematoxylin and eosin (H&E) at 10x magnification (scale bar = 500  $\mu\text{m}$ ) and (B) 40x magnification. (C) PPB staining with nuclear fast red counterstain confirms the presence of iron within MSCs. Black arrows indicate PPB-positive cells. (D) F4/80 staining with hematoxylin counterstain reveals macrophage infiltration within the same region as the MSCs. Expected F4/80 staining is shown in the reference indicator (R). Black arrows indicate F4/80-positive cells. 40x magnification, scale bars = 100  $\mu\text{m}$  (B,C,D).**

## 2.4 Discussion

We have detected and quantified the presence of MSCs and infiltrating macrophages over time using a unique combination of cellular imaging technologies. MSCs were labeled with ferumoxytol and detected in  $^1\text{H}$  images as regions of negative signal (signal void) and in MPI images as regions of positive signal. Macrophages that accumulate at the site of MSC implantation were labeled *in vivo* with a PFC agent, then detected with  $^{19}\text{F}$  MRI. The direct quantification of MPI and  $^{19}\text{F}$  MRI signal was used to estimate the relative number of MSCs and macrophages over time. This multimodality imaging approach allowed for the confirmation of MSC delivery, the measurement of MSC number over time (post implantation), and quantification of inflammation.

### 2.4.1 Ferumoxytol as a dual $^1\text{H}$ MRI and MPI cell tracking agent

In this study, we measured a decrease in the volume of signal loss generated by ferumoxytol-labeled MSCs in  $^1\text{H}$  images and a decrease in MPI signal detected over 12 days following MSC implantation. This occurred in all mice and is consistent with several previous MRI cell tracking studies from our laboratory<sup>8,15,26</sup>. Microscopy obtained on day 12 confirmed that PPB-positive cells were present in muscle tissue at the site of implantation. The decrease in the region of signal loss in MR images and the MPI signal is likely because of MSC apoptosis and clearance of these cells by the immune system. The use of MRI to measure signal void volume gave us an indication that there were fewer cells at day 12 than at day 1. However, this is not a direct measure of the number of MSCs present owing to the blooming artifact and the nonlinear relationship between signal loss and cell number. With MPI we detected a decrease in positive signal produced by ferumoxytol-labeled MSCs over 12 days. This finding was in agreement with our MRI measurements; however, the MPI signal is directly related to iron concentration, which can be related back to MSC number. We can estimate the number of MSCs *in vivo* from the MPI data by comparing the measurements of MPI signal with the mean iron uptake per cell for MSC labeled *in vitro*. MPI data for cell samples showed 2.4 pg iron per MSC on average. This was used to estimate the number of MSCs *in vivo* over time (Figure 17C,D).



The use of ferumoxytol as a tracer for both iron-based  $^1\text{H}$  MRI and MPI cell tracking is appealing, as it is a clinically translatable iron nanoparticle. However, other iron nanoparticles (*i.e.*, ferucarbotran, an SPION) have superior MPI SNR and spatial resolution compared with ferumoxytol<sup>13</sup>. In this study we reported an FWHM of 1.088 cm for 30  $\mu\text{g}$  of ferumoxytol (30  $\mu\text{g}$  iron/ $\mu\text{L}$ ). We also reported a PSF for 5.5  $\mu\text{g}$  ferumoxytol (in 1  $\mu\text{L}$  PBS) to easily compare FWHM and SNR of ferucarbotran (Vivotrax, 5.5  $\mu\text{g}$  iron/ $\mu\text{L}$ ) in the future. The ideal MPI nanoparticle is still under investigation, considering the effects of nanoparticle size and biological properties, that is, surface composition and cell labeling process. The Langevin model predicts a cubic improvement in spatial resolution with increasing nanoparticle size<sup>23,25</sup>. USPIO (ferumoxytol) nanoparticles have a diameter of  $<50$  nm, which is smaller and contain less iron than other available nanoparticles such as SPIONs (50–100 nm) and micron-sized superparamagnetic iron oxides ( $\sim 1$   $\mu\text{m}$ )<sup>27</sup>.

In our study, we used protamine sulfate and heparin to increase uptake of ferumoxytol by MSCs. There is evidence<sup>28</sup> that the use of transfection agents (protamine) can reduce MPI detection; however, this effect is seen mainly at lower drive frequencies (0.4 kHz). The Momentum<sup>TM</sup> MPI scanner uses a 45 kHz alternating magnetic field to excite iron nanoparticles.

We showed that the formation of a calibration line was a robust technique to quantify iron content from measured MPI signal. In this process, the samples of iron (0.75–30  $\mu\text{g}$ ) were imaged using the same settings as the other *in vivo* scans (3D isotropic mode). This linear relationship persists at low iron concentrations (0.75–3  $\mu\text{g}$ ), which is useful in the quantification of ferumoxytol-labeled MSCs (which contained  $\sim 2.4$   $\mu\text{g}$  in  $1 \times 10^6$  cells on day 0).

#### 2.4.2 Imaging inflammation with $^{19}\text{F}$ MRI

This is the first study to use PFC to indicate inflammation associated with iron-labeled stem cells and to track this over time. Following the intravenous administration of PFC, we detected prominent regions of  $^{19}\text{F}$  signal in the limb muscle surrounding the MSC

implant using  $^{19}\text{F}$  MRI. This *in vivo* labeling technique is known to label resident phagocytic immune cells of the reticuloendothelial system<sup>8,10</sup>. We detected a large number of  $^{19}\text{F}$  atoms (on the order of  $10^{19}$ ) in the ipsilateral limb on both day 1 and 12. Microscopy obtained on day 12 confirmed that F4/80-positive cells were present in muscle tissue at the site of implantation. This suggests that the number of PFC-positive macrophages remained constant over this time. We can get a rough estimate of macrophage cell number by comparing the value for total  $^{19}\text{F}$  atoms with the mean  $^{19}\text{F}$  uptake per cell for macrophages labeled *in vitro*. Our previous work has measured  $2.12 \times 10^{11}$   $^{19}\text{F}$  spins per macrophage using NMR<sup>21</sup>. Using this value, we would estimate that  $\sim 7.44 \times 10^7$  cells are present at the site of the MSC implantation on day 1 and  $6.93 \times 10^7$  cells on day 12.

This is the first study to demonstrate the ability to image macrophage infiltration *in vivo* using  $^{19}\text{F}$  on a clinical (3 T) MRI system. Compared with iron-based cell tracking,  $^{19}\text{F}$  MRI has lower sensitivity and consequently, preclinical  $^{19}\text{F}$  cell tracking has only been performed at relatively high magnetic field strengths (>3 T). The bSSFP imaging sequence and surface RF coil play a major role in enhancing sensitivity to enable detection and cell tracking of  $^{19}\text{F}$ -positive cells at 3 T.

### 2.4.3 Potential limitations

The MRI and MPI cell labeling agents used in this study (iron and PFC) may be diluted over time as cells proliferate, and thus, there is some ambiguity in the number of cells detected. Since MSCs are implanted *in vivo* to a suppressive environment that lacks nutrients, we do not expect that MSCs are proliferating substantially. We presume that the reduction ferumoxytol in MSCs, by detection of voids in  $^1\text{H}$  MRI and by MPI, is predominately resulting from MSC death. The presence and detection of ferumoxytol do not reflect cell viability because this agent is retained within apoptotic MSCs. Phagocytic immune cells uptake these apoptotic MSCs and the USPIO nanoparticles for clearance in the liver. Thus, immune cells may be labeled with PFC and ferumoxytol, in a process

called bystander labeling. Hitchens *et al.*<sup>29</sup> previously showed that if iron and  $^{19}\text{F}$  agents are in the same cell, iron-mediated quenching of  $^{19}\text{F}$  signal can occur. This may contribute to ambiguity when detecting and quantifying PFC-labeled macrophages that are involved with clearance of MSCs. However, we did not detect a difference in  $^{19}\text{F}$  signal between mice, which received ferumoxytol-labeled MSCs or unlabeled MSCs. This indicates that while quenching of  $^{19}\text{F}$  signal may be occurring in the presence of ferumoxytol, this effect does not significantly alter the quantification of PFC-labeled macrophages in this application.

We detected unwanted signal in the mouse gut in all 5 mice imaged with MPI (Figure 16) owing to the presence of iron in mouse feed. This gut signal is also present in mice that do not have iron-labeled cells implanted (data not shown). This signal can complicate analysis of MPI using the automatic thresholding tool if the gut signal is much brighter than the region of interest. Because of this, the signal from ferumoxytol-labeled MSCs was manually delineated for 3 of the mice on day 12. This has negligible impact on the signal quantification, rather it is more time-consuming for the user. This gut signal can also create problems if it is in close proximity to other target sources of iron. This did not impact the quantification of iron in this study, as the gut signal was distant enough from the MSC implant; however, this should be considered when designing future experiments.

The *in vivo* scan times for MPI (1 h) are considerably longer than MRI (9 minutes for  $^1\text{H}$  scans and 18 minutes for  $^{19}\text{F}$  scans). This much time under anesthesia is undesirable for cell tracking when images are collected at multiple time points. Although 2-dimensional MPI scans of mice can be acquired within 3 minutes, these images (which appear as maximum intensity projections) do not have volumetric data for accurate quantification of iron present within a 3D geometry.

## 2.5 Conclusion

In this study, we have shown that iron-based  $^1\text{H}$  MRI,  $^{19}\text{F}$  MRI, and MPI can be used together to noninvasively monitor the fate of 2 cell populations *in vivo* (MSCs and macrophages). This is the first time that these 3 modalities are combined to monitor cell populations *in vivo*. We propose that these cellular imaging techniques could be used to monitor MSC engraftment over time and detect the infiltration of macrophages at transplant sites. This could enhance therapeutic monitoring to confirm appropriate MSC delivery, measure the number of MSCs present over time, and quantify immune infiltrate to identify MSC rejection.

## 2.6 Chapter 2 references

1. Le Blanc, K. & Ringdén, O. Immunobiology of human mesenchymal stem cells and future use in hematopoietic stem cell transplantation. *Biology of Blood and Marrow Transplantation* (2005). doi:10.1016/j.bbmt.2005.01.005
2. Samsonraj, R. M. *et al.* Concise Review: Multifaceted Characterization of Human Mesenchymal Stem Cells for Use in Regenerative Medicine. *Stem Cells Transl. Med.* **6**, 2173–2185 (2017).
3. Gao, F. *et al.* Mesenchymal stem cells and immunomodulation: current status and future prospects. *Cell death & disease* (2016). doi:10.1038/cddis.2015.327
4. Li, N. & Hua, J. Interactions between mesenchymal stem cells and the immune system. *Cell. Mol. Life Sci.* **74**, 2345–2360 (2017).
5. Meirelles, L. da S. & Nardi, N. B. Methodology, biology and clinical applications of mesenchymal stem cells. *Front. Biosci. (Landmark Ed.)* **14**, 4281–98 (2009).
6. Borgovan, T., Crawford, L., Nwizu, C. & Quesenberry, P. Stem cells and extracellular vesicles: biological regulators of physiology and disease. *Am. J. Physiol. Physiol.* (2019). doi:10.1152/ajpcell.00017.2019

7. Salazar-Noratto, G. E. *et al.* Concise Review: Understanding and leveraging cell metabolism to Enhance Mesenchymal Stem Cell Transplantation Survival in Tissue Engineering and Regenerative Medicine Applications. *Stem Cells* (2019). doi:10.1002/stem.3079
8. Gaudet, J. M., Hamilton, A. M., Chen, Y., Fox, M. S. & Foster, P. J. Application of dual <sup>19</sup>F and iron cellular MRI agents to track the infiltration of immune cells to the site of a rejected stem cell transplant. *Magn. Reson. Med.* **78**, 713–720 (2017).
9. Makela, A. V. *et al.* Cellular imaging with MRI. *Top. Magn. Reson. Imaging* **25**, 177–186 (2016).
10. Khurana, A. *et al.* Intravenous ferumoxytol allows noninvasive MR imaging monitoring of macrophage migration into stem cell transplants. *Radiology* **264**, 803–811 (2012).
11. Heyn, C., Bowen, C. V., Rutt, B. K. & Foster, P. J. Detection threshold of single SPIO-labeled cells with FIESTA. *Magn. Reson. Med.* (2005). doi:10.1002/mrm.20356
12. Bulte, J. W. M. Superparamagnetic iron oxides as MPI tracers: A primer and review of early applications. *Adv. Drug Deliv. Rev.* **138**, 293–301 (2019).
13. Nejadnik, H. *et al.* Ferumoxytol Can Be Used for Quantitative Magnetic Particle Imaging of Transplanted Stem Cells. *Mol. Imaging Biol.* **21**, 465–472 (2018).
14. Aghighi, M. *et al.* Magnetic resonance imaging of tumor-associated macrophages: Clinical translation. *Clin. Cancer Res.* **24**, 4110–4118 (2018).
15. Gaudet, J. M., Ribot, E. J., Chen, Y., Gilbert, K. M. & Foster, P. J. Tracking the fate of stem cell implants with fluorine-19 MRI. *PLoS One* **10**, 1–12 (2015).
16. Chapelin, F., Capitini, C. M. & Ahrens, E. T. Fluorine-19 MRI for detection and quantification of immune cell therapy for cancer. *J. Immunother. Cancer* **6** (2018).

17. Bulte, J. W. M. *et al.* Quantitative “Hot-Spot” Imaging of Transplanted Stem Cells Using Superparamagnetic Tracers and Magnetic Particle Imaging. *Tomography* **1**, 91–97 (2015).
18. Dousset, V. *et al.* In vivo macrophage activity imaging in the central nervous system detected by magnetic resonance. *Magn. Reson. Med.* **41**, 329–333 (1999).
19. Thu, M. S. *et al.* Self-Assembling Nanocomplexes by combining Ferumoxytol, Heparin And Protamine For Cell Tracking by MRI HHS Public Access Author manuscript. *Nat Med* **18**, 463–467 (2012).
20. Mcfadden, C., Mallett, C. L. & Foster, P. J. Labeling of multiple cell lines using a new iron oxide agent for cell tracking by MRI. *Contrast Media Mol. Imaging* (2011). doi:10.1002/cmml.456
21. Makela, A. V. & Foster, P. J. Preclinical 19 F MRI cell tracking at 3 Tesla. *Magn. Reson. Mater. Physics, Biol. Med.* **32**, 123–132 (2019).
22. Goodwill, P. W. & Conolly, S. M. The X-space formulation of the magnetic particle imaging process: 1-D signal, resolution, bandwidth, SNR, SAR, and magnetostimulation. *IEEE Trans. Med. Imaging* (2010). doi:10.1109/TMI.2010.2052284
23. Tay, Z. W., Hensley, D. W., Vreeland, E. C., Zheng, B. & Conolly, S. M. The Relaxation Wall: Experimental Limits to Improving MPI Spatial Resolution by Increasing Nanoparticle Core size. *Biomed Phys End Express* **3**, 1–21 (2017).
24. Houston, W. V. A compound interferometer for fine structure work. *Phys. Rev.* (1927). doi:10.1103/PhysRev.29.478
25. Arami, H., Ferguson, R. M., Khandhar, A. P. & Krishnan, K. M. Size-dependent ferrohydrodynamic relaxometry of magnetic particle imaging tracers in different environments. *Med. Phys.* **40**, 1–14 (2013).

26. Noad, J. *et al.* MRI tracking of transplanted iron-labeled mesenchymal stromal cells in an immune-compromised mouse model of critical limb ischemia. *NMR Biomed.* **26**, 458–67 (2013).
27. Modo, M., Hoehn, M. & Bulte, J. W. M. Cellular MR imaging. *Molecular Imaging* (2005). doi:10.1162/15353500200505145
28. Suzuka, H., Mimura, A., Inaoka, Y. & Murase, K. Magnetic Nanoparticles in Macrophages and Cancer Cells Exhibit Different Signal Behavior on Magnetic Particle Imaging. *J Nanosci Nanotechnol* **19**, 6857–6865 (2019).
29. Hitchens, T. K. *et al.* Combining perfluorocarbon and superparamagnetic iron-oxide cell labeling for improved and expanded applications of cellular MRI. *Magn. Reson. Med.* **73**, 367–375 (2015).

## Chapter 3

### 3 The Sensitivity of Magnetic Particle Imaging and Fluorine-19 Magnetic Resonance Imaging for Cell Tracking‡

Magnetic particle imaging (MPI) and fluorine-19 ( $^{19}\text{F}$ ) MRI produce images which allow for quantification of labeled cells. MPI is an emerging instrument for cell tracking, which is expected to have superior sensitivity compared to  $^{19}\text{F}$  MRI. Our objective is to assess the cellular sensitivity of MPI and  $^{19}\text{F}$  MRI for detection of mesenchymal stem cells (MSC) and breast cancer cells. Cells were labeled with ferucarbotran or perfluoropolyether, for imaging on a preclinical MPI system or 3 Tesla clinical MRI, respectively. Using the same imaging time, as few as 4000 MSC (76 ng iron) and 8000 breast cancer cells (74 ng iron) were reliably detected with MPI, and 256,000 MSC ( $9.01 \times 10^{16}$   $^{19}\text{F}$  atoms) were detected with  $^{19}\text{F}$  MRI, with  $\text{SNR} > 5$ . MPI has the potential to be more sensitive than  $^{19}\text{F}$  MRI for cell tracking. *In vivo* sensitivity with MPI and  $^{19}\text{F}$  MRI was evaluated by imaging MSC that were administered by different routes. *In vivo* imaging revealed reduced sensitivity compared to *ex vivo* cell pellets of the same cell number. We attribute reduced MPI and  $^{19}\text{F}$  MRI cell detection *in vivo* to the effect of cell dispersion among other factors, which are described.

---

‡ This chapter was previously published and is included here with permission: [Sehl, Olivia C.](#) and Paula J. Foster. The sensitivity of magnetic particle imaging and fluorine-19 magnetic resonance imaging for cell tracking. *Scientific Reports*, 2021; 11(1), 1-12.



## 3.1 Introduction

Cellular imaging with magnetic particle imaging (MPI) and magnetic resonance imaging (MRI) enables the tracking of cellular therapies and the fate of cancer cells. MPI and Fluorine-19 ( $^{19}\text{F}$ ) MRI are advantageous as they provide positive image contrast with quantifiable signal, without the use of ionizing radiation. This allows for specific and longitudinal tracking of cells and linear cell quantification. MRI has been used to image therapeutic cells in patients<sup>1</sup>, whereas MPI is an emerging modality for cell tracking and currently limited to preclinical studies. In this study, we evaluate the sensitivity of preclinical MPI and  $^{19}\text{F}$  MRI on a clinical system for imaging of two cell types: mesenchymal stem cells (MSC) and breast cancer cells.

Therapeutic MSC have great potential for regenerative medicine. There are over 4000 clinical trials ongoing in the U.S, and over 350 in Canada, for stem cell therapies<sup>2</sup>. After administration, many MSC die due to a hostile, pro-inflammatory environment. Importantly, the number of cells that survive and persistence of cells at the implant site provide information on therapeutic status<sup>3</sup>. Critical questions about the safety and success of cell therapies—the delivery, numbers, and persistence of cells—remain unanswered. Cellular imaging has the potential to provide answers, and play a role in optimizing dosage, schedules, and administration routes for cell therapies.

Tracking the fate of cancer cells in preclinical models has been another focus of cellular imaging. Metastasis refers to the spread of cancer from the primary tumor to secondary organs and is the leading cause of death for many types of cancer, including breast cancer. The ability to track the fate of cancer populations provides a powerful tool to study metastasis and potential therapeutics which delay or inhibit metastasis. For cell tracking of MSC and cancer cells, imaging quantification is necessary, and so is the detection of few cells (high cellular sensitivity).

### 3.1.1 Sensitivity for MPI

MPI directly detects superparamagnetic iron oxide nanoparticles (SPIONs), which are used as cell labeling agents. Strong magnetic gradients (T/m) are used to localize SPIONs

by creating a field-free region (FFR), and oscillating excitation fields (mT) are applied to alter the magnetization of SPIONs present in the FFR. The FFR is traversed across the imaging field of view and the change in SPION magnetization is detected by a receive coil. The resulting image has positive contrast, and the signal is directly related to the amount of SPION and cell number.

The type of SPION and the amount of SPION taken up by cells are two major factors that determine the sensitivity of MPI for cell tracking. Optimal SPIONs for MPI will strongly magnetize with magnetic fields outside the FFR and experience fast relaxation rates within the FFR. Monodisperse, single core SPIONs with core sizes of ~25 nm have been considered ideal<sup>4,5</sup>. Cell labeling by SPIONs is typically conducted through co-culture and is dependent on endocytosis. Carbohydrate coatings, such as carboxydextran, increase the interactions of SPIONs with cell membranes, similarly, transfection agents can be used to coat SPIONs to enhance their incorporation to cells.

The most commonly used SPION for MPI is ferucarbotran (VivoTrax™, Magnetic Insight Inc., Alameda, USA), which is repurposed from the original use as an MRI contrast agent (Resovist®, Bayers Healthcare). Ferucarbotran has a carboxydextran coat and is a polydisperse agent; some nanoparticles have a core size of 24 nm (30%) and the majority have 5 nm cores<sup>6</sup>. The *in vitro* detection limit using ferucarbotran has been estimated to be approximately 1000 embryonic stem cells (27 pg/cell)<sup>7</sup>. SPIONs designed specifically for MPI are being investigated and show improved performance; *in vivo*, Wang *et al.* (2020) demonstrated detection of 2500 bone mesenchymal stem cells with cubic nanoparticles (29 pg/cell)<sup>8</sup>. Beyond this, detection limits for SPION-labeled cells have not been carefully studied.

### 3.1.2 Sensitivity for <sup>19</sup>F MRI

For <sup>19</sup>F MRI, cells can be labeled with perfluorocarbon agents such as perfluoropolyether (PFPE) nanoemulsions. Since there is little endogenous <sup>19</sup>F in biological tissues, these cells can be visualized with high specificity. The signal intensity of these images is directly linear to the number of <sup>19</sup>F atoms and cell number. The sensitivity of <sup>19</sup>F MRI cell

tracking is impacted by  $^{19}\text{F}$  cellular loading. PFPE are formulated into nanoemulsions for safe and effective labeling of cells; clinical-grade PFPE agents are available (CS-1000, CelSense Inc.) and have been used in humans<sup>9</sup>. The amount of  $^{19}\text{F}$  uptake is different for various cell types due to differences in cell size and endocytic ability<sup>10</sup>.

MRI hardware and imaging parameters also play a major role in determining  $^{19}\text{F}$  sensitivity. Higher magnetic field strengths improve detectability of cells, additionally, the use of specialized coils is integral. For example, our group has previously demonstrated comparable signal detection at 9.4 T using a birdcage coil compared to 3 T using a surface coil<sup>11</sup>.

$^{19}\text{F}$  cellular detection limits using various field strengths, hardware, and sequences have been reviewed by Srinivas *et al.*<sup>10</sup>. Notably, there were no reported studies at field strengths  $\leq 3$  T. The translation of cellular MRI techniques to the clinic will require the use of human MRI systems at clinical field strengths. Our group has demonstrated a cellular detection limit of 25,000 PFPE-labeled macrophages *in vitro* at 3 T (ref<sup>11</sup>). In the first human clinical trial at 3 T, an *in vivo* cellular detection limit between 1 and 10 million dendritic cells was demonstrated<sup>9</sup>. The sensitivity of  $^{19}\text{F}$  MRI for detection of MSC and breast cancer cells at 3 T has not been evaluated.

MPI and  $^{19}\text{F}$  MRI have similar characteristics for cell tracking (positive contrast and quantitation), and MPI is expected to be more sensitive for cell tracking, however, this has not been carefully compared. The objective of this study is to assess the *in vitro* and *in vivo* cellular sensitivity of MPI and  $^{19}\text{F}$  MRI for MSC and breast cancer cells.

## 3.2 Methodology

### 3.2.1 Cell culture

4T1 murine breast cancer cells (Dr. Fred Miller, Wayne State University, MI, USA) were maintained in Dulbecco's modified Eagle's medium (DMEM) (Gibco, Thermo Fisher Scientific, MA, USA) with 10% fetal bovine serum (FBS) and antimycotic/antibiotic.

MSCs derived from the bone marrow of C57BL/6 mice (MUBMX- 01101 [BE], Cedarlane, Burlington, Ontario, Canada) were cultured in low-glucose DMEM (Thermo Fisher Scientific) with 10% FBS. Cells were maintained at 37 °C and 5% CO<sub>2</sub> and passaged every 2–3 days for 10 days.

### 3.2.2 Cell labeling

$2 \times 10^6$  4T1 cells or MSCs were seeded for labeling in T75 cm<sup>2</sup> flasks. After 24 h, 2.5 mg/mL PFPE nanoemulsion (Cell Sense, Celsense Inc., Pittsburgh, PA, USA) was added to 10 mL complete media and left to co-incubate overnight<sup>12,13</sup>. Alternatively, cells were labeled with 55 µg Fe/mL ferucarbotran (Vivotrax, Magnetic Insight Inc., Alameda, CA, USA) using transfection agents in a protocol described by Thu *et al.*<sup>14</sup>. Briefly, 60 µL protamine sulfate (stock 10 mg/mL) was added to 2.5 mL of serum-free medium, and in a second tube, 20 µL heparin (stock 1000 U/mL) and 90 µL ferucarbotran (stock 5.5 mg/mL) was added to 2.5 mL serum-free medium. These two tubes were individually vortexed, then combined. After adhered 4T1 cells or MSC were washed in PBS, this labeling mix was added to the cells. 4 h later, 5 mL of complete media was added to cells and left to co-incubate overnight.

### 3.2.3 Evaluation of cell labeling

A cytospin of  $100 \times 10^3$  cells was prepared for all labeled cells which were fixed in 3:1 methanol:acetic acid. Iron-labeled cells were stained with Perl's Prussian blue (PPB) to identify iron in cells<sup>15</sup>. <sup>19</sup>F-labeled cells were labeled with nuclear fast red to assess for PFPE nanodroplets<sup>11</sup>. Microscopy of these slides was conducted using the EVOS imaging system (M7000, Thermo Fischer Scientific). The mean intracellular <sup>19</sup>F content in MSC was measured by NMR using a Varian Inova 400 spectrometer (Varian Inc, Paulo Alto, USA) and methods previously described<sup>11</sup>.

### 3.2.4 Preparation of cell pellets for imaging

PFPE-labeled cells or ferucarbotran-labeled cells were washed 3 times in phosphate-buffered saline (PBS) and collected in triplicate samples prepared in a dilution series:

1024, 512, 256, 128, 64, 32, 16, 8, 4, 2, 1, 0.5 ( $\times 10^3$ ) cells. Ferucarbotran-labeled cells were pelleted in 50  $\mu\text{L}$  PBS for MPI.  $^{19}\text{F}$ -labeled cells were pelleted by centrifugation and covered in 50  $\mu\text{L}$  agarose. This process was repeated two more times to produce a total of 9 replicates for each cell number and cell type (4T1 or MSC), with each cell labeling agent (PFPE or ferucarbotran).

### 3.2.5 MPI of ferucarbotran-labeled cells

All MPI was conducted on a MOMENTUM™ system (Magnetic Insight Inc.) (Figure 19A). A small well was secured to the imaging bed where a PCR tube containing the cell pellet could be placed. This allowed for imaging to occur in the identical location and for the user to easily transfer cell samples. Each cell pellet was imaged individually with the following parameters: field of view (FOV) = 6 cm  $\times$  6 cm, gradient strength = 3.0 T/m, dual-channel acquisition (X and Z), excitation amplitude = 22 mT (X-channel) and 26 mT (Z-channel), imaging time = 1.5 min. Cell pellets were imaged in descending order of cell number. Once the cell pellet was undetected, 2D imaging with 8 averages (imaging time = 11.8 min) and 3D imaging was conducted for all 9 replicates, in attempt to improve MPI sensitivity. 3D images combine 35 projections in a FOV = 6  $\times$  6  $\times$  6 cm (imaging time = 22.8 min). If cells were detected in these longer scans, fewer cells were imaged until undetected in 2D (8 averages) and 3D.

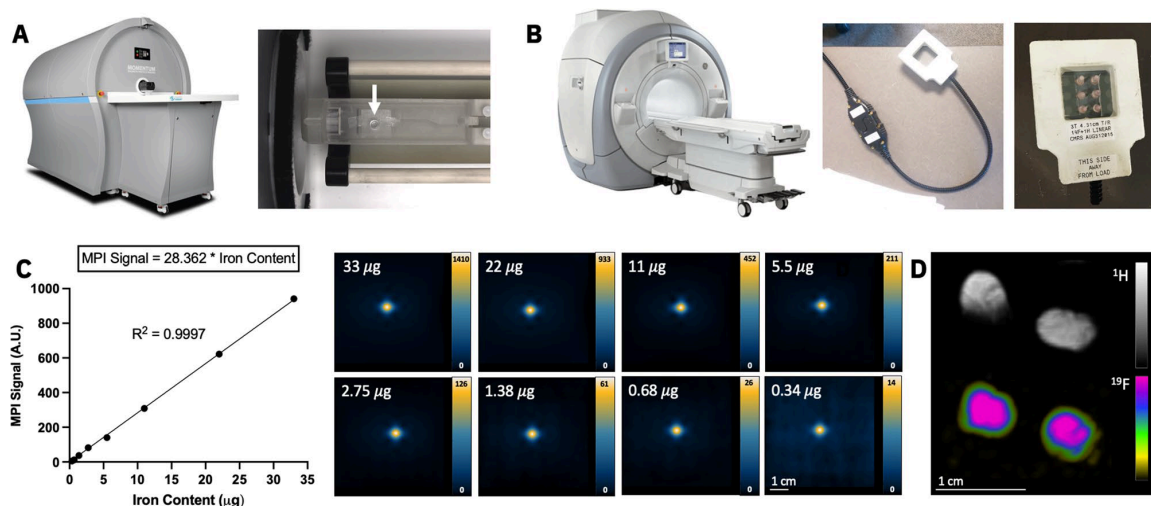


**Figure 19: A)** Image of a preclinical Momentum MPI and sample holder (white arrow), where individual ferucarbotran-labeled cell samples were placed for imaging. **(B)** Photos of a clinical 3 Tesla MRI with the dual-tuned ( $^1\text{H}/^{19}\text{F}$ ) surface coil, used for  $^{19}\text{F}$  imaging of 6 cell samples. **(C)** A strong linear relationship exists between MPI signal and iron mass ( $R^2 = 0.9997$ ). This was determined by imaging multiple samples of ferucarbotran (0.34–33  $\mu\text{g}$ ) and measuring the MPI signal from each sample. The linear equation is subsequently used to convert a measure of MPI signal from ferucarbotran-labeled cells to a measure iron content ( $\mu\text{g}$ ). **(D)**  $^1\text{H}$  and  $^{19}\text{F}$  images of two reference phantoms, containing known amount of  $^{19}\text{F}$  content ( $3.33 \times 10^{16}$   $^{19}\text{F}$  spins/ $\mu\text{L}$ ), are used for quantification of  $^{19}\text{F}$  in cell samples.

### 3.2.6 $^{19}\text{F}$ MRI of perfluorocarbon-labeled cells

$^{19}\text{F}$  images were acquired on a clinical 3 T MRI (Discovery MR750, General Electric) using a  $4.31 \times 4.31$  cm diameter dual tuned ( $^1\text{H}/^{19}\text{F}$ ) surface coil (Clinical MR Solutions, Wisconsin) (Figure 19B). Six samples of 32, 64, 128, 256, 512, 1024 ( $\times 10^3$ ) cells (from the same replicate) were imaged at a time using a 3D balanced steady state free precession (bSSFP) pulse sequence.  $^{19}\text{F}$  imaging parameters were: FOV =  $40 \times 20$  mm,

matrix =  $40 \times 20$ , slice thickness = 1 mm ( $1 \times 1 \times 1$  mm<sup>3</sup> resolution), repetition time/echo time = 5.6 ms/2.8 ms, bandwidth =  $\pm 10$  kHz, and flip angle =  $72^\circ$ . Flip angle was optimized through a series of <sup>19</sup>F images (Figure 39 in Appendix A) and calculated using reported T1 and T2 times at 3 T.<sup>9,16</sup> Cell pellets were imaged with 115 excitations (imaging time of 9.5 min, or 1.5 min/pellet) and 345 excitations (imaging time of 28.3 min, or 4.5 min/pellet).

### 3.2.7 *In vivo* detection of MSC using MPI and <sup>19</sup>F MRI

Seven NOD/SCID/IL2rg<sup>-/-</sup> (NSG) mice were obtained and cared for in accordance with the standards of the Canadian Council on Animal Care. The study was approved by the Animal Use Subcommittee of Western University's Council on Animal Care. All methods were carried out in accordance with relevant guidelines and regulations. This study was carried out in compliance with the ARRIVE guidelines.

In preparation for MPI, 4 mice were fasted for 12 h, by removing food pellets from their cages, and a piece of ex-lax® (regular strength stimulant laxative) was added to the cage. Additionally, cotton bedding, which has been shown to produce MPI signal (unpublished results) was replaced with corn bedding. The goal of these measures was to minimize background signal associated with the iron in the mouse digestive system.

To investigate differences in sensitivity *in vivo*,  $1 \times 10^5$  ferucarbotran-labeled MSC were injected to NSG mice by subcutaneous, intraperitoneal, or intravenous injection. A fourth mouse received  $2 \times 10^6$  ferucarbotran-labeled MSC by subcutaneous injection. Each mouse was imaged with MPI with a FOV = 12 cm  $\times$  6 cm  $\times$  6 cm in 2D (2.2 min). All other imaging parameters are described above. MPI was conducted immediately before injections, to measure background signal, and immediately after injections. MPI signal for each mouse was calculated as the difference between pre-injection signal (background) and post-injection signal. MPI signal from cells *in vivo* was compared to MPI signal from cell pellets.

Similarly,  $2 \times 10^6$  PFPE-labeled MSC were injected to NSG mice by subcutaneous or intraperitoneal injection. A third mouse received fewer PFPE-labeled cells ( $1 \times 10^5$ ) by subcutaneous administration. Following cell administration,  $^{19}\text{F}$  MRI was conducted for each mouse by placing the surface coil directly above the injection site to maximize sensitivity (shown in Figure 25E); the mouse receiving cells by subcutaneous was prone for imaging and the mouse receiving cells by intraperitoneal injection was supine. Imaging parameters are the same as listed above, however with a FOV =  $60 \times 30$  mm with matrix size =  $60 \times 30$  ( $1 \times 1 \times 1$  mm<sup>3</sup> resolution), and 200 excitations (imaging time = 35.5 min). *In vivo*  $^{19}\text{F}$  signal was quantified (described below) and compared to signal detected from cell pellets, which were included alongside the mouse.

### 3.2.8 Image analysis

For MPI signal calibration, an additional 8 samples of ferucarbotran (5.5 mg/mL) were imaged with identical parameters in a dilution series in PBS: 33, 22, 11, 5.5, 2.25, 1.38, 0.68, 0.34  $\mu\text{g}$  ferucarbotran. A linear relationship was found between iron mass and MPI signal (Figure 19C) and the equation of the line was used to calculate associated iron content from each cell sample.

2D MPI of the empty sample holder was conducted at the beginning (0 h), middle (3 h), and end (6 h) of six imaging sessions. The standard deviation of background noise ( $\text{SD}_{\text{noise}}$ ) was measured in these 18 images. To quantify signal from ferucarbotran-labeled cells in pellets and *in vivo*, a threshold of 5 times the average background  $\text{SD}_{\text{noise}}$  was used to mask lower amplitude signal and yield a reliable measurement of MPI signal. This imaging criteria is based on MPI signal with  $\text{SNR} > 5$  (Rose Criterion)<sup>17</sup>. Total MPI signal was calculated as mean MPI signal \* volume of ROI (mm<sup>2</sup> or mm<sup>3</sup>).

Delineation of  $^{19}\text{F}$  signal was conducted using a similar method as MPI ( $5 * \text{SD}_{\text{noise}}$ ). Background  $\text{SD}_{\text{noise}}$  of  $^{19}\text{F}$  signal for each 3D image was measured by drawing an ROI in background noise of one image slice. Due to Rician distribution observed in background



signal noise,  $^{19}\text{F}$  signal between  $5 \cdot \text{SD}_{\text{noise}}$  and  $8 \cdot \text{SD}_{\text{noise}}$  was corrected using a factor of 0.655, as described by Bouchlaka *et al.*<sup>18</sup> (Figure 40 in Appendix A). Total  $^{19}\text{F}$  signal was calculated as mean  $^{19}\text{F}$  signal \* volume of ROI. Two reference phantoms containing  $3.33 \times 10^{16}$   $^{19}\text{F}$  spins/ $\mu\text{L}$  were included in the imaging field of view for calibration (Figure 19D).  $^{19}\text{F}$  content from cell pellets was calculated as:

$$^{19}\text{F spins in ROI} = (\text{signal in ROI}) * \left( 3.33 \times 10^{16} \frac{^{19}\text{F spins}}{\mu\text{L}} \right) * \frac{\text{volume of phantoms in mm}^3}{\text{average signal in phantoms}}$$

We defined MPI and  $^{19}\text{F}$  MRI *in vitro* cell detection limits as the minimum number of MSC and 4T1 cells detected with  $\text{SNR} > 5$ . Thus, cells with signal below the  $5 \cdot \text{SD}_{\text{noise}}$  criteria were considered undetected. The amount of ferucarbotran or PFPE associated with the lowest cell number was calculated as iron mass per cell \* number of cells or  $^{19}\text{F}$  atoms per cell \* number of cells, respectively.

### 3.2.9 Statistical analysis

All statistical analysis were performed using GraphPad Prism version 9. Linear regression was performed for MPI calibration (known iron mass vs. measured MPI signal) to determine the calibration equation. This line is forced through the origin, under the assumption that background MPI signal, without a sample of iron, has an average of 0. Pearson's correlation was conducted for MPI (number of cells vs. measured MPI signal) and  $^{19}\text{F}$  MRI (number of cells vs. measured  $^{19}\text{F}$  signal). Analysis of co-variance (ANCOVA) was used to evaluate whether the MPI sensitivity (slope) was significantly different for ferucarbotran-labeled 4T1 cells and MSC (number of cells vs. measured MPI signal). Analysis of variance (ANOVA) was used to analyse differences between MPI signal measured from each cell number and again for  $^{19}\text{F}$  signal measured from each cell number. A *p*-value of 0.05 was used to determine statistical significance, unless otherwise indicated.

## 3.3 Results

### 3.3.1 MPI cellular sensitivity

The detection of ferucarbotran-labeled cells using 2D MPI (imaging time = 1.5 min) is shown in Figure 20A (4T1 cells) and Figure 21A (MSC). MPI signal measured from samples of 8000–1,024,000 4T1 cells and 4000–1,024,000 MSC had  $\text{SNR} > 5$ . The iron mass significantly increased with cell number for both cell types (Figure 20A and 21A). Importantly, the standard deviation of background noise, measured three times over six imaging sessions, showed no significant differences (Figure 41 in Appendix A).

MPI signal (and the associated iron content) was strongly correlated with cell number for ferucarbotran-labeled 4T1 cells and MSC (Figure 22A). The slope of the line was significantly steeper (factor of 2.07) for MSC compared to 4T1 cells ( $p < 0.0001$ ). Enhanced ferucarbotran labeling was measured in MSC ( $19.09 \pm 2.50$  pg Fe/cell) compared to 4T1 cells ( $9.22 \pm 1.42$  pg Fe/cell), which can be visualized in PPB-stained cells (Figure 22B).

With 2D MPI, the lowest cell numbers detected with  $\text{SNR} > 5$  were 8000 4T1 cells (6/9 replicates, corresponding to 74 ng iron, Figure 20A) and 4000 MSC (8/9 replicates, corresponding to 76 ng iron, Figure 21A). All other replicates of 8000 4T1 cells and 4000 MSC had  $\text{SNR} > 3$ . For both cell types, 2D imaging with 8 averages did not improve cell detection (Figure 20B and 21B). However, additional averaging does reduce the standard deviation of background signal from 0.235 (1 average) to 0.183 (8 averages) ( $p < 0.0001$ ).

In 3D images (22.8 min), detection of 4000 4T1 cells (37 ng iron) was enabled (3 of 9 replicates  $\text{SNR} > 5$ , and 8 of 9 had  $\text{SNR} > 3$ ) (Figure 20C). Improvements to detection of MSC was also seen in 3D; 2000 MSC (38 ng iron) were detected (6 of 9 replicates  $\text{SNR} > 5$ , and 9 of 9 had  $\text{SNR} > 3$ ) (Figure 21C). In 4 of 9 replicates, the detection of 1000 MSC (19 ng iron) was possible in 3D with a threshold of  $\text{SNR} > 3$ .

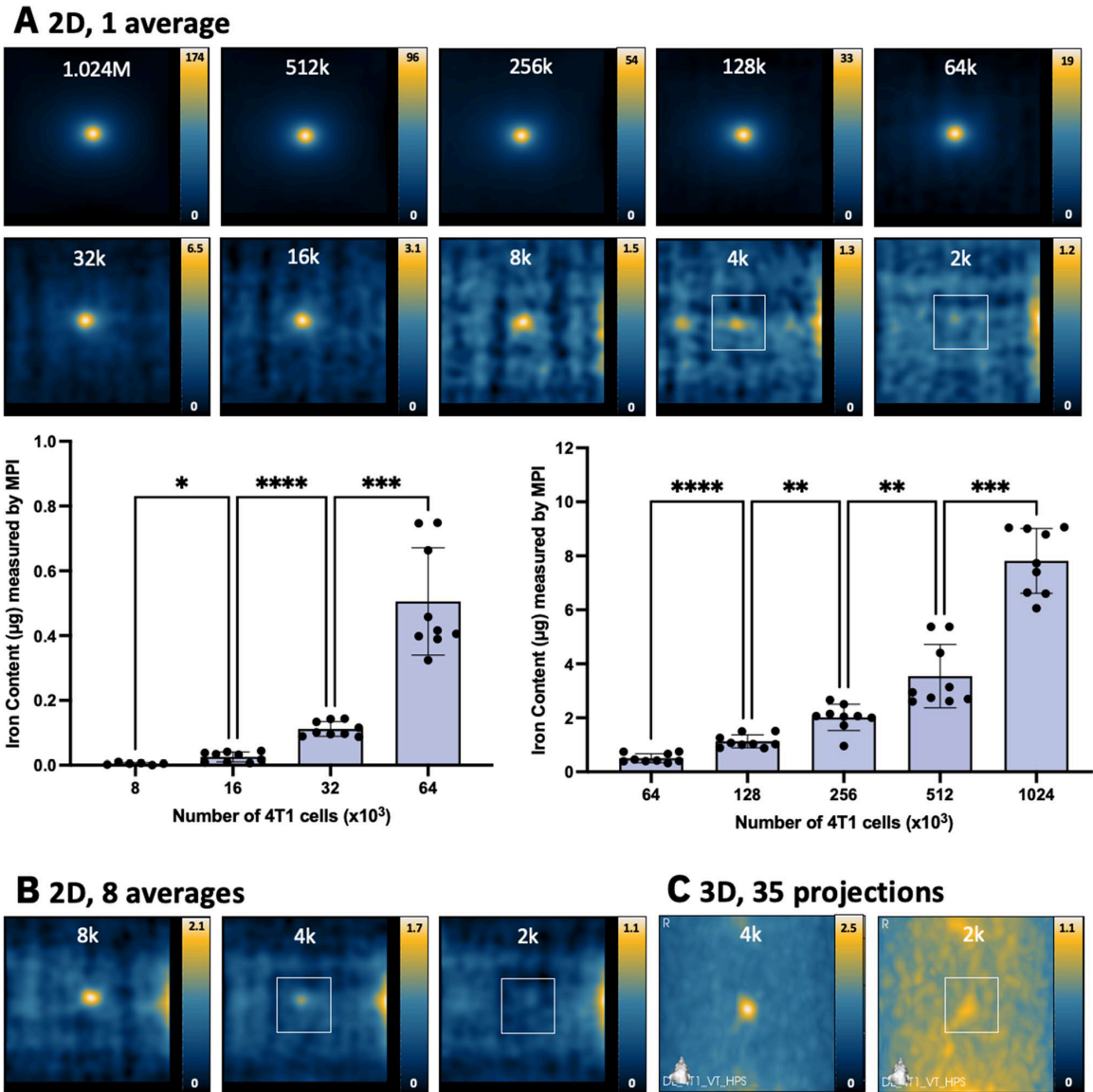


**Figure 20: MPI detection of ferucarbotran-labeled 4T1 cells. (A) 2D MPI of individual 4T1 cell pellets containing the indicated cell numbers ( $M = 10^6$ ,  $k = 10^3$ ). As few as 8000 cells ( $0.074 \mu\text{g}$  ferucarbotran) could be detected with  $\text{SNR} > 5$  in 1.5 min. 2D MPI signal (and the associated iron content) significantly increases with the number of 4T1 cells ( $*p < .05$ ,  $**p < .01$ ,  $***p < .001$ ,  $****p < .0001$ ). (B) With 8 signal averages, the same result was found. (C) In 3D, the detection of 4000 cells ( $0.037 \mu\text{g}$  ferucarbotran) with  $\text{SNR} > 5$  was possible in 23 min. Images with  $\text{SNR} < 5$  have white boxes to indicate the placement of the cell sample.**

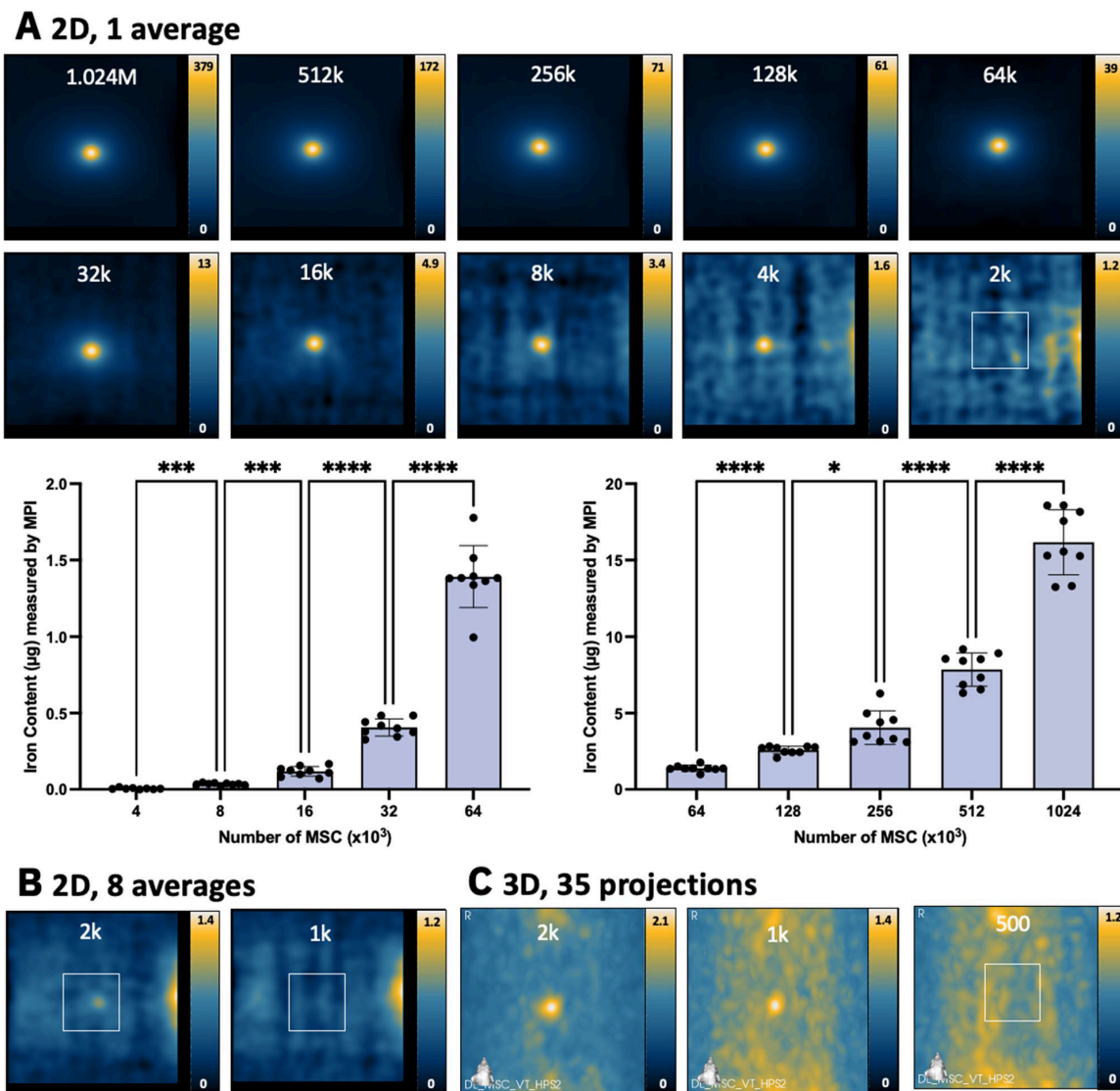


**Figure 21: MPI detection of ferucarbotran-labeled MSC. (A) 2D MPI of individual MSC pellets containing the indicated cell numbers ( $M = 10^6$ ,  $k = 10^3$ ). As few as 4000 MSC ( $0.076 \mu\text{g}$  ferucarbotran) could be detected with  $\text{SNR} > 5$  in 1.5 min. 2D MPI signal (and the associated iron content) significantly increases with the number of MSC ( $*p < .05$ ,  $**p < .01$ ,  $***p < .001$ ,  $****p < .0001$ ). (B) With 8 signal averages, the same result was found. (C) In 3D, the detection of 2000 cells ( $0.038 \mu\text{g}$  ferucarbotran, with  $\text{SNR} > 5$ ) and 1000 cells ( $0.019 \mu\text{g}$  ferucarbotran, with  $\text{SNR} > 3$ ) was possible in 23 min. Images with  $\text{SNR} < 5$  have white boxes to indicate the placement of the cell sample.**

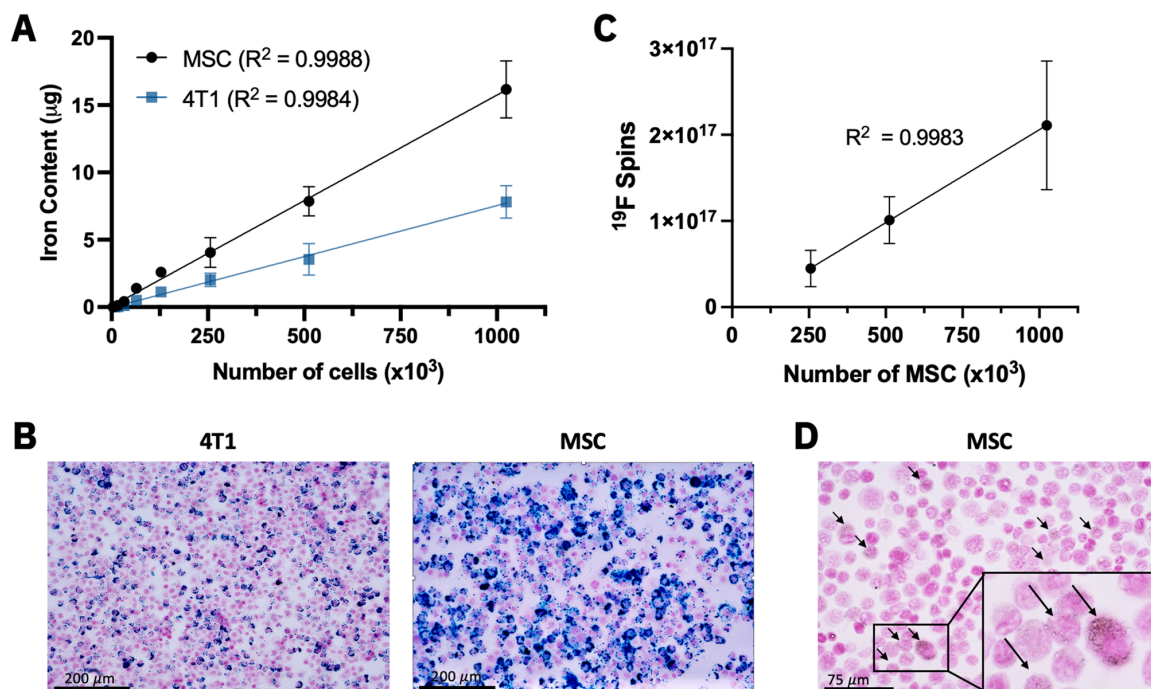


**Figure 22:** (A) The number of ferucarbotran-labeled MSC and 4T1 cells is strongly correlated with iron content measured by MPI ( $R^2 > 0.998$ ). The slope of the line for MSC is higher than 4T1 ( $p < .0001$ ), indicating higher sensitivity and enhanced uptake of iron in MSC compared to 4T1 cells as shown with PPB stain (B). (C) A strong linear correlation exists between the number of PFPE-labeled MSC and detected  $^{19}\text{F}$  signal ( $R^2 = 0.9983$ ). (D) PFPE labeling identified as nanodroplets in microscopy (black arrows).

### 3.3.2 $^{19}\text{F}$ MRI cellular sensitivity

MSC were labeled with  $3.52 \pm 1.55 \times 10^{11}$   $^{19}\text{F}$ /cell (NMR) and the nanodroplets associated with the  $^{19}\text{F}$  agent were identified with microscopy (Figure 22D). The average number of  $^{19}\text{F}$  spins determined by NMR was not significantly different from that measured by MRI in both short ( $p = 0.3648$ ) and long scans ( $p = 0.8541$ ). 4T1 cells did not label sufficiently with PFPE, as  $^{19}\text{F}$  content in  $1 \times 10^6$  cells was undetected by NMR. Thus,  $^{19}\text{F}$  imaging experiments with PFPE-labeled 4T1 cells did not continue.

In  $^{19}\text{F}$  images (with imaging time = 1.5 min/pellet), the range of  $256\text{--}1024 \times 10^3$  PFPE-labeled MSC were detected (Figure 23A) and  $^{19}\text{F}$  signal was strongly correlated with cell number ( $R^2 = 0.9983$ ) (Figure 22C). The average number of cells detected per voxel from these scans was  $1.30 \pm 0.51 \times 10^5$  cells/ $\text{mm}^3$ . The lowest cell number detected from these  $^{19}\text{F}$  scans was  $256 \times 10^3$  MSC ( $9.01 \times 10^{16}$   $^{19}\text{F}$  atoms, 30.21 mM), which was detected in 4 of 9 replicates with  $\text{SNR} > 5$ .  $^{19}\text{F}$  signal measured from  $1.024 \times 10^6$  MSC was significantly higher than signal measured from  $512 \times 10^3$  cells ( $p < 0.01$ ), which was higher than signal measured from  $256 \times 10^3$  cells ( $p < 0.05$ ) (Figure 23C).

With longer imaging times (4.5 min/pellet),  $^{19}\text{F}$  sensitivity was improved (Figure 23B) and the  $\text{SD}_{\text{noise}}$  was significantly reduced compared to 1.5 min/pellet scans ( $p < 0.0001$ ). The average number of cells detected per voxel from these scans was  $8.55 \pm 2.97 \times 10^4$  cells/ $\text{mm}^3$ . As few as  $128 \times 10^3$  MSC ( $4.51 \times 10^{16}$   $^{19}\text{F}$  atoms, 19.01 mM) were detected with  $\text{SNR} > 5$  in 3 of 9 replicates. Additionally,  $^{19}\text{F}$  signal with  $\text{SNR} > 5$  was detected in 7 of 9 replicates of  $256 \times 10^3$  MSC, which corresponds to  $9.01 \times 10^{16}$   $^{19}\text{F}$  atoms (28.01 mM). Significant differences in  $^{19}\text{F}$  signal were measured from 256, 512, and 1024 ( $\times 10^3$ ) MSC (Figure 23C). Furthermore, significantly more  $^{19}\text{F}$  signal was measured from  $1.024 \times 10^6$  cells when using longer imaging times (4.5 min/pellet) compared to 1.5 min/pellet ( $p < 0.01$ ).

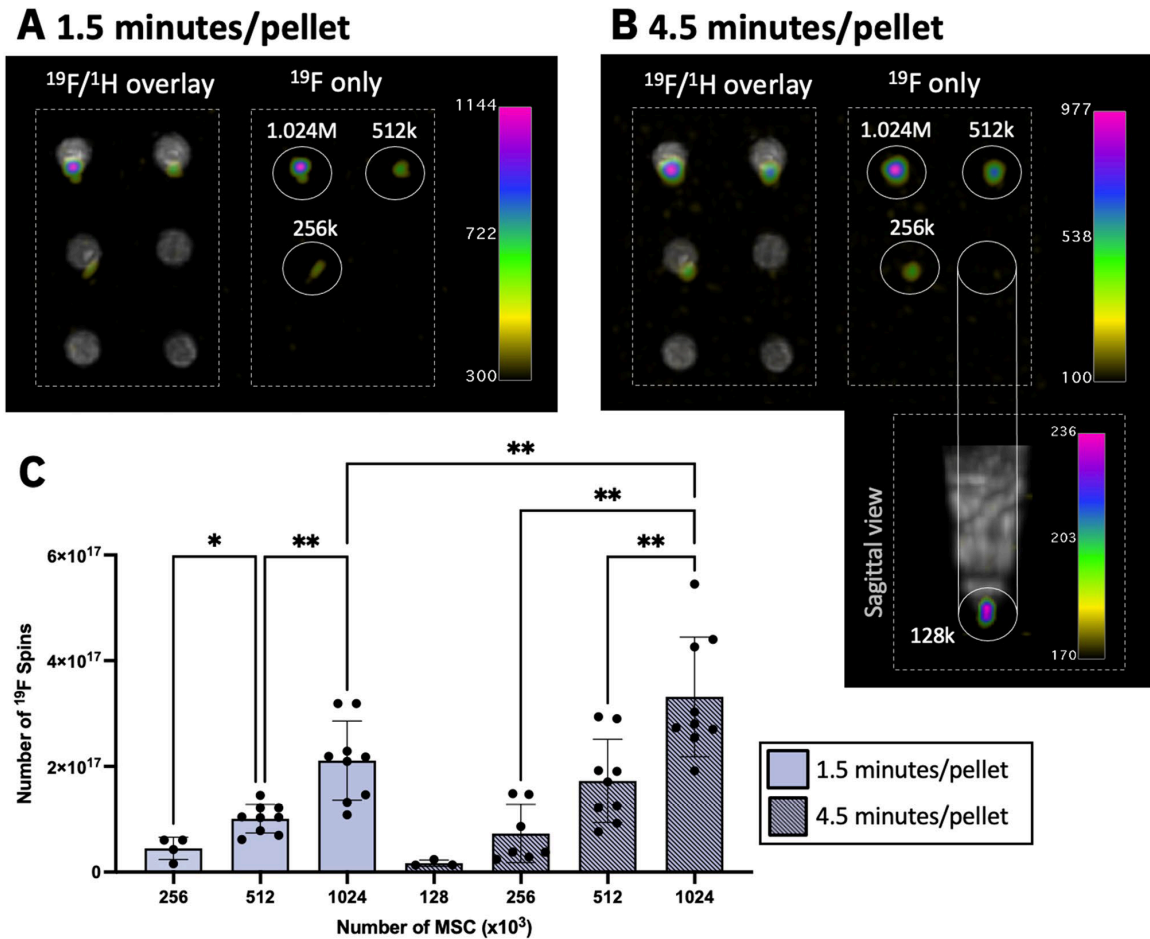


**Figure 23:  $^{19}\text{F}$  MRI detection of PFPE-labeled MSC. (A)  $^{19}\text{F}$  images of six samples with various cell numbers ( $M = 10^6$ ,  $k = 10^3$ ) imaged 1.5 min/pellet. As few as  $256 \times 10^3$  cells ( $9.01 \times 10^{16}$   $^{19}\text{F}$  atoms) could be detected with  $\text{SNR} > 5$ . (B) With longer imaging time (4.5 min/pellet), the detection of  $128 \times 10^3$  cells ( $4.51 \times 10^{16}$   $^{19}\text{F}$  atoms) was possible with  $\text{SNR} > 5$ . (C) Quantification revealed significant differences in  $^{19}\text{F}$  signal between different numbers of MSC (\* $p < .05$ , \*\* $p < .01$ ). Significantly more  $^{19}\text{F}$  signal was detected from  $1.024 \times 10^6$  cell samples with longer imaging times ( $p < .01$ ).**

### 3.3.3 In vivo sensitivity of MPI and $^{19}\text{F}$ MRI

A comparison between MPI signal from a cell pellet and cells *in vivo* was conducted with different injection routes (Figure 24A). These MSC were labeled with  $28.9 \pm 3.4$  pg iron/cell. Compared to a pellet of  $2 \times 10^6$  ferucarbotran-labeled MSC, MPI signal was only reduced by 5% with subcutaneous injection of these cells (Figure 24B,C). Quantification revealed the iron mass measured from the cell pellet ( $52.98 \mu\text{g}$ ) was similar to what was measured after subcutaneous injection ( $50.21 \mu\text{g}$ ). However, for  $1 \times 10^5$  MSC, *in vivo* MPI showed a reduction in MPI signal measured from MSC injected subcutaneously (49%), intraperitoneal (53%), and intravenous (15%), compared to signal from a pellet of  $1 \times 10^5$  MSC (Figure 24D,E). For  $1 \times 10^5$  MSC, the measured iron content was  $3.13 \mu\text{g}$  in the cell pellet, compared to  $1.52 \mu\text{g}$  after subcutaneous injection,  $1.66 \mu\text{g}$  after intraperitoneal injection, and  $0.48 \mu\text{g}$  after intravenous injection. Therefore, the iron content measured from  $1 \times 10^5$  cells *in vivo* was reduced compared to cells in the pellet, despite being the same number of cells. After mouse fasting, the background *in vivo* MPI signal from the mouse digestive system was  $25.8 \pm 10.0$  arbitrary units (A.U.) (shown Figure 24F). This background signal was accounted for in each mouse by signal subtraction, prior to calculation of MPI signal and iron mass measured from cells.



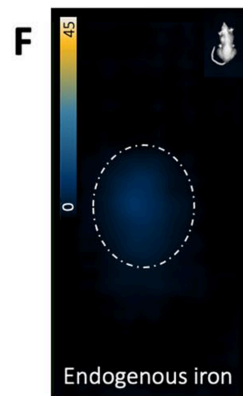
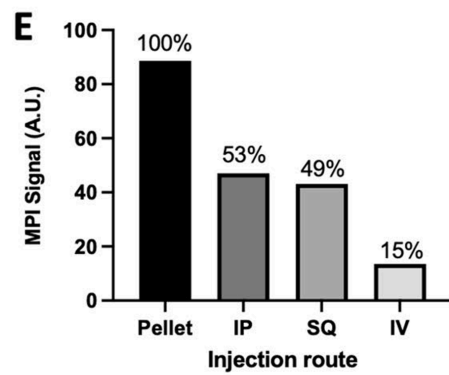
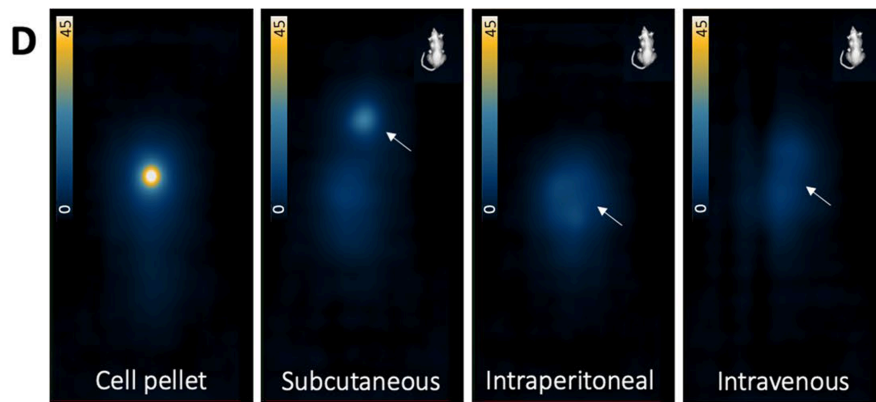
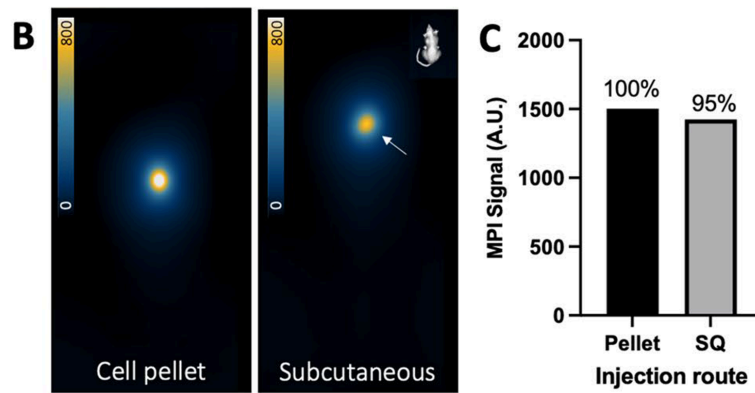
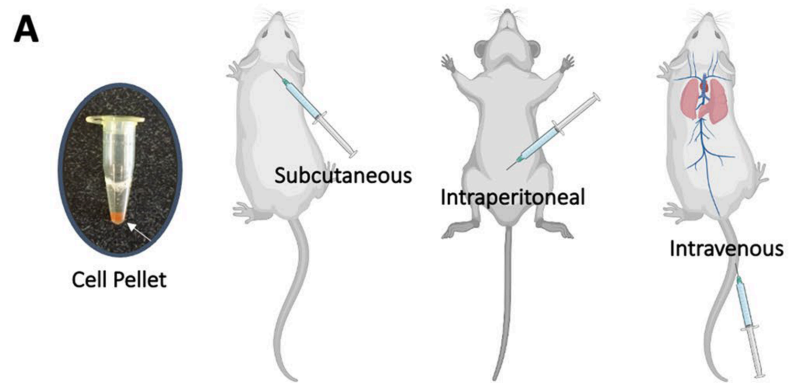


**Figure 24: (A) Cartoon showing subcutaneous (SQ), intraperitoneal (IP), and intravenous (IV) injection in mice. (B) Comparison of MPI signal from 2D scans of  $2 \times 10^6$  ferucarbotran-labeled MSC in a cell pellet to subcutaneous injection. (C) Measured MPI signal from  $2 \times 10^6$  MSC was similar *in vivo* and *ex vivo*. (D) Detection in 2D of  $1 \times 10^5$  ferucarbotran-labeled MSC as a cell pellet and after subcutaneous, intraperitoneal, and intravenous injection. (E) Measured MPI signal from  $1 \times 10^5$  cells is reduced *in vivo* compared to signal in the pellet. (F) Some background MPI signal exists owing to iron in mouse digestion. This signal was minimized with 12-h fasting and accounted for by subtracting pre-injection signal from post-injection signal for each mouse.**

The detection of  $2 \times 10^6$   $^{19}\text{F}$ -labeled MSC *in vivo* was compared to MSC in a pellet (Figure 25). Reduced  $^{19}\text{F}$  signal (72%) was detected from MSC following subcutaneous injection (Figure 25A). After intraperitoneal injection, the same number of cells were dispersed and appeared as lower intensity  $^{19}\text{F}$  signal (Figure 25B), however higher  $^{19}\text{F}$  signal was measured from these cells compared to the pellet by 6.65 times (Figure 25D).  $1 \times 10^5$  MSC administered subcutaneously were undetected as this cell number is below the detection limit (Figure 25C).

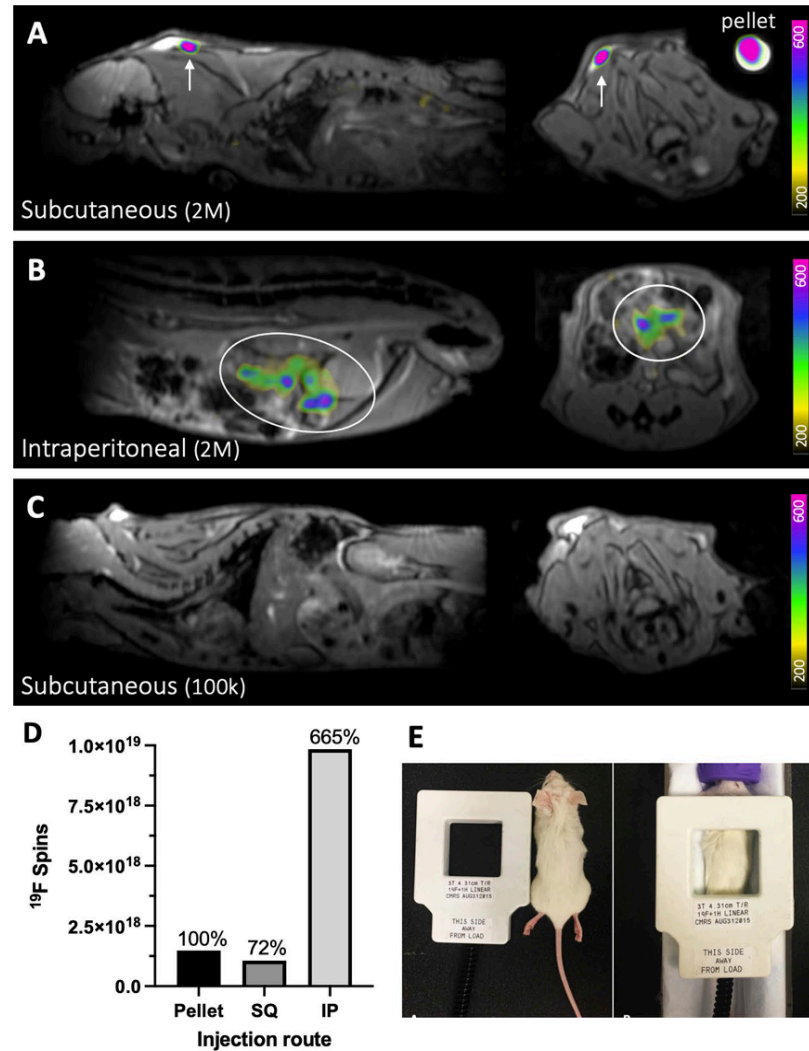


**Figure 25: Detection of  $2 \times 10^6$  PFPE-labeled MSC *in vivo*.  $^{19}\text{F}$  signal is detected at the injection site following (A) subcutaneous injection (white arrows) and (B) intraperitoneal injection (white ovals). A cell pellet of the same cell number was imaged alongside the mouse for comparison (shown in A). (C) After subcutaneous administration,  $1 \times 10^5$  cells were undetected, as this cell number is below the detection threshold for MSC. Images are sagittal (left) and axial (right). M = million, k = thousand. (D)  $^{19}\text{F}$  signal measured from  $2 \times 10^6$  cells injected subcutaneous (SQ) was reduced compared to signal measured from the cell pellet, however, elevated  $^{19}\text{F}$  signal was measured from cells following intraperitoneal (IP) injection. (E) The dual-tuned surface coil is approximately the same size as a mouse and is placed directly over the injection site for imaging.**

### 3.4 Discussion

In this study, we began with an evaluation of *in vitro* sensitivity for MPI and  $^{19}\text{F}$  MRI of cells using ferucarbotran and PFPE nanoemulsions as labeling agents (respectively). Overall, fewer MSC were detected using MPI (4000) compared to  $^{19}\text{F}$  MRI (256,000) using the same imaging time (1.5 min per cell pellet). Compared to ferucarbotran-labeled MSC, more 4T1 cells were required for MPI detection (8000) as a result of lower cell uptake of ferucarbotran. These limits were defined with imaging criteria  $\text{SNR} > 5$  and tested with 9 replicates to provide confidence.

These measurements of lowest cell number detected with MPI and  $^{19}\text{F}$  MRI are reasonable based on previous reports. As described earlier, Zheng *et al.*<sup>7</sup> achieved detection of approximately 1000 ferucarbotran-labeled human embryonic stem cells (27 pg/cell, 27 ng) with  $\text{SNR} > 5$ . Our MSC detection limit was higher (4000 cells or 76 ng) and this is resulting from differences in MPI systems and acquisition. The amount of iron we detected (76 ng) is consistent with findings by Liu *et al.*<sup>19</sup>, where 64 ng ferucarbotran could be detected with mean  $\text{SNR}$  of 3.6, using another MOMENTUM MPI system and the same 2D imaging parameters. With longer imaging times in 3D, we demonstrated a minimum of 1000 ferucarbotran-labeled MSC (19 ng) could be visualized with  $\text{SNR} > 3$ . To the best of our knowledge, this is the lowest report of ferucarbotran detected from labeled cells. This study was the first to measure MPI detection limits for iron-loaded cancer cells (in 3D, as few as 4000 4T1 cells were detected, or 37 ng iron).

Previous investigation into  $^{19}\text{F}$  detection limits at 3 T were conducted in dendritic cells ( $3.7 \times 10^{12} \text{ }^{19}\text{F}/\text{cell}$ )<sup>9</sup> and macrophages ( $7.93 \times 10^{11} \text{ }^{19}\text{F}/\text{cell}$ )<sup>11</sup>, which have greater uptake of PFPE than what we measured in MSC ( $3.52 \times 10^{11} \text{ }^{19}\text{F}/\text{cell}$ ). Ahrens *et al.*<sup>9</sup> established an *in vitro*  $^{19}\text{F}$  MRI detection limit of  $1.0 \times 10^5$  dendritic cells/voxel on a 3 T clinical scanner using a  $2.5 \times \text{SD}_{\text{noise}}$  threshold. Similarly, we achieved detection of  $1.30 \times 10^5$  MSC/voxel (1.5 min/pellet) and  $8.55 \times 10^4$  MSC/voxel in longer scans (4.5 min/pellet) using a  $5 \times \text{SD}_{\text{noise}}$  threshold. In our previous work at 3 T, as few as 25,000 murine macrophages were detected ( $2.27 \times 10^4$  cells/voxel) with longer imaging time<sup>11</sup>.

Cell labeling is fundamental in determining cellular sensitivity for both MPI and  $^{19}\text{F}$  MRI. We previously discussed factors that impact labeling efficiency with SPIONs<sup>20</sup>. In this study, we observed enhanced MPI detectability of MSCs compared to breast cancer cells, owing to increased endocytosis of SPION. Likewise, 4T1 cells did not label with PFPE sufficiently for  $^{19}\text{F}$  MRI detection. Increased uptake of SPION/PFPE is expected in phagocytic cells and cells which have a larger cytoplasmic volume<sup>21</sup>, such as macrophages and dendritic cells. Although MSC is considered a non-phagocytic cell type<sup>22</sup>, enhanced labeling compared to breast cancer cells has been observed with SPIONs<sup>15</sup> and PFPE<sup>10</sup>. The cell labeling protocols used in this study use commonly used concentrations of ferucarbotran and PFPE for cell labeling and have been well established. We, and other groups, have not observed compromises in cell viability or function at these labeling concentrations, even in delicate cell types<sup>12,13,23–27</sup>. In the current study, we use transfection agents to facilitate uptake of ferucarbotran. It is expected that SPION surface modifications will be improve labeling efficiency without transfection agents<sup>8,28</sup>. Further improvements to PFPE nanoemulsions will enhance  $^{19}\text{F}$  cellular sensitivity, such as incorporation of paramagnetic agents<sup>29,30</sup>, or the addition of surface modifications to enhance the uptake of PFPE nanoemulsions<sup>31</sup>.

We recognize it is impossible to directly compare cell detection with MPI and  $^{19}\text{F}$  MRI due to their inherent differences, including structural configurations and imaging parameters. For this study, we attempted to optimize unique aspects of each modality in favor of sensitivity. MPI of cells was conducted using weak gradients (3 T/m) to increase the size of the FFR and enhance sensitivity. For FFL (line) MPI, the use of weak gradients (3 T/m) compared to stronger gradients (*e.g.*, 6 T/m) expands the volume of FFR. This leads to enhancement in sensitivity, at the cost of reduced resolution. It is also expected that signal averaging would improve sensitivity, however this has not been studied for MPI. In 2D, a significant reduction in background noise was measured with 8 averages compared to 1 average, however, this did not improve cell detection with MPI, as we defined it. 3D imaging using 35 projections did offer improvement in sensitivity for both ferucarbotran-labeled MSC (detection of 2000 cells) and breast cancer cells (4000 cells). Lastly, optimization of excitation amplitudes may lead to improved cell sensitivity; in this study we used 22 mT (X-channel) and 26 mT (Z-channel) by default.

$^{19}\text{F}$  MRI of PFPE-labeled cells was conducted at a clinical field strength (3 T). The implementation of the surface coil and optimized 3D bSSFP sequence is crucial to enable  $^{19}\text{F}$  cell tracking at 3 T. The theoretical optimal flip angle for  $^{19}\text{F}$  at 3 T is  $72^\circ$  and our investigation showed highest SNR was produced for flip angles between  $60\text{--}80^\circ$ . However, transmit/receive surface coils provide non-uniform sensitivity, due to spatial variations in applied energy and flip angle<sup>32,33</sup>. For this reason, cell pellets were imaged directly in the center of the coil to maximize sensitivity. Likewise, the surface coil was placed directly above the region of interest for *in vivo*  $^{19}\text{F}$  imaging. High signal averaging was used for  $^{19}\text{F}$  image acquisition (115) to improve SNR. Longer imaging times with 345 signal averages enabled detection of 3 additional pellets of  $256 \times 10^3$  cells and 3 of 9 pellets of  $128 \times 10^3$  PFPE-labeled MSC.

After assessing *in vitro* cell detection limits of MPI and  $^{19}\text{F}$  MRI, a preliminary assessment of *in vivo* detection factors was conducted. It has previously been shown that there is no attenuation of MPI signal from biological tissue<sup>34,35</sup>. In agreement, following subcutaneous injection of  $2 \times 10^6$  MSC, we measured only a small reduction in cell detection with MPI (5%). However, for a lower cell number ( $1 \times 10^5$ ), there was reduction of signal measured *in vivo* compared to the pellet (by 47–85%, depending on injection route). Here we recognize that the dispersion of cells from the injection site reduces the cell density per voxel, leading some cells to fall below the intravoxel detection limit. MPI detection of MSC was most reduced after intravenous injection (85% reduction). It is expected that cells administered intravenously would be most disperse as they circulate through the venous circulation before accumulating in the lung capillaries (shown in Figure 24A). Similarly, previous work by Wang *et al.*<sup>8</sup> showed that  $1 \times 10^5$  ferucarbotran-labeled stem cells could be detected with MPI *in vivo* following subcutaneous injection but not following intravenous injection. In our study, we could achieve detection of  $1 \times 10^5$  cells after intravenous injection, which can be attributed to the choice of gradient strength (3.0 T/m vs. 5.7 T/m).

Likewise for  $^{19}\text{F}$  MRI, dispersion of PFPE-labeled cells ( $1 \times 10^6$ ) in patients was previously reported to limit the detectability of these cells following administration<sup>9</sup>. In our study,  $^{19}\text{F}$  signal detected from a cell pellet of  $2 \times 10^6$  PFPE-labeled MSC was higher

than  $^{19}\text{F}$  signal from the same number of cells injected subcutaneously. Conversely,  $^{19}\text{F}$  signal measured from cells injected to the intraperitoneal space was overestimated. This result could be explained by the large quantification region, as  $^{19}\text{F}$  density per imaging voxel was  $3.79 \times 10^{16} \text{ }^{19}\text{F}/\text{mm}^3$  for cells in a pellet, compared to  $2.03 \times 10^{16} \text{ }^{19}\text{F}/\text{mm}^3$  for cells *in vivo*.

For both MPI and MRI, there are other important considerations which reduce detectability of cells *in vivo*. For MPI, this includes increased background signal associated with mouse digestion<sup>36</sup>. While we accounted for background signal in the mouse using signal subtraction, this technique is not permissible for longitudinal cell tracking studies. Background signal is variable across mice and day-to-day. In our experience, this can be reduced by mouse fasting, however, the amount of signal is unpredictable. Ultimately this background signal may obscure detection of cells, especially in low cell numbers<sup>37</sup>, as it is challenging (at this time, impossible) to distinguish the signal associated with cells from background. Second, there is some evidence that Brownian relaxation of SPION in different tissue environments may be altered, leading to reduced MPI sensitivity<sup>38-40</sup>. Brownian motion refers to the physical rotation of SPIONs; this motion is reduced in tissues with increased stiffness (*e.g.*, muscle) which leads to increased Brownian relaxation times (thus, lower sensitivity and resolution). Ongoing work aims to determine whether this plays a role in the detection of SPION-labeled cells. Another consideration affecting  $^{19}\text{F}$  detection of PFPE-cells *in vivo* is the coil filling factor. The volume of a mouse is much larger than the volume of a cell pellet, thus SNR for detection of cells *in vivo* is expected to be reduced due to increased image noise. Lastly, mouse breathing motion can lead to blurring of signal which will reduce the maximum signal intensity associated with cells and could potentially render cells undetected by MRI and MPI.

### 3.5 Conclusion

MPI has the potential to be more sensitive than  $^{19}\text{F}$  MRI for cell tracking. In this study, commonly used cell labeling agents, ferucarbotran and perfluoropolyether nanoemulsions, were used to label MSC and 4T1 cells to assess cellular sensitivity of MPI and  $^{19}\text{F}$  MRI, respectively. Fewer MSC (4000 cells, 76 ng iron) were detected with MPI than  $^{19}\text{F}$  MRI (256,000 cells,  $9.01 \times 10^{16}$   $^{19}\text{F}$  atoms), using the same scan time. Furthermore, reduced ferucarbotran labeling was observed in 4T1 breast cancer cells compared to MSC, leading to a detection limit of 8000 breast cancer cells (74 ng iron). With longer imaging times, as few as 2000 MSC (38 ng ferucarbotran) and 4000 breast cancer cells (37 ng ferucarbotran) were detected with MPI and 128,000 MSC ( $4.51 \times 10^{16}$   $^{19}\text{F}$  atoms) were detected with  $^{19}\text{F}$  MRI with  $\text{SNR} > 5$ . Determination of these detection thresholds *in vitro* is useful to anticipate the minimum number of cells that are required for detection *in vivo*. However, we demonstrated that there are several factors *in vivo* which led to reduced detectability of cells, particularly the effect of cell dispersion which reduces cell density per imaging voxel. There is no doubt that cellular sensitivity for these modalities will continue to improve with further developments. It is essential to understand and improve cellular sensitivity to advance imaging of cellular therapeutics.

### 3.6 Chapter 3 references

1. Bulte, J. W. M. & Daldrup-Link, H. E. Clinical Tracking of Cell Transfer and Cell Transplantation: Trials and Tribulations. *Radiology* (2018).  
doi:10.1148/radiol.2018180449
2. Clinicaltrials.gov.
3. Daldrup-Link, H. E. *et al.* Detection of stem cell transplant rejection with ferumoxytol MR imaging: Correlation of MR imaging findings with those at intravital microscopy. *Radiology* **284**, 495–507 (2017).



4. Tay, Z. W., Hensley, D. W., Vreeland, E. C., Zheng, B. & Conolly, S. M. The Relaxation Wall: Experimental Limits to Improving MPI Spatial Resolution by Increasing Nanoparticle Core size. *Biomed Phys End Express* **3**, 1–21 (2017).
5. Bauer, L. M., Situ, S. F., Griswold, M. A. & Samia, A. C. S. Magnetic Particle Imaging Tracers: State-of-the-Art and Future Directions. *J. Phys. Chem. Lett.* **6**, 2509–2517 (2015).
6. Eberbeck, D., Wiekhorst, F., Wagner, S. & Trahms, L. How the size distribution of magnetic nanoparticles determines their magnetic particle imaging performance. *Appl. Phys. Lett.* **98**, 1–4 (2011).
7. Zheng, B. *et al.* Magnetic particle imaging tracks the long-term fate of in vivo neural cell implants with high image contrast. *Sci. Rep.* **5**, 1–9 (2015).
8. Wang, Q. *et al.* Artificially Engineered Cubic Iron Oxide Nanoparticle as a High-Performance Magnetic Particle Imaging Tracer for Stem Cell Tracking. *ACS Nano* **14**, 2053–2062 (2020).
9. Ahrens, E. T., Helfer, B. M., O’Hanlon, C. F. & Schirda, C. Clinical cell therapy imaging using a perfluorocarbon tracer and fluorine-19 MRI. *Magn. Reson. Med.* **72**, 1696–1701 (2014).
10. Srinivas, M., Boehm-Sturm, P., Figdor, C. G., de Vries, I. J. & Hoehn, M. Labeling cells for in vivo tracking using <sup>19</sup>F MRI. *Biomaterials* **33**, 8830–8840 (2012).
11. Makela, A. V. & Foster, P. J. Preclinical <sup>19</sup>F MRI cell tracking at 3 Tesla. *Magn. Reson. Mater. Physics, Biol. Med.* **32**, 123–132 (2019).
12. Zhang, X. *et al.* Cellular magnetic resonance imaging of monocyte-derived dendritic cell migration from healthy donors and cancer patients as assessed in a scid mouse model. *Cytotherapy* **13**, 1234–1248 (2011).

13. Fink, C. *et al.* <sup>19</sup>F-perfluorocarbon-labeled human peripheral blood mononuclear cells can be detected in vivo using clinical MRI parameters in a therapeutic cell setting. *Sci. Rep.* **8**, 1–13 (2018).
14. Thu, M. S. *et al.* Self-Assembling Nanocomplexes by combining Ferumoxytol, Heparin And Protamine For Cell Tracking by MRI HHS Public Access Author manuscript. *Nat Med* **18**, 463–467 (2012).
15. Mcfadden, C., Mallett, C. L. & Foster, P. J. Labeling of multiple cell lines using a new iron oxide agent for cell tracking by MRI. *Contrast Media Mol. Imaging* (2011). doi:10.1002/cmml.456
16. Scheffler, K. & Lehnhardt, S. Principles and applications of balanced SSFP techniques. *Eur. Radiol.* **13**, 2409–2418 (2003).
17. Rose, A. The sensitivity performance of the human eye on an absolute scale. *J. Opt. Soc. Am.* **38**, 196–208 (1948).
18. Bouchlaka, M. N. *et al.* <sup>19</sup>F-MRI for monitoring human NK cells in vivo. *Oncoimmunology* **5**, 1–12 (2016).
19. Liu, S. *et al.* Long circulating tracer tailored for magnetic particle imaging. *Nanotheranostics* **5**, 348–361 (2021).
20. Sehl, O. C., Gevaert, J. J., Melo, K. P., Knier, N. N. & Foster, P. J. A perspective on cell tracking with magnetic particle imaging. *Tomography* **6**, (2020).
21. Ahrens, E. T. & Bulte, J. W. M. Tracking immune cells in vivo using magnetic resonance imaging. *Nat. Rev. Immunol.* **13**, (2013).
22. Moonshi, S. S. *et al.* A unique <sup>19</sup>F MRI agent for the tracking of non phagocytic cells: In vivo. *Nanoscale* **10**, 8226–8239 (2018).
23. Fink, C. *et al.* Quantification and characterization of granulocyte macrophage colony-stimulating factor activated human peripheral blood mononuclear cells by

- fluorine-19 cellular MRI in an immunocompromised mouse model. *Diagn. Interv. Imaging* (2020). doi:10.1016/j.diii.2020.02.004
24. Fink, C. *et al.* Fluorine-19 Cellular MRI Detection of In Vivo Dendritic Cell Migration and Subsequent Induction of Tumor Antigen-Specific Immunotherapeutic Response. *Mol. Imaging Biol.* **19**, (2019).
  25. de chickera, S. *et al.* Cellular MRI as a suitable, sensitive non-invasive modality for correlating in vivo migratory efficiencies of different dendritic cell populations with subsequent immunological outcomes. *Int. Immunol.* **24**, 29–41 (2012).
  26. Rivera-rodriguez, A. *et al.* Tracking Adoptive T Cell Therapy Using Magnetic Particle Imaging. *Nanotheranostics* **5**, 431–444 (2021).
  27. Parkins, K. M., Melo, K. P., Chen, Y., Ronald, J. A. & Foster, P. J. Visualizing tumour self-homing with magnetic particle imaging. *Nanoscale* **13**, 6016–6023 (2021).
  28. Lu, C. *et al.* Engineering of magnetic nanoparticles as magnetic particle imaging tracers. *Chem. Soc. Rev.* **50**, 8102–8146 (2021).
  29. Jahromi, A. H. *et al.* Fluorous-Soluble Metal Chelate for Sensitive Fluorine-19 Magnetic Resonance Imaging Nanoemulsion Probes Amin. *ACS Nano* **13**, 143–151 (2019).
  30. Rho, J. *et al.* Paramagnetic Fluorinated Nanoemulsions for in vivo F-19 MRI. *Mol. Imaging Biol.* **22**, 665–674 (2020).
  31. Hingorani, D. V. *et al.* Cell penetrating peptide functionalized perfluorocarbon nanoemulsions for targeted cell labeling and enhanced fluorine-19 MRI detection. *Magn. Reson. Med.* **83**, 974–987 (2020).
  32. Vernikouskaya, I., Pochert, A., Lindén, M. & Rasche, V. Quantitative <sup>19</sup>F MRI of perfluoro-15-crown-5-ether using uniformity correction of the spin excitation and signal reception. *Magn. Reson. Mater. Physics, Biol. Med.* **32**, 25–36 (2019).

33. Mihara, H., Iriguchi, N. & Ueno, S. A method of RF inhomogeneity correction in MR imaging. *Magn. Reson. Mater. Physics, Biol. Med.* **7**, 115–120 (1998).
34. Zheng, B. *et al.* Quantitative magnetic particle imaging monitors the transplantation, biodistribution, and clearance of stem cells in vivo. *Theranostics* (2016). doi:10.7150/thno.13728
35. Saritas, E. U. *et al.* Magnetic particle imaging (MPI) for NMR and MRI researchers. *J. Magn. Reson.* **229**, 116–126 (2013).
36. Sehl, O. C., Makela, A. V., Hamilton, A. M. & Foster, P. J. Trimodal Cell Tracking In Vivo: Combining Iron- and Fluorine-Based Magnetic Resonance Imaging with Magnetic Particle Imaging to Monitor the Delivery of Mesenchymal Stem Cells and the Ensuing Inflammation. *Tomogr. (Ann Arbor, Mich.)* **5**, 367–376 (2019).
37. Boberg, M. *et al.* Simultaneous imaging of widely differing particle concentrations in MPI: problem statement and algorithmic proposal for improvement. *Phys. Med. Biol.* (2021).
38. Arami, H., Ferguson, R. M., Khandhar, A. P. & Krishnan, K. M. Size-dependent ferrohydrodynamic relaxometry of magnetic particle imaging tracers in different environments. *Med. Phys.* **40**, 1–14 (2013).
39. Utkur, M., Muslu, Y. & Saritas, E. U. Relaxation-based color magnetic particle imaging for viscosity mapping. *Appl. Phys. Lett.* **115**, (2019).
40. Draack, S. *et al.* Multiparametric Magnetic Particle Spectroscopy of CoFe<sub>2</sub>O<sub>4</sub> Nanoparticles in Viscous Media. *J. Phys. Chem. C* **123**, 6787–6801 (2019).

## Chapter 4

### 4 MPI region of interest (ROI) analysis and quantification of iron in different volumes<sup>∇</sup>

MPI directly detects superparamagnetic iron oxides (SPIONs), which should enable precise, accurate, and linear quantification. However, selecting a region of interest (ROI) has strong effects on MPI quantification results. Ideally, ROI selection should be simple, user-independent, and widely applicable. In this work, we describe and compare four MPI ROI selection methods and assess their performance *in vitro* and *in vivo*. To explore the effect of ROI selection, ten ferucarbotran phantoms were imaged, each contained the same amount of iron but varied in volume. Three users tested the accuracy of the ROI methods for quantification of these samples. Lastly, the four ROI methods were applied to quantify ferucarbotran *in vivo* after intravenous, intramuscular, and subcutaneous injections in mice. We discuss the strengths and limitations of each ROI method, such as the ability to capture MPI signals of custom shapes, degree of user variability, speed of analysis, and quantification accuracy of SPIONs in different volumes.

---

<sup>∇</sup> This chapter was previously published and is included here with permission: [Sehl, Olivia C., Brice Tiret, Maryam A. Berih, Patrick Goodwill, and Paula J. Foster. MPI region of interest \(ROI\) analysis and quantification of iron in different volumes. \*International Journal of Magnetic Particle Imaging\*, 2022; 8\(1\).](#)

## 4.1 Introduction

Magnetic particle imaging (MPI) is a quantitative modality that directly detects superparamagnetic iron oxide nanoparticles (SPIONs). MPI quantification of SPIONs provides unique opportunities in tracking cell therapies, imaging inflammation, and magnetic hyperthermia. MPI can be used to track and quantify adoptive cells as they move within the body by first labeling them with SPIONs *in vitro*<sup>1-4</sup>. Here, quantification is necessary to understand the success of adoptive cell therapies which rely on a sufficient number of cells arriving at a target site while minimizing off-target accumulation of cells. Development of SPIONs for imaging inflammatory sites is another area of research requiring robust quantification<sup>5-7</sup>. SPIONs are administered intravenously and are internalized by phagocytic cells at inflammatory sites and in the reticuloendothelial system (liver, spleen, bone marrow, and lymph nodes)<sup>5,6,8,9</sup>. Quantification of inflammatory cells within these sites can be used to assess the degree of inflammation, the response to immunomodulatory therapies<sup>9,10</sup> and the density of tumor-associated macrophages (TAMs)<sup>11-13</sup>. MPI-guided magnetic hyperthermia involves exciting SPIONs with alternating magnetic fields, within a region defined by stronger gradient fields. Precise localization and quantification of SPIONs in the specified region is necessary to apply a specific heating prescription, as described<sup>14-16</sup>.

Our development of cell tracking techniques<sup>3</sup> has identified a demand for standardized, reproducible, and accurate quantification methods for MPI. *In vivo*, SPIONs can be dispersed in larger volumes (*e.g.*, a tumor, 1 cm<sup>3</sup>), whereas MPI quantification is conducted using calibration samples, of known amounts of iron, typically in small fluid volumes (~ 10  $\mu$ L). Careful and rigorous choice of the region of interest (ROI) is thus essential for quantification. Previous work by Hayat *et al.*<sup>17</sup> used a K-means++ machine learning algorithm for segmentation of ROIs and demonstrated accurate quantification of transplanted ferucarbotran-labeled cells *in vivo*. However, for some MPI users without such computational background, more straightforward methods would be of value.

Positron emission tomography (PET) is another imaging modality that provides hotspot images with direct quantification. Quantification of PET signals are typically conducted

by reporting the maximum standard uptake value (SUV). There is concern that the maximum value does not represent the signal(s) of interest and this is discussed particularly in the application of heterogeneous tumors with distributed PET signals. There are similar concerns for MPI as the distribution of SPIONs can influence the maximum value of the point spread function (PSF). Additional methods for PET quantification involve ROIs defined by manual delineations<sup>18,19</sup>, anatomical scans (whole organ segmentations)<sup>20</sup>, fixed diameter circular ROI<sup>18</sup>, or an ROI threshold defined as a percentage of the maximum signal<sup>18,19</sup>, however these are not routine clinical practices. Importantly, the quantitative outcome for PET is dependent on the method of ROI selection, involving the size, shape, and placement of the ROI. This has been a concern for several decades<sup>21</sup>.

Many of these ROI selection methods used for PET have been used for MPI. A common method for ROI definition with MPI has been to select pixels which are a percentage of the maximum value (e.g. 50% maximum)<sup>22-27</sup>. Other groups have used manual delineations of MPI signal<sup>5,28,29</sup>, fixed circular ROIs<sup>7,30-33</sup>, or standard thresholding<sup>17,34,35</sup>. These ROIs have been applied to MPI images with both field free line (FFL) and field free point (FFP) acquisitions, with X-space reconstruction and other methods. For quantification of stenosis there are unique methods described<sup>36</sup>. For MPI, the PSF extends beyond the borders of the SPION source and the extent of this depends on many factors, including the SPION resolution, amount of SPION, and the acquisition and reconstruction methods. In this paper, we hope to expand the toolbox for MPI quantification, by describing and directly comparing four methods of ROI selection, including both custom and ‘one-size-fits-all’ approaches.

#### 4.1.1 Study objectives

We first developed four unique ROI selection methods and assessed their linearity of quantification using *in vitro* ferucarbotran phantoms. We then evaluated the inter-user reproducibility of these ROI methods. Lastly, these methods were applied to quantify SPIONs that were administered locally or systemically in mice.

## 4.2 Methodology

### 4.2.1 *In vitro* sample preparation and imaging

Ten ferucarbotran phantoms (Vivotrax<sup>TM</sup>, 5.5  $\mu\text{g Fe}/\mu\text{L}$ , Magnetic Insight Inc., Alameda, CA, USA) were prepared, each containing the identical amount of iron (34.4  $\mu\text{g}$ ) mixed with increasing volumes of saline, up to 1.2 mL (Table 4). These samples were imaged in a 1.5 mL Eppendorf tube which is approximately 5 mm in diameter at the base. The tube widens to a diameter of 10 mm, therefore as saline is added to the sample the volume expands in all directions.

For MPI signal calibration, a separate series of calibration samples containing different, known amounts of ferucarbotran in the same fluid volume (range 0.34 – 55  $\mu\text{g Fe}$  in 10  $\mu\text{L}$ ) were prepared. An additional five samples of ferucarbotran (range 10 – 150  $\mu\text{g}$ ) were imaged for calibration of *in vivo* images (refer to part II.V for imaging protocol).

Each ferucarbotran sample was imaged separately using a MOMENTUM<sup>TM</sup> MPI system (Magnetic Insight Inc.). Images were acquired in 2D with a 6 cm x 6 cm field of view, 5.7 T/m selection field gradient, and drive field strengths of 20 mT and 26 mT in the X and Z axes, respectively. The images were reconstructed using x-space methods described<sup>37</sup>. Images from the X and Z planes were combined using signal averaging. The image pixels are 250 x 250  $\mu\text{m}$  and the resolution of a ferucarbotran point source using a 5.7 T/m gradient is expected to be 1.73 mm, based on MP relaxometry measurements<sup>38</sup>.



**Table 4: Ten samples created by dilution of ferucarbotran in different volumes of saline.**

<b>#</b>	<b>Total sample volume (<math>\mu\text{L}</math>)</b>	<b>Volume ratio (Vivotrax: saline)</b>	<b>Iron Concentration (<math>\mu\text{g}/\mu\text{L}</math>)</b>
<b>1</b>	6.25	1:0	5.500
<b>2</b>	12.5	1:1	2.750
<b>3</b>	25.0	1:3	1.375
<b>4</b>	50.0	1:7	0.688
<b>5</b>	100.0	1:15	0.344
<b>6</b>	200.0	1:31	0.172
<b>7</b>	400.0	1:63	0.086
<b>8</b>	600.0	1:95	0.057
<b>9</b>	800.0	1:127	0.042
<b>10</b>	1200.0	1:191	0.029

#### 4.2.2 ROI selection methods

All of the 2D images obtained were analyzed using four ROI selection methods using Horos imaging software (Annapolis, MD, USA). Each method is shown visually in Figure 26A and described in the sections below. For each ROI, the MPI signal (A.U.) was calculated as a product of average pixel value (A.U./ $\text{mm}^2$ ) and the ROI volume ( $\text{mm}^2$ ).

#### 4.2.2.1 Method 1: ROI threshold set by the maximum signal

An ROI was drawn at *pixel value*  $> \alpha \cdot s_{max}$ , where  $\alpha$  is a scaling factor  $< 1$  and  $s_{max}$  (A.U./mm<sup>2</sup>) is the maximum value for the signal of interest. We used  $\alpha = 0.1, 0.5$ , and  $0.7$  for *in vitro* analysis and  $\alpha = 0.5$  *in vivo*.

#### 4.2.2.2 Method 2: Circular ROI with the diameter determined visually, with scaling factor

A line profile was drawn through the maximum value of the signal of interest, and the distance between the two points of maximum curvature was estimated ( $\Delta x$ ) (see Figure 26B). This spatial distance was used to define a circular ROI with diameter  $d = b \cdot \Delta x$ , where  $b$  is a scaling factor  $> 1$  that increases the ROI diameter to account for user variability and capture more of the signal from the wide PSF. We used a scaling factor  $b = 2$ , and the peak signal of the ROI was visually centered on the maximum value of the signal of interest.

#### 4.2.2.3 Method 3: Large circular ROI

ROI diameters were measured for all images in the dataset using Method 2. Then, all images were quantified with the same circular ROI with diameter  $d = b \cdot \Delta x_{max}$ , where  $\Delta x_{max}$  is the largest ROI diameter in the dataset.

#### 4.2.2.4 Method 4: ROI threshold set by image noise characteristics

The standard deviation of system noise,  $SD$ , was measured by imaging an empty sample holder using the same image settings. A mask was generated that selected pixels with *pixel value*  $> c \cdot SD$ , where  $c$  is a multiplier chosen to select signal produced by the sample while rejecting noise produced by the imaging system. We used  $c = 5$  to select signals with Signal to Noise Ratios (SNR)  $> 5$  according to the Rose Criterion<sup>39</sup> for *in vitro* and *in vivo* datasets. Higher thresholds were also tested with  $c = 10$  and  $c = 25$  for *in vitro* ferucarbotran samples. This method makes the reasonable assumption that the system noise is similar in each image in the dataset.

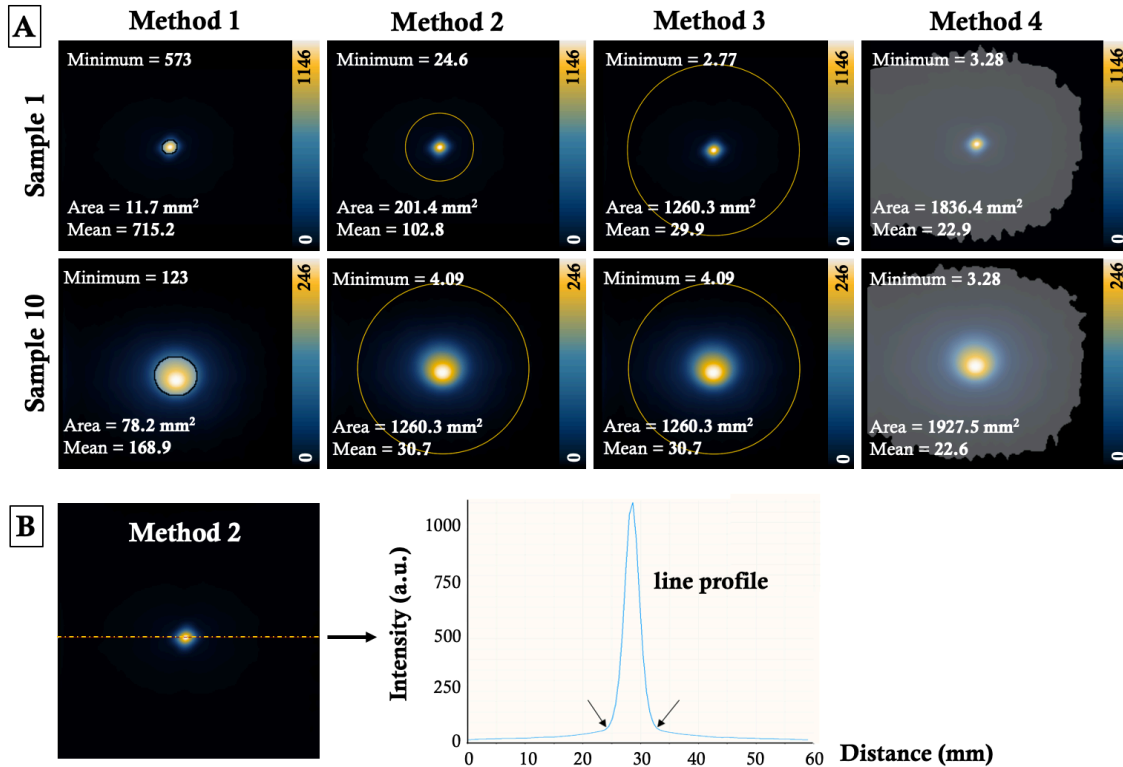


**Figure 26: (A) A demonstration of ROI methods 1 – 4 on two samples of ferucarbotran (Samples 1 and 10). The minimum value (a.u.), area (mm<sup>2</sup>), and mean value (a.u.) is recorded for each ROI. (B) A depiction of ROI selection method 2.**

#### 4.2.3 MPI signal calibration

After the MPI signal associated with calibration samples was measured, calibration lines were formed to determine the relationship between known iron mass ( $\mu\text{g}$ ) and MPI signal. A linear equation was obtained for each ROI selection method (MPI signal = slope \* iron mass) and the intercept of the line was set at (0,0). These equations were rearranged as:

$$\text{Estimated iron content } (\mu\text{g}) = \frac{\text{MPI signal (A.U.)}}{\text{Calibration slope}}$$

This equation was used to estimate the iron mass from ferucarbotran phantoms and ferucarbotran *in vivo* using each ROI method.

#### 4.2.4 Inter-user reproducibility

The ROI analysis (part II.II. and II.III) was repeated by 2 additional users on the same set of images. The pairwise differences in the user's measurements of iron mass were calculated, and for each ROI method, the average of these differences was determined. Bland-Altman plots were used to display the difference between user's measurements of iron mass compared to their average measurements. The absolute inter-user variability was calculated as the standard error of measurement (SEM):

$$SEM = SD (value\ 1, value\ 2, value\ 3)$$

SEM was calculated for each of the ten samples of ferucarbotran and the average SEM for each ROI method was reported. As an additional measurement, the coefficient of variation (CoV) was calculated as:

$$CoV\ (\%) = \frac{SEM}{Average\ (value\ 1, value\ 2, value\ 3)} * 100$$

and this value represents the relative interobserver variability. When the user's measurements are in perfect correspondence, SEM and CoV are equal to 0 (ref<sup>19</sup>).

#### 4.2.5 ROI selection for *in vivo* quantification

Two Nu/Nu mice were obtained and cared for per the standards of the Canadian Council on Animal Care, under an approved protocol by the Animal Use Subcommittee of Western University's Council on Animal Care.

The first mouse received 25 µg ferucarbotran by intramuscular point injection in the left hind limb. This mouse was imaged immediately before and after a second injection of 25 µg subcutaneously. The second mouse received 100 µg ferucarbotran intravenously and was imaged 20 hours later. Ferucarbotran is expected to accumulate predominately in the liver, and to a lesser extent the spleen<sup>7,23,40-42</sup>. Isotropic 2D MPI images were acquired using a 3.0 T/m selection field gradient, a larger field of view (12 x 6 cm), and the same

parameters listed in II.I. For a 3.0 T/m gradient, the image resolution for a ferucarbotran point source is expected to be 3.29 mm<sup>38</sup>. Separate calibration with ferucarbotran (10 – 150 µg) was conducted for these parameters and applied to *in vivo* images to quantify SPION mass, using the same methods described in II.III.

## 4.3 Results

### 4.3.1 MPI signal calibration

The MPI images of the calibration samples are visually similar in shape and primarily differ in signal amplitude (Figure 27A). This is due to all samples having the same volume but with different iron quantities. Quantification of calibration points from all methods resulted in a linear ( $R^2 > 0.998$ ) relationship between iron mass and measured MPI signal (Figure 27B). More MPI signal (steeper slope, m) was collected for methods with larger ROIs (*i.e.* Method 3 and 4). The linear equations for each quantification method are used to estimate the iron contents of the *in vitro* and *in vivo* samples.

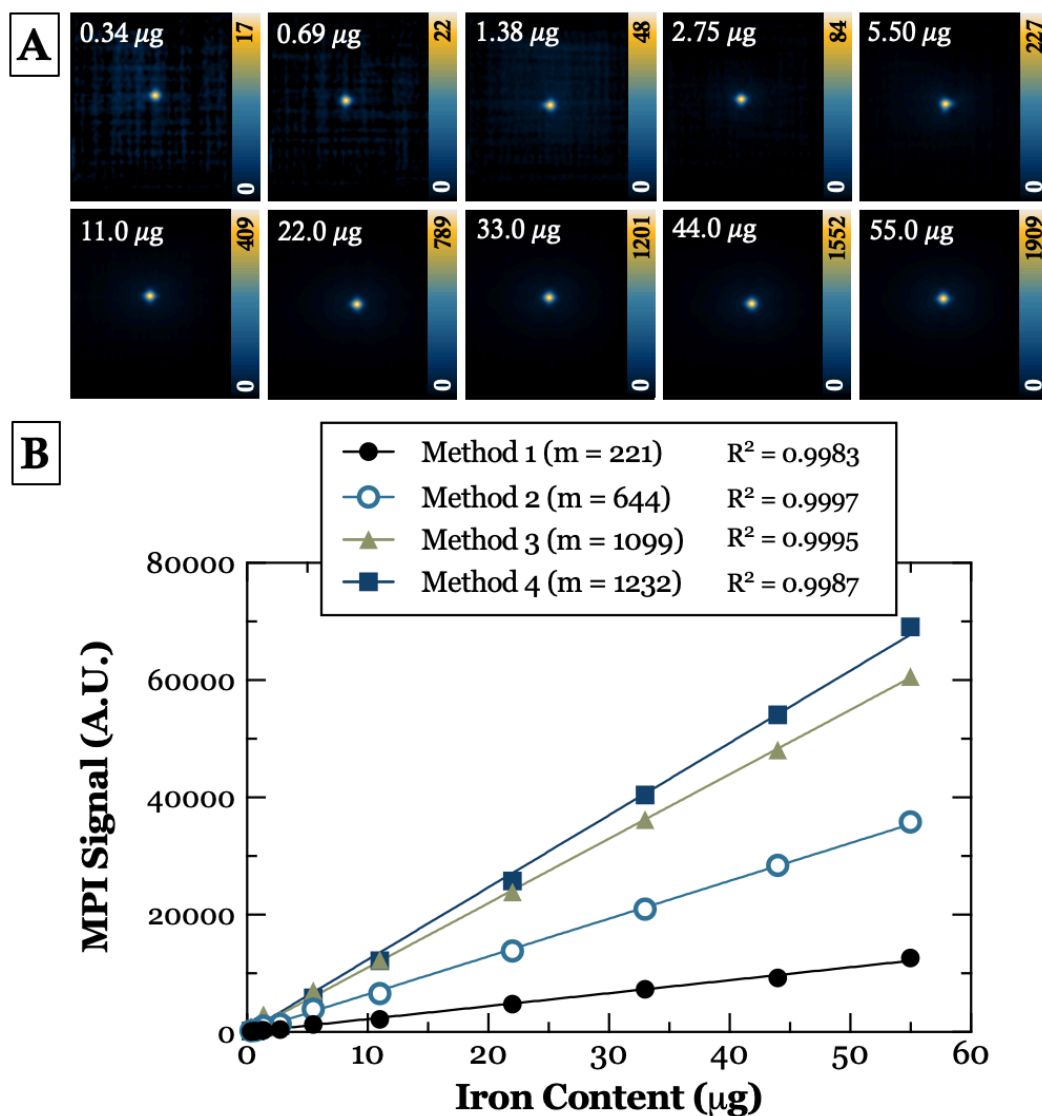
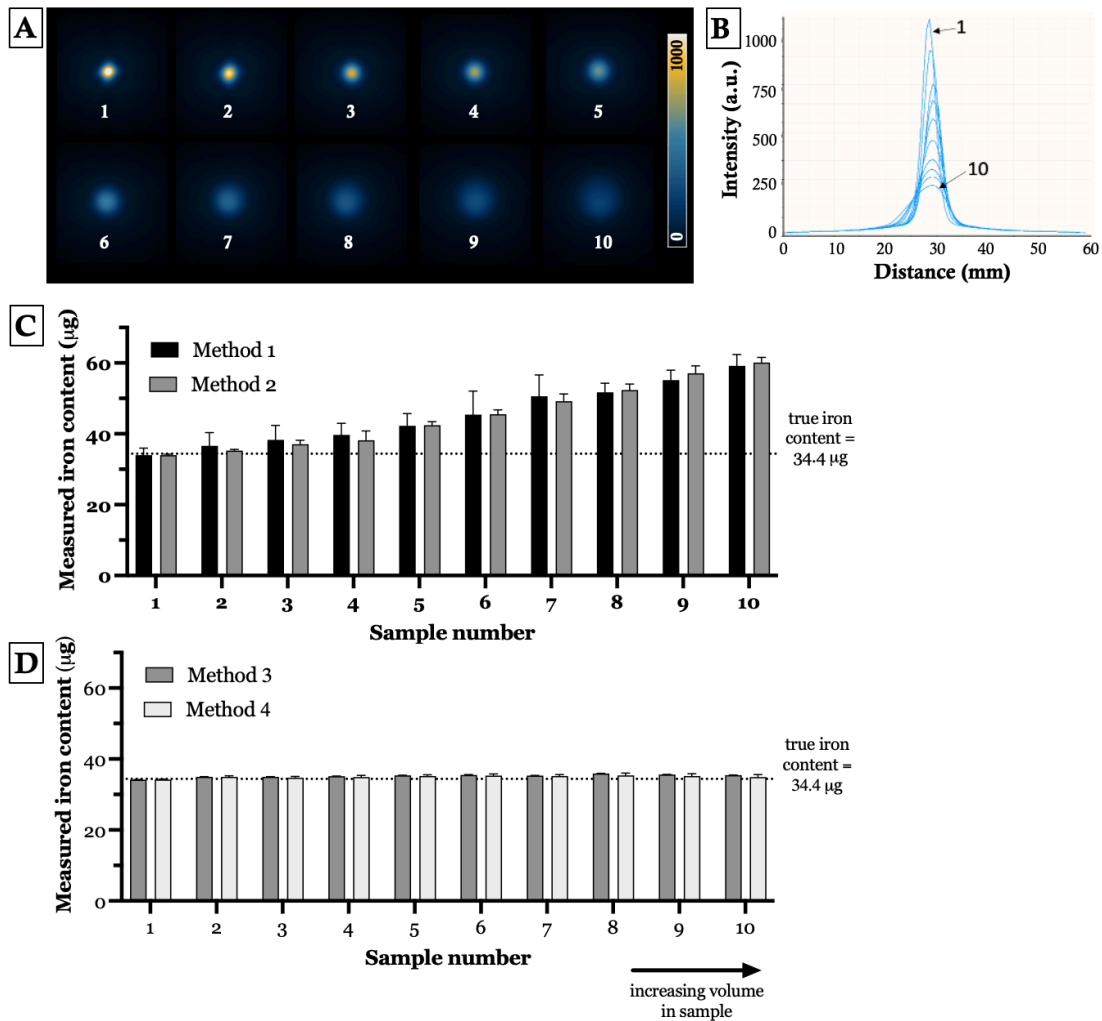


Figure 27: (A) MPI calibration performed by imaging 10 samples of known ferucarbotran mass (0.34 – 55  $\mu\text{g}$ ). (B) Using each ROI method, a linear relationship between iron content and MPI signal was established as MPI signal (A.U.) =  $m \cdot$  iron content ( $\mu\text{g}$ ), where  $m$  is the slope of each line.

### 4.3.2 Quantification of *in vitro* phantoms

MPI images of Samples 1-10 are shown in Figure 28A and line profiles through these images are shown in Figure 28B. As the fixed mass of ferucarbotran tracer is diluted with increasing amounts of saline, the volume of the sample expands. Thus, the MPI signal is localized over a larger region and the effective amount of iron per imaging voxel is reduced, leading to a diminished peak signal intensity and broadened width of the PSF.

As shown in Figure 28C, ROI methods 1 and 2 accurately quantified the iron mass for samples with volumes similar to the calibration samples (*i.e.*, 10  $\mu\text{L}$ ). Unfortunately, as the sample is diluted, methods 1 and 2 overestimated iron mass by up to 70%. For method 1, this pattern persists with different threshold factors (Figure 29A). ROI methods 3 and 4 are larger ROIs and adequately capture the broader extents of the MPI signal. This leads to a more accurate estimation (<5% error) of iron mass, regardless of sample volume (Figure 28D). Method 4 was accurate when thresholding with higher values of  $c$  (Figure 29B). For ROIs defined by  $c = 10$ , the estimation of iron mass in phantoms was  $35.22 \pm 0.44 \mu\text{g}$ . For  $c = 25$ , the iron mass was estimated at  $33.69 \pm 0.50 \mu\text{g}$ , therefore a slight systematic underestimation was observed.



**Figure 28:** (A) Projection images showing the same amount of ferucarbotran (34.4  $\mu\text{g}$ ) increasing volumes of saline. Image values displayed are 0-1000 A.U. (B) Line profiles showing differences in signal intensity and resolution from Samples 1-10. Undiluted ferucarbotran (Sample 1) produces higher signal intensity as the sample is concentrated, while the point source spreads out more as the sample is diluted. Iron content ( $\mu\text{g}$ ) measured from Samples 1-10 using methods 1 and 2 (C), and methods 3 and 4 (D).



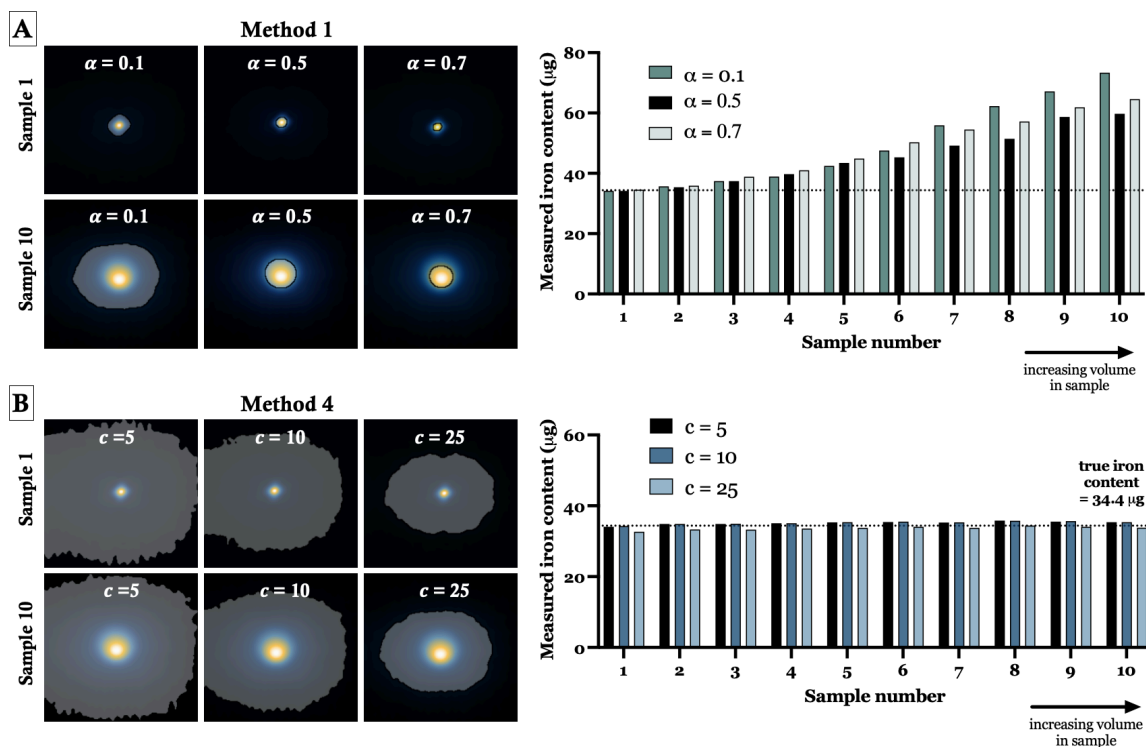


**Figure 29: (A) Various threshold factors are applied to the maximum value ( $\alpha = 0.1$ ,  $0.5$ , and  $0.7$ ) to quantify Samples 1-10. For ROI method 1, quantification of iron is overestimated for dilute samples regardless of the scaling factor. (B) Various threshold factors are applied to the background SD ( $c = 5, 10, 25$ ). Using method 4, iron mass is consistent across scaling factors and accurate with dilution of ferucarbotran.**

### 4.3.3 Inter-user reproducibility

All three users estimated less accurately and precisely using methods 1 and 2 and more accurately and precisely using methods 3 and 4. Box plots of the iron mass mean and range estimated by each user for each method are shown in Figure 30A. Bland-Altman plots show that method 4 has the highest accuracy with an average  $0.08 \mu\text{g}$  difference between the estimated iron content (Figure 30B). Method 2 shows the largest variation between users, averaging a difference of  $4.84 \mu\text{g}$  iron and with a maximum difference of  $13.25 \mu\text{g}$ .

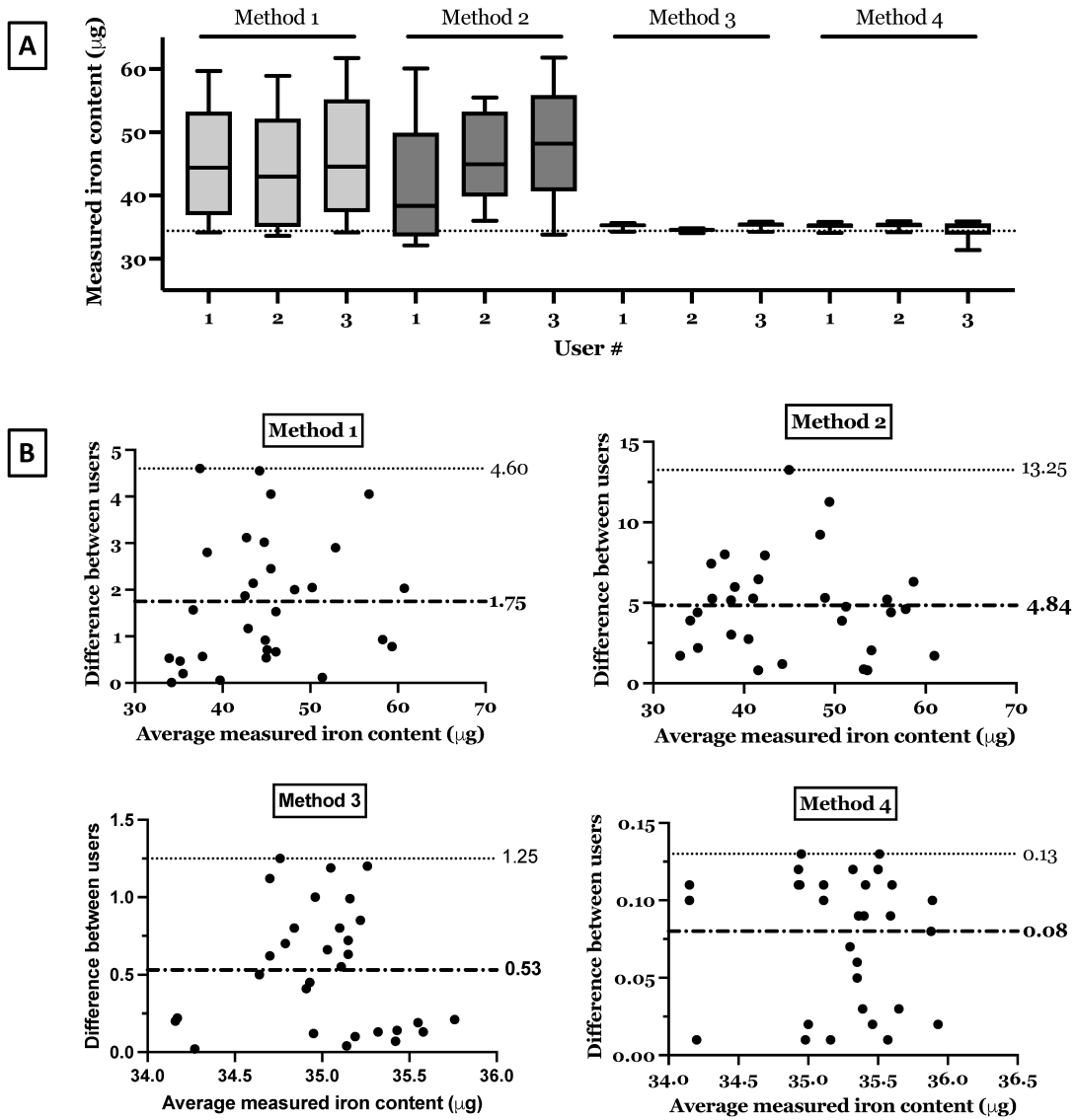


**Figure 30: Analysis of inter-user reproducibility for ROI methods 1-4. (A) For each method, the range of iron content measured by each user for samples 1-10 is shown.**

The dotted line indicates the true iron mass ( $34.4 \mu\text{g}$ ). (B) Bland-Altman plots comparing absolute difference between users with average measured iron content ( $\mu\text{g}$ ). The dotted lines indicate the maximum difference and the average difference (bolded line) between users. Method 4 had the lowest user differences (mean =  $0.08 \mu\text{g}$ ).

Table 5 summarizes the agreement parameters: average difference, SEM, and CoV. The SEM and CoV are lowest for method 4, indicating that this method has the smallest inter-user variability.

**Table 5: Inter-user reproducibility measures for ROI methods 1-4. The average difference for each user pair, standard error of measurement (SEM) and coefficient of variance are reported.**

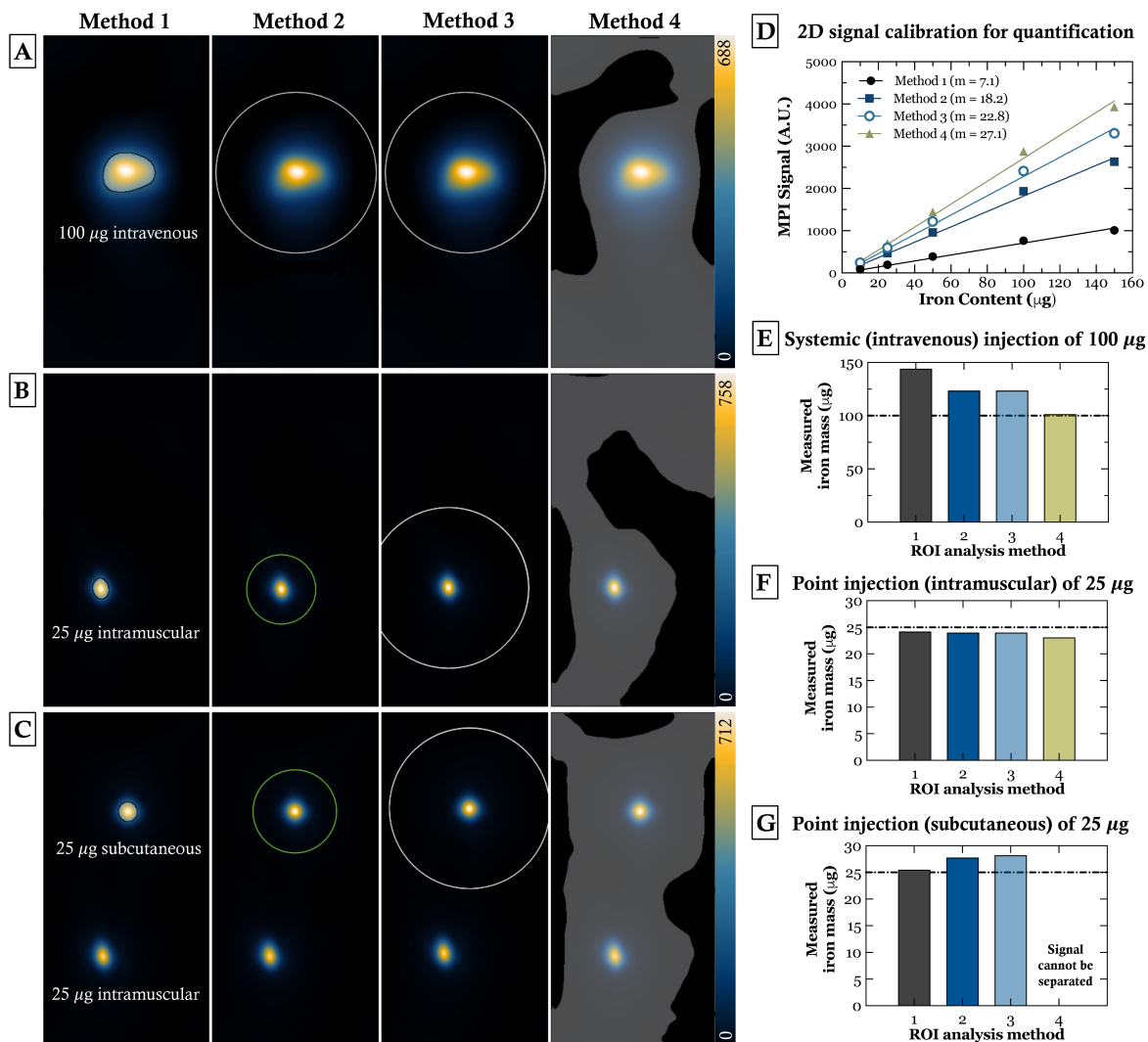
<b>ROI method</b>	<b>1</b>	<b>2</b>	<b>3</b>	<b>4</b>
<b>Average difference (A.U.)</b>	1.75	4.84	0.53	0.08
<b>SEM (A.U.)</b>	1.389	3.770	0.433	0.061
<b>CoV (%)</b>	3.02	8.49	1.23	0.17

#### 4.3.4 *In vivo* quantification

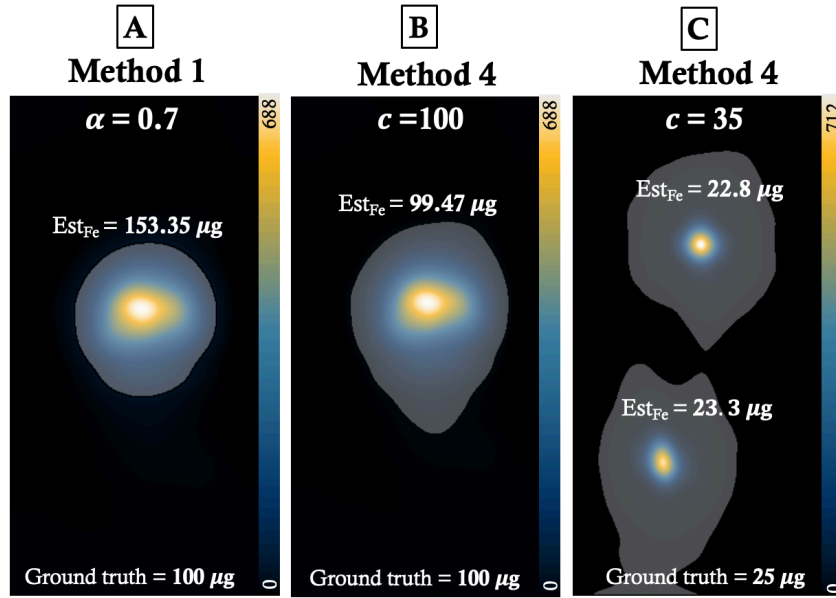
The application of ROI methods 1-4 for *in vivo* quantification of iron is demonstrated in Figure 31. Each ROI selection method is shown for the three *in vivo* images in Figure 31A-C. The iron mass estimated from each ROI was calculated using the slope from the corresponding calibration curves (Figure 31D).

Figure 31A shows 2D MPI of a mouse administered 100  $\mu\text{g}$  ferucarbotran intravenously. From the bloodstream, ferucarbotran accumulates in the phagocytic cells and is primarily distributed throughout the liver and spleen. Method 1 uses the smallest ROI and while method 2 ROI is customized, the circular ROI is applied to a non-circular MPI shape, complicating the aim of including more MPI signal. The use of these ROI methods resulted in overestimation of iron mass measured from the mouse liver and spleen (method 1: 144  $\mu\text{g}$ , method 2: 123.5  $\mu\text{g}$ , Figure 31E). Note that ROI method 2 and 3 are the same for this image because disperse signal in the mouse liver and spleen resulted in the largest PSF in the dataset. Next, we applied higher values of  $\alpha$  with method 1, in attempt to increase the amount of signal included in the ROI while maintaining a custom ROI shape (Figure 32A). However, this did not improve the accuracy of this method for quantifying the SPION mass in the mouse liver and spleen (153.35  $\mu\text{g}$ ).

Compared to the other ROI methods, method 4 with  $c = 5$  creates the largest ROI with signal spread occupying most of the MP image (Figure 31A). Thus, the liver and spleen signal is adequately sampled and results in accurate iron quantification (101.4  $\mu\text{g}$ , Figure 31E). A smaller ROI with a customized shape can be achieved in this application by using a higher threshold value, *i.e.* setting  $c = 100$  with Method 4. As shown in Figure 32B, the ROI is confined to the liver and spleen signal and quantitation accuracy is maintained (99.47  $\mu\text{g}$ ).



**Figure 31: Demonstration of in vivo quantification using methods 1-4 following the (A) intravenous administration of 100  $\mu\text{g}$  ferucarbotran or an (B) intramuscular injection of 25  $\mu\text{g}$  ferucarbotran, followed by a (C) subcutaneous injection of 25  $\mu\text{g}$  ferucarbotran. (D) Signal calibration to determine the relationship between iron mass (ferucarbotran) and MPI signal using 3.0 T/m gradients (the same parameters as *in vivo* images). MPI signal of calibration samples was measured using all 4 methods. (E-G) Iron mass measured from respective *in vivo* images A-C, comparing ROI methods 1-4.**



**Figure 32: Application of alternative threshold values using methods 1 and 4 for in vivo analysis. (A) ROI method 1 with  $\alpha = 0.7$  was applied to the signal associated with ferucarbotran in the mouse liver and spleen. This creates a larger ROI than  $c = 0.5$  but did not return an accurate estimate of SPION mass (153.3  $\mu\text{g}$ ). (B) ROI method 4 with high value of  $c$  ( $= 100$ ) applied to the same mouse results in accurate quantification (99.47  $\mu\text{g}$ ). (C) With ROI method 4, increasing  $c$  ( $=35$ ) allows for separate quantification of two iron sources *in vivo* but quantitative accuracy is reduced.**

For point injections *i.e.* intramuscular injection (Figure 31B) and subcutaneous injection (Figure 31C), the MPI signal originates from ferucarbotran in a smaller volume. For quantification of ferucarbotran point sources, all ROI methods return accurate estimates of iron mass (Figure 31F,G; ground truth = 25  $\mu\text{g}$ ). However, as shown in Figure 31C, it is challenging to separate two sources of MPI signal when using ROI selection method 4 with  $c = 5$  since the ROI boundaries for each source overlap. Next, using method 4 we applied higher values of  $c$  in attempt to distinguish these two signals. At  $c = 35$ , these two point sources of SPION could be separately quantified (Figure 32C). However, since a smaller ROI is applied, the quantitative accuracy is compromised; the subcutaneous injection of 25  $\mu\text{g}$  was estimated to have 22.8  $\mu\text{g}$  ferucarbotran and the intramuscular injection to have 23.3  $\mu\text{g}$  ferucarbotran.

## 4.4 Discussion

MPI directly detects SPIONs, which should enable precise, accurate, linear quantification. However, selection of an ROI has strong effects on MPI quantification results. Ideally ROI selection should be simple, user-independent, and applicable to *in vitro* and *in vivo* situations. This manuscript describes four MPI ROI selection methods and assesses their performance *in vitro* and *in vivo*. Methods 1-4 use different sized ROIs to quantify MPI signal and each approach has suitable applications. These are discussed below and summarized in Table 6. The methods were first tested on 10 ferucarbotran phantoms with identical iron mass but varying sample volumes (6.25 – 1200  $\mu\text{L}$ ). The resulting images presented a quantification challenge since the point source spreads out as the ferucarbotran samples is diluted and the overall MPI signal intensity is reduced. To assess user-reproducibility, the samples were analyzed by three users. Last, these methods were applied to *in vivo* quantification of ferucarbotran after intravenous administration or point injection (intramuscular and subcutaneous) to mice.

**Table 6: Comparison of ROI methods 1-4 in terms of size of the ROI, time spent on analysis, user variability, the ability to create custom shaped ROIs, and the quantification accuracy of iron in different volumes.**

ROI method	1	2	3	4
Size of ROI	Small	Medium	Large	Large
Speed	Medium	Slow	Medium	Fast
User variability	Medium	High	Medium	Low
Custom shapes	Yes	No	No	Yes
Different volume samples	Poor	Poor	Good	Good

Method 1 selects an ROI based on the peak signal value within the target volume. Pixels are included in the ROI by selecting a threshold, e.g.  $0.5 \cdot s_{max}$ , and including all pixels with values larger than the threshold. This approach is beneficial to generate small ROIs, which helps achieve separation of multiple adjacent signals present in a single image. For example, Method 1 can separately quantify the MPI signal from ferucarbotran administered to multiple regions of a mouse with accuracy (Figure 31C). Ultimately this method is best suited for high-SNR signals from samples in a similar volume. We saw that samples of ferucarbotran in small volumes lead to sharp signals with high intensities relative to larger volumes, which produce broader signals. Since dilute samples have broader signal with lower peak intensity, the  $\alpha \cdot s_{max}$  threshold is lower and includes more area in the ROI (Figure 26A and 29A). Thus, an overestimation of iron mass is expected for dilute samples, which is confirmed *in vitro* (Figure 28C and 29A). This is also true for *in vivo* quantification of ferucarbotran that is administered intravenously, which disperses throughout the mouse liver and spleen, regardless of the value chosen for  $\alpha$  (Figure 31E and 32A). This suggests that when using method 1, the fluid volume in the calibration samples must be carefully controlled to match that of the signals that are being quantified.

Method 2 selects a circular ROI that is manually placed on the peak signal, with the ROI diameter selected from the line profile. These ROIs are larger than method 1 and include more of the PSF; however, the quantitative accuracy of dilute *in vitro* samples of ferucarbotran did not improve. Likewise, the quantification of dilute ferucarbotran in the mouse liver and spleen after intravenous administration was overestimated. For *in vivo* analysis, line profiles tend to be less sharp and consequently the determination of the PSF width is challenging. For non-circular objects, automatic image thresholding in the presence of high SNR (e.g. Otsu's method) could help to identify the initial ROI. This method is quantitative only for high-SNR and high-resolution signals and breaks down for more complex images. Method 2 was accurate for quantifying *in vitro* phantoms of small volumes (Figure 28C) and point injections *in vivo* (Figure 31F,G).

Method 3 uses ROIs with fixed dimensions on all images in a dataset, using the largest-sized ROI from method 2. This method is optimal for image datasets that assume the



same physical layout of objects and can be used for quantification across a large SNR range. With the ROI diameter tied to the largest signal spread, this method guarantees sampling of signals at lower concentrations, and the amount of noise introduced to the ROI is consistent for each image. Method 3 provided precise and accurate iron mass measurement *in vitro* (Figure 28D) and this approach is faster than method 2.

Method 4 uses an SNR threshold-based segmentation system (*e.g.*  $\text{SNR} \geq 3$ ) and has many advantages and few disadvantages (Table 6). This method is simple to perform and can be conducted quickly. The size of the ROI depends on the standard deviation of the background signal, the threshold factor ( $c$ ), and the size of the PSF. Method 4 applies the same lower threshold *i.e.*  $c \cdot SD$  to all images in the dataset (including calibration samples), regardless of MPI signal strength and dimensions. For low SNR thresholds (*e.g.*  $\text{SNR} \sim 3$ ), this technique produces large ROIs compared to methods 1 and 2, and similar to method 3 (shown in Figure 26A). This method illustrates that the MPI signal is spreading in nature, with image pixels being affected despite their distance from the source. Our results show that method 4 returns accurate quantification of ferucarbotran in varying volumes both *in vitro* (Figure 28D) and *in vivo* (Figure 31E,F). For higher threshold values (*e.g.*  $25 \cdot SD$ ) the method results in smaller ROIs without compromising accuracy if a consistent threshold is used (Figure 29B and 32B). However, this technique can struggle to quantify multiple overlapping signal sources *in vivo*. As shown in Figure 31C, two ferucarbotran sources separated by 5.3 cm could not be separately quantified using a  $5 \cdot SD$  threshold. We observed that a minimum threshold of  $35 \cdot SD$  was necessary to separate two sources of 2D MPI signal *in vivo* (Figure 32C) although this led to loss in quantitative accuracy. At higher threshold values ( $c > 5$ ), more MPI signal is neglected at which point the quantification accuracy may be degraded. In our experience, overlapping signals is less of an issue in 3D data sets. Overall, there exists an important tradeoff between ROI area and quantification result, and this is dependent on many factors including MPI acquisition, SPION mass (and therefore, the intensity of the MPI signal), and SPION type.

All three MPI users analyzed the identical set of images, therefore user differences reported in III.III are attributed solely to image analysis. Overall, we observed that

method 4 has the highest reproducibility as shown by the smallest user differences, and method 2 had the greatest variability. We would expect Method 1 and 2 to be more error prone and show increased user differences because a different, unique ROI threshold is applied to all ten ferucarbotran phantoms and all ten calibration samples. In contrast, method 3 and 4 would be expected to have lower user differences because they apply a uniform ROI or threshold value to all 20 images. ROI method 1 is a semi-automatic method. When calculating the threshold value ( $\alpha \cdot S_{max}$ ), we would expect there to be rounding errors depending on how many decimal places the user included. Method 2 is the most manual and error-prone method since it requires on 3-user inputs per image. The first is a subjective measurement of the PSF edges, and though a multiplication factor ( $b$ ) is applied to mitigate it, inherent user variability is expected. Finally, the ROI is placed manually over the peak of the signal, which may also contribute to user differences. Method 3 has reduced user variability compared to method 2 since there is only a single manual bias. Lastly, method 4 may show differences resulting from the measurement of the background standard deviation from the same blank MPI image. There could be slight differences in the selected region that would subsequently lead to a different threshold value ( $c \cdot SD$ ).

The applicability of these methods presented is transferrable to other reconstructions than X-space. For reconstructions that have more localized signal, the different ROIs resulting from the methods presented would look more similar, as the majority of the signal is confined in the same region and the transition at peak curvature would be more pronounced. For such a dataset, with relatively lower background signal, method 4 would be recommended as it would be the easiest and most reliable to implement. Furthermore, a lower scaling factor would be needed to capture an ROI close to the object imaged. Note that using methods like deconvolution lowers the peak SNR and caution is recommended where sensitivity may be compromised. With reconstructions that provide more confined MPI signals, other groups have used ROIs defined by the sample position or anatomy for quantification<sup>43,44</sup>.

Methods 3 and 4 use large ROIs for quantifying SPIONs. We have considered an additional approach, where the entire image serves as the ROI. Interestingly, this method

was accurate for quantification of ferucarbotran phantoms (Part III.II) and ferucarbotran *in vivo* (Part III.III). This approach led to estimation of  $34.68 \pm 0.61 \mu\text{g}$  ferucarbotran in Samples 1-10 (truth =  $34.4 \mu\text{g}$ ). For ferucarbotran administered intravenously, this ROI method yielded an estimate of  $100.1 \mu\text{g}$  from the entire image (truth =  $100 \mu\text{g}$ ). Lastly, for ferucarbotran administered intramuscularly, this ROI yielded an estimate of  $22.2 \mu\text{g}$  (truth =  $25 \mu\text{g}$ ). Overall, this approach could serve as a quick, crude analysis technique for quantifying images with a single signal source.

In this study we observed that the dispersion of SPIONs reduces the quality of MPI quantification when using ROI selection methods 1 and 2. There are additional factors which influence reliable quantification of SPION with MPI, including SPION immobilization<sup>3,45-48</sup> and degradation<sup>30,48</sup>. Immobilization of SPION occurs with protein binding or cellular internalization and is expected to increase Brownian relaxation times, leading to MPI signal reduction and blurring. As SPIONs undergo degradation over time, their MPI sensitivity can be variable<sup>30</sup>. Importantly, ferucarbotran in this study was vortexed before use and stored at appropriate conditions to avoid clustering and degradation. *In vivo* imaging was conducted immediately or within 1 day of iron administration, therefore SPION degradation is expected to be negligible.

## 4.5 Conclusion

There is an unmet need for standardized, reproducible, simple, and accurate ROI methods for quantification of MPI signal. Here we described and tested four ROI selection method approaches. All four methods showed a strong linear relationship between ferucarbotran mass and quantified MPI signal for iron samples of the same fluid volume.

Each ROI method has advantages. Method 1 relies on segmentation at a fraction of the maximum MPI signal and forms the smallest ROIs. This method provided accurate quantification of ferucarbotran in small volumes and ferucarbotran administered by point injection *in vivo*. This method is beneficial for separately quantifying multiple sources of iron present in a single image. Ultimately ROI method 1 was not accurate for

quantification of ferucarbotran in larger fluid volumes and after systemic administration *in vivo*. Method 2 applies a custom size ROI to each MPI signal by assessing the PSF. While this method includes more MPI signal than method 1, the quantitative accuracy for dilute ferucarbotran *in vitro* and *in vivo* did not improve. It can be challenging to assess the PSF of low-SNR signals and dilute iron, particularly *in vivo*. Method 3 addresses this by applying the largest ROI established from method 2 to all images in a dataset, regardless of MPI signal strength and dimensions. Lastly, method 4 uses a uniform threshold-based segmentation at a factor of the background SD ( $c \cdot SD$ ) which results in larger ROIs. This method provided accurate and precise estimates of ferucarbotran mass for *in vitro* phantoms, including samples which were in larger fluid volumes. Likewise, *in vivo* quantification of ferucarbotran administered systemically was accurate with method 4. The limitation of this method is the use of large ROIs which can be challenging when attempting to quantify multiple MPI signals in a single image. ROI method 4 overall has many advantages, including quick analysis, simplicity, and high reproducibility between users.

No single method meets all desired criteria (Table 6), therefore a careful choice of ROI selection method must be made for analyzing each dataset. This paper was focused on quantification of ferucarbotran but these ROI methods are applicable for other SPIONs. Our hope is these ROI selection methods will be widely adopted by MPI users to improve the accuracy and consistency of SPION quantification.

## 4.6 Chapter 4 references

1. Martín-Fontecha, A. *et al.* Regulation of dendritic cell migration to the draining lymph node: Impact on T lymphocyte traffic and priming. *J. Exp. Med.* **198**, 615–621 (2003).
2. Chapelin, F., Capitini, C. M. & Ahrens, E. T. Fluorine-19 MRI for detection and quantification of immune cell therapy for cancer. *J. Immunother. Cancer* **6**, 1–11 (2018).
3. Sehl, O. C., Gevaert, J. J., Melo, K. P., Knier, N. N. & Foster, P. J. A perspective on cell tracking with magnetic particle imaging. *Tomography* **6**, (2020).
4. Rivera-rodriguez, A. *et al.* Tracking Adoptive T Cell Therapy Using Magnetic Particle Imaging. *Nanotheranostics* **5**, 431–444 (2021).
5. Makela, A. V. *et al.* Magnetic Particle Imaging of Macrophages Associated with Cancer: Filling the Voids Left by Iron-Based Magnetic Resonance Imaging. *Mol. Imaging Biol.* (2020). doi:10.1007/s11307-020-01473-0
6. Chandrasekharan, P. *et al.* Non-radioactive and sensitive tracking of neutrophils towards inflammation using antibody functionalized magnetic particle imaging tracers. *Nanotheranostics* **5**, 240–255 (2021).
7. Liu, S. *et al.* Long circulating tracer tailored for magnetic particle imaging. *Nanotheranostics* **5**, 348–361 (2021).
8. Dousset, V. *et al.* In vivo macrophage activity imaging in the central nervous system detected by magnetic resonance. *Magn. Reson. Med.* **41**, 329–333 (1999).
9. Nejadnik, H., Tseng, J. & Daldrup-Link, H. Magnetic resonance imaging of stem cell–macrophage interactions with ferumoxytol and ferumoxytol-derived nanoparticles. *Wiley Interdiscip. Rev. Nanomedicine Nanobiotechnology* **11**, 1–13 (2019).

10. Ren, G. *et al.* Imaging cancer immunology: Monitoring CD47 mAb treatment in vivo by magnetic particle imaging. *AACR* (2020).
11. Iv, M. *et al.* Quantification of macrophages in high-grade gliomas by using ferumoxytol-enhanced MRI: A pilot study. *Radiology* **290**, 198–206 (2019).
12. Aghighi, M. *et al.* Magnetic resonance imaging of tumor-associated macrophages: Clinical translation. *Clin. Cancer Res.* **24**, 4110–4118 (2018).
13. Makela, A. V., Gaudet, J. M. & Foster, P. J. Quantifying tumor associated macrophages in breast cancer: a comparison of iron and fluorine-based MRI cell tracking. *Sci. Rep.* **7**, (2017).
14. Hensley, D. *et al.* Combining Magnetic Particle Imaging and Magnetic Fluid Hyperthermia in a Theranostic Platform. *Phys Med Biol* **62**, 3483–3500 (2017).
15. Tay, Z. W. *et al.* Magnetic Particle Imaging-Guided Heating in Vivo Using Gradient Fields for Arbitrary Localization of Magnetic Hyperthermia Therapy. *ACS Nano* (2018). doi:10.1021/acsnano.8b00893
16. Healy, S. *et al.* Clinical magnetic hyperthermia requires integrated magnetic particle imaging. *Wiley Interdiscip. Rev. Nanomedicine Nanobiotechnology* 1–20 (2022). doi:10.1002/wnan.1779
17. Hayat, H. *et al.* Artificial Intelligence Analysis of Magnetic Particle Imaging for Islet Transplantation in a Mouse Model. *Mol. Imaging Biol.* **23**, 18–29 (2021).
18. Krak, N. C. *et al.* Effects of ROI definition and reconstruction method on quantitative outcome and applicability in a response monitoring trial. *Eur. J. Nucl. Med. Mol. Imaging* **32**, 294–301 (2005).
19. Jauw, Y. W. S. *et al.* Interobserver reproducibility of tumor uptake quantification with <sup>89</sup>Zr-immuno-PET: a multicenter analysis. *Eur. J. Nucl. Med. Mol. Imaging* **46**, 1840–1849 (2019).

20. Sato, N. *et al.* In Vivo Tracking of Adoptively Transferred Natural Killer Cells in Rhesus Macaques Using <sup>89</sup>Zirconium-Oxine Cell Labeling and PET Imaging. *Clin. Cancer Res.* **26**, 2573–2581 (2020).
21. Keyes Jr, J. SUV: standard uptake or silly useless value? *J. Nucl. Med.* **36**, 1836–1839 (1995).
22. Sarna, N. S. *et al.* An anatomically correct 3D printed mouse phantom for magnetic particle imaging studies . *Bioeng. Transl. Med.* (2022).  
doi:10.1002/btm2.10299
23. Keselman, P. *et al.* Tracking short-term biodistribution and long-term clearance of SPIO tracers in magnetic particle imaging. *Phys. Med. Biol.* **62**, 3440–3453 (2017).
24. Griese, F., Knopp, T., Werner, R., Schlaefer, A. & Möddel, M. Submillimeter-Accurate Marker Localization within Low Gradient Magnetic Particle Imaging Tomograms. *Int. J. Magn. Part. Imaging* **3**, (2017).
25. Wöckel, L. *et al.* Long-term stable measurement phantoms for magnetic particle imaging. *J. Magn. Magn. Mater.* **471**, 1–7 (2019).
26. Zhong, J., Schilling, M. & Ludwig, F. Simultaneous Imaging of Magnetic Nanoparticle Concentration, Temperature, and Viscosity. *Phys. Rev. Appl.* **16**, 1 (2021).
27. Szwargulski, P. *et al.* Monitoring Intracranial Cerebral Hemorrhage Using Multicontrast Real-Time Magnetic Particle Imaging. *ACS Nano* (2020).  
doi:10.1021/acsnano.0c06326
28. Wang, P. *et al.* Magnetic particle imaging of islet transplantation in the liver and under the kidney capsule in mouse models. *Quant. Imaging Med. Surg.* **8**, 114–122 (2018).

29. Haegele, J. *et al.* Magnetic particle imaging: Visualization of instruments for cardiovascular intervention. *Radiology* **265**, 933–938 (2012).
30. Guzy, J. *et al.* Complex relationship between iron oxide nanoparticle degradation and signal intensity in magnetic particle imaging. *ACS Appl. Nano Mater.* **3**, 3991–3999 (2020).
31. Paysen, H. *et al.* Cellular uptake of magnetic nanoparticles imaged and quantified by magnetic particle imaging. *Sci. Rep.* **10**, 1–8 (2020).
32. Kaul, M. G. *et al.* Pulmonary blood volume estimation in mice by magnetic particle imaging and magnetic resonance imaging. *Sci. Rep.* **11**, 1–10 (2021).
33. Makela, A. V., Schott, M. A., Madsen, C., Greeson, E. & Contag, C. H. Magnetic particle imaging of magnetotactic bacteria as living contrast agents is improved by altering magnetosome structures. *bioRxiv* 1–28 (2021).  
doi:10.1021/acs.nanolett.1c05042
34. Sehl, O. C. & Foster, P. J. The sensitivity of magnetic particle imaging and fluorine-19 magnetic resonance imaging for cell tracking. *Sci. Rep.* **11**, 1–12 (2021).
35. Dieckhoff, J. *et al.* In vivo liver visualizations with magnetic particle imaging based on the calibration measurement approach. *Phys. Med. Biol.* **62**, 3470–3482 (2017).
36. Herz, S. *et al.* Magnetic Particle Imaging for Quantification of Vascular Stenoses: A Phantom Study. *IEEE Trans. Med. Imaging* **37**, 61–67 (2018).
37. Konkle, J. J. *et al.* A convex formulation for magnetic particle imaging X-space reconstruction. *PLoS One* **10**, 1–15 (2015).
38. Gevaert, J. J., Fink, C., Dikeakos, J., Dekaban, G. A. & Paula, J. Magnetic Particle Imaging is a sensitive in vivo imaging modality for the quantification of dendritic cell migration. *Mol. Imaging Biol.* 1–29 (2021). doi:10.1007/s11307-022-01738-w



39. Rose, A. The sensitivity performance of the human eye on an absolute scale. *J. Opt. Soc. Am.* **38**, 196–208 (1948).
40. Siegers, G. M. *et al.* Pre-Labeling of Immune Cells in Normal Bone Marrow and Spleen for Subsequent Cell Tracking by MRI. *Tomography* **2**, 26–34 (2016).
41. Lawaczeck, R. *et al.* Magnetic Iron Oxide Particles Coated with Carboxydextran for Parenteral Administration and Liver Contrasting. *Acta radiol.* **38**, 584–597 (1997).
42. Soares, G. A. *et al.* Long-Term Clearance and Biodistribution of Magnetic Nanoparticles Assessed by AC Biosusceptometry. *Materials (Basel)*. **15**, (2022).
43. Paysen, H. *et al.* Imaging and quantification of magnetic nanoparticles: Comparison of magnetic resonance imaging and magnetic particle imaging. *J. Magn. Magn. Mater.* **475**, 382–388 (2019).
44. Graeser, M. *et al.* Design of a head coil for high resolution mouse brain perfusion imaging using magnetic particle imaging. *Phys. Med. Biol.* **65**, (2020).
45. Suzuka, H., Mimura, A., Inaoka, Y. & Murase, K. Magnetic Nanoparticles in Macrophages and Cancer Cells Exhibit Different Signal Behavior on Magnetic Particle Imaging. *J. Nanosci. Nanotechnol.* **19**, 6857–6865 (2019).
46. Utkur, M., Muslu, Y. & Saritas, E. U. Relaxation-based color magnetic particle imaging for viscosity mapping. *Appl. Phys. Lett.* **115**, (2019).
47. Arami, H., Ferguson, R. M., Khandhar, A. P. & Krishnan, K. M. Size-dependent ferrohydrodynamic relaxometry of magnetic particle imaging tracers in different environments. *Med. Phys.* **40**, 1–14 (2013).
48. Teeman, E., Shasha, C., Evans, J. E. & Krishnan, K. M. Intracellular dynamics of superparamagnetic iron oxide nanoparticles for magnetic particle imaging. *Nanoscale* **11**, 7771–7780 (2019).

## Chapter 5

### 5 Fluorine-19 MRI as a quantitative *in vivo* migration assay for regulatory T cell immunotherapy

Regulatory T cell (Treg) and chimeric antigen receptor (CAR) Treg therapies have proven effective against transplant rejection and autoimmune diseases. However, it is unknown if, and how many of these cells migrate to target locations following administration, including lymph nodes and transplant sites. The objective of this work is to use fluorine-19 ( $^{19}\text{F}$ ) MRI to visualize and directly quantify *in vivo* migration of perfluorocarbon (PFC) labeled human Treg and targeted homing of CAR Tregs in immunocompromised mice. Human Tregs were efficiently labeled with PFC without impacting viability or phenotype. Longitudinal *in vivo*  $^{19}\text{F}$  MRI was conducted using clinically applicable methodology, including a  $^1\text{H}/^{19}\text{F}$  dual-tuned surface coil at 3 Tesla. PFC+ Tregs were administered intravenously or subcutaneously then tracked in mice to lymph nodes and the spleen, with different  $^{19}\text{F}$  signals occurring at each timepoint and with each administration route. This quantification suggests that the route of cellular administration may impact the treatment efficacy. Intravenously administered PFC+ CAR Tregs preferentially migrated to antigen+ tumors compared to contralateral parental tumors, with peak signals occurring at 48 hours and a >10-fold difference in tumor homing. The presence of Tregs were confirmed in excised lymph nodes and tumors with histology following the last MRI exam.  $^{19}\text{F}$  MRI is a suitable imaging modality to image and quantify PFC+ Treg *in vivo* migration.

## 5.1 Introduction

Regulatory T cells (Tregs) are CD4<sup>+</sup> helper T cells which have numerous immunosuppressive functions with the main role of balancing immune tolerance<sup>1</sup>. Tregs produce anti-inflammatory cytokines which lead to local immunosuppression, including interleukin (IL)-10 and transforming growth factor (TGF)- $\beta$  (ref<sup>1-3</sup>). Furthermore, Tregs express CD25 (a chain of the high-affinity IL-2 receptor) that sequesters and consumes local IL-2, favoring the growth of Tregs over surrounding effector T cells<sup>3</sup>. Additionally, Tregs express inhibitory receptors which lead to systemic immunosuppression, such as cytotoxic T lymphocyte associated protein (CTLA)-4, which inhibit the activity of antigen-presenting cells (APC) and activation of effector T cells<sup>3-5</sup>. Therefore, Tregs act both locally and systemically. Tregs have been proposed as a cellular immunotherapy for the treatment of conditions that involve overactivation of the immune system, such as autoimmune diseases (*e.g.*, rheumatoid arthritis, type 1 diabetes, multiple sclerosis) and rejection of solid organ transplants<sup>3,6,7</sup>. Treg immunotherapies may eventually replace conventional drug-based immunosuppressants, which are short acting and non-specific.

The overall goal of Treg cell therapy is to shift the balance between effector and regulatory T cells to favor immune tolerance<sup>8,9</sup>. This is achieved by expanding Treg cell populations *ex vivo* to obtain sufficient cell numbers for infusion<sup>2</sup>. Tregs are commonly collected from whole blood by leukapheresis, however, the scarcity of Tregs in blood mandates extensive expansion<sup>3,7,8</sup>. Recently, CD4<sup>+</sup> CD25<sup>+</sup> Foxp3<sup>+</sup> Helios<sup>+</sup> Tregs have been isolated from the pediatric thymus, which have a high abundance of Tregs (~ 3-500 million cells/thymus)<sup>9</sup> and are routinely removed during cardiac surgeries<sup>10,11</sup>. Treg immunosuppression occurs in local microenvironments therefore it is important that Tregs home to target locations efficiently. For therapeutic success, Tregs must migrate to secondary lymphoid tissues including the spleen and lymph nodes and in sufficient numbers to interact with APC. In the application of organ transplantation, Treg migration to the allograft is also critical to induce local immunity.

In current clinical trials, the location and number of infused Tregs that reach target sites is unknown. Instead, the status of Treg therapies is monitored by blood-borne biomarkers,

such as counts of circulating Tregs, the composition of white blood cells, inflammatory markers, or organ function tests (if applicable)<sup>12-14</sup>. These measurements provide little information on the migration or persistence of Tregs at target tissues and it may be months before these metrics become useful. Target tissues include a site of organ transplantation or tissue being affected by autoimmune disease, as well as secondary lymphoid tissues (including the spleen and lymph nodes) where Tregs interact with antigen presenting cells.

Cellular imaging strategies have great potential to evaluate the migration patterns and density of Tregs at these locations in real time, ultimately enhancing our understanding of clinical outcomes. Before Tregs are infused to patients, they are expanded *in vitro*, which provides an opportunity to label cells with an imaging tracer. Imaging metrics can provide information on cell therapeutic status before other clinical markers become available, which can help to predict patient response or promote early physician intervention. Preclinical cellular imaging of Tregs is expected to play a role in accelerating development of Treg therapies by optimizing cell source, culturing methods, dose, administration routes. Furthermore, *in vivo* imaging can provide information to evaluate Treg modification strategies, including those which enhance migration to target sites and induce specific tolerance through expression of a chimeric antigen receptor (CAR). This is a timely pursuit as the first CAR Treg clinical trial is currently underway for recipients undergoing kidney transplantation (NCT04817774).

There are a few examples of Treg tracking, with bioluminescence imaging (BLI), single-photon emission computed tomography (SPECT), and positron emission tomography (PET)<sup>15-19</sup>. BLI has been used to show biodistribution of polyclonal murine Tregs after infusion to mice, showing their migration to lymph nodes and the spleen within 24-48 hours and expand to peak intensity at day 4 (reference<sup>15</sup>). More recently, BLI tracked human-derived Tregs engineered with HLA-A2 specific CAR preferentially to HLA-A2 expressing skin grafts in mice, with maximal signals at 1 week<sup>17</sup>. While informative, BLI is only semi-quantitative owing to scattering of light in tissues and cannot provide a measure of the number of cells at a target site. SPECT is a quantitative modality and excitingly has been used to track autologous <sup>111</sup>Indium tropolonate-labeled Tregs

clinically. Tregs were detected in the spleen and liver of patients with autoimmune hepatitis at 4, 24, and 72 hours after infusion. However, SPECT has low resolution and lacks anatomical information required for cell localization, especially in intricate anatomies such as lymph nodes<sup>20</sup>. PET has relatively higher resolution and sensitivity than SPECT and has recently been used to track <sup>89</sup>Zirconium oxine labeled Tregs in mice. Unfortunately, PET may be unfit for Treg tracking as even at low doses of 0.1 Bq/cell, Treg survival and expansion was compromised owing to radiation-induced toxicity<sup>19</sup>.

<sup>19</sup>Fluorine (<sup>19</sup>F) magnetic resonance imaging (MRI) cell tracking can provide direct, quantitative, and hotspot images of perfluorocarbon (PFC)-labeled cells. Labeling cells with <sup>19</sup>F-PFCs has very minimal or no effect on viability or function in a wide range of concentrations and cell types<sup>21-30</sup>. Importantly, <sup>19</sup>F MRI signal is directly quantitative and can be related to a measure of cell number based on the density of <sup>19</sup>F atoms detected in a region of interest and prior knowledge of cellular <sup>19</sup>F loading. <sup>19</sup>F MRI seems suitable for Treg tracking after many years of T cell tracking in mice<sup>26-32</sup>, and has been performed in humans<sup>24</sup>. The objective of this study is to use <sup>19</sup>F MRI to visualize and directly quantify in vivo migration of PFC<sup>+</sup> human Treg and targeted homing of PFC<sup>+</sup> CAR Tregs in immunocompromised mice.

## 5.2 Methodology

### 5.2.1 Treg isolation

Human thymus tissue was dissociated as described<sup>33</sup>, then Tregs were isolated by CD25 positive selection using Releasable RapiDspheres followed by CD8 depletion using a custom magnetic cell isolation kit and manufacturer's protocol (STEMCELL Technologies). Isolated Tregs were cryopreserved in CryoStor CS10 (STEMCELL Technologies) until expansion.

### 5.2.2 Polyclonal Treg expansion

Human polyclonal Tregs were thawed and then activated using Dynabeads Treg Xpander (Thermo Fisher Scientific, Waltham, MA, USA) at a 4:1 bead to cell ratio and expanded in ImmunoCult<sup>TM</sup>-XF T Cell Medium (STEMCELL Technologies) supplemented with

1% penicillin/streptomycin (Thermo Fisher Scientific), 1000 IU/mL recombinant human IL-2 (Proleukin, San Diego, CA, USA), and 100 ng/mL rapamycin (Sigma Aldrich, St Louis, MO, USA). Cultures were fed every 2 days starting from day 3, refreshing media and additives. Tregs were restimulated on day 11 by adding additional Dynabeads Treg Xpander at a 1:1 bead to cell ratio, expanded for 2 additional days, then cryopreserved in CryoStor CS10. This process was repeated for 4 donor cell populations prior to subcutaneous administrations (n = 2) or intravenous administrations (n = 2) to mice (see below, *part 5.2.9*).

### 5.2.3 HER2-CAR Treg generation

Human polyclonal Tregs were thawed and then activated using irradiated (75 Gy) L cells loaded with 100 ng/mL anti-CD3 monoclonal antibody (mAb) (Clone: OKT3, University of British Columbia AbLab) at a 1:1 ratio. Cells were cultured in ImmunoCult™-XF T Cell Expansion Medium supplemented with 1000 IU/mL IL-2. 100 ng/mL rapamycin (Sigma Aldrich) was also added from day 0-7 of culture. Tregs were transduced 1 day after activation by adding lentivirus for human epidermal growth factor receptor 2 (HER2)-CAR (multiplicity of infection (MOI) = 10 virus particles per cell) and with GFP-expressing lentivirus (MOI = 5). Treg cultures were replenished with IL-2- and rapamycin-supplemented media every 2-3 days. On day 7, transduced GFP<sup>+</sup> Tregs underwent fluorescence activated cell sorting sorted on day 7 on BD FACSAria II. Sorted HER2-CAR Treg were then restimulated using irradiated L cells loaded with anti-CD3 as on day 0. Tregs were expanded until day 14, with fresh media replenished every 2-3 days. Tregs were further expanded on day 14 with Dynabeads Treg Xpander added at a 1:1 bead to cell ratio, expanded for 2 additional days, then cryopreserved in CryoStor CS10. Treg isolation and engineering occurred at the University of British Columbia then sent to Robarts Research Institute for downstream use. This process occurred once for a single donor population prior to intravenous administration to tumor-bearing mice (n = 3) (*see below, part 5.2.9*)

#### 5.2.4 <sup>19</sup>F-PFC labeling of Tregs

Cryopreserved Tregs were thawed at 37C, washed with phosphate buffered saline (PBS) and then resuspended in pre-warmed ImmunoCult™-XF T Cell Expansion Medium supplemented with IL-2 (1000 IU/mL), penicillin (100 U/mL), streptomycin (100 ug/mL) and L-Glutamine (0.3 mg/mL) at 2.5x10<sup>6</sup> cells/mL. Two hours later, red fluorescent or non-fluorescent PFC (5 mg/mL) was added and Tregs were further cultured overnight. The red fluorescent PFC was only used for assessing PFC uptake by fluorescent microscopy or flow cytometry (shown in Figure 33A-E). Tregs not cultured with PFC served as unlabeled (UL) control Tregs.

Cryopreserved CAR Tregs (both luc<sup>+</sup> and HER2-CAR+luc<sup>+</sup>) were thawed at 37C and then expanded in IL-2-supplemented ImmunoCult™-XF T cell media (1 x 10<sup>6</sup> cells/mL) with ImmunoCult™ human CD3/CD28/CD2 T cell activator (25 uL/mL cell suspension). Following 24 hour expansion, CAR Tregs were resuspended at 2.5x10<sup>6</sup> cells/mL and labeled with PFC in Immunocult™-XF T cell media as described above. At the end of culture, Tregs and/or CAR Tregs were collected and extensively washed with PBS prior to downstream application.

#### 5.2.5 Treg viability and phenotype assessment

Following culture, PFC<sup>+</sup> (or control UL) Tregs and/or CAR Tregs were washed and resuspended in PBS containing Zombie NIR™ fixable vital dye for 20 minutes at room temperature to determine viability. Cells were then stained for cell surface expression of CD4, CD8 and CD25 in the presence of Human TruStain FcX™ for 25 mins at 4C. After extensive washing in HBSS + 0.1% BSA, cells were resuspended in a fixation/permeabilization buffer for 30 minutes at 4°C and washed twice in a permeabilization buffer, both buffers of which are components of a commercially available Foxp3/transcription factor staining buffer set. Cells were then intracellularly stained for Foxp3 and Helios in permeabilization buffer containing Human TruStain FcX™ for 30 minutes at room temperature. After repeated washing in permeabilization buffer and HBSS + 0.1% BSA, data was acquired on a LSRII analytical flow cytometer (BD Biosciences, San Jose, USA). Where applicable, flow cytometry was also employed

to assess eGFP fluorescence in transduced Tregs and red fluorescence due to red fluorescent PFC incorporation. All flow cytometric data was analyzed using FlowJo Software (v10, Tree Star, Inc., Ashland, USA).

### 5.2.6 Fluorescence microscopy

Fluorescence microscopy was used in addition to flow cytometry to assess red fluorescent PFC uptake by Tregs. Both PFC<sup>+</sup> and UL Tregs ( $1 \times 10^5$  cells) were cytopun on to a Superfrost Plus microscope slide and then fixed with 4% paraformaldehyde. Nuclei were stained with aqueous mounting media containing DAPI, coverslipped and imaged using an EVOS™ M7000 Imaging System. Additional oil immersion 63X objective images were taken using a confocal microscope (TCS SP8, Leica Microsystems).

### 5.2.7 <sup>19</sup>F NMR spectroscopy

The average number of <sup>19</sup>F spins per cell was ascertained by NMR spectroscopy using a previously defined protocol (29330541) and a Varian Inova 400 MHz spectrometer (Varian, Inc., Palo Alto, CA, USA) or Bruker 600 Neo NMR spectrometer (Bruker, Billerica, MA, USA). Briefly, a pellet  $1 \times 10^6$  PFC<sup>+</sup> Treg cell number was lysed and transferred to a 5 mm diameter NMR tube (New Era Enterprises, Inc.) containing D<sub>2</sub>O and trifluoroacetic acid (0.1% v/v in H<sub>2</sub>O) as a reference peak. The spectroscopy parameters were frequency = 367.12 MHz (Varian) or 564.8 MHz (Bruker), tip angle = 45 degrees, recycle delay = 6 s, acquisition time = 1.8 s, sample spinning rate = 20 Hz, spectral width = 50 ppm (18.9 kHz Varian or 27.8 kHz Bruker), number of scans = 100 (Varian) or 64 (Bruker).

### 5.2.8 Animal work

Eleven female CB17/Icr-Prkdcscid/IcrIcoCrl (CB-17) mice (6-8 weeks old) were obtained from Charles River Laboratories Inc. (Senneville, CAN) and monitored in accordance with the standards of the Canadian Council on Animal Care, under an approved protocol by the Animal Use Subcommittee of Western University's Council on Animal Care.



For tumor-bearing animal studies, CB-17 mice (n=3) were inoculated with  $6 \times 10^5$  human HER2-expressing mouse epithelial cell-like bladder (MBT2.1, ref PMID 406041) cancer cells and an equivalent number of parental (HER2<sup>-</sup>) MBT2.1 tumor cells on the contralateral side six days prior to Treg adoptive cell transfer. Tumor cells were administered subcutaneously in 40 uL PBS on the posterior side of the mouse and animals were monitored twice daily for the duration of study. Both parental and HER2<sup>+</sup> MBT2.1 cells were cultured in complete DMEM and HER2 expression was maintained under Geneticin™ (G418 sulfate, 0.6 mg/mL) selection. Prior to inoculation, MBT2.1 cell surface expression of HER2 was measured using an antibody specific for human HER2 and data was acquired using a LSRII analytical flow cytometer.

### 5.2.9 Adoptive cell transfer

*PFC<sup>+</sup> Tregs*:  $10 \times 10^6$  Tregs were combined with an equivalent number of human peripheral blood mononuclear cells (PBMC) immediately prior to subcutaneous hind limb or intravenous tail vein administration (n = 4 mice each), injection volume = 150-200 uL PBS.

*PFC<sup>+</sup> HER2-CAR Tregs*:  $4 \times 10^6$  HER2-CAR Tregs were adoptively transferred by intravenous tail vein administration into tumor-bearing mice (n=3) that received  $10 \times 10^6$  human PBMC in 100 uL PBS by intraperitoneal administration one day prior. All injections were in a final volume of 100 uL PBS.

In this study, PBMC were administered to CB-17 mice to repopulate lymph nodes of these immunocompromised mice and improve the migration and retention of Tregs in lymph nodes. A separate <sup>19</sup>F MRI experiment showing PFC<sup>+</sup> PBMC trafficking *in vivo* after intraperitoneal administration is included in Appendix B (Part 7.2.3).

### 5.2.10 <sup>19</sup>F MRI acquisition and analysis

*In vivo* <sup>1</sup>H/<sup>19</sup>F MRI was performed +24 and +48 hours after adoptive cell transfer of PFC<sup>+</sup> Tregs. MRI was performed on a 3 Tesla human scanner (Discovery MR750, GE) using a dual tuned (<sup>1</sup>H/<sup>19</sup>F MRI) 4.3 cm diameter surface coil. The imaging field of view was 6 cm (length of mouse) x 3 cm (width of mouse) x 3.4 cm (depth of mouse) and

included reference phantoms of known  $^{19}\text{F}$  content. Mice were anesthetized with 2% isoflurane in 100% oxygen during these scans.

All mice were imaged prone with the surface coil placed as close to the imaging targets to maximize detection sensitivity. For mice receiving Tregs by subcutaneous injection, the coil was placed to focus on the site of Treg administration and nearby lymph nodes (lower half of the mouse body). For mice receiving Tregs by intravenous injection, the coil was positioned over the mouse body core, to include expected locations of Treg migration (*i.e.*, lungs, lymph nodes, and tumors if applicable).

Both  $^1\text{H}$  and  $^{19}\text{F}$  images were acquired using an optimized sensitive 3D balanced steady state free precession (bSSFP) imaging sequence.  $^1\text{H}$  images were acquired with 0.4 mm isotropic voxels, repetition time (TR)/echo time (TE) = 12.8/6.4 ms, flip angle (FA) =  $20^\circ$ , bandwidth (BW) =  $\pm 31.25$  kHz, phase cycles = 12, total scan time = 9 minutes.  $^{19}\text{F}$  images were acquired with  $1\text{mm}^3$  isotropic voxels, TR/TE = 5.6/2.8 ms, FA =  $72^\circ$ , BW =  $\pm 10$  kHz, number of excitations = 200, total scan time = 36 minutes.

Image analysis was performed in Horos software (Horos is a open source code software program that is distributed free of charge under the LGPL license at [Horosproject.org](http://Horosproject.org) and sponsored by Numbler Co LLC d.b.a Purview in Annapolis, MD, USA).  $^{19}\text{F}$  images were overlaid to  $^1\text{H}$  images for anatomical context of *in vivo* signal. The figures in this manuscript were obtained by viewing  $^{19}\text{F}/^1\text{H}$  overlays in 3D to capture an optimal section, with the aim of displaying as many signals as possible in a single plane. For image quantification, first the standard deviation of background noise in  $^{19}\text{F}$  images was measured from an image slice with no introduced  $^{19}\text{F}$  source. *In vivo*  $^{19}\text{F}$  regions of interest (ROIs) were selected at a threshold of 7 times the background standard deviation, therefore only  $^{19}\text{F}$  signals which exceed background levels were confidently selected.  $^{19}\text{F}$  signal in an ROI was calculated as the product of the ROI volume ( $\text{mm}^3$ ) and the average signals (arbitrary units). Similar analysis was performed for reference standard with known  $^{19}\text{F}$  content and included in the imaging field of view. A ratio of  $^{19}\text{F}$  signals was performed between reference standard and  $^{19}\text{F}$  signals *in vivo*, to obtain a measure of  $^{19}\text{F}$  atoms present at each *in vivo* ROI. From these values, an estimate of cell number was

calculated from  $^{19}\text{F}/\text{cell}$  measurements obtained with  $^{19}\text{F}$  NMR. Importantly, this estimation of cell number used  $^{19}\text{F}/\text{cell}$  measurements that were specific to each individual set of donor cells, not the average  $^{19}\text{F}/\text{cell}$  for Tregs. A percent of total cells injected (% injected dose, ID) was also calculated.

### 5.2.11 Post MRI verification of *in vivo* $^{19}\text{F}$ signal

At experimental endpoint, mouse lymph nodes were excised and gently passed through a 70  $\mu\text{m}$  cell strainer to generate a single cell suspension. Cell suspension was washed in PBS, resuspended in Hank's balanced salt solution (HBSS) + 0.1% bovine serum albumin (BSA) and then incubated on ice for 25 minutes with an antibody that specifically detects human CD45+ cells. Following washing, the cell suspension was resuspended in HBSS + BSA staining buffer and data was acquired on a LSRII analytical flow cytometer (BD Biosciences, San Jose, USA) and analyzed using FlowJo Software (v10, Tree Star, Inc, Ashland, USA).

## 5.3 Results

### 5.3.1 $^{19}\text{F}$ -PFC labeling of Tregs

To qualitatively assess PFC uptake by Tregs, flow cytometry and fluorescence microscopy was performed with red PFC (Figure 33A-E). Using flow cytometry, nearly 100% of Tregs incorporated red PFC compared to unlabeled Tregs (Figure 33A). The red fluorescent PFC was localized to the cytosol as confirmed with confocal microscopy (Figure 33B-E). Quantitative NMR showed that the Treg labeling efficiency with PFCs was on average  $8.673 \times 10^{11}$   $^{19}\text{F}$  atoms per cell, with a maximum of  $3.11 \times 10^{12}$   $^{19}\text{F}/\text{cell}$  and minimum of  $1.42 \times 10^{11}$   $^{19}\text{F}/\text{cell}$  ( $n = 5$ ) (Figure 33I).

The flow cytometry gating strategy is shown in Figure 33F. Tregs displayed a small decrease in viability with PFC labeling, with on average 84.7% viability in unlabeled cells compared to 75.6% viability for PFC labeled cells (Fig. 1G,  $p < .01$  by paired t-test). Human Tregs were defined as  $\text{CD4}^+\text{CD8}^-\text{CD25}^+\text{Foxp3}^+\text{Helios}^+$  and this phenotype was unchanged following PFC labeling ( $p > 0.05$ ) (Figure 33H).

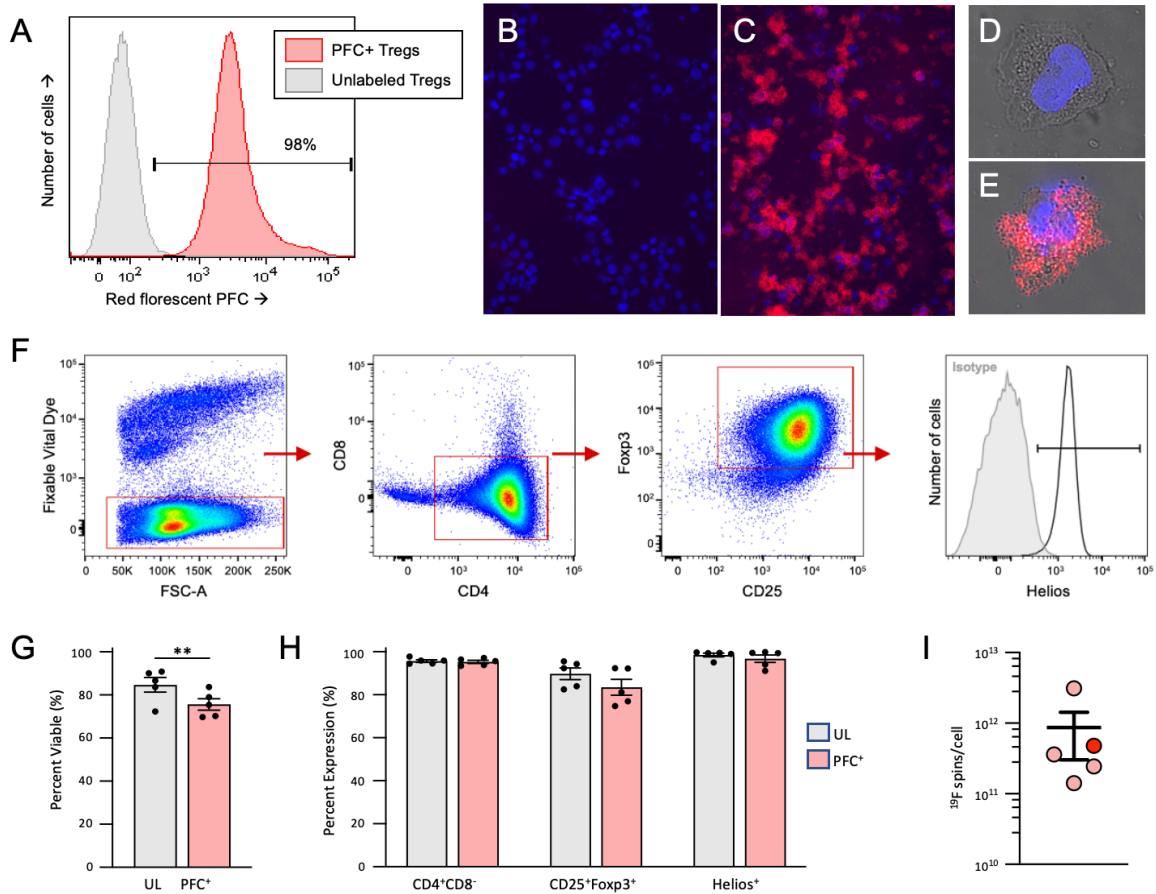


**Figure 33: PFC labeling of Tregs.** **A.** Compared to unlabeled Tregs, 98% of Tregs had associated red-fluorescent signal from incorporated PFC. Microscopy images of **(B)** unlabeled Tregs and **(C)** red-PFC<sup>+</sup> Tregs reveal that red-PFC is localized intracellularly surrounding DAPI-stained nuclei. Additional confocal microscopy reveals that compared to **(D)** unlabeled cells, **(E)** red-PFC is localized in the cytoplasm of labeled Tregs. **(F)** Treg viability was measured with fixable vital dye and Tregs were phenotype for CD4, CD8, CD25, Fcpx3, and Helios expression with flow cytometry. **(G)** Treg viability is reduced by < 10% when comparing donor cells with or without (UL = unlabeled) PFC labeling ( $n = 5$ , paired t-test,  $p < .01$ ). **(H)** No differences in Treg phenotype were detected with PFC labeling ( $n = 5$ , paired t-tests,  $p > .05$ ). **(I)** <sup>19</sup>F NMR measurements of non-fluorescent PFC<sup>+</sup> Tregs indicate that Tregs incorporate an average of  $8.673 \times 10^{11}$  <sup>19</sup>F atoms per cell. The dark red data point corresponds to a trial with HER2<sup>+</sup> CAR Tregs.

### 5.3.2 $^{19}\text{F}$ MRI monitors PFC<sup>+</sup> Tregs biodistribution *in vivo*

$^{19}\text{F}$  MRI reveals that PFC<sup>+</sup> Tregs traffic to lymph nodes and the spleen at multiple timepoints following subcutaneous (Figure 34) and intravenous (Figure 35) administration. All  $^{19}\text{F}$  signals had SNR > 7, with an average SNR of 8.7. The following estimates of the number of Tregs are based on the  $^{19}\text{F}$  signal measured at each location and the corresponding cell number based on  $^{19}\text{F}/\text{cell}$  measured by NMR.

Following subcutaneous administration of  $10 \times 10^6$  PFC<sup>+</sup> Tregs,  $^{19}\text{F}$  signal is detected in inguinal lymph nodes (range  $4.60 \times 10^4$  –  $1.61 \times 10^6$  Tregs), popliteal lymph nodes (range  $3.09 \times 10^4$  –  $1.42 \times 10^6$  Tregs), and the spleen (range  $4.82 \times 10^4$  –  $3.38 \times 10^6$  Tregs) (Figure 34 and 42 in Appendix A). The average number of cells migrating to lymph nodes was  $1.17 \times 10^6$  cells (14.5% ID) 24h p.i. and  $7.70 \times 10^5$  cells (10.88% ID) 48h p.i. The  $^{19}\text{F}$  signal in the spleen was associated with  $1.22 \times 10^6$  cells (15.2% ID) at 24h p.i. and  $4.09 \times 10^5$  cells (6.04% ID) at 48h p.i. Note that the calculations of % ID take into consideration that 1 mouse of 4 received  $5 \times 10^6$  cells instead of  $10 \times 10^6$  cells.

Following intravenous administration of  $10 \times 10^6$  PFC<sup>+</sup> Tregs,  $^{19}\text{F}$  signal is detected in axillary lymph nodes (range  $1.40$  –  $5.59 \times 10^5$  Tregs), renal lymph nodes (range  $7.39 \times 10^3$  –  $1.08 \times 10^6$  Tregs), lumbar lymph nodes (range  $3.12 \times 10^4$  –  $3.60 \times 10^6$  Tregs), and inguinal lymph nodes (range  $2.72 \times 10^4$  –  $2.13 \times 10^5$  Tregs) (Figure 35 and 43 in Appendix A). The average number of cells migrating to lymph nodes per mouse was  $1.91 \times 10^6$  cells (19% ID) after 24h p.i.,  $2.96 \times 10^6$  cells (30% ID) after 48h p.i. and  $1.43 \times 10^5$  cells (1.4% ID) after 72h p.i. Additionally,  $^{19}\text{F}$  signal was identified in the spleen in one mouse after 24h p.i. with the equivalent signal of  $3.63 \times 10^5$  Tregs (3.6% ID) and after 48h p.i. with  $1.62 \times 10^4$  Tregs (0.2% ID).

The presence of intact human CD45<sup>+</sup> cells in excised lymph nodes provides evidence that human cells (Tregs and/or PBMC) have migrated to lymph nodes. Human CD45<sup>+</sup> cells were confirmed in the popliteal lymph node and spleen after PFC<sup>+</sup> Tregs and unlabeled PBMC were administered subcutaneously (Figure 34C,D). Prior to tissue collection, this mouse had  $^{19}\text{F}$  signals in these organs (Figure 34A). Likewise, human CD45<sup>+</sup> cells were confirmed in the inguinal lymph node and spleen after PFC<sup>+</sup> Tregs and unlabeled PBMC

were administered intravenously (Figure 35C,D). Interestingly, the spleen from this mouse did not have  $^{19}\text{F}$  signal prior to sacrificing the animal, suggesting that CD45+ Tregs in the spleen did not produce signals above the  $^{19}\text{F}$  MRI detection threshold or these cells were overly disperse in the spleen for detection.

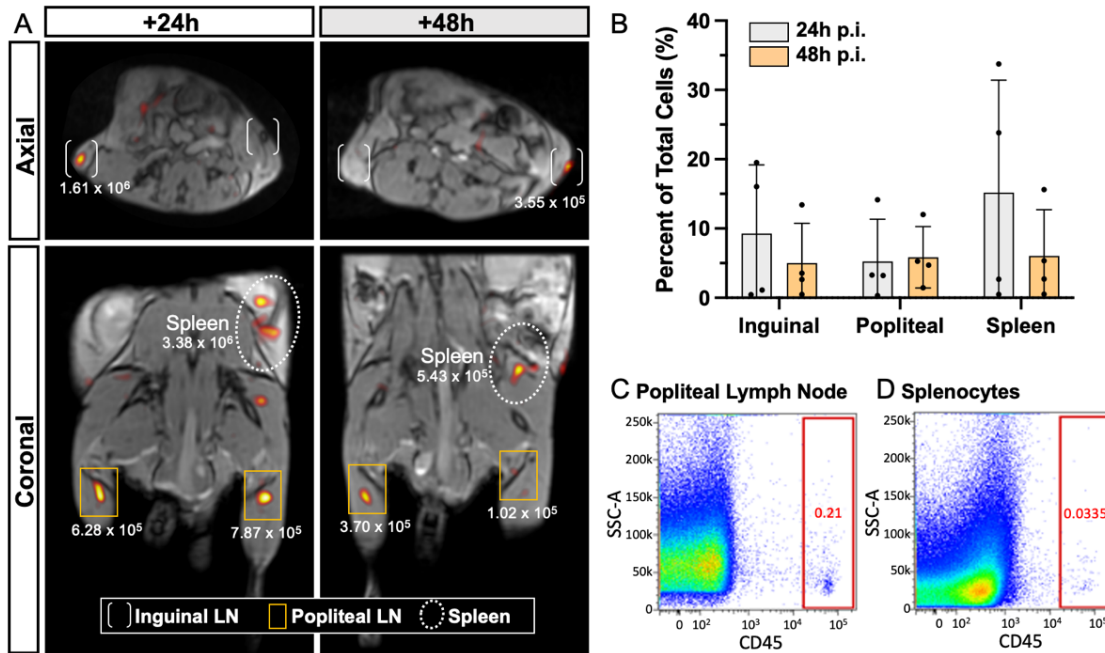


**Figure 34: PFC+ Treg biodistribution after subcutaneous administration. A.**  $^{19}\text{F}/^1\text{H}$  MRI shows  $^{19}\text{F}$  signal from PFC+ Tregs in inguinal lymph nodes (shown in axial sections), popliteal lymph nodes, and the spleen (shown in coronal sections), 24h and 48h p.i. The estimated number of cells based on  $^{19}\text{F}$  content at each location is recorded for this representative mouse. See Figure 42 in Appendix A for similar images and quantification of Tregs in the other 3 mice. **B.** Quantification of number of Tregs (% of total administered cells) for all 4 mice at 24h and 48h p.i. show no statistical differences (paired t-tests). Lymph node signals are a sum of the signals on left/right sides of the mouse. **C.** Excised popliteal lymph node and spleen analysed with flow cytometry reveals positive human CD45 staining.

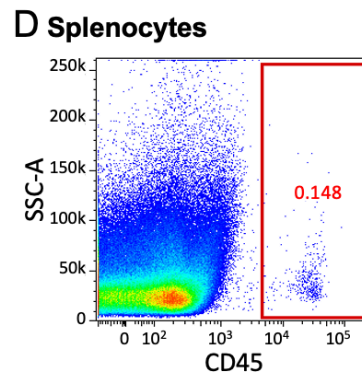
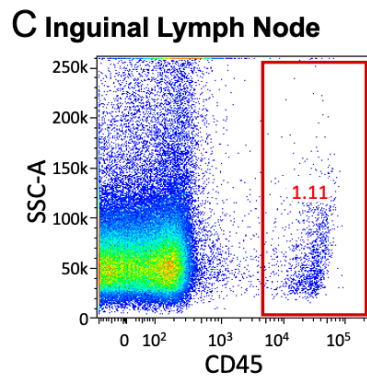
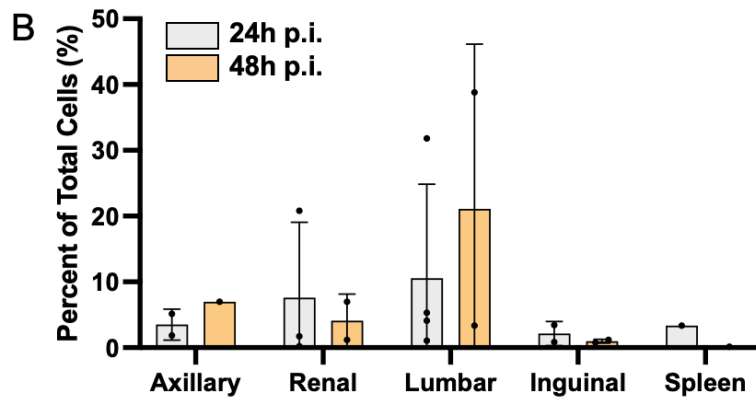
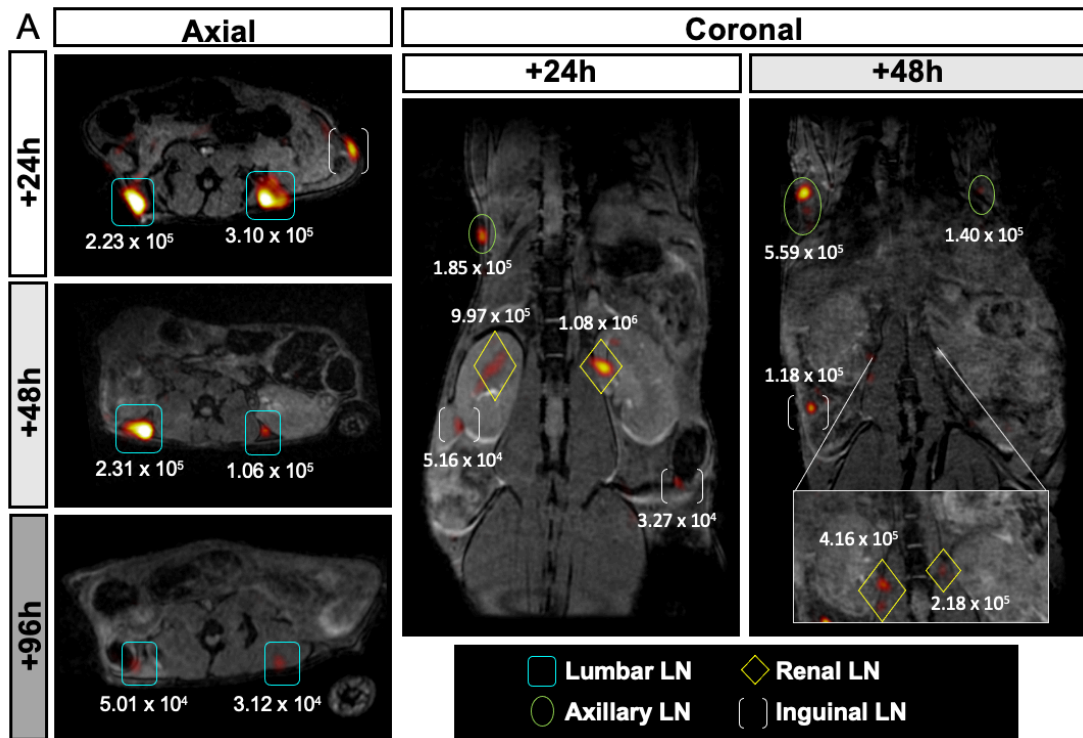


**Figure 35: PFC+ Treg biodistribution after intravenous administration. A.**  $^{19}\text{F}/^1\text{H}$  MRI shows  $^{19}\text{F}$  signal from PFC+ Tregs in lumbar lymph nodes (shown in axial sections), and the inguinal, renal, and axillary lymph nodes (shown in coronal sections), 24h, 48h, and 96h p.i..  $^{19}\text{F}$  signals were also found in the spleen of one mouse (see Figure 43 in Appendix A). The estimated number of cells based on  $^{19}\text{F}$  content at each location is recorded for this representative mouse. See Figure 43 in Appendix A for similar images and quantification of Tregs in the other 3 mice. **B.** Quantification of number of Tregs (% of total administered cells) for all 4 mice at 24h and 48h p.i. show no statistical differences (paired t-tests). Lymph node signals are a sum of the signals on left/right sides of the mouse. **C.** Excised inguinal lymph node and spleen analysed with flow cytometry reveals positive human CD45 staining.

### 5.3.3 HER2-CAR Tregs preferentially home to HER2+ MBT2.1 tumors and populate sentinel lymph nodes

HER2-expression in engineered MBT2.1 tumor cells was confirmed with flow cytometry (Figure 44 in Appendix A).  $^{19}\text{F}$  MRI signal was detected in all HER2+ MBT2.1 tumors ( $n = 3$ ) after intravenous administration of PFC+ HER2-CAR Tregs at 24h p.i. (Figure 36A and 45 in Appendix A). Furthermore, in one mouse (Figure 36A),  $^{19}\text{F}$  signal was seen in the HER2+ MBT2.1 tumor at all 3 timepoints (24h, 48, and 72h p.i.).  $^{19}\text{F}$  MRI signal was also measured at parental MBT2.1 tumors on day 1 and 2 in this same mouse, however with significantly lower associated cell numbers (Figure 36A,B). In the other two mice (Figure 45 in Appendix A), no  $^{19}\text{F}$  signal was detected in either MBT2.1 tumors at 48h p.i. and for one mouse,  $^{19}\text{F}$  signal was present in the HER2+ MBT2.1 tumor by 72h p.i. Therefore, there are individual differences in HER2-CAR Treg tumor-migration patterns between mice.

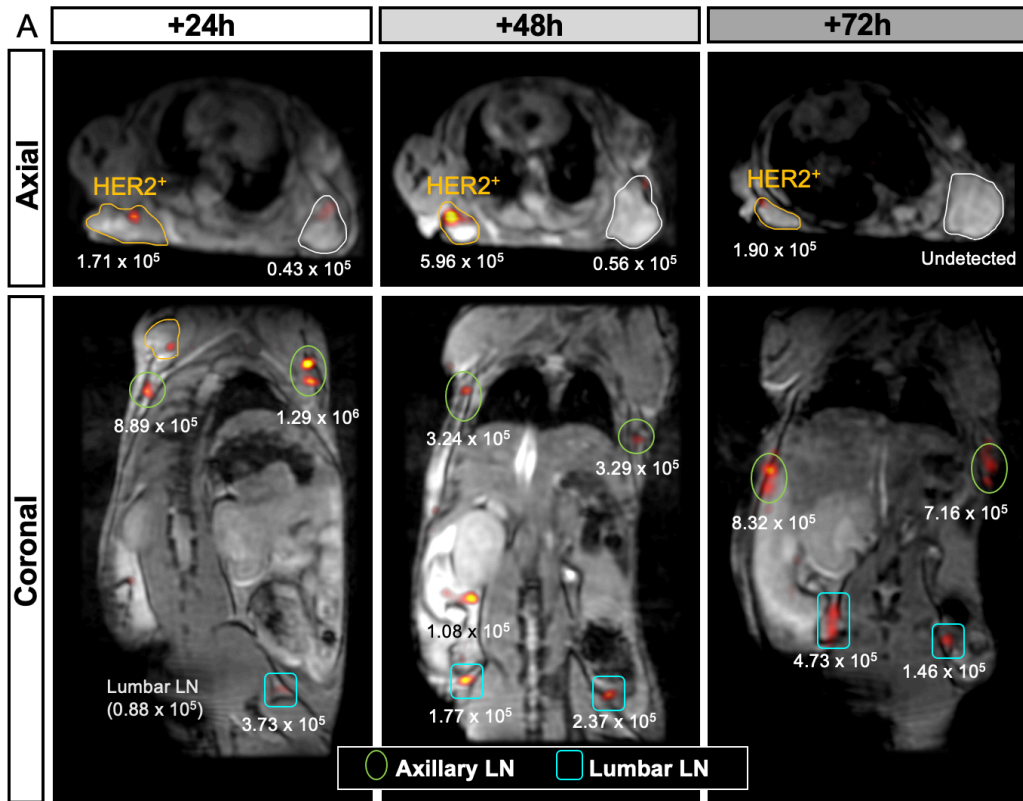
On average, the estimated number of Tregs that were detected at HER2+ MBT2.1 tumors was  $9.72 \times 10^4$  (2.4% ID) at 24h p.i.,  $5.96 \times 10^5$  (15% ID) at 48h p.i., and  $5.03 \times 10^5$  (13% ID) at 72h p.i. The estimated number of cells in the parental MBT2.1 tumor was 4.3



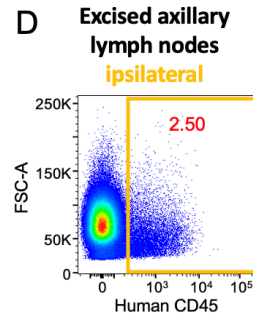
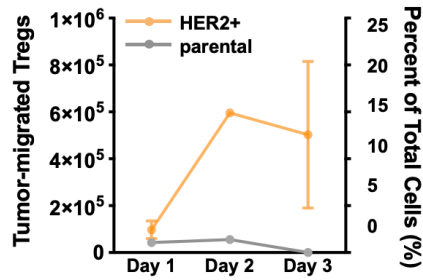
$\times 10^4$  (1.1% ID) at 24h p.i. and  $5.6 \times 10^4$  (1.4% ID) at 48h p.i. This corresponds to greater than 2-fold higher (24h p.i.) and 10-fold higher (48h p.i.)  $^{19}\text{F}$  signal in HER2+ compared to parental MBT2.1 tumors. These results indicate that PFC+ HER2-CAR Tregs preferentially migrate and remain at HER2+ MBT2.1 tumors compared to parental MBT2.1 tumors, with highest  $^{19}\text{F}$  signal occurring at 48h p.i.

PFC+ HER2-CAR Tregs were also detected in sentinel/axillary and lumbar lymph nodes following intravenous administration on all 3 imaging days (Figure 36A), with similar biodistribution to PFC+ Tregs (Figure 35).  $^{19}\text{F}$  signals on the ipsilateral and contralateral side of the HER2+ MBT2.1 tumor were not significantly different (Figure 36C). At 24h p.i., on average  $3.85 \times 10^5$  HER2-CAR Tregs (10% ID) were detected on the ipsilateral side and  $9.71 \times 10^5$  cells (24% ID) were detected on the contralateral side. At 48h p.i., on average  $3.77 \times 10^5$  HER2-CAR Tregs (9% ID) were detected on the ipsilateral side and  $2.22 \times 10^5$  cells (8% ID) on the contralateral side. Lastly at 72h p.i., on average  $10.3 \times 10^5$  HER2-CAR Tregs (26% ID) were detected on the ipsilateral side compared to  $4.59 \times 10^5$  cells (11% ID) on the contralateral side. At experimental endpoint, single cell suspensions of excised axillary LNs both ipsilateral and contralateral to HER2+ tumors contained human CD45+ cells as assessed by flow cytometry (Figure 36D).

There were 6 timepoints where  $^{19}\text{F}$  signal from PFC+ HER2-CAR Tregs was captured in HER2+ MBT2.1 tumors; at 24h p.i.  $n = 3/3$ , at 48h p.i.,  $n = 1/3$ , and at 72h p.i.  $n = 2/3$  mice. Interestingly, 5 of 6 of these instances also had  $^{19}\text{F}$  signal in the sentinel/axillary lymph node. Therefore, there seems to be a close relationship in HER2-CAR Treg migration to the HER2+ tumor and the sentinel/axillary lymph node.



**B HER2-CAR Treg migration to tumors**



**C HER2-CAR Treg migration to lymph nodes**

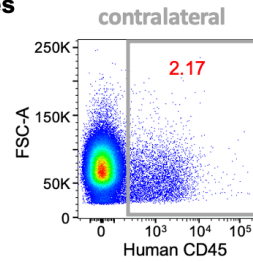
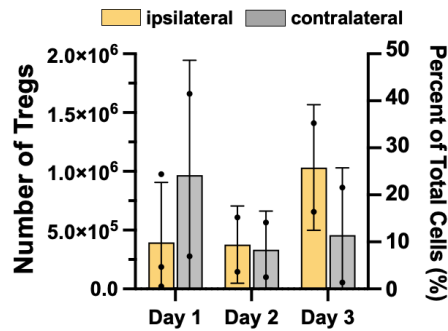


**Figure 36: PFC+ HER2-CAR Treg biodistribution after intravenous administration to HER2+ and parental MBT2.1 tumor-bearing mice. A.  $^{19}\text{F}/^1\text{H}$  MRI shows  $^{19}\text{F}$  signal from PFC+ HER2-CAR Tregs in HER2+ and parental MBT2.1 tumors (shown in axial sections), and the axillary and lumbar lymph nodes (coronal sections) at 24h, 48h, and 72h p.i. The estimated number of cells based on  $^{19}\text{F}$  content at each ROI is recorded. B. Quantification of number of Tregs (and % of total administered cells) reaching HER2+ (orange) and parental (grey) MBT2.1 tumor across the 3 timepoints. C. Quantification of the number of Tregs (and % total of administered cells) reaching lymph nodes on the side ipsilateral or contralateral to the HER2+ MBT2.1 tumor. There were no significant differences between the  $^{19}\text{F}$  signal on either side of the mouse. D. Excised sentinel/axillary lymph nodes analysed with flow cytometry reveals positive human CD45 staining on both the side ipsilateral (orange) and contralateral (grey) to the HER2+ MBT2.1 tumor.**

## 5.4 Discussion

Numerous clinical trials have shown that Treg therapies have proven safe and effective against transplant rejection and autoimmune diseases<sup>11,14,34-39</sup>. However, questions remain about the optimal cell dose, route of administration, timing, and cell product optimization, including the design of CAR Tregs. Ultimately, little is known about the *in vivo* biodistribution and fate of administered Tregs in therapy recipients. In this work, we demonstrate  $^{19}\text{F}$  MRI is a suitable imaging modality to image and quantify PFC+ human Treg *in vivo* migration.

### 5.4.1 Labeling Tregs with PFCs

First, we demonstrate successful PFC labeling of human Tregs. To the best of our knowledge, this is the first attempt to label human Tregs with PFC and to track human-derived Tregs with MRI. Intracellular Treg labeling with PFC was successful with high labeling efficiencies (nearly 100%) within the range of  $1.42 \times 10^{11}$   $^{19}\text{F}$ /cell to  $3.11 \times 10^{12}$

$^{19}\text{F}/\text{cell}$ . Due to the large range in Treg  $^{19}\text{F}/\text{cell}$  loading, the quantification and estimation of cell number from  $^{19}\text{F}$  images was based on individual donor uptake of  $^{19}\text{F}/\text{Treg}$  rather than average  $^{19}\text{F}/\text{Treg}$ . Notably, labeling HER2-CAR Tregs with PFCs resulted in similar  $^{19}\text{F}$  uptake as untransduced Tregs. Tregs may theoretically have improved uptake of PFCs relative to other T cell subsets owing to an overall larger cytoplasmic volume<sup>40,41</sup>.

Treg phenotype was unchanged with PFC labeling. There was a reduction in cell viability when comparing PFC+ Tregs to unlabeled control Tregs but the difference in viability was less than 10%. In all instances of Treg cell labeling, Treg viability was  $\geq 70\%$ , which meets the minimum criteria defined by the United States Food and Drug Administration as of 2020 (ref<sup>42</sup>).

#### 5.4.2 *In vivo* tracking of PFC+ Tregs

*In vivo* migration of PFC+ Tregs to lymph nodes and the spleen was quantified with  $^{19}\text{F}$  MRI. Tregs are expected to migrate to these secondary lymphoid tissues to exert their function. The mice in this study also received unlabeled PBMC which promote Treg migration to lymph nodes and we have previously tracked PBMC with  $^{19}\text{F}$  MRI to lymph nodes and spleen (see Appendix B, Part 7.2.3). Interestingly, the locations and number of Tregs quantified at lymph nodes and spleen were different for each administration route and over time. After subcutaneous administration, a higher number of PFC+ Tregs are detected with  $^{19}\text{F}$  MRI at lymph nodes at 24h p.i. compared to 48h p.i. We expect this is predominately due to the death of Tregs and clearance of PFC since the polyclonal Tregs do not have an antigen target to be stimulated by. A loss of  $^{19}\text{F}$  signal may also be due to proliferation of Tregs and dilution of PFC per cell, however this is not likely since this requires IL-2 (which has low *in vivo* abundance), TCR signalling, and co-stimulation for Tregs to proliferate *in vivo*. Conversely, following intravenous administration, a higher number of PFC+ Tregs are detected at lymph nodes at 48h p.i. compared to 24h p.i. with  $^{19}\text{F}$  MRI. This indicates that after intravenous administration, Tregs continue to accumulate in lymph nodes over time and the increasing density of PFC molecules per voxel heightens detected  $^{19}\text{F}$  signal. Subsequently,  $^{19}\text{F}$  signal reduces at later timepoints, again most likely due to lack of relevant antigen Treg targets and cell death. This may be

an important consideration when determining the optimal window of time for imaging. This *in vivo* imaging view of immune cell traffic has not been demonstrated before.

When comparing intravenous versus subcutaneous injection, we report that PFC<sup>+</sup> Tregs are detected with <sup>19</sup>F MRI at different lymph nodes; for subcutaneous administration, Tregs were found in popliteal and inguinal nodes, whereas after intravenous administration, Tregs were found in inguinal, lumbar, renal, and axillary lymph nodes. This signifies that Tregs have different migration patterns based on their administration route and access to lymph nodes. On average, a higher number of Tregs migrate to lymph nodes after intravenous administration (30% ID at optimal timepoint) compared to subcutaneous administration (14.5% ID at optimal timepoint), however, this is not a statistically significant difference likely due to large variability between mice and low sample size (n = 4 mice). The two administration routes were expected to result in different Treg biodistributions, since with intravenous administration circulating Tregs have improved access to lymph nodes, compared to subcutaneously administered Tregs which have a less direct path to tissue draining lymph nodes. Conversely, a higher number of Tregs consistently migrate to the spleen after subcutaneous administration but below detection limits after intravenous administration (except for n = 1 of 4 mice). The spleen is a secondary lymphoid tissue which is nearby the injection site. Therefore, we learn from cellular <sup>19</sup>F MRI that the route of Treg administration may impact the treatment efficacy, *i.e.*, the number of Tregs reaching lymph nodes or spleen.

Next, Tregs were engineered with a HER2 specific CAR using lentiviral technology and we assessed the homing capacity of these cells to HER2<sup>±</sup> grafts with <sup>19</sup>F MRI. As shown by <sup>19</sup>F MRI, CAR Tregs rapidly trafficked to tumors and lymph nodes (within 24 hours), with 3/3 mice showing signal in the HER2<sup>+</sup> tumor and only 1/3 mice showing signal in the HER2<sup>-</sup> tumor. Overall a greater number of PFC<sup>+</sup> CAR Tregs were present at HER2<sup>+</sup> tumors, with up to 10-fold higher <sup>19</sup>F signals in HER2<sup>+</sup> tumors (at 48h p.i.), demonstrating that CAR-directed specificity can affect Treg trafficking and persistence *in vivo*. Similar results were obtained by our group using HLA-A2 as the CAR Treg target<sup>17</sup>, with BLI showing preferential migration of CAR Tregs to the HLA-A2<sup>+</sup> graft over the HLA-A2<sup>-</sup> graft by a similar ratio. We are excited by the feasibility of <sup>19</sup>F MRI tracking of

CAR Tregs because of direct quantification of  $^{19}\text{F}$  atoms and potential for clinical translation.

### 5.4.3 $^{19}\text{F}$ MRI sensitivity and novel findings

Excitingly, this is the first published demonstration of  $^{19}\text{F}$  detection of intravenously infused PFC+ T cells to target sites *in vivo*. The majority of  $^{19}\text{F}$  MRI cell tracking studies involve direct administration (*e.g.*, to a tumor) rather than systemic administration. Bouchlaka *et al.* (2016)<sup>43</sup> compare administration routes and show that  $10 \times 10^6$  NK cells ( $3.8 \times 10^{11}$   $^{19}\text{F}$  atoms/cell) could be detected with  $^{19}\text{F}$  MRI after direct intratumoral administration, but not after intravenous administration. Similarly, Saini *et al.* (2019)<sup>32</sup> demonstrate that  $5 \times 10^6$  T cells ( $7 \times 10^{12}$   $^{19}\text{F}$  atoms/cell) could be detected with  $^{19}\text{F}$  MRI after subcutaneous administration (with SNR of 8) but not after intravenous administration. Furthermore, a similar finding was seen with dendritic cells ( $3.7 \times 10^{12}$   $^{19}\text{F}$  atoms/cell) in patients, with failure to detect migrated DC with  $^{19}\text{F}$  MRI in a nearby sentinel lymph node<sup>24</sup>. Ultimately, it is challenging to detect migrated cells *in vivo* with  $^{19}\text{F}$  MRI, where cells become dispersed, because of the minimum required  $^{19}\text{F}$  density per voxel.

Importantly, Treg therapies in clinical trials are most commonly administered by intravenous infusion<sup>13,14,34–39</sup>, therefore we sought to track these cells with this methodology and with clinically feasible 3 T MRI. Our ability to detect relatively few Tregs (on the order of  $10^4$  cells) with  $^{19}\text{F}$  MRI may come from many factors. First,  $^{19}\text{F}$  images at 3 T were acquired with a custom surface coil, which focuses the imaging region and enhances sensitivity, and a sensitive 3D bSSFP imaging sequence. bSSFP is a rapid sequence allowing for 200 averages to be acquired to increase SNR within a 40-minute scan. Furthermore, steady state imaging enhances the amount of signal that can be acquired<sup>44</sup>. Based on our previous studies with the same setup<sup>45,46</sup>, the theoretical detection limit of PFC+ Tregs on our system could be between  $6.4 \times 10^3$  and  $1.5 \times 10^4$  cells (with maximum achieved  $3.11 \times 10^{12}$   $^{19}\text{F}$  atoms/cell).  $^{19}\text{F}$  detection of PFC+ cells requires a high number of locally accumulated labeled cells. For Treg biodistribution studies,  $10 \times 10^6$  Tregs were administered alongside  $10 \times 10^6$  unlabeled human PBMC. Even fewer cells were administered for CAR Treg biodistribution studies ( $4 \times 10^6$ ) and

were successfully detected *in vivo*. The expression of the CAR enhances migration of Treg to HER2+ tumors and though increasing PFC+ cell density per voxel, improves <sup>19</sup>F sensitivity. Longitudinal sensitivity is known to be influenced by cell proliferation and PFC dilution, however Tregs are expected to only slowly proliferate *in vivo*.

#### 5.4.4 Limitations

Direct labeling approaches, such as the PFC labeling protocol used in this work, may only enable short-term cell tracking (on the order of days) compared to reporter gene approaches<sup>47,48</sup>. As we demonstrate, short term cell tracking with a direct labeling approach can provide important information on cell delivery and initial cell trafficking by <sup>19</sup>F MRI. Additionally, accurate quantification of <sup>19</sup>F signals and cell number is feasible for slowly proliferating cells in this time period. However, it could be plausible that the death of Tregs and their uptake by macrophages could contribute to non-specific signals. This effect is known as bystander cell uptake. Six days after administration of PFC-labeled NK cells to mouse tumors, Lechuga *et al.*<sup>49</sup> performed detailed histology to show that 54% of NK cells contained PFC and only 0.3% of surrounding cells contained PFC. Of this 0.3%, only 29% expressed the macrophage marker F4/80. While this result does not negate the possibility of false <sup>19</sup>F signals due to bystander uptake at early timepoints after cell administration, this impressive finding demonstrates that <sup>19</sup>F signal was highly associated with the adoptively transferred cells.

Comparatively, reporter gene approaches offer long-term and repeated tracking of cells, where signal is specific to live, engineered cells, but only offer indirect quantification (no measurement of cell number). Jacob J. *et al.* (2021)<sup>18</sup> demonstrate long term tracking (up to 6 weeks) of human-derived Tregs to skin transplant sites in mice. Tregs had been engineered with sodium iodide symporter (NIS) which enables repeat imaging of engineered cells after infusion of [<sup>99m</sup>Tc]TcO<sub>4</sub><sup>-</sup>. It was shown that this approach had no negative effects on Tregs but that there was off-target uptake of the radiotracer in clearance organs. Reporter gene imaging may be feasible with low regulatory hurdles for CAR Tregs, which already require genetic engineering of the cell product. While SPECT reporter gene imaging has low spatial resolution and poor anatomical information, MRI reporter gene imaging may be promising for CAR Treg long-term tracking<sup>50</sup>.

## 5.5 Conclusion

For successful application of Treg cellular therapeutics, infused Tregs must migrate in sufficient numbers to target locations, including secondary lymphoid tissues and tissue grafts (if applicable). There is an immediate clinical need for an imaging technique that can visualize and quantify Treg migration. In this work, we successfully label human Tregs with PFC and track their *in vivo* anatomical location in the days following administration using  $^{19}\text{F}$  MRI at 3 Tesla. There were quantitative differences in  $^{19}\text{F}$  signals and migration patterns that occurred with Treg administration routes and for CAR Tregs homing to tumors. Additionally,  $^{19}\text{F}$  measurements captured subtle individual differences in migration efficiencies between mice. This study represents the first to track human Tregs with MRI and this contributed to our understanding of *in vivo* Treg migration in preclinical models. Additionally, improvements to  $^{19}\text{F}$  cellular imaging strategies allowed for the detection of intravenously infused cells to target sites for the first time. Overall,  $^{19}\text{F}$  MRI is suitable as a non-invasive modality to predict the effectiveness of cellular immunotherapies and compared to other available imaging techniques for Treg tracking,  $^{19}\text{F}$  MRI is safe, quantitative, and clinically feasible.  $^{19}\text{F}$  MRI has the potential to provide information that can inform clinical status of Treg therapies in the days following administration and to aid further preclinical testing and development of Treg therapies.



## 5.6 Chapter 5 references

1. Romano, M., Fanelli, G., Albany, C. J., Giganti, G. & Lombardi, G. Past, present, and future of regulatory T cell therapy in transplantation and autoimmunity. *Front. Immunol.* **10**, (2019).
2. Giganti, G. *et al.* Treg cell therapy: How cell heterogeneity can make the difference. *Eur. J. Immunol.* **51**, 39–55 (2021).
3. Raffin, C., Vo, L. T. & Bluestone, J. A. Treg cell-based therapies: challenges and perspectives. *Nat. Rev. Immunol.* **20**, 158–172 (2020).
4. Togashi, Y., Shitara, K. & Nishikawa, H. Regulatory T cells in cancer immunosuppression — implications for anticancer therapy. *Nat. Rev. Clin. Oncol.* **16**, (2019).
5. Qureshi, O. S. *et al.* Trans-endocytosis of CD80 and CD86: A molecular basis for the cell-extrinsic function of CTLA-4. *Science (80-. ).* **332**, 600–603 (2011).
6. Trzonkowski, P. *et al.* Hurdles in therapy with regulatory T cells. *Sci. Transl. Med.* **7**, 1–11 (2015).
7. Ferreira, L. M. R., Muller, Y. D., Bluestone, J. A. & Tang, Q. Next-generation regulatory T cell therapy. *Nat. Rev. Drug Discov.* **18**, 749–769 (2019).
8. Wardell, C. M., MacDonald, K. N., Levings, M. K. & Cook, L. Cross talk between human regulatory T cells and antigen-presenting cells: Lessons for clinical applications. *Eur. J. Immunol.* **51**, 27–38 (2021).
9. MacDonald, K. N., Piret, J. M. & Levings, M. K. Methods to manufacture regulatory T cells for cell therapy. *Clin. Exp. Immunol.* **197**, 52–63 (2019).
10. Dijke, I. E. *et al.* Discarded human thymus is a novel source of stable and long-lived therapeutic regulatory T cells. *Am. J. Transplant.* **16**, 58–71 (2016).

11. Bernaldo-de-quiros, E. *et al.* “First-in-human” clinical trial employing adoptive transfer of autologous thymus-derived Treg cells (thyTreg) to prevent graft rejection in heart-transplanted children. **104**, (2020).
12. Chandran, S. *et al.* Polyclonal Regulatory T Cell Therapy for Control of Inflammation in Kidney Transplants. *Am. J. Transplant.* **17**, 2945–2954 (2017).
13. MacMillan, M. L. *et al.* First-in-human phase 1 trial of induced regulatory T cells for graft-versus-host disease prophylaxis in HLA-matched siblings. *Blood Adv.* **5**, 1425–1436 (2021).
14. Sawitzki, B. *et al.* Regulatory cell therapy in kidney transplantation (The ONE Study): a harmonised design and analysis of seven non-randomised, single-arm, phase 1/2A trials. *Lancet* **395**, 1627–1639 (2020).
15. Nguyen, V. H. *et al.* In vivo dynamics of regulatory T-cell trafficking and survival predict effective strategies to control graft-versus-host disease following allogeneic transplantation. *Blood* **109**, 2649–2656 (2007).
16. Sharif-Paghaleh, E. *et al.* In vivo SPECT reporter gene imaging of regulatory T cells. *PLoS One* **6**, 1–8 (2011).
17. Dawson, N. A. J. *et al.* Systematic testing and specificity mapping of alloantigen-specific chimeric antigen receptors in regulatory T cells. *JCI Insight* **4**, (2019).
18. Jacob, J. *et al.* Spatiotemporal in vivo tracking of polyclonal human regulatory T cells (Tregs) reveals a role for innate immune cells in Treg transplant recruitment. *Mol. Ther. - Methods Clin. Dev.* **20**, 324–336 (2021).
19. Jacob, J. *et al.* Radiolabeling of polyclonally expanded human regulatory T cells (Treg) with <sup>89</sup>Zr-oxine for medium-term in vivo cell tracking. *Molecules* **28**, (2023).

20. De Vries, I. J. M. *et al.* Magnetic resonance tracking of dendritic cells in melanoma patients for monitoring of cellular therapy. *Nat. Biotechnol.* **23**, 1407–1413 (2005).
21. Ahrens, E. T., Flores, R., Xu, H. & Morel, P. A. In vivo imaging platform for tracking immunotherapeutic cells. *Nat. Biotechnol.* **23**, 983–987 (2005).
22. Helfer, B. M. *et al.* Functional assessment of human dendritic cells labeled for in vivo <sup>19</sup>F magnetic resonance imaging cell tracking. *Cytotherapy* **12**, 238–250 (2010).
23. Fink, C. *et al.* Fluorine-19 Cellular MRI Detection of In Vivo Dendritic Cell Migration and Subsequent Induction of Tumor Antigen-Specific Immunotherapeutic Response. *Mol. Imaging Biol.* **19**, (2019).
24. Ahrens, E. T., Helfer, B. M., O’Hanlon, C. F. & Schirda, C. Clinical cell therapy imaging using a perfluorocarbon tracer and fluorine-19 MRI. *Magn. Reson. Med.* **72**, 1696–1701 (2014).
25. Fink, C. *et al.* <sup>19</sup>F-perfluorocarbon-labeled human peripheral blood mononuclear cells can be detected in vivo using clinical MRI parameters in a therapeutic cell setting. *Sci. Rep.* **8**, 1–13 (2018).
26. Janjic, J. M., Srinivas, M., Kadayakkara, D. K. K. & Ahrens, E. T. Self-delivering nanoemulsions for dual fluorine-19 MRI and fluorescence detection. *J. Am. Chem. Soc.* **130**, 2832–2841 (2008).
27. Srinivas, M., Morel, P. A., Ernst, L. A., Laidlaw, D. H. & Ahrens, E. T. Fluorine-19 MRI for visualization and quantification of cell migration in a diabetes model. *Magn. Reson. Med.* **58**, 725–734 (2007).
28. Chapelin, F. *et al.* Fluorine-19 nuclear magnetic resonance of chimeric antigen receptor T cell biodistribution in murine cancer model. *Sci. Rep.* **7**, 1–12 (2017).

29. Hingorani, D. V. *et al.* Cell penetrating peptide functionalized perfluorocarbon nanoemulsions for targeted cell labeling and enhanced fluorine-19 MRI detection. *Magn. Reson. Med.* 974–987 (2019). doi:10.1002/mrm.27988
30. Gonzales, C. *et al.* In-vivo detection and tracking of T cells in various organs in a melanoma tumor model by <sup>19</sup>F-fluorine MRS/MRI. *PLoS One* **11**, 1–18 (2016).
31. Dubois, V. P., Sehl, O. C., Foster, P. J. & Ronald, J. A. Visualizing CAR-T cell Immunotherapy Using 3 Tesla Fluorine-19 MRI. *Mol. Imaging Biol.* (2021). doi:10.1007/s11307-021-01672-3
32. Saini, S. *et al.* Challenges for labeling and longitudinal tracking of adoptively transferred autoreactive T lymphocytes in an experimental type-1 diabetes model. *Magn. Reson. Mater. Physics, Biol. Med.* **32**, 295–305 (2019).
33. MacDonald, K. N. *et al.* Consequences of adjusting cell density and feed frequency on serum-free expansion of thymic regulatory T cells. *Cytotherapy* **24**, 1121–1135 (2022).
34. Trzonkowski, P. *et al.* First-in-man clinical results of the treatment of patients with graft versus host disease with human ex vivo expanded CD4+CD25+CD127- T regulatory cells. *Clin. Immunol.* **133**, 22–26 (2009).
35. Brunstein, C. G. *et al.* Infusion of ex vivo expanded T regulatory cells in adults transplanted with umbilical cord blood: Safety profile and detection kinetics. *Blood* **117**, 1061–1070 (2011).
36. Brunstein, C. G. *et al.* Umbilical cord blood-derived T regulatory cells to prevent GVHD: Kinetics, toxicity profile, and clinical effect. *Blood* **127**, 1044–1051 (2016).
37. Di Ianni, M. *et al.* Tregs prevent GVHD and promote immune reconstitution in HLA-haploidentical transplantation. *Blood* **117**, 3921–3928 (2011).

38. Martelli, M. F. *et al.* HLA-haploidentical transplantation with regulatory and conventional T-cell adoptive immunotherapy prevents acute leukemia relapse. *Blood* **124**, 638–644 (2014).
39. Theil, A. *et al.* Adoptive transfer of allogeneic regulatory T cells into patients with chronic graft-versus-host disease. *Cytotherapy* **17**, 473–486 (2015).
40. Chapelin, F., Capitini, C. M. & Ahrens, E. T. Fluorine-19 MRI for detection and quantification of immune cell therapy for cancer. *J. Immunother. Cancer* **6**, 1–11 (2018).
41. Ahrens, E. T. & Bulte, J. W. M. Tracking immune cells in vivo using magnetic resonance imaging. *Nat. Rev. Immunol.* **13**, (2013).
42. U.S. Department of Health and Human Services. Food and Drug Administration (FDA). *Chemistry, Manufacturing, and Control (CMC) Information for Human Gene Therapy Investigational New Drug Applications (INDs): Guidance for Industry.* (2020).
43. Bouchlaka, M. N. *et al.* 19F-MRI for monitoring human NK cells in vivo. *Oncoimmunology* **5**, 1–12 (2016).
44. Scheffler, K. & Lehnhardt, S. Principles and applications of balanced SSFP techniques. *Eur. Radiol.* **13**, 2409–2418 (2003).
45. Makela, A. V. & Foster, P. J. Preclinical 19F MRI cell tracking at 3 Tesla. *Magn. Reson. Mater. Physics, Biol. Med.* (2018). doi:10.1007/s10334-018-0715-7
46. Sehl, O. C. & Foster, P. J. The sensitivity of magnetic particle imaging and fluorine-19 magnetic resonance imaging for cell tracking. *Sci. Rep.* **11**, 1–12 (2021).
47. Iafrate, M. & Fruhwirth, G. O. How Non-invasive in vivo Cell Tracking Supports the Development and Translation of Cancer Immunotherapies. *Front. Physiol.* **11**, 1–30 (2020).

48. Helfer, B. M. *et al.* Options for imaging cellular therapeutics in vivo: a multi-stakeholder perspective. *Cytotherapy*, 1–17 (2021).
49. Lechuga, L. M. *et al.* Detection and viability of murine NK cells in vivo in a lymphoma model using fluorine-19 MRI. *NMR Biomed.* **34**, 1–14 (2021).
50. Nyström, N. N. *et al.* A Genetically Encoded Magnetic Resonance Imaging Reporter Enables Sensitive Detection and Tracking of Spontaneous Metastases in Deep Tissues. *Cancer Res.* 673–685 (2022). doi:10.1158/0008-5472.can-22-2770

## 6 Summary and Future Work

Cellular therapeutics involve the isolation, expansion, modification, and re-administration of immune cells or stem cells for the treatment of a growing list of diseases and conditions. This thesis is focused on MSC and Treg therapies. MSC can be differentiated to replenish and restore tissues damaged by injury or disease and can exert paracrine functions through release of growth factors and inflammatory mediators. Ultimately, the proper delivery (location) and number of MSC that persist are critical for therapeutic success. Tregs are immunosuppressive cells that act both locally, through the release of anti-inflammatory cytokines, and systemically, through the interaction with other immune cells. Tregs are expected to migrate to inflamed tissues (e.g., those impacted by autoimmune disease or transplantation sites) and to lymph nodes. Similar to MSC therapy, the location and number of Tregs that reach these targets can act as a biomarker to predict patient outcomes. Currently, not much is known about the immediate fate of these cellular therapies after their administration without invasive biopsy.

This thesis is focused on developing and applying cellular imaging technologies, including SPION-based and  $^{19}\text{F}$  MRI and MPI. SPION-based MRI used for several decades for cell tracking, and while highly sensitive has two major limitations: lack of quantitation and signal specificity.  $^{19}\text{F}$  MRI has surfaced as a PFC-based cellular imaging technique and while signals are specific (hotspot without appreciable background) and directly quantitative, is challenged with low sensitivity. Therefore, SPION-based MRI and  $^{19}\text{F}$  MRI are considered complimentary. In the past few years, MPI is becoming popular and has great potential for SPION-based cell tracking as it is sensitive, specific, and directly quantitative. However, techniques for MPI cell tracking are new and there is a need to study its sensitivity relative to other modalities and to establish reproducible and accurate quantification techniques.

These comparisons are supported by this thesis. In Chapter 2, SPION-based MRI and MPI are directly compared for detection of MSC *in vivo* and combined with  $^{19}\text{F}$  MRI for tracking a second immune cell population (macrophages). In Chapter 3, the cellular detection sensitivity of  $^{19}\text{F}$  MRI is determined and directly compared to the newly emerging cellular imaging modality MPI. In Chapter 4, quantitative methods are developed for MPI. Finally, in Chapter 5,  $^{19}\text{F}$  MRI is applied to tracking and quantification of Tregs *in vivo*.

## 6.1 Discussion and conclusions

### 6.1.1 Chapter 2

In this chapter, we apply a trimodal imaging approach that combines SPION-based MRI,  $^{19}\text{F}$  MRI, and MPI to enable tracking of 2 cell populations *in vivo* (MSC and infiltrating macrophages). MSC were labeled with ferumoxytol then administered to mice and tracked by MRI and MPI after 1 and 12 days. These mice also received PFC nanoemulsion intravenously to label and detect resident immune cells *in vivo* by  $^{19}\text{F}$  MRI at the same timepoints. The main findings were as follows:

- 1. Ferumoxytol can be used as a dual MRI/MPI tracer for cell tracking and each imaging modality provides unique information on cell fate.** With MRI, ferumoxytol-labeled MSC are detected as a hypointense region *in vivo* and MSC delivery relative to anatomy was confirmed with high spatial resolution. However, this signal void was often difficult to locate nearby other tissues (e.g., bones) and could not provide an estimate of cell number. Comparatively, ferumoxytol-labeled MSC are detected as hotspot signals by MPI and were quantified over time, showing a reduction in estimated number of MSCs. MPI signals were directly linear with ferumoxytol content (between 0.75 ug – 30 ug) and MSCs were labeled with 2.4 pg Fe/cell. While ferumoxytol can be detected by MPI and  $^1\text{H}$  MRI, this USPIO produces low SNR MPI signals with poor MPI resolution (FWHM of 66.3 mT), therefore we would not recommend using ferumoxytol as a cell tracking agent for MPI.



- 2. Intravenous PFC delivery and  $^{19}\text{F}$  MRI enabled imaging of immune infiltration (macrophage influx) associated with cell transplantation.** PFC accumulated in the mouse limb ipsilateral to the site of MSC implantation and was detected by  $^{19}\text{F}$  MRI.  $^{19}\text{F}$  signals were present on both day 1 and 12, with no significant differences in the amount of signal at these two timepoints.

Overall, we demonstrate that this unique combination of cellular imaging modalities can be used to confirm MSC delivery, estimate the number of cells present over time, and assess immune infiltration to transplant site with quantitative methods. In the future, this trimodal imaging approach could be applied to study MSC fate and measure macrophage influx in other mouse models of MSC transplantation with varying level of immune rejection status (e.g., allograft vs. isograft)<sup>1</sup>. Our next step is to apply MPI to quantitate MSC survival *in vivo* and study bioscaffolds that improve viability (refer to 6.3.1).

### 6.1.2 Chapter 3

This chapter provides knowledge on the lowest cell numbers that could be detected by PFC-based  $^{19}\text{F}$  MRI, compared to SPION-based MPI. Two cell types (MSC and 4T1 cancer cells) were labeled with PFC nanoemulsions or ferucarbotran using commonly used labeling protocols. Cell pellets were prepared in a range of  $>10^6$  cells down to  $10^3$  cells by serial dilution and imaged by  $^{19}\text{F}$  MRI (PFC-labeled cells) or MPI (SPION-labeled cells). A consistent imaging time (1.5 minutes per cell pellet) was used for comparison. The lowest cell number detected by each imaging modality was determined. Additionally, *in vitro* signals (in a cell pellet) were compared with *in vivo* signals (after administration) for each imaging modality. The main findings of this study were:

- 1. SPION-based MPI shows superior cellular sensitivity compared to PFC-based  $^{19}\text{F}$  MRI.** As few as 4000 MSC (76 ng Fe) could be detected with MPI and  $256 \times 10^3$  MSC ( $9.01 \times 10^{16}$   $^{19}\text{F}$  atoms) could be detected with  $\text{SNR} > 5$  within the same imaging time. MPI and  $^{19}\text{F}$  MRI signals each scaled linearly with cell number.

2. **Cellular sensitivity is affected by scan time and cell type.** With longer imaging times, as few as 1000 MSC (19 ng Fe) could be detected by MPI. Similarly, with longer imaging time, fewer MSC ( $128 \times 10^3$  cells,  $4.51 \times 10^{16}$   $^{19}\text{F}$  atoms) could be detected with  $^{19}\text{F}$  MRI. 4T1 cancer cells (9.22 pg Fe/cell) incorporated approximately half the amount of Fe compared to MSC (19.09 pg Fe/cell) using the same cell labeling protocol. The lowest number of 4T1 cells detected by MPI was 8000 cells (74 ng Fe).
3. **The ability to detect labeled cells by MPI and  $^{19}\text{F}$  MRI can be reduced *in vivo* compared to *in vitro*.** Using MPI, the signal produced by MSC ( $1 \times 10^5$  cells) was reduced by 51% following subcutaneous injection of cells. Similarly, with  $^{19}\text{F}$  MRI, a reduction in signals (by 28%) are observed following administration of MSC ( $2 \times 10^6$  cells). This means that the  $^{19}\text{F}$  MRI and MPI signal detected from cells was reduced immediately after injection. There are multiple factors that contribute to this effect, including number of cells administered and the route of administration.

We demonstrate that MPI which is a newly emerging method for *in vivo* cell tracking, with the potential for clinical application, has superior sensitivity over  $^{19}\text{F}$  MRI. This work is crucial to improve cellular sensitivity and to understand cell detection limits which is urgently needed prior to design of clinical trials. The detection limits determined in this work are intended to serve as a baseline for making improvements to sensitivity for both imaging modalities. There are especially many opportunities to improve cellular detection with MPI. Since completing this study, our group has been testing custom-designed SPIONs for MPI with Dr. Carlos Rinaldi-Ramos at University of Florida and Dr. Adam Shuhendler at University of Ottawa, which are expected to improve MPI cellular sensitivity [manuscript in preparation].

### 6.1.3 Chapter 4

In this chapter, we develop and test 4 segmentation strategies for MPI and assess their accuracy for quantification of SPION. We created 10 test samples which had the same amount of iron (10 ug) but varied in volume (6.25 uL to 1.2 mL) then these samples were imaged individually with MPI. Three users drew ROIs on the resulting images to quantitate the signals and obtain a measure of iron content (ug). Two of the ROI methods were smaller in area and applied unique segmentations for each signal (Methods 1 and 2), and the other 2 methods were larger in area and applied consistent delineations to each signal (Methods 3 and 4). The main findings were:

- 1. MPI signal scales directly with the amount of SPION present, however more dilute samples of SPION have lower signal intensities that are localized over a larger region.** This means that despite having the same mass of SPION, a dilute sample would appear to have lower a MPI signal intensity compared to a concentrated sample. This poses an image quantification challenge.
- 2. There exists a tradeoff between ROI size and quantitative accuracy for dilute samples of SPION.** For concentrated samples of SPION that produce high SNR MPI signals, any of the 4 segmentation methods provided accurate quantification of SPION. However, for more dilute samples of SPION, larger ROIs were required to adequately capture the broader extents of MPI signals to achieve accurate quantification.
- 3. Users had more accurate and precise SPION quantification with lower variability when using larger ROIs and ROIs that have fewer manual inputs (i.e., Method 4).** Each user analysed the identical set of images, therefore the differences between user's measurements are solely due to image analysis.

The impact of this study is that standardized, reproducible, and accurate MPI quantification methods have become available to the MPI community. Our group is now especially cautious about the choice of ROI method for *in vivo* cell tracking applications, where SPIONs can become dilute with cell trafficking. Since completing this study, we have conducted a cross-laboratory study with Dr. Carlos Rinaldi-Ramos at University of Florida. The study looks at inter-user effects resulting from a combination of SPION

sample preparation, imaging on two systems, method of image calibration and ROI segmentation [manuscript under review at Molecular Imaging and Biology]. Among several findings, this work showed that there were significant differences in MPI signals produced by two different imagers, further highlighting the requirement for standard MPI quantification methods. Additionally, we reproduced the finding that 5\*SD segmentation (ROI Method 4) shows lower user variability and higher quantification accuracy than 0.5\*Max segmentation (ROI Method 1) across both laboratories.

#### 6.1.4 Chapter 5

This chapter demonstrates the feasibility for *in vivo*  $^{19}\text{F}$  MRI cell tracking of PFC-labeled human-derived Tregs and engineered CAR Tregs. After co-incubation of PFC and Tregs in culture, the *in vivo* trafficking of Tregs was assessed by  $^{19}\text{F}$  MRI, 24 and 48 hours after subcutaneous or intravenous administration to mice. Furthermore, Tregs were engineered with HER2-targeting CAR and following PFC labeling were administered intravenously to mice bearing both HER2+ and naïve tumors. CAR Treg migration in these mice was visualized and quantified with  $^{19}\text{F}/^1\text{H}$  MRI at 24h, 48h, and 72h after administration. The main findings were:

1. **PFC labeling had no effect on Treg phenotype and only minimal effect on viability (< 10% difference).** Tregs label with an average of  $3.11 \times 10^{12}$   $^{19}\text{F}$  atoms/cell and PFC is localized to the cell cytoplasm.
2.  **$^{19}\text{F}$  MRI reveals that PFC<sup>+</sup> Treg trafficking patterns *in vivo* are dependent on route of administration.** Following subcutaneous administration, PFC<sup>+</sup> Tregs are detected in the inguinal and popliteal lymph nodes, as well as the spleen. The average number of detected cells was higher at 24 hours (29.7% I.D.) compared to 48 hours (16.9% I.D.). After intravenous delivery of PFC<sup>+</sup> Tregs,  $^{19}\text{F}$  signals were localized to the axillary, renal, lumbar, and inguinal lymph nodes. The average number of cells detected at lymph nodes was higher after 48 hours (30% I.D.) compared to 24 hours (19% I.D.).

- 3. PFC<sup>+</sup> CAR Tregs showed preferential homing to HER2<sup>+</sup> tumors with <sup>19</sup>F MRI.** 24 hours after administration of CAR Tregs, <sup>19</sup>F signals were detected in all HER2<sup>+</sup> tumors, but in only 1 naïve tumor, with the signal being greater than 2 time higher in the HER2<sup>+</sup> tumors. After 48 hours, <sup>19</sup>F signals in HER2<sup>+</sup> tumors were greater than 10 time higher compared to naïve tumors, instigating antigen-dependent migration and enhanced retention of CAR Tregs in antigen-expressing tumors.

We demonstrate *in vivo* longitudinal tracking and quantification of human Treg to mouse lymph nodes and CAR Treg trafficking to antigen-expressing grafts with <sup>19</sup>F MRI. This was the first attempt to image human Tregs with MRI and with a clinical imaging approach. This project is ongoing and we recognize that validations of Treg trafficking are required. Additional cohorts of mice will be pursued to obtain further post-mortem histological and flow cytometry confirmation of Treg trafficking to lymph nodes and tumors. We are also interested in pairing <sup>19</sup>F MRI with bioluminescence imaging, which provides complimentary information on cell viability *in vivo*.

## 6.2 Challenges and limitations

### 6.2.1 Surface coil for MRI

For <sup>19</sup>F MRI in this thesis, a surface coil was used for *in vivo* imaging of inflammation (Chapter 2), imaging of cell pellets (Chapter 3), and *in vivo* cell tracking of MSC (Chapter 3) and Tregs (Chapter 5). This was a dual-tuned surface coil used to acquire both <sup>1</sup>H (anatomical) and then <sup>19</sup>F images (of PFC<sup>+</sup> cells) within the same field of view for co-registration. The surface coil did not have to be moved during the imaging session. This technique allows for dual-cell tracking of SPION-labeled cells and PFC-labeled cells (Chapter 2).

The major reason for using a surface coil is the significant boost in <sup>19</sup>F detection sensitivity<sup>2,3</sup>. Our group has previously shown that the surface coil at 3 T provided similar sensitivity (SNR) as a volume coil at 9.4 T for detection of PFC<sup>+</sup> cells with <sup>19</sup>F

MRI<sup>4</sup>. However, a surface coil provides a limited field of view and is expected to have non-uniform transmit/receive sensitivity, that drops off with distance from the center of the coil<sup>5,6</sup>. For this reason, cell pellets were placed directly in the center of the coil for imaging (Figure 19) or the surface coil was placed directly above the expected region of PFC-labeled cells *in vivo* (Figure 25) to optimize <sup>19</sup>F signal. To correct for non-uniform sensitivity in <sup>19</sup>F images, variations in surface coil transmit/receive must be known for compensation by acquiring an image of a uniform phantom to produce a sensitivity map with image intensities that represent only the behaviors of the coil. This process is known as B1 mapping<sup>5-7</sup>. This may help to correct coil inhomogeneities, but it requires additional scan time and expertise. The field of view offered by the surface coil was large enough to cover 6 cm (length, frequency direction) x 3 cm (width, phase direction) x 3 cm (depth from coil), which is large enough to capture a mouse body. A similar surface coil was used in a clinical study<sup>8</sup>.

### 6.2.2 Commercial availability of PFCs and SPIONs

Currently there are no commercially available PFC agents for human use. PFC nanoemulsions had previously been available as a clinical grade product, however CS-1000 used in this thesis is now discontinued as of December 2021. There are several groups that produce their own PFC nanoemulsions in lab<sup>9-13</sup>, which brings about the opportunity to customize PFC load and surface chemistry optimized for cellular uptake<sup>14</sup>. PFCs have a high safety profile for cell tracking and have been used for several decades as oxygen delivery agents<sup>15-18</sup>. PFCs are biologically inert due to covalent bonding between C-F atoms; there are no known enzymes that can metabolize these bonds *in vivo* nor do they degrade at lysosomal pH values<sup>15,19</sup>. Additionally, PFCs are hydrophobic and lipophobic so do not incorporate into cell membranes therefore can be packaged as a biocompatible nanoemulsion for cell uptake. The effect of PFC nanoemulsions on cell health and function has been tested in a range of concentrations and cell types showing no detrimental effects<sup>13,20-22</sup>. *However, a recent study reveals and discusses a trade-off between high <sup>19</sup>F loading and cell viability and function*<sup>23</sup>.

A more recently emerging agent for <sup>19</sup>F MRI are nanoparticles with a PFC core and a poly D,L-lactic-co-glycolic acid (PLGA) polymer coat<sup>11,24</sup>. These PFC nanoparticles are

considered highly suitable for imaging inflammation as they degrade and clear faster *in vivo* by 15-fold compared to PFC nanoemulsions<sup>11</sup>. These PFC nanoparticles have also been used to label cell populations *in vitro* without affecting cell viability or function<sup>11,25,26</sup>. Furthermore these PFC nanoparticles are approved for a clinical trial for dendritic cell therapy (NCT02574377)<sup>26</sup>. Interestingly, PLGA-PFC nanoparticles rely on active endocytosis therefore may be well suited for cell tracking of naturally phagocytic cell types such as dendritic cells<sup>11</sup>.

SPIONs are biocompatible and nonionizing, allowing for their safe use for longitudinal imaging in humans. A review article highlights 9 in-human SPION-based MRI cell tracking studies<sup>27</sup>. Clinically approved tracers (by the FDA) include ferucarbotran (Magtrace®, Endomagnetics; Feridex®, Berlex Laboratories Inc.; Resovist®, Bayer Healthcare) and ferumoxytol (Feraheme®, AMAG Pharmaceuticals). There are several investigational SPIONs including PrecisionMRX® nanoparticles (Imagion), FerroTrace (Ferronova)<sup>28</sup> (NCT05038098 and NCT05092750) and MegaPro® particles (NCT03407495). Many of these SPIONs were developed for MRI applications and their use for MPI requires optimization and testing.

For cell tracking, not all SPIONs are taken up effectively by simple co-incubation. Transfection agents are commonly used to facilitate or enhance cellular incorporation of SPIONs into cells, including poly-L-lysine, lipofectamine, and protamine sulfate (often with heparin)<sup>29-31</sup>. In this thesis, transfection agents protamine sulfate and heparin were used to enhance uptake of ferumoxytol (Chapter 2) and ferucarbotran (Chapter 3) by MSC. Transfection agents coat the surface of SPIONs and improve the rate and/or amount of iron taken up by cells. However, there are several limitations associated with using transfection agents. SPION complexes formed by transfection agents may clump SPIONs and cells together and can lead to higher amounts of free iron in cell preparations<sup>31</sup>. Transfection agents may alter cell functionality or phenotype, for example, certain TAs reduce the immunopotency of dendritic cells<sup>32</sup>. We have also shown that transfection agents can worsen MPI relaxation characteristics of SPIONs owing to clustering of iron cores<sup>33</sup>.

### 6.2.3 Quantification and Interpretation of MRI and MPI

When interpreting measurements of cell number from  $^{19}\text{F}$  MRI and MPI images, it is important to consider factors related to cell labeling which introduce uncertainty. First, the measurement of  $^{19}\text{F}$  or Fe/cell is an average value; some cells will contain more, some less. The calculation of cell number from images assumes that cells maintain the average  $^{19}\text{F}$  or Fe/cell over time. However as cells proliferate, the amount of PFC/cell or SPION/cell is reduced, leading to lower  $^{19}\text{F}$  MRI or MPI signals and underestimation of the number of cells detected (see Appendix B, part 7.2.1). Second, the amount of  $^{19}\text{F}$  or Fe per cell achieved with each cell labeling experiment has a range of values, even for the same labeling protocol, depending on precise timing and culture conditions. Uniform PFC and SPION labeling is optimal for cell tracking but is difficult to achieve. Magnetic sorting (SPIONs) or fluorescence-activated cell sorting (fluorescent-PFCs) of cells is one strategy to improve the uniformity of labeled cells by removing cells that have low incorporation of PFC or SPION. For in situ labeling of immune cells, quantification of cell number is not straightforward because the uptake of PFC per cell *in vivo* is unknown. This value can be estimated by loading mouse macrophages *in vitro* with PFCs, however this will likely result in an overestimation since macrophage labeling *in vitro* is expected to be more optimal and uniform than is achieved *in situ*.

There is an expectation that some quantity of therapeutic cells will undergo apoptosis upon administration. Upon cell death, PFCs or SPIONs will be taken up by phagocytes for clearance by the liver. Bystander labeling of phagocytes has the potential to lead to misinterpretation of the source of imaging signal. This has been well documented for SPIONs used for cell tracking studies<sup>34–36</sup> and has been shown to lead to misleading conclusions regarding the health of the cell population<sup>35</sup>. These studies have clearly demonstrated that macrophages become secondarily labeled this way, although the macrophages have been shown to contain significantly less iron<sup>37</sup>. For  $^{19}\text{F}$  MRI, bystander cell uptake is generally considered less problematic in view of the lower detection limits<sup>38</sup>.

Additional considerations exist for MPI since it is sensitive to changes in magnetic relaxation. For example, a difference in the environment surrounding SPIONs can alter



magnetic relaxation and signals produced can be reduced (see Appendix B, part 7.2.2). Furthermore, intracellular SPIONs that exist within endosomal compartments may be susceptible to degradation by lysosomes<sup>39,40</sup>. This degradation process can reduce the superparamagnetism of iron oxide nanoparticles, thereby altering their cellular MPI detectability<sup>41,42</sup>. This is a largely understudied phenomenon; however, it may be reasonable to assume that this effect depends on the biological inertness of the SPION and cellular lysosomal capacity.

## 6.3 Future work

### 6.3.1 Improving the MSC microenvironment with image assistance

A major reason for failed MSC transplants is the poor retention and viability of transplanted cells. Immediately upon transplantation, MSC can experience unfavorable environments including ischemia, inflammation, and hypoxia *in vivo*, resulting in a high burden and cell death. One strategy has been to precondition MSCs in culture to these harsh conditions before administration<sup>43,44</sup>. Perhaps more promising is the use of engineered biomaterials to serve as artificial niches and support MSC retention *in vivo*. Hydrogels are biocompatible and biodegradable materials that serve as a cell anchoring matrix. Hydrogels have been shown to enhance viability, metabolic activity, secretion of angiogenic factors, and retention of MSC *in vivo*, as well as improve tissue repair and functional recovery for MSC therapy<sup>45,46</sup>. Finally, co-administration of MSC with anti-inflammatory drugs can prevent immune responses against the MSC<sup>47</sup>. In future work, these strategies could be applied along with our trimodal imaging approach to quantify to what extent they enhance MSC survival and reduce inflammatory influx.

While MPI and MRI do not provide direct measurements of SPION-labeled MSC survival *in vivo*, the relationship between image characteristics and MSC outcomes can be elucidated. Several studies have shown that successful versus apoptotic stem cell transplants can be distinguished with MRI, long before clinical scores of cartilage repair become indicative<sup>48–50</sup>. Viable SPION-labeled MSC proliferated and expanded, and this caused a lack of signal voids in MRI after 2 weeks. Comparatively, apoptotic cells did

not expand but were rapidly eliminated from the transplant sites after phagocytosis by macrophages, resulting in elimination of MR signals. Therefore, the persistence of the SPION-induced signal void in MRI past 1 week was associated with favorable outcomes. A great opportunity for future work is to quantitate these signal changes by MPI to be able to distinguish outcomes with mixed live/apoptotic MSC and MSC co-administered with hydrogels or anti-inflammatory drugs.

### 6.3.2 Anatomical co-registration

MPI lacks anatomical information and must be paired with another modality such as computed tomography, optical photographs, or MRI. MRI provides superior localization owing to soft tissue contrast that provides detailed anatomy, as well as the ability to validate the position of MPI signal as a region of signal void in MRI. However, there are currently no dual MRI/MPI systems. This poses a challenge because the exact alignment of MRI/MPI is difficult to achieve, especially if the position of the mouse has changed between scans. This error may be minimized through the use of a body-conforming animal mold (BCAM) with alignment fiducials for co-registration<sup>51,52</sup>. There is a need to develop a pipeline and easy-to-use software for MRI/MPI co-registration. In general, a minimum of 3 fiducial markers containing probes detected by both imaging modalities are required to co-register 3D datasets.

### 6.3.3 Multispectral “color” imaging for cell tracking

In Chapter 2 of this thesis, a trimodal imaging approach with MRI and MPI is performed to image two cell populations (MSC and macrophages). Multispectral imaging is becoming increasingly prevalent, which refers to the ability to take two images with the same system, eliminating the need for two separate imagers. For <sup>19</sup>F MRI, this is achieved by using two PFC probes with sufficiently different resonance frequencies and then two separate <sup>19</sup>F acquisitions at these frequencies<sup>53,54</sup>. Similarly, for MPI two excitation amplitudes or two excitation frequencies can be exploited to separately image two SPIONs which differ in relaxation properties<sup>55</sup>.

Multispectral imaging can provide exciting opportunities for dual cell tracking. Partlow *et al.*<sup>53</sup> showed a simple demonstration (1 timepoint) that two MSC populations can be

separately imaged in a mouse with  $^{19}\text{F}$  MRI. More recently,  $^{19}\text{F}$  MRI has been used to image intravenously delivered PFCs to mice bearing glioblastoma tumors, one PFC was given before and after radiotherapy<sup>54</sup>. Interestingly, two spatially and temporally distinct niches of tumor-associated macrophages existed before and after radiotherapy. Therefore, the multispectral approach is applicable to dual cell tracking and dual *in vivo* labeling (imaging inflammation) and foreseeably, one PFC could be used for cell tracking and another to image inflammatory influx. D. Hensley and colleagues demonstrate that Ne'el and Brownian relaxation-dominated SPIONs can be separately imaged with MPI using different excitation amplitudes<sup>55</sup>. The application of this multispectral MPI technique to dual cell tracking is a possible area of future work.

## 6.4 Concluding statement

Cellular imaging can provide fundamental information regarding the location, persistence, and numbers of therapeutic cells after their administration, including MSC and Tregs. This can greatly improve patient safety and outcomes by identifying failed therapies quickly. In a preclinical setting, cell therapies can be rapidly optimized in animal models using cellular imaging modalities. Cellular imaging provides a quantitative *in vivo* migration assay to maximize therapeutic benefits. Imaging on the day of transplantation provides important information about cell delivery and subsequent imaging sessions can help to determine whether these labeled therapeutic cells reached their target and in what quantity.

## 6.5 Chapter 6 references

1. Gaudet, J. M., Ribot, E. J., Chen, Y., Gilbert, K. M. & Foster, P. J. Tracking the fate of stem cell implants with fluorine-19 MRI. *PLoS One* **10**, 1–12 (2015).
2. Helfer, B. M. *et al.* Options for imaging cellular therapeutics in vivo: a multi-stakeholder perspective. *Cytotherapy* **000**, 1–17 (2021).
3. Waiczies, S., Srinivas, M., Flögel, U., Boehm-Sturm, P. & Niendorf, T. Special issue on fluorine-19 magnetic resonance: technical solutions, research promises and frontier applications. *Magn. Reson. Mater. Physics, Biol. Med.* **32**, 1–3 (2019).
4. Makela, A. V. & Foster, P. J. Preclinical 19F MRI cell tracking at 3 Tesla. *Magn. Reson. Mater. Physics, Biol. Med.* (2018). doi:10.1007/s10334-018-0715-7
5. Vernikouskaya, I., Pochert, A., Lindén, M. & Rasche, V. Quantitative 19 F MRI of perfluoro-15-crown-5-ether using uniformity correction of the spin excitation and signal reception. *Magn. Reson. Mater. Physics, Biol. Med.* **32**, 25–36 (2019).
6. Mihara, H., Iriguchi, N. & Ueno, S. A method of RF inhomogeneity correction in MR imaging. *Magn. Reson. Mater. Physics, Biol. Med.* **7**, 115–120 (1998).
7. Hu, L. *et al.* Advanced Detection Techniques and Hardware: Simultaneous 19F/1H MRI. in *Fluorine Magnetic Resonance Imaging* (2017).
8. Ahrens, E. T., Helfer, B. M., O’Hanlon, C. F. & Schirda, C. Clinical cell therapy imaging using a perfluorocarbon tracer and fluorine-19 MRI. *Magn. Reson. Med.* **72**, 1696–1701 (2014).
9. Garello, F. *et al.* Imaging of Inflammation in Spinal Cord Injury : Novel Insights on the Usage of PFC-Based Contrast Agents. 1–27 (2021).
10. Jacoby, C. *et al.* Probing different perfluorocarbons for in vivo inflammation imaging by 19F MRI: Image reconstruction, biological half-lives and sensitivity. *NMR Biomed.* **27**, 261–271 (2014).

11. Staal, A. H. J. *et al.* In vivo clearance of <sup>19</sup>F MRI imaging nanocarriers is strongly influenced by nanoparticle ultrastructure. *Biomaterials* **261**, (2020).
12. Flogel, U. *et al.* In vivo monitoring of inflammation after cardiac and cerebral ischemia by fluorine magnetic resonance imaging. *Circulation* **118**, 140–148 (2008).
13. Hingorani, D. V. *et al.* Cell penetrating peptide functionalized perfluorocarbon nanoemulsions for targeted cell labeling and enhanced fluorine-19 MRI detection. *Magn. Reson. Med.* 974–987 (2019). doi:10.1002/mrm.27988
14. Srinivas, M., Heerschap, A., Ahrens, E. T., Figdor, C. G. & de Vries, I. J. M. <sup>19</sup>F MRI for quantitative in vivo cell tracking. *Trends Biotechnol.* **28**, 363–370 (2010).
15. Janjic, J. M. & Ahrens, E. T. Fluorine-containing nanoemulsions for MRI cell tracking. *Wiley Interdiscip. Rev. Nanomedicine Nanobiotechnology* **1**, 492–501 (2009).
16. Hill, S. E. Perfluorocarbons: Knowledge gained from clinical trials. *Shock* **52**, 60–64 (2019).
17. Krafft, M. P. & Riess, J. G. Perfluorocarbons: Life sciences and biomedical uses dedicated to the memory of Professor Guy Ourisson, a true RENAISSANCE man. *J. Polym. Sci. Part A Polym. Chem.* **45**, 1185–1198 (2007).
18. Riess, J. G. & Riess, J. G. Oxygen carriers ('blood substitutes') - Raison d'être, chemistry, and some physiology. *Chem. Rev.* **101**, 2797–2919 (2001).
19. Chapelin, F., Capitini, C. M. & Ahrens, E. T. Fluorine-19 MRI for detection and quantification of immune cell therapy for cancer. *J. Immunother. Cancer* **6**, 1–11 (2018).
20. Fink, C. *et al.* Fluorine-19 Cellular MRI Detection of In Vivo Dendritic Cell Migration and Subsequent Induction of Tumor Antigen-Specific Immunotherapeutic Response. *Mol. Imaging Biol.* **19**, (2019).

21. Fernando Bonetto *et al.* A novel <sup>19</sup>F agent for detection and quantification of human dendritic cells using magnetic resonance imaging. *Int. J. Cancer* **129**, 365–373 (2011).
22. Lechuga, L. M. *et al.* Detection and viability of murine NK cells in vivo in a lymphoma model using fluorine-19 MRI. *NMR Biomed.* **34**, 1–14 (2021).
23. Cooke, F. *et al.* Fluorine labelling of therapeutic human tolerogenic dendritic cells for <sup>19</sup>F-magnetic resonance imaging. *Front. Immunol.* **13**, 1–11 (2022).
24. Srinivas, M., Boehm-Sturm, P., Figdor, C. G., de Vries, I. J. & Hoehn, M. Labeling cells for in vivo tracking using <sup>19</sup>F MRI. *Biomaterials* **33**, 8830–8840 (2012).
25. Swider, E. *et al.* Design of triphasic poly(lactic-co-glycolic acid) nanoparticles containing a perfluorocarbon phase for biomedical applications. *RSC Adv.* **8**, 6460–6470 (2018).
26. Swider, E. *et al.* Clinically-applicable perfluorocarbon-loaded nanoparticles for in vivo photoacoustic, <sup>19</sup>F magnetic resonance and fluorescent imaging. *Nanotheranostics* **2**, 258–268 (2018).
27. Bulte, J. W. M. & Daldrup-Link, H. E. Clinical Tracking of Cell Transfer and Cell Transplantation: Trials and Tribulations. *Radiology* (2018).  
doi:10.1148/radiol.2018180449
28. Krishnan, G. *et al.* Preclinical evaluation of a mannose-labeled magnetic tracer for enhanced sentinel lymph node retention in the head and neck. *Nanomedicine Nanotechnology, Biol. Med.* **42**, 102546 (2022).
29. Arbab, A. S. *et al.* Intracytoplasmic tagging of cells with ferumoxides and transfection agent for cellular magnetic resonance imaging after cell transplantation: Methods and techniques. *Transplantation* **76**, 1123–1130 (2003).

30. Thu, M. S. *et al.* Self-Assembling Nanocomplexes by combining Ferumoxytol, Heparin And Protamine For Cell Tracking by MRI HHS Public Access Author manuscript. *Nat Med* **18**, 463–467 (2012).
31. Van Buul, G. M. *et al.* Ferumoxides-protamine sulfate is more effective than ferucarbotran for cell labeling: Implications for clinically applicable cell tracking using MRI. *Contrast Media Mol. Imaging* **4**, 230–236 (2009).
32. Rughetti, A. *et al.* Transfected human dendritic cells to induce antitumor immunity. *Gene Ther.* **7**, 1458–1466 (2000).
33. Sehl, O. C., Gevaert, J. J., Melo, K. P., Knier, N. N. & Foster, P. J. A perspective on cell tracking with magnetic particle imaging. *Tomography* **6**, (2020).
34. Amsalem, Y. *et al.* Iron-oxide labeling and outcome of transplanted mesenchymal stem cells in the infarcted myocardium. *Circulation* **116**, I38-45 (2007).
35. Terrovitis, J. *et al.* Magnetic resonance imaging overestimates ferumoxide-labeled stem cell survival after transplantation in the heart. *Circulation* **117**, 1555–1562 (2008).
36. Huang, Z. *et al.* Magnetic resonance hypointensive signal primarily originates from extracellular iron particles in the long-term tracking of mesenchymal stem cells transplanted in the infarcted myocardium. *Int. J. Nanomedicine* **10**, 1679–1690 (2015).
37. Pawelczyk, E. *et al.* In Vitro Model of Bromodeoxyuridine or Iron Oxide Nanoparticle Uptake by Activated Macrophages from Labeled Stem Cells: Implications for Cellular Therapy. *Stem Cells* **26**, 1366–1375 (2008).
38. Bouchlaka, M. N. *et al.* 19F-MRI for monitoring human NK cells in vivo. *Oncoimmunology* **5**, 1–12 (2016).
39. Golovko, D. M. *et al.* Accelerated stem cell labeling with ferucarbotran and protamine. *Eur. Radiol.* **20**, 640–648 (2010).

40. Toth, G. B. *et al.* Current and Potential Imaging Application of Ferumoxytol for Magnetic Resonance Imaging. *Kidney Int.* **92**, 47–66 (2017).
41. Suzuka, H., Mimura, A., Inaoka, Y. & Murase, K. Magnetic Nanoparticles in Macrophages and Cancer Cells Exhibit Different Signal Behavior on Magnetic Particle Imaging. *J. Nanosci. Nanotechnol.* **19**, 6857–6865 (2019).
42. Guzy, J. *et al.* Complex relationship between iron oxide nanoparticle degradation and signal intensity in magnetic particle imaging. *ACS Appl. Nano Mater.* **3**, 3991–3999 (2020).
43. Petrus-Reurer, S. *et al.* Immunological considerations and challenges for regenerative cellular therapies. *Commun. Biol.* **4**, 798 (2021).
44. Zhang, J. *et al.* The challenges and promises of allogeneic mesenchymal stem cells for use as a cell-based therapy. *Stem Cell Res. Ther.* **6**, 1–7 (2015).
45. Dhillon, J. *et al.* Peptide-modified methacrylated glycol chitosan hydrogels as a cell-viability supporting pro-angiogenic cell delivery platform for human adipose-derived stem/stromal cells. *J. Biomed. Mater. Res. - Part A* **107**, 571–585 (2019).
46. Jia, P. *et al.* The RGD-modified self-assembling D-form peptide hydrogel enhances the therapeutic effects of mesenchymal stem cells (MSC) for hindlimb ischemia by promoting angiogenesis. *Chem. Eng. J.* **450**, (2022).
47. Nejadnik, H., Tseng, J. & Daldrup-Link, H. Magnetic resonance imaging of stem cell–macrophage interactions with ferumoxytol and ferumoxytol-derived nanoparticles. *Wiley Interdiscip. Rev. Nanomedicine Nanobiotechnology* **11**, 1–13 (2019).
48. Hossein Nejadnik, H. E. D. MR Imaging of Stem Cell Transplants in Arthritic Joints. *J. Stem Cell Res. Ther.* (2014). doi:10.4172/2157-7633.1000165
49. Theruvath, A. J. *et al.* Tracking stem cell implants in cartilage defects of minipigs by using ferumoxytol-enhanced MRI. *Radiology* **292**, 129–137 (2019).



50. Henning, T. D. *et al.* Magnetic resonance imaging of ferumoxide-labeled mesenchymal stem cells in cartilage defects: In vitro and in vivo investigations. *Mol. Imaging* **11**, 197–209 (2012).
51. Makela, A. V. *et al.* Tracking the fates of iron-labeled tumor cells in vivo using magnetic particle imaging. *Nanoscale Adv.* **4**, 3617–3623 (2022).
52. Klose, A. D. & Paragas, N. Automated quantification of bioluminescence images. *Nat. Commun.* **9**, (2018).
53. Partlow, K. C. *et al.* <sup>19</sup>F magnetic resonance imaging for stem/progenitor cell tracking with multiple unique perfluorocarbon nanobeacons. *FASEB J.* **21**, 1647–1654 (2007).
54. Croci, D. *et al.* Multispectral fluorine-19 MRI enables longitudinal and noninvasive monitoring of tumor-associated macrophages. *Sci. Transl. Med.* **14**, 1–18 (2022).
55. Chandrasekharan, P. *et al.* *Magnetic Particle Imaging for Vascular, Cellular and Molecular Imaging. Molecular Imaging* (Brian D. Ross and Sanjiv Sam Gambhir, 2021). doi:10.1016/b978-0-12-816386-3.00015-6

## 7 Appendices

### 7.1 Appendix A: Supplementary figures

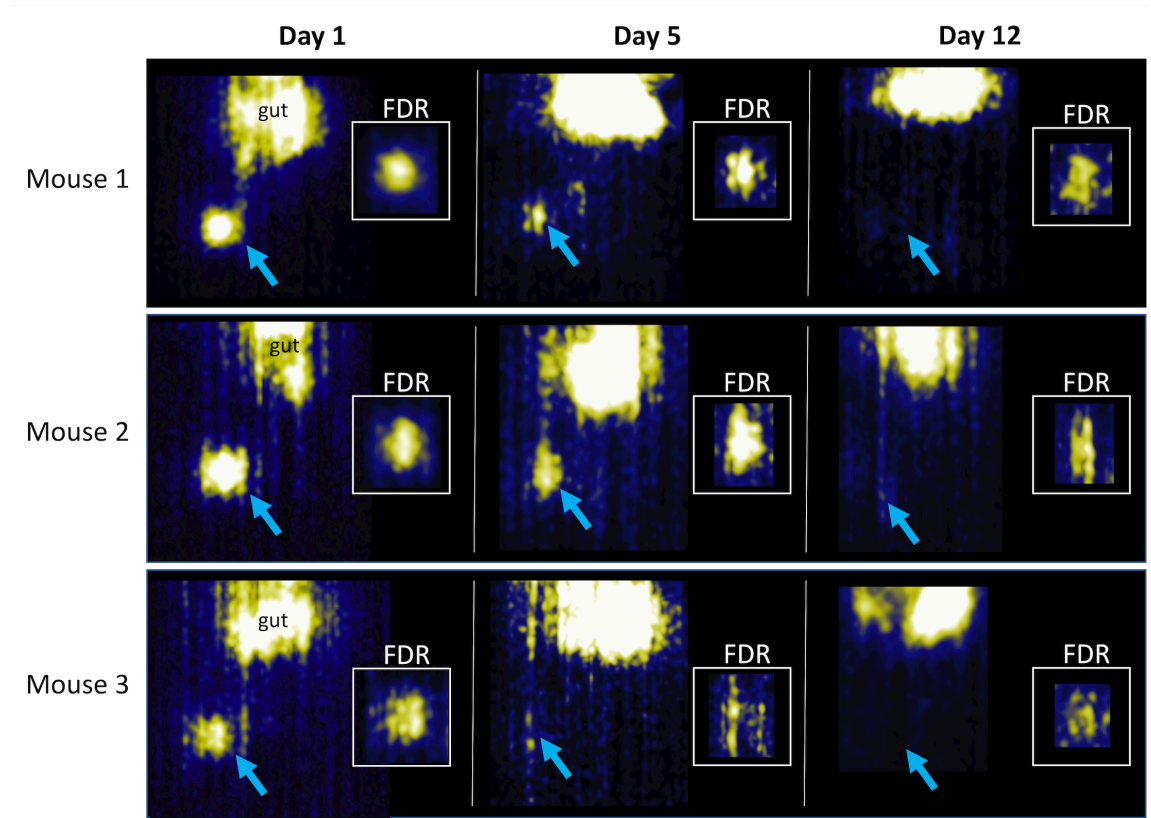


**Figure 37: Full MPI image set for 3 mice, showing changes in detected ferumoxytol-labeled MSCs, 1, 5, and 12 days following MSC implantation. The full dynamic range (FDR) of the region where MSCs were implanted is displayed for each mouse.**

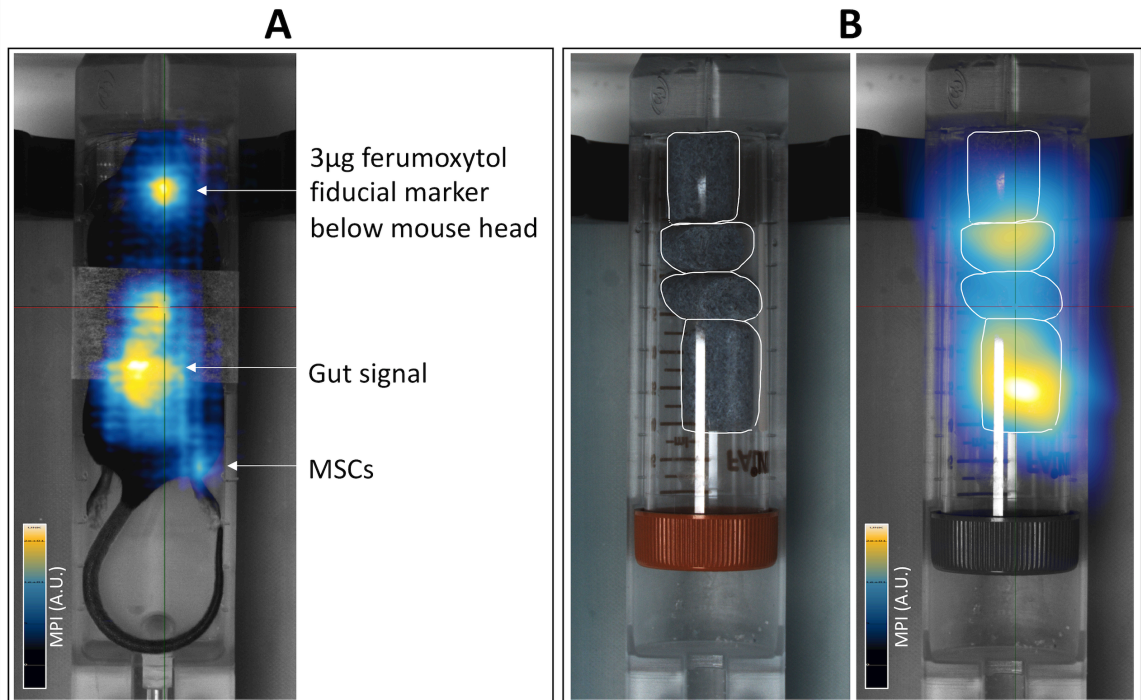


**Figure 38: Overlay of 2D MPI acquisition to optical image of mouse. MPI signal is localized to the gut and the region where ferumoxytol-labeled MSCs were implanted. (B) Overlay of 2D MPI acquisition to optical image shows MPI signal from mouse feed.**

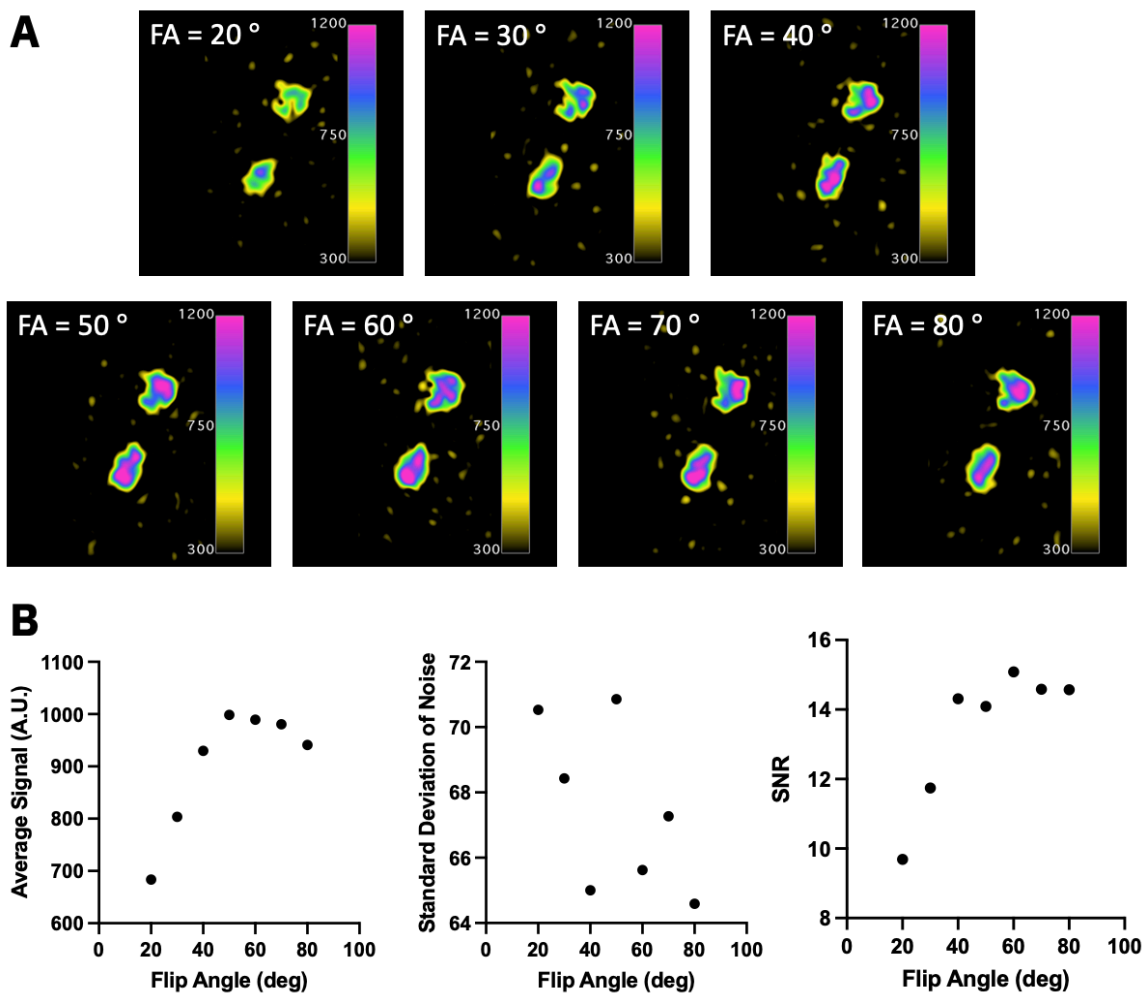


**Figure 39: Optimization of  $^{19}\text{F}$  flip angle at 3 T. (A) Two reference phantoms ( $3.33 \times 10^{16}$   $^{19}\text{F}$  spins/ $\mu\text{L}$ ) were imaged using 3D bSSFP with 80 excitations and various flip angles: 20, 30, 40, 50, 60, 70, and 80 degrees. (B) The average signal of the reference tubes, the standard deviation of background noise, and the SNR were measured for each flip angle.**

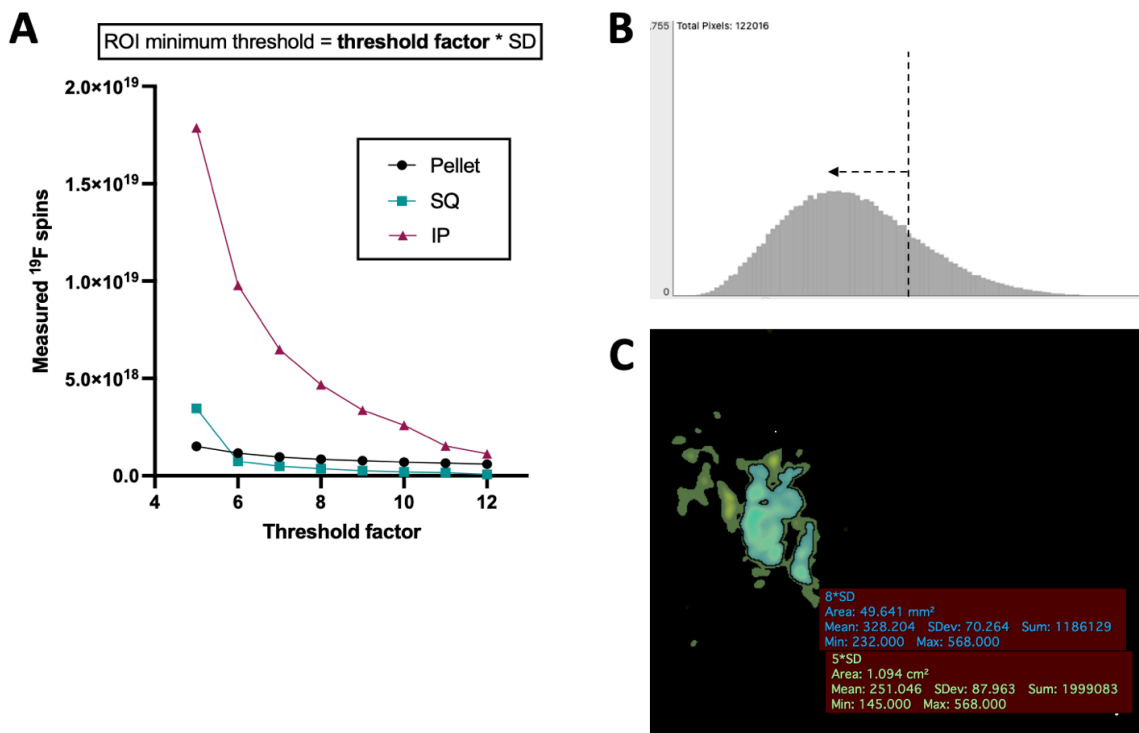


**Figure 40:** (A) Various threshold ( $5 \times \text{SD}_{\text{noise}}$  -  $12 \times \text{SD}_{\text{noise}}$ ) were used to segment  $^{19}\text{F}$  signal from  $2 \times 10^6$  PFPE-labeled MSC, in a pellet or *in vivo* (subcutaneous; SQ, intraperitoneal; IP). These images are shown in Figure 25. Regardless of the threshold value used,  $^{19}\text{F}$  signal measured from cells administered IP exceeded that of SQ and from pellets. In this quantification there is no correction applied to signal values. (B) Voxel distribution of background  $^{19}\text{F}$  noise was non-Gaussian and left-skewed, indicating there is a Rician distribution of noise. (C) A demonstration of the segmentation method described in Bouchlaka *et al.* (2016) from a single coronal slice of the mouse administered PFPE-cells IP (also shown in Figure 7B).  $^{19}\text{F}$  signal between  $5 \times \text{SD}_{\text{noise}}$  -  $8 \times \text{SD}_{\text{noise}}$  (green) was corrected with a factor of 0.655 and  $^{19}\text{F}$  signal exceeding  $8 \times \text{SD}_{\text{noise}}$  (blue) was not corrected. Signal above  $5 \times \text{SD}_{\text{noise}}$  was included for  $^{19}\text{F}$  quantification.

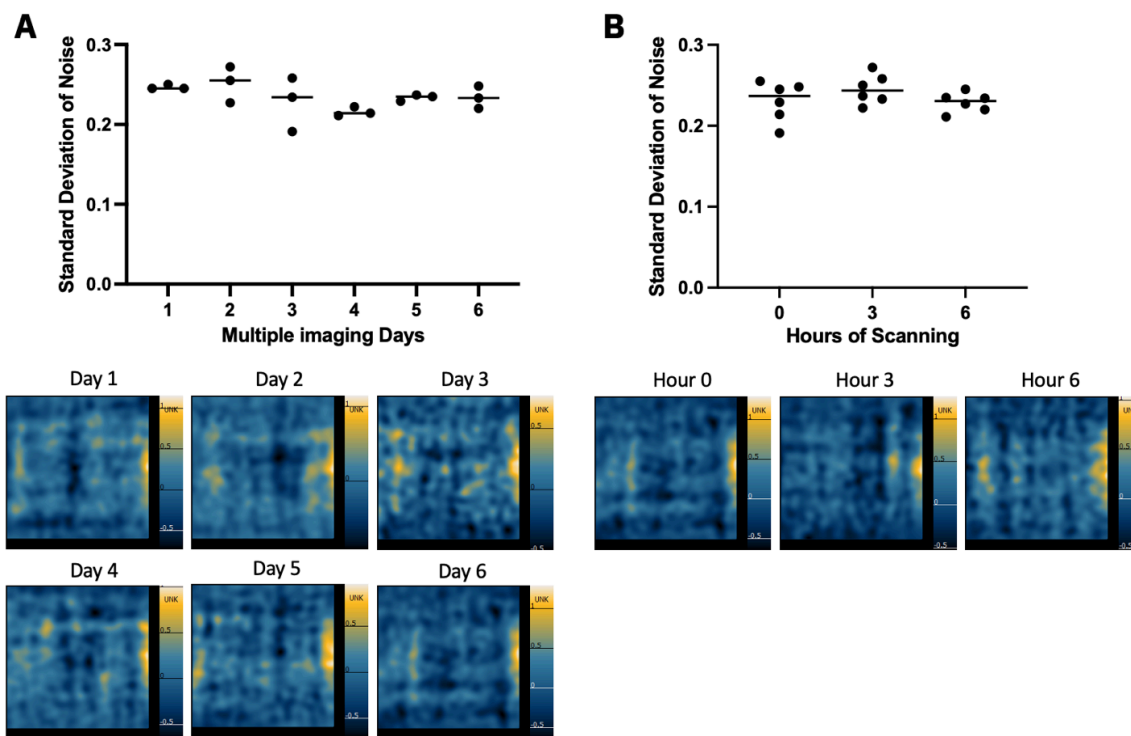
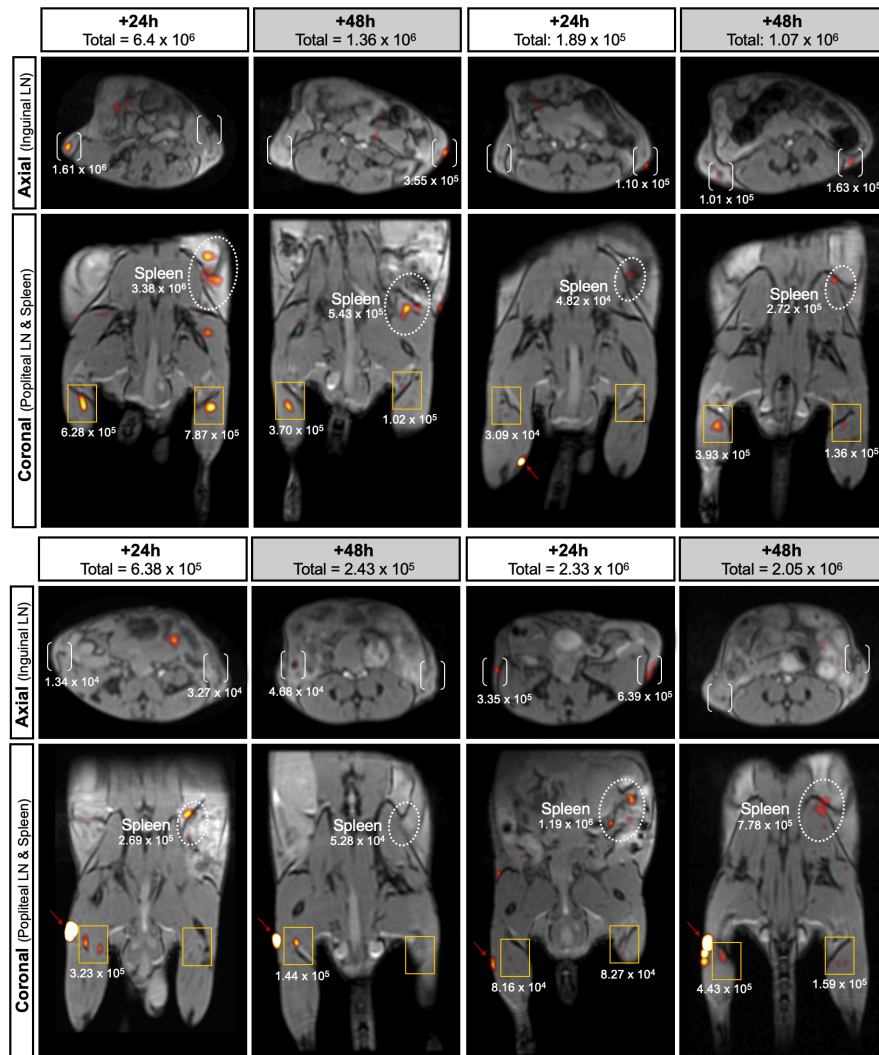


**Figure 41:** The standard deviation of background noise ( $SD_{noise}$ ) for MPI was measured from an empty sample holder at the beginning ( $t = 0h$ ), middle ( $t = 3h$ ), and end ( $t = 6h$ ) of six imaging sessions. There were no significant differences in measured  $SD_{noise}$  between (A) imaging days or (B) the 3 timepoints.



\* This mouse received  $5 \times 10^6$  Tregs

**Figure 42:**  $^1\text{H}/^{19}\text{F}$  MRI for all 4 mice receiving  $10 \times 10^6$  PFC+ Tregs by subcutaneous administration (except for the final mouse that received  $5 \times 10^6$  PFC+ Tregs). The experiment was repeated with cells from the same donor ( $n = 2$  mice per replicate). The first replicate of Tregs were labeled with  $3.15 \times 10^{11}$   $^{19}\text{F}$  atoms/cell (left) and the second replicate of Tregs were labeled with  $3.62 \times 10^{11}$   $^{19}\text{F}$  atoms/cell (right). The red arrows indicate the injection site (if within the selected plane). Each mouse was imaged at 24h and 48h p.i.  $^{19}\text{F}$  signals were seen in the spleen (white dotted ovals), and the popliteal (orange boxes) and inguinal (white brackets) lymph nodes of all mice at both time points. The estimated Treg cell numbers associated with each  $^{19}\text{F}$  signal are indicated and the total sum signal per mouse is recorded.

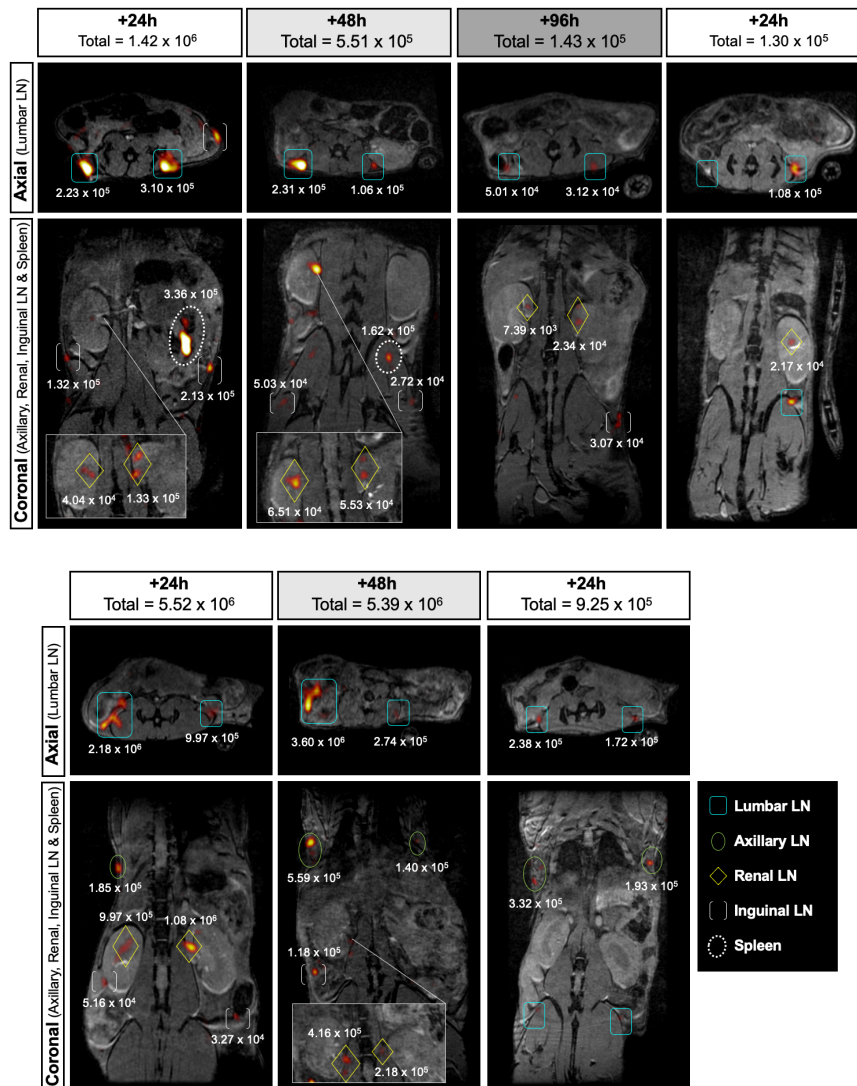


**Figure 43:**  $^1\text{H}/^{19}\text{F}$  MRI for all 4 mice receiving  $10 \times 10^6$  PFC+ Tregs by intravenous administration. The experiment was repeated with cells from the same donor ( $n = 2$  mice per replicate). The first replicate of Tregs were labeled with  $5.6 \times 10^{12}$   $^{19}\text{F}$  atoms/cell (left) and the second replicate of Tregs were labeled with  $6.28 \times 10^{11}$   $^{19}\text{F}$  atoms/cell (right). Each mouse was imaged at 24h and 48h p.i, and for one mouse a later timepoint was explored (96h p.i.). Mice with no signals present at 48h p.i. are not shown.  $^{19}\text{F}$  signals were seen in the spleen (one mouse, white ovals), and the lumbar (teal boxes), axillary (green circle), renal (yellow diamonds), and inguinal (white brackets) lymph nodes of mice. The estimated Treg cell numbers associated with each  $^{19}\text{F}$  signal are indicated and the total sum signal per mouse is recorded.



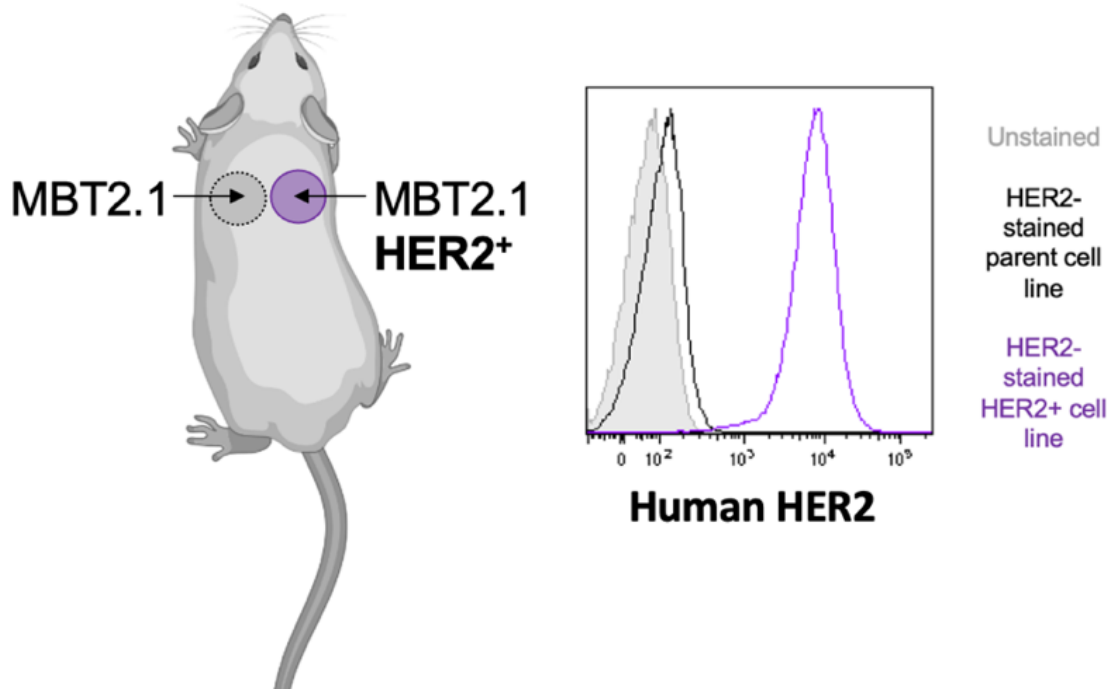


**Figure 44: Establishment of parental (mouse left) and HER2+ (mouse right) MBT2.1 tumors for HER2-CAR Treg in vivo migration study. Flow cytometry confirms HER2 expression in HER2 engineered MBT2.1 cells (purple) and confirmed lack of HER2 expression in parental MBT2.1 cells (black) and against control unstained HER2-expressing MBT2.1 cells (grey).**

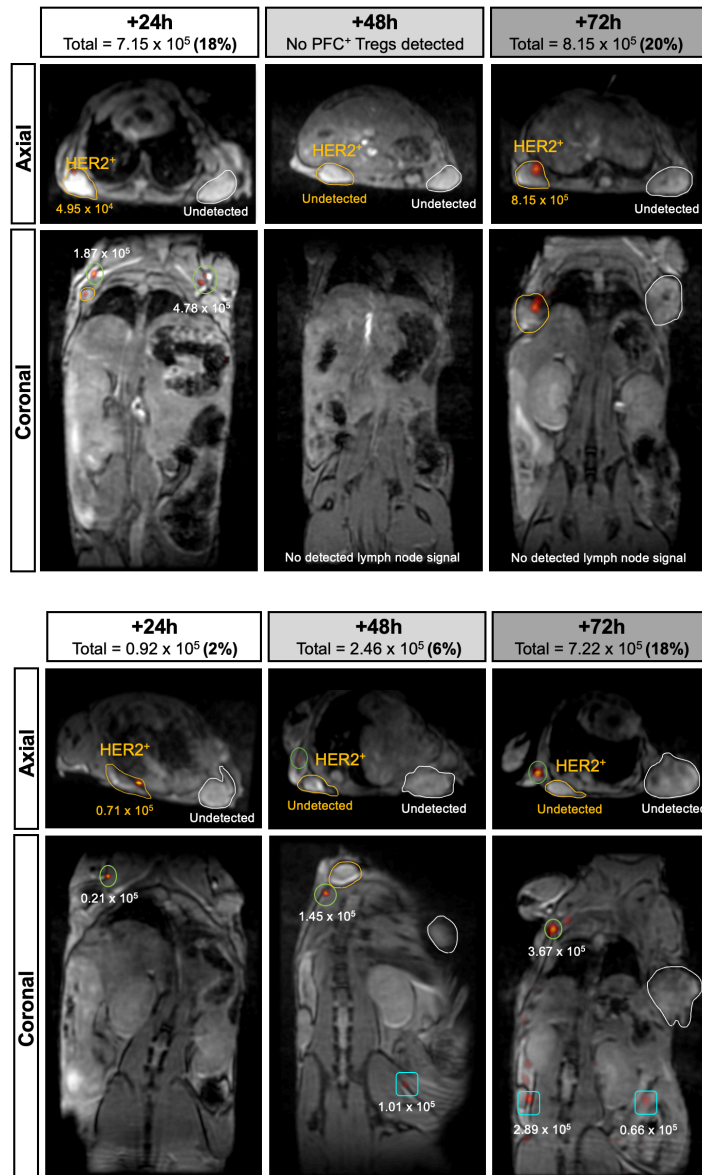


**Figure 45:  $^1\text{H}/^{19}\text{F}$  MRI for the other 2 mice receiving  $4 \times 10^6$  PFC<sup>+</sup> HER2-CAR Tregs by intravenous administration. These HER2-CAR Tregs were loaded with  $4.79 \times 10^{11}$   $^{19}\text{F}$  atoms/cell. Axial  $^{19}\text{F}/^1\text{H}$  MRI shows  $^{19}\text{F}$  signal from PFC<sup>+</sup> HER2-CAR Tregs in HER2<sup>+</sup> MBT2.1 tumors (orange) but not parental MBT2.1 tumors (white) in these 2 mice. Coronal images show that PFC<sup>+</sup> HER2-CAR Tregs were also detected in the axillary (green circles) and lumbar (teal boxes) lymph nodes at 24h, 48h, and 72h p.i. The estimated number of cells based on  $^{19}\text{F}$  content at each ROI is recorded.**

## 7.2 Appendix B: Additional experiments

### 7.2.1 Understanding the dynamics of cellular iron uptake and retention using live cell microscopy and magnetic particle imaging

This work was submitted to the World Molecular Imaging Congress and the Robarts Research Retreat in 2022.

Authors: Olivia C. Sehl, Maryam A. Berih, Paula J. Foster

#### 7.2.1.1 Introduction

Cell tracking with magnetic particle imaging (MPI) provides valuable information on the location and number of therapeutic cells after administration *in vivo*. For MPI detection, cells must be labeled with superparamagnetic iron oxide nanoparticles (SPION) by co-incubation in cell culture. Transfection agents (TAs) are commonly used to enhance cellular incorporation of SPIO into cells<sup>1-3</sup>. Achieving high iron cell labeling permits the sensitive tracking of cells. There have been several longitudinal *in vivo* MPI cell tracking studies<sup>4-9</sup>, however, cell proliferation is expected to reduce the SPION per cell. In this study, we use MPI and microscopy to study mechanisms of SPION uptake and retention in stem cells. These techniques provide complimentary information; MPI provides quantitative measurements of average iron per cell and microscopy allows for visualization of cell labeling uniformity. Live cell microscopy is used to observe dynamics of SPION endocytosis and partitioning with cell division, which occurs on the timescale of minutes.

#### 7.2.1.2 Methodology

Mesenchymal stem cells were co-incubated with ferucarbotran (VivoTrax<sup>TM</sup>, Magnetic Insight Inc.) for 4 hours with 60 g/mL protamine sulfate and 3 U/mL heparin<sup>3</sup> in 5 mL serum free low-glucose DMEM. Live cell microscopy was conducted with the Lux3 microscope (CytoSmart Inc.) using a 10x objective every 5 minutes. Then, 5 mL complete media was added for overnight incubation. Cells were washed 3 times with saline then  $1 \times 10^6$  iron-labeled cells were collected for MPI (n = 4). The remaining cells were returned to culture and live cell microscopy was repeated to observe iron partitioning in dividing cells. Cells were collected from culture every day for 5 days for

MPI. 2D MPI images were acquired on a Momentum™ system (Magnetic Insight Inc.) with a 5.7 T/m selection field gradient and drive fields 20 mT (X-channel) and 26 mT (Z-channel). A cell cytospin was performed daily to assess iron labeling efficiency with Perl's Prussian blue (PPB) stain<sup>10</sup>.

### 7.2.1.3 Results

With live cell microscopy, ferucarbotran endocytosis by stem cells can be visualized. Self-assembling nanocomplexes of heparin, protamine, and ferucarbotran form that are approximately 100 - 200 um in diameter (Figure 46i). In multiple instances, cells are seen to approach these ferucarbotran clusters and engulf a small portion of the nanocomplex (Figure 46ii). The MPI signal generated from ferucarbotran-labeled stem cells diminishes over time (Figure 46iii). Quantification from images reveals on day 1, stem cells were labeled with 18 pg iron/cell and the iron loading per cell decreased over time (Figure 46iv). Perl's Prussian blue stain shows that on day 1, nearly all cells are labeled with iron but in variable amounts. An overall reduction in cellular iron content is visualized over time (Figure 46v). Live cell microscopy shows that iron is shared between daughter cells as cells divide (Figure 46vi).

### 7.2.1.4 Conclusion

Ferucarbotran is a common cell labeling agent for both MRI and MPI, therefore understanding the uptake and retention mechanisms are valuable. To the best of our knowledge, the phenomenon of detachment and cellular uptake of ferucarbotran clusters from larger nanocomplexes has not been previously reported. The reduction in the amount of iron per cell, resulting from cell proliferation, leads to diminishing MPI cellular sensitivity over time. After 5 days in cell culture, the amount of iron (0.15 pg/cell x 1,000,000 cells = 150 ng) approaches a previously reported detection limit (76 ng)<sup>11</sup>. While MPI can provide direct measurements of SPION mass, it does not represent the number of cells that are present in longitudinal cell tracking studies. *In vivo* stem cells are expected to divide much more slowly, still this work can be applied to any proliferative cell type. Overall, this study contributes important knowledge for monitoring SPION-labeled cells with MPI.

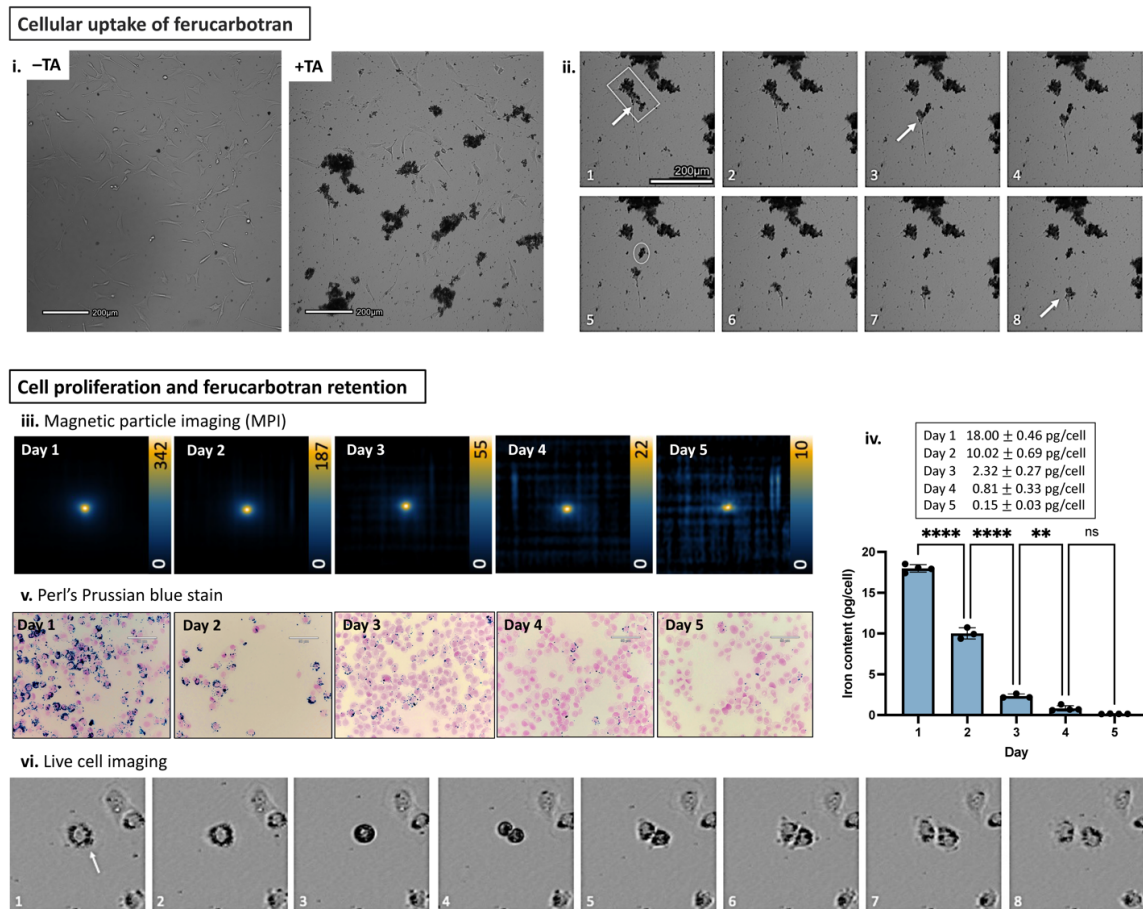


**Figure 46: (i) Microscopy of mesenchymal stem cells incubated with ferucarbotran without (left) and with (right) TAs. (ii) Time course imaging shows cells approach ferucarbotran nanocomplexes and engulf a portion of the cluster. The movement of a cell away from the cluster is shown with the white arrow over 8 frames. In the process, a portion of the ferucarbotran nanocomplex detaches from the cell and is not incorporated (white circle). (iii-vi) Proliferation of stem cells reduces the amount of iron per cell. (iii) MPI of  $1 \times 10^6$  ferucarbotran-labeled stem cells collected from culture over 5 days shows decreasing MPI signal over time. Scale bars indicate the image full dynamic range. (iv) Quantification of iron mass (pg) per cell with MPI shows significant decreases over time (\*\*  $p < 0.01$ , \*\*\*\*  $p < 0.0001$ ). (v) PPB stain validates a decrease in intracellular iron over time. (vi) Live cell imaging showing partitioning of iron in daughter progeny of a dividing cell.**

### 7.2.1.5 References

1. A. S. Arbab *et al.*, “Efficient magnetic cell labeling with protamine sulfate complexed to ferumoxides for cellular MRI,” *Blood*, vol. 104, no. 4, pp. 1217–1223, 2004.
2. E. Wuerfel *et al.*, “Electrostatically stabilized magnetic nanoparticles - An optimized protocol to label murine cells for in vivo MRI,” *Front. Neurol.*, pp. 1–9, 2011.
3. M. S. Thu *et al.*, “Self-Assembling Nanocomplexes by combining Ferumoxytol, Heparin and Protamine For Cell Tracking by MRI.” *Nat Med*, vol. 18, no. 3, pp. 463–467, 2012.
4. B. Zheng *et al.*, “Magnetic particle imaging tracks the long-term fate of in vivo neural cell implants with high image contrast,” *Sci. Rep.*, vol. 5, no. March, pp. 1–9, 2015.
5. B. Zheng *et al.*, “Quantitative magnetic particle imaging monitors the transplantation, biodistribution, and clearance of stem cells *in vivo*,” *Theranostics*, 2016.
6. P. Wang *et al.*, “Magnetic particle imaging of islet transplantation in the liver and under the kidney capsule in mouse models,” *Quant. Imaging Med. Surg.*, vol. 8, no. 2, pp. 114–122, 2018.
7. G. Song *et al.*, “Janus Iron Oxides @ Semiconducting Polymer Nanoparticle Tracer for Cell Tracking by Magnetic Particle Imaging,” *Nano Lett.*, vol. 18, no. 1, pp. 182–189, 2018.
8. H. Nejadnik, *et al.* “Ferumoxytol Can Be Used for Quantitative Magnetic Particle Imaging of Transplanted Stem Cells,” *Mol. Imaging Biol.*, vol. 21, no. 3, pp. 465–472, 2018.
9. Q. Wang *et al.*, “Artificially Engineered Cubic Iron Oxide Nanoparticle as a High-Performance Magnetic Particle Imaging Tracer for Stem Cell Tracking,” *ACS Nano*, vol. 14, no. 2, pp. 2053–2062, 2020.
10. Mcfadden, C. L. Mallett, and P. J. Foster, “Labeling of multiple cell lines using a new iron oxide agent for cell tracking by MRI,” *Contrast Media Mol. Imaging*, 2011.
11. O. C. Sehl and P. J. Foster, "The sensitivity of magnetic particle imaging and fluorine-19 magnetic resonance imaging for cell tracking." *Scientific Reports* 11.1, pp. 1-12, 2021.

## 7.2.2 The environment surrounding iron oxide nanoparticles influences sensitivity and resolution for magnetic particle imaging

This work was submitted to the Imaging Network of Ontario (IMNO) conference in 2022.

Authors: Maryam A. Berih, Olivia C. Sehl, Paula J. Foster

### 7.2.2.1 Introduction

Magnetic particle imaging (MPI) is an emerging imaging technique that directly detects superparamagnetic iron oxide nanoparticles (SPIONs) using magnetic gradients and excitation fields<sup>1</sup>. There are exciting opportunities for cellular imaging with MPI, which involves labeling cells with SPIONs, to learn about the fate of cellular therapies and cancer cells in preclinical models<sup>2</sup>. There is some evidence that the ability of the SPIO to respond to the changing magnetic fields is influenced by the nanoparticle's surroundings<sup>3</sup>. For imaging SPIONs *in vivo*, where tissues have varying stiffness<sup>4</sup>, it is not understood how surrounding tissue effects the sensitivity and resolution of MPI signal. Our aim is to measure changes in MPI sensitivity and resolution resulting from suspending SPION and SPION-labeled cells tissue-mimicking agarose phantoms.

### 7.2.2.2 Methodology

5.5 µg ferucarbotran (SPION) was suspended in saline, 0.5%, 2.5%, or 5% agarose (n = 3). These agarose phantoms mimic the Young's Modulus (stiffness) of liver, lung, and cartilage tissues, respectively<sup>4,5</sup>. Mesenchymal stem cells (MSC) were labeled by coinubation of ferucarbotran and transfection agents in culture<sup>6</sup>.  $5 \times 10^5$  MSC were suspended in these same four conditions (n = 3). MPI relaxometry was used to characterize the sensitivity (maximum intensity) and resolution (full width half maximum, FWHM) using rf amplitude 20 mT and bandwidth  $\pm 160$  mT. MPI images of these samples were acquired using 5.7 T/m gradient and 20 mT excitation.

### 7.2.2.3 Results

Comparing ferucarbotran in saline to 5% agarose, MPI relaxometry exhibited a 36% reduction in sensitivity and a 55% increase in FWHM ( $p < 0.05$ ) (Figure 47A,C). This

can be visualized in MPI images (Figure 47E) as a reduction in signal amplitude from SPIO in 5% agarose, despite being the same amount of SPIO. For ferucarbotran-labeled cells, a similar trend is observed with MP relaxometry (Figure 47B,D). Compared to cells in saline, MPI sensitivity was reduced by 21% and resolution by 11% for cells in 5% agarose, however these results were statistically non-significant. The images of ferucarbotran-labeled cells in saline and 5% agarose produce similar observable MPI signal (Fig. F).

#### 7.2.2.4 Conclusion

As agarose concentrations increase a relative reduction in MPI amplitude (sensitivity) and increase in FWHM (resolution) are observed for ferucarbotran. This is likely due to partial immobilization of SPION within agarose suspensions that contribute to delayed magnetic relaxation<sup>7</sup>. Changes in sensitivity and resolution with agarose concentration were non-significant for ferucarbotran-labeled cells. We reason that cellular internalization of ferucarbotran may shield the SPIONs from experiencing the surrounding environment. This work contributes to our understanding of how the surrounding environment can influence SPION relaxation. This has important implications for in vivo imaging and quantification of SPIONs using MPI.



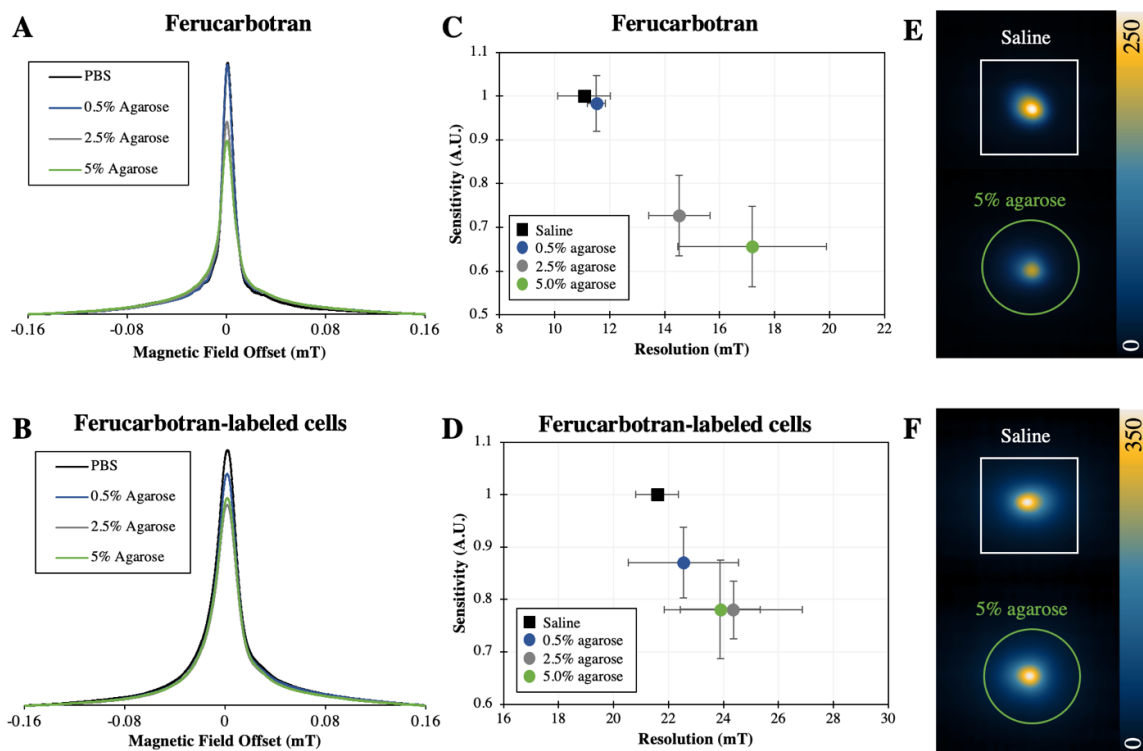


**Figure 47: MPI relaxometry curves for ferucarbotran (A) and ferucarbotran labeled cells (B) in saline, 0.5%, 2.5%, or 5% agarose. The adjacent plots show measurements of sensitivity and resolution from these curves (C, D). MPI images of ferucarbotran (E) in saline or 5% agarose also show differences in MPI signal intensity and resolution, but ferucarbotran-labeled cells (F) do not.**

#### 7.2.2.4.1 References

1. Saritas, Emine U., et al. "Magnetic particle imaging (MPI) for NMR and MRI researchers." *Journal of Magnetic Resonance* 229 (2013): 116-126.
2. Sehl, Olivia C., et al. "A perspective on cell tracking with magnetic particle imaging." *Tomography* 6.4 (2020): 315-324.
3. Utkur, Mustafa, Yavuz Muslu, and Emine Ulku Saritas. "Relaxation-based color magnetic particle imaging for viscosity mapping." *Applied Physics Letters* 115.15 (2019): 152403.
4. Salati, Mohammad Amin, et al. "Agarose-based biomaterials: opportunities and challenges in cartilage tissue engineering." *Polymers* 12.5 (2020): 1150.
5. Yang, Yueh-Hsun Kevin, Courtney R. Ogando, and Gilda A. Barabino. "In vitro evaluation of the influence of substrate mechanics on matrix-assisted human chondrocyte transplantation." *Journal of Functional Biomaterials* 11.1 (2020): 5.
6. Sehl, Olivia C., and Paula J. Foster. "The sensitivity of magnetic particle imaging and fluorine-19 magnetic resonance imaging for cell tracking." *Scientific Reports* 11.1 (2021): 1-12.
7. Arami, Hamed, and Kannan M. Krishnan. "Intracellular performance of tailored nanoparticle tracers in magnetic particle imaging." *Journal of Applied Physics* 115.17 (2014): 17B306.

### 7.2.3 $^{19}\text{F}$ MRI detection of PFC+ PBMC after intraperitoneal administration to mice

This work was completed by Olivia Sehl, Corby Fink, Gregory Dekaban, and Paula Foster.

#### 7.2.3.1 Introduction

Peripheral blood mononuclear cells (PBMC) are a heterogeneous cell population comprised of monocytes, dendritic cells, T and B lymphocytes, and NK cells. PBMC can be isolated from whole blood as precursors to an FDA-approved immunotherapy for prostate cancer (Sipuleucel-T, PROVENGE)<sup>1-4</sup>. PBMC are considered an attractive alternative to DC immunotherapies since they are less expensive and less complicated to prepare. For PBMC therapy, the magnitude of the tumor-specific T cell response is proportional to the number of PBMC that migrate to secondary lymphoid tissues<sup>3,4</sup>. Therefore, it is crucial to know whether the cells have migrated to lymph nodes (LNs) and spleen, and in what quantity.

Fluorine-19 MRI has the potential to answer these fundamental questions. The first report of PBMC labeling with PFCs was in 2018 (ref<sup>3</sup>). Greater than 99% of PBMC were labeled without affecting functionality (proliferation, antigen presentation) or viability. PFC labeling was reported to vary between donors and was related to the heterogeneity of the cell population and differences in cell lineage percentages with each donor. Subsequently<sup>4</sup>, it was determined that PBMC treatment with granulocyte macrophage colony-stimulating factor (GM-CSF) improved PFC uptake by PBMC and the migration of PBMC to lymph nodes. With GM-CSF treatment, PBMC migration to lymph nodes could be detected in 6 of 8 mice, whereas without treatment only 1 of 8 mice had detected migration with  $^{19}\text{F}$  MRI at 9.4 T. Then our group showed that  $^{19}\text{F}$  MRI at 3 Tesla can be used to visualize and quantify perfluorocarbon (PFC)-labeled PBMC migration to lymph nodes following intradermal administration to the mouse footpads<sup>4</sup>. In this section, we sought to track PFC-labeled PBMC following intraperitoneal administration to mice as an exploratory study. This work has not been published in a scientific journal.

### 7.2.3.2 Methodology

Human PBMC were collected from peripheral blood, treated with GM-CSF, and labeled through co-incubation with 5 mg/mL PFC as described in ref<sup>4</sup>. Five million PFC-labeled cells were administered to the intraperitoneal cavity of Nu/Nu mice (n = 2). Mice underwent <sup>1</sup>H/<sup>19</sup>F MRI at both 24 and 48 hours post injection on a 3 T clinical MRI scanner (MR750, GE Healthcare) using the same protocol as described in Tregs (Part 5.2.10). Image analysis and quantification were also conducted in the same way (Part 5.2.10).

### 7.2.3.3 Results

PBMC were labeled with an average of  $2.03 \times 10^{12}$  <sup>19</sup>F/cell. As previously reported, nearly 100% of PBMC were labeled and the labeling process did not significantly alter cell viability or the % composition of each cell type in PBMC<sup>4</sup>. 24 and 48 hours following *in vivo* administration to the mouse intraperitoneal cavity, <sup>19</sup>F signals were observed in the mouse popliteal LNs, inguinal LNs, and the spleen (Figure 48). The total number of cells detected at lymph nodes was  $7.01 \times 10^5$  PBMC (14% I.D.) at 24h p.i. and  $1.43 \times 10^5$  PBMC (3%) at 48h p.i. The number of PBMC quantified in the spleen was  $7.38 \times 10^5$  cells (15% I.D.) at 24h p.i. and  $5.93 \times 10^5$  cells (12% I.D.) at 48h p.i.

### 7.2.3.4 Conclusion

Here we demonstrate detection and quantification of PFC-labeled PBMC which accumulate at lymph nodes and the spleen after intraperitoneal administration. Splenic homing of cells is a new finding for our group since with previous SPION-based MRI cell tracking, it is challenging to identify signal voids in the spleen which is surrounded by tissues of varying image contrast. Comparatively, <sup>19</sup>F MRI identifies with hotspot signals the presence of these PFC<sup>+</sup> cells in the spleen and with quantitation (15% I.D. at 24h p.i.). Interestingly, we can compare % migration of PBMC to lymph nodes after intraperitoneal administration to intradermal administration<sup>4</sup>. At 24h p.i., on average 21% I.D. PBMC were quantified in lymph nodes after intradermal administration compared to 14% I.D. after intraperitoneal. At 48h p.i., on average 9% I.D. PBMC were quantified in lymph nodes after intradermal administration compared to 3% I.D. after intraperitoneal

administration. This suggests that the route of administration could impact the therapeutic efficacy (*i.e.*, the number of PBMC reaching secondary lymphoid tissues) but no statistical comparisons were made owing to low sample sizes ( $n = 4$  intradermal,  $n = 2$  intraperitoneal administration). In Chapter 5 of this thesis, unlabeled PBMC are administered to mice by intraperitoneal injection prior to administration of PFC-labeled Tregs. The data from this supplemental work supports that PBMC populate lymph nodes and spleen prior to Treg administration. Overall,  $^{19}\text{F}$  cell tracking has played a central role to understand the fate of PBMCs after administration and could help to improve therapeutic benefit for receiving PBMC treatments<sup>3</sup>.

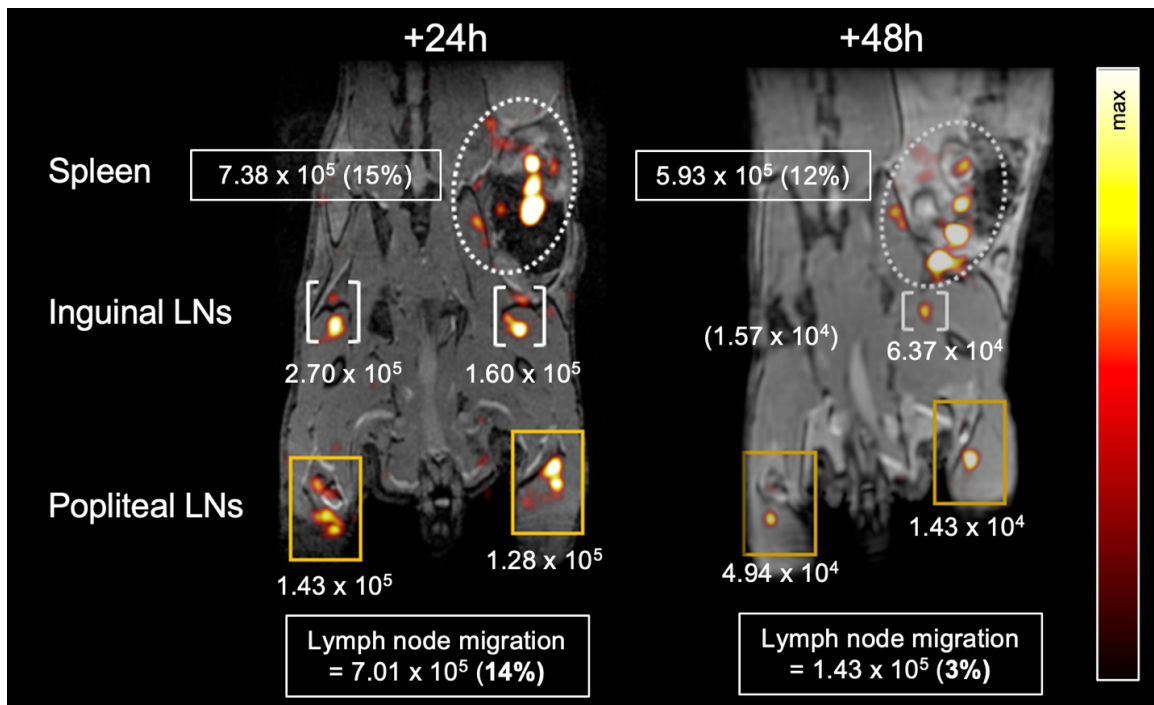


**Figure 48:  $^{19}\text{F}/^1\text{H}$  MRI overlay of mice showing detection of  $5 \times 10^6$  PFC+ PBMC after intraperitoneal administration. PFC+ cells accumulate in popliteal lymph nodes (LNs), inguinal lymph nodes, and the spleen. The measurement of cells from each lymph node is indicated. Images were acquired both at 24 and 48 hours after administration. The color scale bar represents  $^{19}\text{F}$  spins.**

### 7.2.3.5 References

1. Handy, Catherine E., and Emmanuel S. Antonarakis. "Sipuleucel-T for the treatment of prostate cancer: novel insights and future directions." *Future oncology* 14.10 (2018): 907-917.
2. Small, Eric J., *et al.* "Placebo-controlled phase III trial of immunologic therapy with sipuleucel-T (APC8015) in patients with metastatic, asymptomatic hormone refractory prostate cancer." *J clin Oncol* 24.19 (2006): 3089-94.
3. Fink, Corby, *et al.* "<sup>19</sup>F-perfluorocarbon-labeled human peripheral blood mononuclear cells can be detected in vivo using clinical MRI parameters in a therapeutic cell setting." *Scientific reports* 8.1 (2018): 590.
4. Fink, C., *et al.* "Quantification and characterization of granulocyte macrophage colony-stimulating factor activated human peripheral blood mononuclear cells by fluorine-19 cellular MRI in an immunocompromised mouse model." *Diagnostic and Interventional Imaging* 101.9 (2020): 577-588.

## 7.3 Appendix C: Permissions

Sehl, O. C., Makela, A. V., Hamilton, A. M., & Foster, P. J. (2019). Trimodal cell tracking *in vivo*: combining iron-and fluorine-based magnetic resonance imaging with magnetic particle imaging to monitor the delivery of mesenchymal stem cells and the ensuing inflammation. *Tomography*, 5(4), 367-376.

Sehl, O. C., Gevaert, J. J., Melo, K. P., Knier, N. N., & Foster, P. J. (2020). A perspective on cell tracking with magnetic particle imaging. *Tomography*, 6(4), 315-324.

### Copyright and Licensing

For all articles published in MDPI journals, copyright is retained by the authors. Articles are licensed under an open access Creative Commons CC BY 4.0 license, meaning that anyone may download and read the paper for free. In addition, the article may be reused and quoted provided that the original published version is cited. These conditions allow for maximum use and exposure of the work, while ensuring that the authors receive proper credit.

In exceptional circumstances articles may be licensed differently. If you have specific condition (such as one linked to funding) that does not allow this license, please mention this to the editorial office of the journal at submission. Exceptions will be granted at the discretion of the publisher.

Sehl, O. C., & Foster, P. J. (2021). The sensitivity of magnetic particle imaging and fluorine-19 magnetic resonance imaging for cell tracking. *Scientific Reports*, 11(1), 1-12.

### Author reuse

Authors have the right to reuse their article's Version of Record, in whole or in part, in their own thesis. Additionally, they may reproduce and make available their thesis, including Springer Nature content, as required by their awarding academic institution.

Authors must properly cite the published article in their thesis according to current citation standards.

Sehl, O. C., Tired, B., Berih, M. A., Makela, A. V., Goodwill, P. W., & Foster, P. J. (2022). MPI region of interest (ROI) analysis and quantification of iron in different volumes. *International Journal of Magnetic Particle imaging* 8(1).

#### IWMPI & IJMPI - Copyright and Licensing

Authors retain the copyright of their manuscripts. All open access articles are licensed under the Creative Commons Attribution 4.0 International License (CC BY 4.0): <https://creativecommons.org/licenses/by/4.0/>. That means, licensees are free to share a copy and redistribute the material in any medium or format and to adapt, i.e. remix, transform, and build upon the material, for any purpose, even commercially. The authors cannot revoke these freedoms as long as you follow the license terms:

**Attribution** — The licensee must give appropriate credit, provide a link to the license, and indicate if changes were made. The licensee may do so in any reasonable manner, but not in any way that suggests the licensor endorses you or your use.

**No additional restrictions** — The licensee may not apply legal terms or technological measures that legally restrict others from doing anything the license permits.

The use of general descriptive names, trade names, trademarks, and so forth in this publication, even if not specifically identified, does not imply that these names are not protected by the relevant laws and regulations. The submitting author is responsible for securing any permissions needed for the reuse of copyrighted materials included in the manuscript.

While the advice and information in this journal are believed to be true and accurate on the date of its going to press, neither the authors, the editors, nor the publisher can accept any legal responsibility for any errors or omissions that may be made. The publisher makes no warranty, express or implied, with respect to the material contained herein.



## 7.4 Appendix D: Curriculum Vitae

**Name:** Olivia C. Sehl

### **Education**

09/18 – 05/23 **PhD Medical Biophysics (Molecular Imaging)**  
University of Western Ontario, London, ON

09/14 – 04/18 **BMSc Medical Biophysics**  
University of Western Ontario, London, ON

### **Scholarships and Awards**

09/20 – 08/23 **Canada Postgraduate Scholarship- Doctoral (PGS-D)**  
**(\$21,000/year)**  
Natural Science and Engineering Research Council (NSERC)

09/18 – 08/23 **Western Graduate Research Scholarship (WGRS)**  
**(\$5,000/year)**  
University of Western Ontario, Department of Medical Biophysics

10/22 **WIMIN Scholar Award (\$200)**  
Women in Molecular Imaging Network (WIMIN)

10/22 **Student Travel Stipend (\$500)**  
World Molecular Imaging Congress (WMIC)

08/22 **Norman E. Nixon & Marie Rämö Nixon Award (\$2,600)**  
Schulich Medicine & Dentistry Internal Graduate Awards

07/22 **Young Investigator's Award (\$250)**  
The Future of Molecular MR Conference (Pasadena, CA)

06/22 **Top Scoring Oral Presentation (\$200)**  
Robarts Research Retreat

03/21 **Trainee Educational Stipend (\$250)**  
International Society for Magnetic Resonance in Medicine (ISMRM)

09/19 – 08/20 **Canada Graduate Scholarship-Master's (CGSM) (\$17,500)**  
Natural Science and Engineering Research Council (NSERC)

09/18 – 08/19 **Ontario Graduate Queen Elizabeth II Scholarship (OGS)**  
**(\$15,000)**

- 09/18 – 08/19      **Translational Breast Cancer Research Unit (TBCRU) Scholarship (\$2,500)**  
London Regional Cancer Program, Breast Cancer Society of Canada
- 07/19                **Young Investigator’s Award (\$250)**  
The Future of Molecular MR Conference (St. John’s, NL)
- 05/18 – 04/18      **Cancer Research and Technology Transfer (CARTT) Summer Studentship (\$5,000)**  
London Health Sciences Center

### Related Work Experience

- 05/22 – 04/23      **Trainee Representative**  
Molecular and Cellular Imaging Study Group, International Society for Magnetic Resonance in Medicine (ISMRM)
- 01/21 – 04/23      **Graduate Research Assistant**  
Robarts Research Institute
- 10/19 – 04/23      **Research Mentor**  
Robarts Research Institute
- 09/18 – 04/23      **Journal Clubs**  
Translational Immuno-Oncology Research Group  
Molecular Imaging Collaborative Program
- 09/18 – 03/22      **Graduate Teaching Assistant**  
Department of Medical Biophysics

### Publications

1. Shalaby N., Kelly J., **Sehl O.C.**, Gevaert J.J., Fox M., Qi Q., Foster P.J., Thiessen J., Hicks J., Scholl T., Ronald J.A. Complementary early-phase magnetic particle imaging and late-phase positron emission tomography reporter imaging of mesenchymal stem cells *in vivo*. *Nanoscale* 7, January 2023.
2. Williams R.J., **Sehl O.C.**, Gevaert J.J., Liu S., Kelly J., Foster P.J., Ronald J.A. Dual magnetic particle imaging and akaluc bioluminescence imaging for tracking cancer cell metastasis. *Tomography* 9(1), 178-194, January 2023.
3. Gevaert J.J., Van Beek K., **Sehl O.C.**, Foster P.J. Vivotrax+ improves the detection of cancer cells with magnetic particle imaging. *International Journal of Magnetic Particle Imaging* 8 (1), October 2022.

4. **Sehl O.C.**, Tired B., Berih M.A., Makela A.V., Goodwill P., Foster P.J. MPI region of interest (ROI) analysis and quantification of iron in different volumes. *International Journal of Magnetic Particle Imaging 8 (1)*, August 2022.
5. Makela A.V., Schott M.A., **Sehl O.C.**, Gevaert J.J., Foster P.J., Contag C.H. Tracking the fates of iron-labeled tumor cells in vivo using magnetic particle imaging. *Nanoscale Advances*, July 2022.
6. Knier N.N., **Sehl O.C.**, Gevaert J.J., Makela A.V., Foster P.J. Imaging Neuroinflammation. Chapter 8: Magnetic Particle Imaging. Elsevier/Academic Press, Editors: Corree Laule and John Port. 2022.
7. **Sehl O.C.**, Makela A.V., Foster P.J. Fluorine magnetic resonance imaging: Methods and applications in biomedicine. Chapter: <sup>19</sup>F for quantitative tracking of immune cells involved in cancer progression and therapy. Editors: Ulrich Fogel and Eric Ahrens. 2022.
8. Dubois V.P., **Sehl O.C.**, Foster P.J., Ronald J.A. Visualizing CAR-T cell immunotherapy using 3 Tesla fluorine-19 MRI. *Molecular Imaging and Biology, Special Issue: Imaging in Immuno-oncology*, 1-11, November 2021.
9. **Sehl O.C.**, Foster P.J. The sensitivity of magnetic particle imaging and fluorine-19 magnetic resonance imaging for cell tracking. *Scientific Reports 11(1)*:22198, November 2021.
10. **Sehl O.C.**, Gevaert J.J., Melo K.P., Knier N.N., Foster P.J. A perspective on cell tracking with magnetic particle imaging. *Tomography 6(4)*: 315-324, December 2020.
11. Fink C., Smith M., **Sehl O.C.**, Gaudet J.M., Meagher T.C., Sheikh N., Dikeakos J.D., Reider M., Foster P.J., Dekaban G. Quantification and characterization of GM-CSF activated PBMC *in vivo* by fluorine-19 cellular MRI. *Diagnostic and Interventional Imaging*, 1278, January 2020.
12. Makela A.V., Gaudet J.M., Schott M.A., **Sehl O.C.**, Contag C.H., Foster P.J. Magnetic particle imaging of macrophages associated with cancer: Filling the voids left by iron-based magnetic resonance imaging. *Molecular Imaging and Biology*, 1-12, January 2020.
13. **Sehl O.C.**, Makela A.V., Hamilton A.M., Foster P.J. Trimodal cell tracking *in vivo*: Combining iron- and fluorine-based magnetic resonance imaging and magnetic particle imaging to monitor the delivery of mesenchymal stem cells and the ensuing inflammation. *Tomography 5(4)*: 367-376, December 2019.

### Conference Presentations

Oral: 20

Poster: 14